STUDIES ON NON-LINEAR CURRENT-VOLTAGE (I-V) CHARACTERISTICS IN DOPED SnO_2 AND RELATED SYSTEMS: SYNTHESIS AND CHARACTERIZATION

A thesis submitted to the

University of Pune

for the award of degree of

Doctor of Philosophy** in **chemistry

in faculty of science

By

Dhage S. R.

Physical and Materials Chemistry Division
National Chemical Laboratory
Pune-411 008, India

August 2005

Date: 29th August 2005

CERTIFICATE

This is to certify that the thesis entitled "**Studies on non-linear current-voltage (I-V) characteristics in doped SnO_2 and related systems: synthesis and characterization**" describe the original research work done by **Mr. Dhage S. R.** under my supervision for the degree of **Doctor of Philosophy** in **Chemistry** under the faculty of science of the **University of Pune**. Such material as has been obtained from other sources has been duly acknowledged in this thesis.

Dr. V. Ravi
Scientist
Physical and Materials Chemistry Division
National Chemical Laboratory
Pune-411 008, India

…DEDICATED TO MY BELOVED FAMILY

Acknowledgement

*I gratefully acknowledge my guide, **Dr. V. Ravi**, for his valuable guidance, timely help and contribution of time and energy to work.*

*I express my profuse heartful gratitude to **Dr. P. A. Joy**, for his encouragement and help during the course of my research work.*

*I would like to express my sincere appreciation and wholehearted thanks to **Dr. S. K. Date**, **Dr. H. S. Potdar,** and **Dr. S. B. Deshpande** for the great care they have taken to help and encourage me for the execution of my research work.*

I also wish to acknowledge the help and co-operation I received from all the Materials Characterization Laboratory (CMC) staff with special mention to Dr. S.R. Sainkar, Mr. A.B. Gaikwad, Mrs. Renu Pasricha, Dr. N.R. Pavaskar, Dr. S.D. Pradhan, Dr. S.P. Gokhale and Ms. Violet Samuel, catalysis division.

I express my sincere thanks to Dr. T. S. Mahata & Mr. R. Lenka, BARC Mumbai, and Prof. G. S. Kumar & Mr. Raghvendra, Osmania University, Hyderabad for allowing me to carry out the Impedance measurements in their lab and for useful discussions.

It is my pleasant duty to thank Mr. Dipak Jori for valuable support he has given throughout the course of this work. Mr. D. B. Harawade (Kaka) needs special acknowledgment for his good will and sincere help he rendered during my research work.

I have had great pleasure of working with Dr. Joly, Dr. Yogesh, Dr. Seema, Rajsankar, Shekhar, Sasanka and Ganga, my labmates. Their support and their friendship have meant a great deal to me. Their contributions have been enormous, boundless and I thank them for all their efforts wholeheartedly.

I like to thank Bhalchandra, for being a close friend and giving me the support I need.

My sincere thanks to Smitarani, Shalaka and Chandramohan for their help.

I gratefully acknowledge the considerable influence and encouragement from my dear friends Dushyant, Sachin, Vivek, Hasmukh, Prem, Nirmal, Niranjan, Jadab, Dipali, Girish, Mahima, Mrudula, Kannan, Vivek, Meera, Sudesh, Vijayanand, Shrija, Hrushikesh, Nivrutti, Nilkanth, Arun, Nagendra, Tatyarao, Narayan, Rajshekhar, Amit, Satyanarayana, Piplad, Sunil and many others.

I am thankful to each and every person who helped and supported me during this research period.

I am thankful to Head, Physical and Materials Chemistry Division and Director, NCL for allowing to submit this work in the form of Ph. D. thesis.

Department of Science and Technology, India is acknowledged for financial support.

Last but not least I am thankful to my beloved parents and brothers who have always been by my side in good and bad times…

Sanjay R. Dhage

Contents

Chapter 1 Introduction and literature survey

Chapter 2 Experimental

Chapter 3 Influence of various donors

Chapter 4 (Sn, Ti)O_2 solid solution

Chapter 5 Influence of rare earth

Chapter 6 Role of alkali earth

List of abbreviations

A	-Richardson's constant
a	-Lattice parameter
Å	-Angstrom
At. %	-Atom percent
C	-Capacitance
c	-Lattice parameter
C_{gb}	-Grain boundary capacitance
d	-d spacing
DTA	-Differential thermal analysis
E	-Applied field
e	-Electron charge
E_A	-Activation energy
E_B	-Breakdown field
eV	-Electron volt
f	-Frequency
FWHM	-Full width at half maxima
h	-Planck constant
hrs	-Hours
I	-Current
I_C	-Capacitive current
I_l	-Leakage current
I_R	-Resistive current
J	-Current density
K_B	-Boltzmann constant
m	-Electron mass

r	-Grain number per unit length
RT	-Room temperature
SEM	-Scanning electron microscope
T	-Temperature in Kelvin
TEM	-Transmission electron microscope
TGA	-Thermogravimetric analysis
T_M	-Maximum shrinkage rate temperature
TMA	-Thermal mechanical analyzer
V	-Voltage
XRD	-X-ray diffraction
Z	-Complex impedance
Z'	-Real resistance
Z''	-Imaginary resistance
β	Full width at half maxima
β	-Constant
Φ_B	-Barrier height
ρ	-Resistivity
ρ	-Density
α	-Non-linear coefficient
Γ	-Relaxation time
ω	-Barrier width
λ	-Wavelength of X-ray radiation
θ	-Angle of diffraction
θ	-Phase
ρ_g	-Grain resistivity
ρ_{gb}	-Grain boundary resistivity

Chapter 1

Introduction and literature survey

This chapter is comprised of general introduction about electroceramics and the importance of the present investigation for its potential applications. The detailed discussion on the most important performance parameters of the varistors and its application in various fields is based upon the earlier reports on ZnO, SnO_2 and other varistor systems.

1.1 Ceramics

Ceramics are nonmetallic, inorganic materials typically formed as powders and often sintered into useful forms [1]. The advance ceramics are developed from chemical synthesis routes or from naturally occurring materials that have been finely refined [2], semiconducting solids, solid oxide fuel cell electrodes, and thermally stable structural materials. Carbon materials obtained from graphite, diamond and carbon nanotubes are comprised of many useful physical properties found in ceramics [3]. Engineering ceramics are materials with exceptional mechanical properties such as stiffness, toughness, and low creep, which make them valuable in the manufacture of structural products like gears or electronic devices. Photooxidative stabilizers are often incorporated into structural polymers to help in preventing photodegradation [4].

A variety of new ceramics have been developed in the last 50 years. These are of particular interest for their unique and outstanding properties so as to indicate the active state of development in electrooptic ceramics such as $LiNbO_3$, La modified lead zirconate titanate (PLZT) and lead scandium niobate (PSN) for providing medium by which optical function can be performed on command of an electrical signal [5]. Ferrites ceramics and ferromagnetic materials have been considered for magnetic memory units in computers and are highly important for their electrical properties [6]. Ceramics used for repair and reconstruction of diseased or damaged part of the musculo-scalatol system termed as bioceramics, may be bioinert (e.g. Alumina and zirconia), resorbable (e.g. tricalcium phosphate), bioactive (e.g. hydroxyapatite, bioactive glasses and glass ceramics) or porous of tissue in growth (e.g. hydrooxyapatite coated metals) [7]. Nanostructured electroceramics are used as electrochemical devices for energy conversion and storage, e.g. several forms of carbon are being used for hydrogen storage, alkali doped carbon nanotubes and nanosize SiC powders are also being used [8]. Ceramic fuel cells conventionally termed as solid oxide fuel cell (SOFC) utilizes yettria stabilized zirconia (YSZ) containg typically 8 mole % Y as electrolyte: a ceramic metal composite (cermet) comprised of Ni + YSZ as the anode and $La_{1-x}Sr_xMnO_{3-\delta}$ (Lanthanum strontium mangnite or LSM) as the cathode [9]. A few functions, properties and application of the ceramics are listed in *Table I* [10].

Table I. Advanced ceramics classification according to function properties and the corresponding applications.

Function	**Properties**	**Application (example)**
Thermal	Insulation	High temperature furnace lining for insulation (oxide fibers e.g. SiO_2, Al_2O_3 and ZrO_2
	Refractoriness	High temperature furnace lining for insulation and containment of molten metals and slags
	Thermal conductivity	Heat sinks for electronic packages (AlN)
Electrical and dielectric	Conductivity	Heating elements for furnace (SiC, ZrO_2, $MoSi_2$)
	Ferroelectricity	Capacitors (Ba-titanate based materials)
	Low-voltage insulator	Ceramic insulation (porcelain, steatite, forsterite)
	Electronic insulators	Substrate for electronic packaging and electrical insulators in general (Al_2O_3, AlN)
	Hostile environments insulators	Spark plugs (Al_2O_3)
	Ion-conducting	Sensors, fuel cells and solid electrolytes (ZrO_2, β-alumina, etc.)
	Semiconducting	Thermistors and heating elements (oxides of Fe, Co, Mn)
	Nonlinear I-V characteristic (varistor)	Current surge protector (SiC, ZnO, SnO_2)
	Gas-sensitivity	Gas sensors (SnO_2, ZnO)
Magnetic and superconductive	Hard magents	Ferrite magnets [$(Ba,Sr)O.6Fe_2O_3$]
	Soft magents	Transformer cores [$(Zn,M)Fe_2O_3$ with M=Mn, Co, Mg]: magnetic tapes (rare-earth garnets)

	Superconductivity	Wires and SQUID magnetometers ($Yba_2Cu_3O_7$)
Optical	Transparancy	Windows (soda-lime glasses), cables for optical communication (ultra-pure silica)
	Translucency and chemical inertness	Heat and corrosion-resitantmaterials, usually for Na lamps (Al_2O_3, MgO)
	Nonlinearity	Switching devices for optical computing ($LiNbO_3$)
	IR transparency	Infrared laser windows (CaF_2, SrF_2, NaCl)
Nuclear	Fission	Nuclear fuel (UO_3, UC), fuel cladding (C, SiC) neutron moderators (C, BeO)
	Fusion	Tritium breeder materials (Zirconates and Silicates of Li, Li_2O); fusion reactor lining (C, SiC, Si_3N_4, B_4C_3)
Chemical	Catalysis	Filters (Zeolites); purification of exaust gases
	Anticorrosion	Heat exchange (SiC), chemical equipments in corrosive eiviornments
	Biocompatility	Artificial joint prostheses (Al_2O_3)
Mechanical	Hardness	Cutting tools (SiC whisker-reinforced Al_2O_3, Si_3N_4)
	High-temperature strength retention	Stators and turbine blades, ceramic engine (Si_3N_4)
	Wear resistance	Bearings (Si_3N_4)

1.2 Advanced ceramics

Advanced ceramics are spearheading new product designs and capabilities, from the insulating tiles of the space shuttle to new, lightweight automobile engine components, the electronics market has undergone remarkable changes in the past few decades. The advanced ceramics are generally classified as;

(a) Structural ceramics: Ceramics in structural applications are in use principally because of their ability to facilitate more efficient energy conversion, as in heat engines or heat exchangers are those used as cutting tools, wear components, heat exchanges and adiabatic engine components. The range of materials covers the major series of compounds derived from the ceramic oxide, carbide, nitride, boride and oxynitride chemical families are typical examples of structural ceramics.

(b) Coating materials: Coating is the process by which a surface is modified, yielding a composition or property gradient between the bulk and the surface. Coating is often performed to alter or improve properties of the component. Chemical vapours deposited (CVD) diamond for cutting tools and also for electronic application are examples of coating materials. Amorphous carbon films were prepared by means of Plasma Enhanced Chemical Vapour Deposition and Microwave Plasma Chemical Vapour Deposition [11]

(c) Eelectroceramics: They are used as insulators, substrate and other components used in electronic equipments. They include insulators, substrates, capacitors, integrated packages, magnetic ferrites, piezoelectric ceramics, semiconductors and superconductors. Materials such as barium titanate ($BaTiO_3$), Zinc oxide (ZnO), lead zirconate titanate ($Pb(Zr_xTi_{1-x})O_3$), lithium niobate ($LiNbO_3$), lanthanum strontium cuprate ($LaSrCuO_4$) are few of the materials that come under this category.

(d) Composites: These materials have two or more dissimilar constituents, which are used to display a combination of preferred characteristics of each of the components. One of the principal areas of composite growth has been in the toughening of structural ceramics though whisker and fiber reinforcements. For example, SiC-fiber and Si-C particulate reinforced Al_2O_3 now have many applications like cutting tools. In order to obtain high performance ceramics soft chemistry routes are applied for ultrastructural processing. Novel approach for optimized and improvement in powder processing and forming technology will improve the reliability of advanced ceramics [12]. The present investigation we give emphasis to electroceramics and detailed introduction is given in the next section.

1.3 Electroceramics

While ceramics have traditionally been admired for their mechanical and thermal stability, their unique electrical, optical and magnetic properties have become of increasing importance in many key technologies including communications, energy conversion and storage, electronics and automation. Such materials are now classified under *Electroceramics* as distinguished from other functional ceramics such as advanced structural ceramics. With the development and commercialization of new technologies such as mobile communication, personal computers and the internet, came the need for miniaturization and high-performance electroceramics.

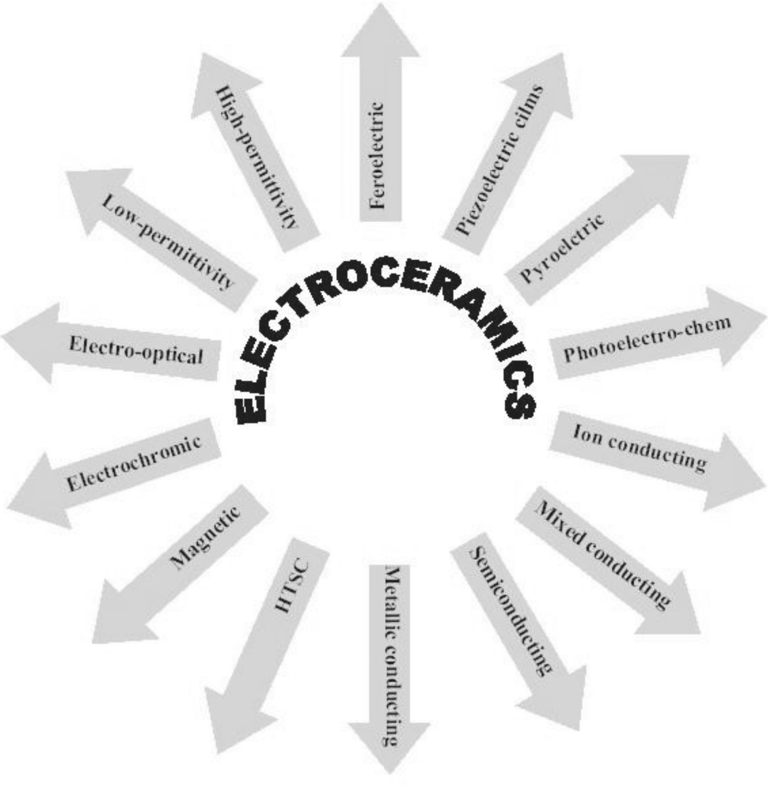

FIG. 1.1 Application of electroceramics.

Historically, developments in the various subclasses of Electroceramics have paralleled the growth of new technologies. Examples include: *Ferroelectrics* - high dielectric capacitors, non-volatile memories; *Ferrites*-data and information storage; *Solid Electrolytes* - energy storage and conversion; *Piezoelectrics*-sonar; *Semiconducting Oxides* -environmental monitoring.

The performance of electroceramics materials and devices depends on the complex interplay between processing, chemistry, structure at many levels and device physics and therefore it requires a truly interdisciplinary effort by individuals from many fields. Articles in the professional literature tend to deal with the processing, characterization, structure, properties, modeling and performance of electroceramics. *Fig 1.1* shows the wide area of application of electroceramics. A brief explanation of some of the types of electroceramic materials is discussed in the following section.

1.3.1 Piezoelectric, pyroelectric and ferroelectric materials

Piezoelectricity is defined as a change in electric polarization with a change in applied stress (direct piezoelectric effect). The converse piezoelectric effect is the change of strain or stress produced in the material due to an applied electric field. The microscopic origin of the piezoelectric effect is the displacement of ionic charges within a crystal structure. In the absence of external strain, the charge distribution within the crystal is symmetric and the net electric dipole moment is zero. However when an external stress is applied, the charges are displaced and the charge distribution is no longer symmetric and a net polarization is created. A material can be only piezoelectric, if the crystallographic unit cell has no center of inversion. Furthermore, a permanently-polarized material such as quartz (SiO_2) or barium titanate ($BaTiO_3$) will produce an electric field when the material changes dimensions as a result of an imposed mechanical force [13]. The standard piezoelectric material commonly in use for medical imaging processes is lead zirconate titanate (PZT). In some cases a crystal posses a unique polar axis even in the unstrained condition. This can result in a change of the electric charge due to the uniform change in temperature. This is called the **pyroelectric** effect. One of the most common thermal sensors used in the infrared (IR) applications is the pyroelectric detector. Pyroelectric sensors made from lithium tantalate ($LiTaO_3$) generate electric charges with small temperature changes, and are stable, uniform and durable.

Ferroelectric materials are a sub-class of pyroelectric materials in which the direction of the electric dipole can be reversed by applying an electric field. The number of ferroelectric materials known today includes large number of ceramic solid solution compositions. Most outstanding feature of ferroelectric ceramic is its hysteresis loop (polarization vs electric field). It describes the nonlinear polarization switching behavior as a function of field. Example of ferroelectric ceramics are barium titanate, lead zirconate titanate (PZT), lead niobate, bismuth titanate, sodium potassium niobate, lead titanate relaxor ferroelectrics and polymer composites [14]. **Electrostriction** is another electromechanical effect that exists in ferroelectric ceramics. In electrostriction the sign of the deformation that occurs with an electric field is independent of the polarity of the field and is proportional to the even powers of the field [15].

The application of piezoelectric, pyroelectric and ferroelectric materials, for sensing and actuation spans in most of the industrial sectors. This includes medical diagnostics such as ultrasonic imaging, aerospace such as accelerometers and micro-positioners, automotive such as solid-state piezoelectric fuel injectors, and chemical and process control, which requires the use of thermal, strain and force sensors.

1.3.2 Dielectric materials

Dielectric materials are insulators used for their exceptional dielectric properties. When a material is introduced between two plates of a capacitor, the total charge stored in the capacitor will change. The change depends on the ability of the material to polarize under an electric field. The dielectric constant or permitivity of a material determines the change in charge storage. For high capacity applications, a high dielectric constant is needed. Since the dielectric constant depends on the polarization in the material, ferroelectric materials are usually the materials of choice. High dielectric constant materials are also called **high K materials**. In some cases capacity is a side effect of the structure and needs to be minimized. For these applications material with a low dielectric constant is required. These materials are also referred to as **low K materials.**

This property is useful in capacitors, especially at radio frequencies. Dielectric materials are also used in the construction of radio-frequency transmission lines. In practice, most dielectric materials are solid. Examples include ceramic (typically alumina or aluminosilicates), mica, glass, plastics, and the oxides of various metals (for example, titanium, zirconium and hafnium oxides, or tantalum oxide) as well as multi-metallic oxides (for example barium strontium titanate) [16]. The dielelctric materials used for ceramic capacitor are classified as film capacitors, multilayer capacitor, barrier layer capacitor and grain boundary barrier layer (GBBL) capacitors [17].

1.3.3 Electro-optic and electro-chromic materials

The **electro-optic** effect is the change in the refractive index as a function of an externally applied electric field. In unisotropic materials the index of refraction depends on the direction of propagation and the direction of polarization of the light (optical birefingence). This means that the two components of light polarization can propagate at a different speed inside the material. This in turn causes a rotation of the overall polarization direction. Applying an electric field will change the index of refraction by a different amount for the two polarizations, causing further rotation of the polarization vector. By placing the electro-optic material between two polarizers one can control the amount of light passing through by changing the voltage. The electro-optic ceramic compositions are PLZT (La modified lead zirconate titanate) PSN (lead scandium niobate, $MgA1_2O_4$ (spinel), ALON (aluminium oxynitride), $A1_2O_3$-MgO (lucalox), MgO, MgF_2, CaO, CaF_2, Y_2O_3-ThO_2 (yttralox), etc. However, PLZT is the best optically-transparent ceramic material. The electrooptic properties of PLZT materials are intimately related to their ferroelectric properties. Consequently, varying the ferroelectric polarization with an electric field, such as in a hysteresis loop, also produces a change in the optical properties of the ceramic [15]. PLZT materials are also known to possess many special photosensitive phenomena that are directly linked to their microstructural, chemical, electronic and optical properties, including photoconductivity, photovoltaic properties, photo-assisted domain switching, ion-implantation-enhanced photosensitivity, photochromic effect, photomechanical (photostrictive) behavior, photorefractive effects and photoexcited space charge phenomena [18].

1.3.4 Photo-electro-chemical materials

Corrosion protection of metals and alloys is achieved by the formation of passive metal, which usually exhibits semiconductive properties. Photovoltaics, the conversion of sunlight to electrical power has been dominated by solid-state junction devices, often made of silicon [19].

1.3.5 Semiconductors, ionic conductors and mixed conductors

Most structural ceramics are known for their high resistance to charge transfer, and are therefore useful as electric insulators. Some electroceramics, however, are very useful for the exact opposite reason that they can accommodate charge transfer. There are several methods of conducting in ceramic materials. The first is electronic conduction, similar to that of metals, and the second is ionic conduction, where charged atoms serve as carriers. As mentioned before, **ionic conduction** is achieved by the movement of ions (atoms of positive or negative charge) through the solid. This transfer is usually done via point defects called vacancies in the crystal lattice. Such movement can require high energy, making ionic conduction very strongly dependent on temperature. Ionic conductors are useful in gas sensors, fuel cells and batteries. Materials that can accomodate electron conductivity as well as ionic conductivity are known as **mixed conductors**.

1.3.6 Magnetic materials and superconductors

Ceramics based materials compose a major share of both hard and soft magnetic materials. Permanent magnet applications are found in the aerospace, automotive, computer electronics, instrumentation, medical, telecommunications etc. These permanent or hard ferrite materials are part of family of complex oxide having the general composition $MO.6Fe_2O_3$ (eg: $SrO.6Fe_2O_3$, $BaO.6Fe_2O_3$) The performance characteristics of the **ferrites** are being improved following many chemical approaches. Soft magnets are important in many electrical and electronic systems. Soft ferrites can be classified further according to the frequency of use and crystal structure Mn-Zn, Ni-Zn and Mg-Zn ferrites are widely used soft ferrites depending on the frequency of interest. Under some conditions, such as extremely low temperature, some ceramics exhibit superconductivity. The exact reason for this is not known, but there are two major families of **superconducting** ceramics [20].

1.3.7 Responsive (smart) materials

Smart materials respond to environmental stimuli with particular changes in some variables. For that reason they are often also called responsive materials. Depending on changes in some external conditions, smart materials change their properties (mechanical, electrical, appearance), their structure or composition, or their functions. Mostly, smart materials are embedded in systems whose inherent properties can be favorably changed to meet performance needs.

1.3.8 Multilayer ceramic technology (MLC)

MLC is one of the most challenging growth areas in the ceramic industry today. The technology lends itself to computer control of the process, including the design and artwork, and this has become one of the most sophisticated ceramic technologies yet developed. Successful design of an MLC substrate depends on complete understanding of the green and fired properties of the ceramic and the metallurgy used and careful matching of shrinkage curves between metal and ceramic during firing.

1.4 Electroceramic sensors

Among the wide area of applications of electroceramic materials that are discussed above, the field of interest in this thesis is electroceramic sensors. Ceramic sensors have currently become an integral part of the society and are being used in a variety of fields like industry defense and various household appliances.

Table II. Ceramic materials which are applicable as sensors.

Sensor	*Output*	*Effect*		*Materials*	*Remarks*
Temperature	Change in resistance	Temperature changes carrier density	NTC	NiO, FeO, CuO, MnO, CoO, Al_2O_3, SiC	Thermometer, bolometer
			PTC	Semiconductive, $BaTiO_3$	Overheat protection sensor
		Semi-conductor metal phase transition		VO_2, V_2O_5	Thermal switch
	Change in magnetism	Ferrimagnetism paramagnetism transition		MnZn Ferrite	Thermal switch
	Electromotive force	Concentrated oxygen cell		Stabilized zirconia	High temperature corrosion resistance thermometer
Speed/ position	Change in Waveform of reflected wave	Piezoelectric effect		PZT: ($PbTiO_3$, $PbZrO_3$)	Fish finder, flaw detector, blood flow meter
Opto	Electromotive force	Cooling effect		$LiNbO_3$,$LiTaO_3$, PZT, $SrTiO_3$	IR Detection
		Anti-stokes measuremants		LaF_3 (Vb, Pr)	IR Detection
		Progressive wave doubling effect		Piezoelectrics, LiNbO3 $Ba_2NaNb_3O_{15}$,	
	Visible light	Fluoresence		ZnS (Cu, Al), Y2O2S(Eu)	Color TV CRT
				ZnS (Cu, Al)	X-ray monitor
		Thermal fluorescence		CaF_2	Thermal fluorescence dosimter
Gas	Change in resistance	Inflamable gas contain combustion reaction heat		Pt catalyst/ aluminium pt line	Inflammable gas thermometer and alarm

		Migration of charge due to adsorption and desorption of gas from an oxidised semiconductor	SnO_2, In_2O_3, ZnO, WO_3, NiO, γ-Fe_2O_3, NiO, CoO, Cr_2O_3, TiO_2, $LaNiO_3$, (La, Sr)CoO_3, (Ba, La)TiO_3	Gas alarm
		Temperature changes in thermistor due to gas heat conductive dissipation	Thermistor	High-density gas sensor
		Stochimetric change in oxide semiconductor	TiO_2, CoO, MgO	Automobile exhaust gas sensor
	Electromotive force	High temperature solid electrolyte concentrated oxygen cell	Stabilized zirconia (ZrO_2, CaO, ZrO_2, Y_2O_3, La_2O_3)	Exhaust gas sensor
	Amount of electricity	Coulomb titration	Stabilized zirconia	Lean combustion oxygen sensor
Humidity	Change in resistance	Moisture absorption in conductivity	LiCl, P_2O_5, ZnO, Li_2O	Hygrometer
		Oxide semiconductor	TiO_2, $NiFe_2O_4$, ZnO, $MgCr_2O_4$, Ni ferrite, Fe_3O_4 colloid	Hygrometer
	permittivity	Change in permittivity due to moisture absortion	Al_2O_3	Hygrometer
Ion	Electromotive force	Solid electrolytic film concentrated cell	AgX, LaF_2, Ag_2S_3, Thin glass film CaS, AgI	Ion concentration sensor
	Resistance	Gate adsorption effect MOSFET	Si (Gate material II for Si_3N_4/ SiO_2, S_2 for :Ag_2S, Xfor: AgX, PbO	Ion sensitivity FET (II SET

Electroceramics are ceramic materials that have been specially formulated for specific electrical, electro-magnetic or optical properties. Their properties can be tailored for operation as insulators, ferroelectric materials, highly conductive ceramics, electrodes as well as sensors and actuators. Key factors in developing electroceramics include the presence of ionic-covalent bonding, microstructures comprising inorganic crystal compounds and/or amorphous glass in varying proportion and thermal processing conducted at elevated temperatures. Electroceramics include dielectric ceramics, ferrites, ferrogarnets, electrorestrictive ceramics, and piezoelectric ceramics. In addition to the above classification, *Table II* [21] gives a listing of these electroceramic materials, which are applicable as sensors.

1.5 Voltage sensors or varistors

Despite its many benefits, one of the few drawbacks of semiconductor technology is the vulnerability of solid-state devices to over voltages. Even voltage pulses of very low energy can produce interference and damage, sometimes with far-reaching consequences. So, as electronics makes its way into more and more applications, optimum over voltage or transient suppression becomes a design factor of decisive importance. The power fluctuations/over-voltage usually encountered due to natural lightning and switching operations can permanently damage the electronic/electrical devices. It is essential to suppress/bypass these over voltages to protect the sensitive components/device. A device which performs the duty of protecting electronic/electrical device is called the voltage sensors/Voltage dependent resistors (VDR) or transient voltage suppressor or surge arrestors or more popularly called the VARISTOR. Varistors (**Var**iable Res**istors**) are voltage-dependent resistors with a symmetrical *V/I* characteristic curve (*Fig 1.2*) whose resistance decreases with increasing voltage. Connected in parallel with the electronic device or circuit that is to be guarded, they form a low-resistance shunt when voltage increases and thus prevent any further rise in the over voltage. In early days, spark gaps were used for over voltage protection and guarding the sensitive device. Spark gaps and gas tubes are crowbar devices that change from an insulator to an almost ideal conductor during an over voltage. These spark gaps remains short-circuited after the first spark and hence were not repeatedly usable. The development of Silicon carbide (SiC) based voltage sensors have occurred around 1930 [22]. Silicon carbide varistors [23] were the most common type of varistor used before the metal oxide varistors.

Made from specially processed silicon carbide, they handle high-power, high-voltage surge arrester applications. However, the relatively low impedance values of this material produce one of the following two results. Either the protective level is too high for a device capable of withstanding line voltage or for a device producing an acceptable protective level, excessive standby current would be drawn at normal voltage if directly connected across the line. Therefore, they require a series gap to block the normal voltage. **Silicon avalanche diodes** find use in both low-voltage dc applications and in higher voltage ac mains protection. Avalanche diodes have a wider junction than a standard zener diode, which gives them a greater ability than a zener to dissipate energy. The biggest disadvantage to using the avalanche diode as a transient suppressor on an ac mains line is its low peak current handling capability. The main breakthrough in the field of over voltage protectors/limiters came when in 1969 Matsuoka et al [24] announced the development of varistors based on Zinc oxide compositions. His more detailed paper describes many of the essential features of varistors, as we know them today [25]. When exposed to surges, the zinc oxide material exhibits a bulk action characteristic, permitting it to conduct large amounts of current without damage. Metal oxide varistor (MOV) are cost and size effective, are widely available, and do not have a significant amount of overshoot. They have no follow-on current and their response time is often sufficient for the types of transients encountered in the ac mains environment.

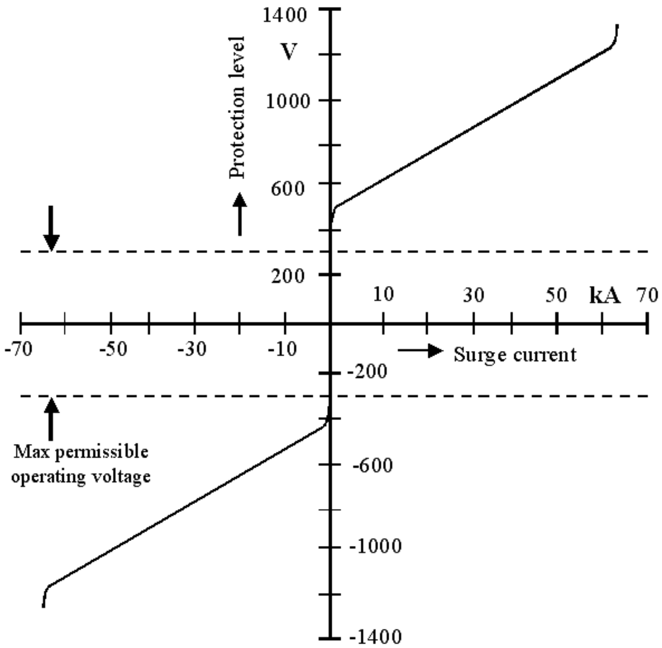

FIG. 1.2 Typical I-V characteristics of varistors on linear scale.

1.6 Zinc oxide varistors

Zinc oxide varistors [26] are nonlinear two-electrode semiconductor voltage-dependant resistors. The current in a varistors is proportional to applied voltage raised to a power. Upon application of a high voltage pulse (such as lighting) they conduct a large current, thereby absorbing the pulse energy in the bulk of the material with only a relatively small increase in voltage, thereby protecting the circuit and to do so repeatedly without being destroyed. The ZnO based ceramic semiconductor devices with highly nonlinear current-voltage characteristics are similar to back to back Zener diodes but with much greater current and energy handling capabilities [25, 27].

Zinc oxide varistors are ZnO based ceramic semiconductor device with highly nonlinear current-voltage characteristics. *Fig 1.3* shows typical current-voltage (I-V) curve of a practical varistor. The device can be regarded as 'insulating' up to a certain field, the breakdown field (E_B) above which it becomes highly conducting. Varistor is variable resistor whose resistance is a function of the applied voltage. The current-voltage behavior can be divided into three regions [28].

(i) Under the low applied voltage, the varistor functions as an open circuit, (No or small conductivity, which satisfies Ohm's law (linear behavior))

(ii) At voltage above certain critical value, its resistance decreases, enabling a large current to flow though the varistor, indicating that the varistor becomes short-circuited and does not obey Ohm's law (nonlinear behavior)

(iii) If the voltage is further increased, beyond the critical value, the varistor again behaves like linear device

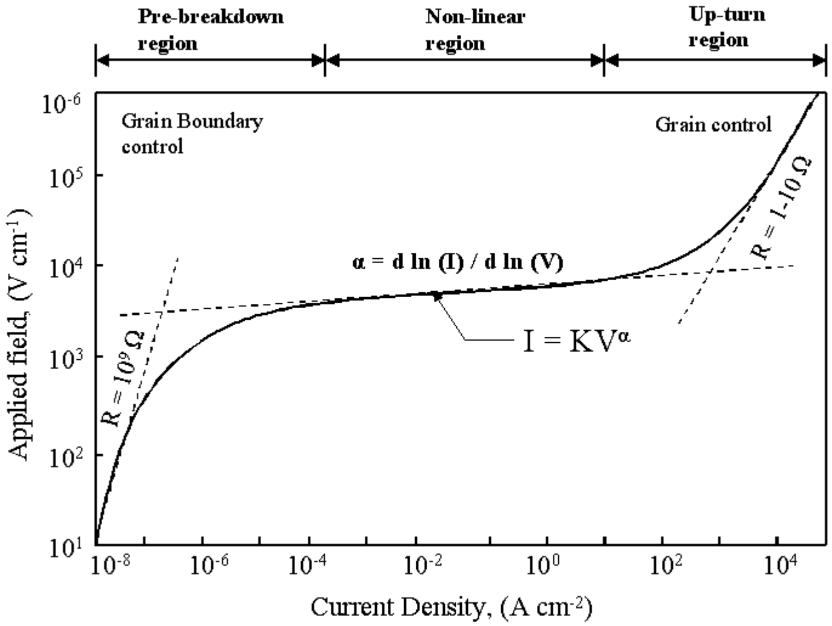

FIG. 1.3 Typical Current-Voltage curve of practical varistor.

These features of a varistor indicate that it is a voltage dependent resistor (VDR), whose primary function is to sense and limit the transient voltage surges and to do so repeatedly without getting itself destroyed. ZnO is distinguished by minimal leakage current under normal conditions of operation and an excellent protection level in pulse applications, resulting in low continuous power dissipation and minimal residual voltage. These features can be highlighted by referring to three important regions of the curve.

(A) Leakage/Low-Current/ Prebreakdown, Linear region

The I-V characteristic is ohmic in this region ($<10^{-4}$ A cm^{-2}) and is defined as pre-breakdown region. The ac current is about 2 orders of magnitude higher than the dc current for a given operating voltage. The difference can be attributed to the contribution of the dielectric loss upon application of an ac voltage. The total ac current is composed of capacitive current (I_C) and a resistive current (I_R) and is determined by the impedance of the grain boundaries.

(B) Varistor/Intermediate, Nonlinear region

The nonlinear region of the intermediate current is the heart of ZnO varistors, wherein the device conducts an increasingly large amount of current for a small increase in voltage. The nonlinear region may extend over 6 to 7 orders of magnitude of current. In the nonlinear regime, the relation between current and voltage is often expressed in terms of power law

$I \propto V^{\alpha}$

Where V is the applied voltage, I is the current passing through the varistor and α is the nonlinearity exponent. The degree of nonlinearity is determined by the flatness of the nonlinear region, the flatter the I-V curve in this region, the better the device.

(C) Upturn/High Current region

In the high current region ($>10^{3}$ A cm^{-2}), the I-V characteristic is again linear, similar to that of low-current region, with the voltage rising faster with current than in the nonlinear region. This is also known as up-turn region. This region is controlled by the impedance of grain in the microstructure. As a result of dopants which are known to control electrical resistivity of the grains exercise great influence on the high current upturn properties.

To characterize a varistor device, it is desirable to determine the I-V curve for all three regions of the varistor. However due to the wide range of currents involved, it is not possible to use the same measurement technique for all regions. Usually, I-V characteristic below 100 mA cm^{-2} are measured by dc or 60-Hz and those above 1 mA cm^{-2} are measured by impulse current with a typical waveshape of 8-μs rise time to peak value, and 20-μs decay time to half the peak value (known as 8 x 20 μs waveshape)

1.6.1 Performance parameters of varistor

The two most important performance parameters of the varistors are the Non-linear coefficients (α) and breakdown field (E_B). There are several critical application parameters which are associated with the various regions of the I-V curve and which serve various functions in the design and operation if a surge protector which, are important in commercial point of view. The performance parameter for device application are summarized in *Table III*

Table III. Parameters for Device application.

Parameter	Function	Equation*
Nonlinear coefficient	Protective level	$I = (V/C)^{\alpha}$
Nonlinear voltage	Voltage rating	$C = V/I^{1/\alpha}$ V at 1 mA
Leakage current	Watt loss/operating voltage	$I_R = V_{ss}/R_{gb}$
Life	Stability	$P_G < P_D$
Energy absorption	Survival	J = IVT

I is current, V is voltage, C is a constant, I_R is resistive current, V_{ss} is steady-state voltage, R_{gb} is grain boundary resistance, P_g is power generated, P_D is power dissipated, J is joules, and t is time.

(a) Nonlinear coefficient (α)

The most important parameter of the varistor is the nonlinear coefficient (α), the varistor characteristic follows the equation:

$I = kV^{\alpha}$

Where V is applied voltage across the sample, I is the current flowing through the sample k is a constant related to material and the exponent α defines the degree of nonlinearity. Alpha is a figure of merit and can be determined from the slope of the V-I curve or calculated from the formula:

$\alpha = \ln (I_2/I_1)/ \ln (V_2/V_1)$

Where V_1 and V_2 are the voltages at currents I_1 and I_2 ($I_1 < I_2$)

The α value increases in pre-breakdown region, reaches a maximum value in the breakdown region and then diminishes in the upturn region. Because of this change in α value with current, it is important to determine the value of α with reference to the magnitude of currents over which the application is desired.

(b) Breakdown/Nonlinear field (E_B)

The ZnO varistor is characterized by a voltage, which marks the transition from linear to nonlinear mode. The voltage at the onset of this nonlinearity, just above the 'knee' of the I-V curve, is the nonlinear voltage, which determines the voltage rating of the device. Because of a lack of sharpness of the transition in the I-V curve (Fig 1.3), the exact location of this voltage is difficult to determine in most varistors. However from equation below, the nonlinear voltage can be defined as:

$C = V/I^{1/\alpha}$ V at 1 mA

So, the convention followed by the researchers in this area is by defining the breakdown voltage as the voltage observed when 1 mA current flows through the system. The breakdown voltage of the varistor is controlled by the grain size and the thickness of the material. For a given grain size, the breakdown voltage of the varistor can be manipulated to suit the application by changing the device size.

To calculate varistor parameters, the current density, J (A cm^{-2}) Vs Applied field, E (V cm^{-1}) curves were plotted on log scale from which the slope of this curve in the nonlinear region directly give the value of nonlinear coefficient (α) and the voltage corresponding to 1 mA as the breakdown voltage which can be calculated from the curve. The factors that influence the nonlinear coefficient, breakdown voltage and other performance parameters (energy handling capability and life time) are well studied [29].

1.6.2 Microstructure of ZnO varistors

ZnO varistors are polycrystalline materials composed of n-type semiconducting ZnO grains with their attendant insulating grin boundaries. The resistivity of ZnO grain is 1-10 ohm-cm. The grain boundaries are highly resistive and show non-ohomic properties. The breakdown voltage per grain boundaries is about 3 V. The breakdown voltage of the sintered body is proportional to the number of grain boundaries between the two electrodes. This indicates that the breakdown voltage is proportional to the inverse of the ZnO grain size. The size of the ZnO grains are usually 5-20 µm and depend on the material composition, sintering temperature and time. The microstructure of the ZnO varistor has been extensively studied and several reviews are available in the literature [30].

During the heat treatment of ZnO with the appropriate amount of additives e.g. Bi_2O_3, Sb_2O_3, Co_3O_4, Cr_2O_3, SiO_2, MnO_2, MgO, BaO Al_2O_3 etc, the phases forms are ZnO, Spinel, Pyrochlore, and many bismuth rich phases as listed in *Table IV*

The research efforts have led to a microstructural electrical model for ZnO varistor. During the processing time, various dopants species are distributed in the matrix in such a way that the near grain boundary region becomes highly resistive ($\rho_{gb} \approx 10^{12}$ ohm-cm) and the grain interior highly conductive ($\rho_g \approx 1$ to 10 ohm-cm)

Table IV. Microstructural components of the ZnO varistor comprising various crystalline phases, their chemical formulation and dopants in various phases.

Compound	Chemical formulation	Doping element	Location
ZnO	ZnO	Co, Mn	Grains
Spinel	$Zn_7Sb_2O_{12}$	Co, Mn, Cr	Intergranular phase
Pyrochlore	$Bi_2(Zn_{4/3}Sb_{2/3})O_6$	Co, Mn, Cr	Intergranular phase
Bi-Rich phase	$12Bi_2O_3.Cr_2O_3$	Zn, Sb	Triple point
	$14Bi_2O_3.Cr_2O_3$	Mg, Al	
	δ-Bi_2O_3		
	β-Bi_2O_3		
	$12Bi_2O3.SiO_2$		

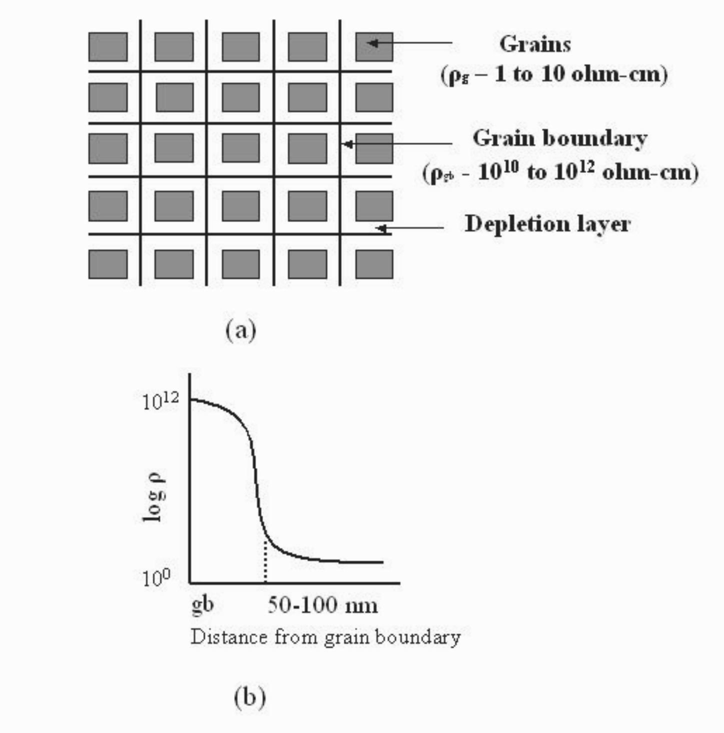

FIG. 1.4 Schematic of microstructure and electrical characteristics: (a) grain versus grain boundary resistivity (b) resistivity profile at depletion layer

Fig 1.4 (a) shows the schematic diagram of varistor microstructure. Here we presume the device to be made conducting ZnO grains, shown by squares, separated by insulating grains boundaries (thick lines). A sharp drop in resistivity occurs from the grain boundary to grain within a distance of few nanometer length (≈ 100 nm) known as the depletion layer. This steep drop is shown schematically in *Fig 1.4 (b)*

This understanding of the grain and grain boundary distribution and their resistivity has led to the correlation of the microstructural and electrical properties. When a voltage is applied to a varistor in the pre-breakdown region, the leakage current is entirely controlled by the grain boundary impedance and the high current region or the upturn region is entirely controlled by the impedance of the grain. The intermediate non-linear region is indirectly controlled by the resistivity differential between the grain boundary and grain.

The breakdown voltage of a varistor can also be controlled by the change in microstructure. For a given varistor, the breakdown voltages corresponding to singly barrier will be relatively constant, at all the point in the sample. Therefore, if a sample of given thickness is taken, we can change the breakdown voltage of that device by changing the grain size. If E_{gb} is considered as the breakdown voltage per grain boundary, E_B is the breakdown voltage per mm of the sample and n_g is the number of grains per mm of the sample, then

$E_{gb} = E_B/n_g$

Hence it is clear from the equation that for a given sample size, the breakdown voltage can be manipulated by changing the grain size. Similarly for a given grain size, the breakdown voltage can be changed by increasing or decreasing the thickness of the varistor dense compacts.

1.6.3 Microstructural development of varistor

Varistor properties are changed by changing the microstructure and by creating intermediate energy states in the ZnO grains and grains boundary structures. This is brought about by dopants distribution in the sample. This particular area in the materials science where the properties of the varistor are engineered to suit the application known as microstructural engineering of varistor [31].

ZnO has wurtzite structure. In this structure, the oxygen atoms are arranged in a hexagonal close packed type of lattice with Zn atoms present at half the tetrahedral sites. Zn and O atoms are tetrahedrally coordinated to each other. The ZnO structure is then relatively open with half the octahedral sites being empty. There are enough empty sites available to accommodate the dopants, which have considerable influence on the nature of defects and mechanism of diffusion of defects in ZnO structure. The band gap of ZnO has been found to be 3.3 eV. It is known that thermodynamically formed natural defects occupy the donor and acceptor levels within the band gap. The natural defects that are formed during the thermodynamic process are discussed in the review [26(b)].

The study of grain boundary is more difficult since the grain boundary itself, a defect between two grains The microstructure of varistor is such that the grain boundary has an excess negative charge of acceptor defect that are balanced by equal an apposite positive charge of donor defect that penetrate some distance into the grains and thereby forming the depletion layer.

The important aspect of grain boundary can be summarized as (i) they have a relatively open structure having characteristic width for easier accommodation of foreign atoms and for relaxation of structure upon doping. (ii) They provide a rapid diffusion path for ions, especially for anions. (iii) They have the ability to segregate charges when the ceramic is cooled from the fabrication temperatures. (iv) The ease of formation of vacancies and interstitials is greater in the grain boundaries.

The ZnO varistor system provides a way to study the effect of dopants on grains, grain boundaries intergranular layer. This arises from the fact that the current-voltage characteristic of a varistor is microstructure dependent. As explained in *section 1.6.2* the properties which are grain specific will show up in the upturn region. Those, which are grain boundary specific, will appear in the pre-breakdown region. By monitoring the dopant effects on the upturn and low current regions, it is possible to know whether the dopant is grain specific or grain boundary specific. Combining this knowledge with the defect models for these regions, it can be determined whether the dopants act as donor, acceptor or some cases even both.

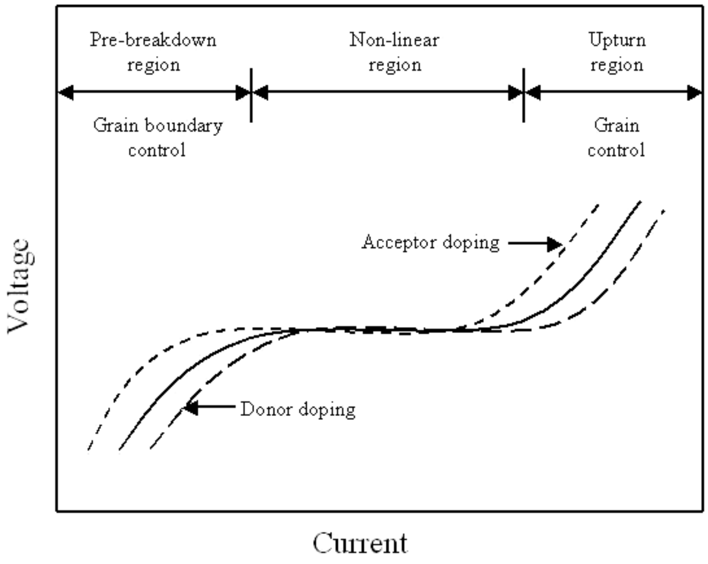

FIG. 1.5. Effect of donor and acceptor doping on the current-voltage characteristics of a ZnO varistor.

Fig 1.5 shows the perturbations of I-V curve as a result of donor or acceptor doping in the grains and grain boundaries. Consider the upturn region, if the grain impedance is determined by donor doping, the voltage rise will be retarded and upturn will be delayed to higher current densities. On the other hand, if impedance of the grain is increased by acceptor doping the upturn will be at lower current densities. Similar effects are also found in the grain boundaries and is seen at the pre-breakdown region of the current voltage curve. This is experimentally tested [32].

The basic structure of ZnO varistor is formed by adding Bi_2O_3 to ZnO. Bi_2O_3 makes potential barriers at the grain boundaries by becoming itself a layer of intergranular material and by supplying ions to the ZnO grain boundaries. The non-ohmic property appears by adding at least 0.1 mole % of Bi_2O_3 to ZnO. However, the α values never exceed 10 i.e. the potential barriers are not good enough to show the highly non-ohmic property. By adding transition metal oxides such as MnO and CoO, the non-ohmic property is dramatically improved. The α values not only exceed 10, but reach as high as 50 [33]. The high α value of Mn doped samples are found to be counter balanced by degradation of electrical behavior which is related to the ability of Mn to adopt several oxidation states (Mn^{2+}, Mn^{3+}, Mn^{4+}) [34]. In case of Cr_2O_3 addition, with very small percentages of dopants (0.1 mole %) there is certainly increase in α value [35], but if large amount of Cr_2O_3 is added as dopants, it lowers the height of the potential barrier at grain boundaries, increases the leakage current and decreases the α value [36]. Cobalt is another dopant which is used to improve the nonlinear behavior of varistor. There are reports comparing the addition of CoO/Co_2O_3 in the ZnO varistor system and studying the effect of dopants [37]. It is seen that the donor concentration is lowered by increasing the Co dopant concentration. The carrier mobility was found to increase with Co_2O_3 concentration but above 0.5 mole % Co_2O_3 decreased the carrier mobility.

It is postulated that the transition metal oxides are involved in the formation of interfacial states and deep bulk traps, both of which contribute to the highly non-ohmic property. By adding Sb_2O_3 to ZnO in addition to Bi_2O_3-CoO-MnO, the grain size becomes smaller and the non-ohmic property is further improved. Furthermore the I-V characteristics become stable against electrical stresses, as shown by the higher breakdown voltage. This is important in the practical applications of these materials. Two roles are postulated for Sb_2O_3. One is to suppress grain growth by forming spinel phase, $Zn_7Sb_2O_{12}$. The other is to enhance the solubility of ions, such as Zn in the Bi_2O_3 rich liquid phase. The later role is vary important for the defect distribution formed at the grain boundaries during cooling. The potential barriers having the highly non-ohmic property are created and determine by using those four additives [38]. Although there is great variety in elemental composition of ZnO varistor materials, they contain approximately 90 % ZnO and balancing mixture of other oxides. The most common additives are Bi_2O_3, Sb_2O_3, MnO and CoO. A number of other additives have also been reported Be, Mg, Ca, Sr, Ba, Sn, Pr, La, V, Nd, Sm, Gd, Cu, Ag, Si, Al, Ti, Zr and B [39]. There are several additives that show similar effects to Bi_2O_3 such as rare earth oxides and alkaline earth oxides (BaO, SrO). However the performance are not as good as Bi_2O_3 [40]. The one exception was the use of Pr_2O_3 in place of Bi_2O_3 [41] except for Pr_6O_{11}. Studies on influence additives e.g. Y, Dy, Er have been reported on $ZnO–Pr_6O_{11}–CoO–Cr_2O_3$ system [42].

In all the ZnO systems so far discussed, it was found that oxide of Bi, Pr, Sb as one of the necessary dopants for varistor characteristics. These are materials, which led to an effective insulating grain boundary layer, which are essential to the varistor behavior. Hence the varistor dopants can be mainly classified in to three different groups the first group can be called as *Varistor former* This group consist of oxides of Bi, Sb, Pr, Pb etc. These are found to be essential for varistor. The second group is called as *Performance enhancers*. Their function is to improve the nonlinear behavior of the varistor. These are oxide of Mn, Co, Cr, Ni etc. The third group of dopants are called as *performance highlighters* These group consist of elements like Al, Na, Li, K etc. The performance highlighters are added in very small concentrations, usually in the ppm range. The varistor formers are added in comparatively large amount, several mole %. All these studies led to some important rules, which are essential to successfully engineer the materials. These rules are summarized below

(i) The host material must be a semiconducting material having wide band gap that allows energy levels to be formed in the forbidden gap, when dopants are added.
(ii) Polycrystallinity.
(iii) The site preferences of the dopant ions arise from the localized reduction of free energy.
(iv) Relative size of the host/guest ions with their crystal structure.
(v) An open crystal structure of the host will allow for better accommodation of guest in case of ZnO.

There are dopants, which changes the grain size distribution and thereby affect the breakdown voltage characteristics of the varistor [43]. Generally the dopants, which are found to affect the grain size are Al_2O_3, TiO_2 and MgO. MgO was found to be a grain growth inhibitor. This in turn, has led to an increase in breakdown voltage of the varistor materials of a particular size. Also the addition of MgO improved the microstructure to give a homogeneous distribution and this was checked by impedance also. Similar effect was found in the case of sample doped with Al_2O_3 and SiO_2 [44]. Doping with TiO_2 increase the grain size [45] this will decrease the breakdown voltage of the varistor. A similar effect of grain growth enhancement was observed when the sample was doped with BaO [46].

1.6.4 Electron Transport across a charged grain boundary

The essential concept underlying varistor action is that the current–voltage characteristics are controlled by the existence of an electrostatic barrier at the grain boundaries. The origin of the barrier can be understood from the thought experiment introduced by Pike [47], who considers the formation of a grain boundary by joining together two identical semiconducting grains with an intervening layer of grain boundary material. (*Fig 1.6*) The grain-boundary material is assumed to consist of the same semiconducting material but contains defects and dopants. As a result, its Fermi level is different from that of the two grains, and it also has electronic states because of the defects and dopants within the band gap energy. The three pieces of material are now joined together to form the grain boundary. In order to achieve thermodynamic equilibrium, electrons flow until the Gibbs free energy per electron is the same everywhere.

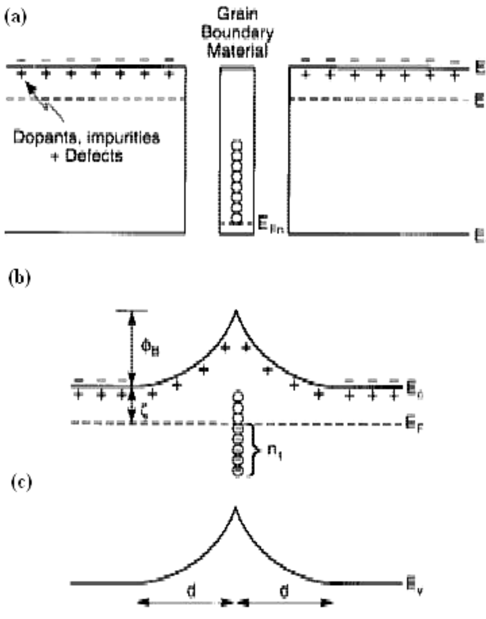

FIG. 1.6 Thought experiment for the formation of a potential barrier at a grain boundary [Ref 49].

In this simple picture, electrons flow to the grain boundary, where they are trapped by the defects and dopants, to increase the local fermi level until it is the same throughout the material. At equilibrium, the chemical (binding) energy gained by an electron occupying a trap state is equal to the electrostatic energy spent in moving an electron from the interior of the grains to the boundary. The result of this equilibrium is that the trapped electrons act as a sheet of negative charge at the boundary, leaving behind a layer of positively charged donor sites on either side of the boundary, and create an electrostatic field with a barrier at the boundary. Assuming that the discrete nature of the charges can be ignored, the magnitude of the potential barrier can be calculated by solving the Poisson *equation 1.1* for the potential, F(*x*), from a knowledge of the grain-boundary charge density, r(*x*)

$$\frac{d^2}{dx^2}\Phi(x) = \frac{\rho(x)}{\varepsilon\varepsilon_0} \qquad 1.1$$

where ε is the relative permittivity and ε_o the permittivity of free space. For a boundary, the charge can be represented by a sheet of trapped charge of areal density, n_t. From the solution of the Poisson equation, two important parameters result the barrier height, Φ_B, and the width, *d,* of the depletion layer these are given by the relations in *equation 1.2*

$$\begin{aligned} \Phi_B(V{=}0) &= \frac{e^2 n_t^2}{8\varepsilon\varepsilon_0 n_0} = \frac{Q_t^2}{8e\varepsilon\varepsilon_0 n_0} \\ d &= \frac{Q_t}{2n_0} \approx \left(\frac{\varepsilon\Phi_B}{n_0}\right)^{1/2} \end{aligned} \qquad 1.2$$

where n_o is the carrier concentration in the grains. When a voltage (*V*), is now applied across the grain boundary, the band structure changes, as shown in *Fig 1.7.* The mechanism by which current flows across the boundary is generally consistent with a thermionic emission process. At the same time, additional electrons can be trapped at the boundary, and there is a dynamic flow of trapped charges between the grains and the boundary. Detailed analyses of the voltage dependence of the current density have been presented, but, in the simplified picture presented here, the current density (*J*), is related to the applied voltage by the relationship given in *equation 1.3*

$$J = A^{*}T^{2} \exp[-(e\Phi_{B}(V) + \varepsilon_{\xi})/kT] \exp(-eV/kT) \tag{1.3}$$

where A^* is the Richardson constant, T the temperature, ε_ξ the Fermi level in the adjoining grains, and k the Boltzmann constant. The barrier height is dependent on the applied voltage and on the energy distribution of interface states. However, it can be approximated [48] in terms of a critical voltage (Vc), as given *equation 1.4.*

$$\Phi_{B}(V) = \frac{V_{C}}{4}\left(1 - \frac{V}{V_{C}}\right)^{1/2} \tag{1.4}$$

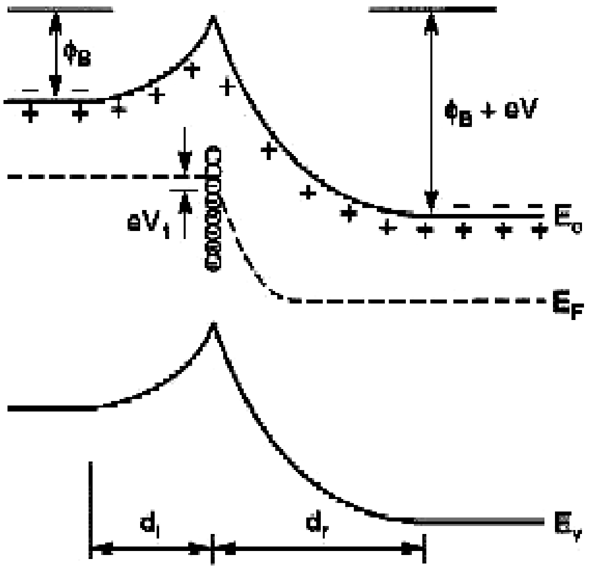

FIG. 1.7 Effect of applied voltage on the band structure at a grain boundary (schematic).

Effect of applied voltage on the band structure at a grain Although this description is standard and can be found in different textbooks [49] and in a variety of papers [50] dealing with electrical properties of ceramics, solar cells, and semiconductor junctions, it is important to note a number of key features. As indicated by *Equation 1.2*, the barrier height decreases with increasing grain conductivity; therefore, if the conductivity is too high, the barrier collapses. Less obvious from the equations is that, if the grain conductivity is too low, the barrier does not exist.

Because the formation of the barrier requires a difference in Fermi level between the grains and the grain boundary, if the Fermi level is too low, the states in the gap cannot be filled. Moreover, because the grains and grain boundaries are in series, if the conductivity is too low, then the overall conductivity of the device is insufficient to be useful. As a result of these competing factors, there is an optimum doping for devices that relies on the existence of a grain-boundary potential barrier. Analysis of experimental data indicates that, for a varistor, the typical values for the trap density, conductivity, and barrier height are 10^{13} cm^{-2}, 10^{17} cm^{-3}, and ~ 0.8 eV, respectively. With these values, the depletion width is ~ 0.1 μm and the corresponding electric field in the vicinity of the grain boundary is ~ 1 mV cm^{-1}.

Although useful for pedagogical purposes, this continuum description is too simple. Spatial variations in the charge along grain boundaries and variations in the spatial distribution of ionized donors in the depletion region, in turn, cause spatial variations in the barrier height and in the current density flowing across the barrier. The magnitude of these spatial fluctuations has been calculated to be ~ 0.1 eV [50]. For the particular case where there is a Gaussian distribution of barrier heights, Werner and Guttler [51] have developed analytical expressions for the effective barrier height.

The method of detecting the interface celectronic states is by observing the recovery of non-equilibrium grain boundary capacitance. [52] These results indicated that a large density of electron trap is observed 0.6 to 0.7 eV below the conduction band edge in ZnO varistor. The most commonly used techniques are Deep Level Transient Spectroscopy (DLTS) [53], Isothermal Capacitance Transient Spectroscopy (ICTS) [54]. From all the measurements large density of interface states were observed 0.9 - 1 eV [55] and 0.6 - 0.7 eV [56] below the conduction band edge. However, it must be remembered that these studies will not give a clear idea about the origin of interface state. The possible candidate for the origin of the interface states are found to be absorbed excess oxygen [57], impurities in the form of transition metal ions [58], dangling bounds of ZnO lattice [59] and strain effects caused by large ions such as Bi, and Pr in ZnO [60].

The identity of the grain-boundary states is not specified. This, and associating them with specific chemical species, remains one of the biggest challenges today. However, it should also be said that although the identity of the states is necessary in understanding the role of individual dopants, the key electrical parameters are the existence of the grain-boundary states and their density.

The role of grain boundary oxygen in the formation of trap level has been proved by X-ray photoelectron spectroscopy [61]. These studies even indicate that the role of Bi as varistor former may be limited to supplying excess oxygen to the grain boundaries. Measurements using Auger electron spectroscopy do agree to the above conclusions [62].

1.6.5 Degradation (aging) phenomena

One of the major challenges in the continuing development of varistors has been to reduce their long-term degradation. This degradation can take a number of forms but usually refers to the steady increase in leakage current when the varistor is subject to a series of pulses or to a constant applied dc or ac voltage [63]. Under extreme conditions, especially at elevated temperatures, the increase in leakage current can be sufficient for the associated Joule heating to cause thermal runaway of the varistor [64]. The extent of degradation can be quantified in a number of ways. One is to express the resistive component of the leakage current, at a fixed voltage, according to a power-law given in *equation 1.5*

$$I_R(t) = K_d\, t^n \qquad 1.5$$

where K_d is an effective rate constant and n an exponent. For a stable varistor, $n \approx 0$, whereas, for an unstable varistor, it can range from 0.5 to 1.0. Although there is utility of using a power law to represent data, its general validity and its range of applicability remain to be established.

The extent of degradation can be minimized by appropriate heat treatments, and some varistor formulations are less susceptible to degradation than others. Morever, the original J-E characteristics generally can be restored by annealing the degraded varistor at relatively low temperature (~ 200 ^oC) Annealing is accompanied by the generation of current (thermally stimulated currents), indicating that charges is traped during the degradation process and can be released from relatively shallow traps in the degraded material by thermal activation [65].

The two principle mechanisms for degradation have been proposed. The first is a form of electromigration, in which ions within the depletion layer diffuse preferentially in the direction of current flow. On reaching the grain boundary, they combine with the defects forming the electrostatic barrier, thereby lowering the potential and correspondingly increasing the leakage current [66]. The second mechanism assumes that the interface states are associated with chemisorption of oxygen at the grain boundaries and that, during degradation, oxygen desorption occurs. Whether this is accompanied by electromigration of oxygen into the positively biased depletion layer of the adjoining grain remains to be established [61]. There has been a considerable effort to understand the degradation processes in zinc oxide varistors and their relation to microstructure [67].

1.6.6 Theoretical models for electrical conduction

Several different models have been proposed to explain the grain-grain conduction at breakdown. The first model, proposed by Matsuoka [25] was the 'space charge limited current (SCLC)' in the Bi_2O_3 rich intergranular layer. The second model was 'Tunneling though a thin layer at the grain boundary' by Levinson and Philipp [27(c)]. The third model was tunneling through 'Schottky barriers cause by interface states.' In this case there were two model proposed one did not take into consideration the heterojunctions composed of ZnO and the Bi_2O_3 rich intergranular layer [68]. These reports proposed that the type III structure as describe earlier was essential for the highly non-ohmic property. The other model took into consideration the heterojunctions [69]. The fourth model was 'tunneling though Schottky barriers whith hole creations' [27(d)], this model demonstrate the importance of minority carrier (holes) at the grain boundaries. The fifth model was 'Tunneling though homojunction of ZnO' [70] which pointed out the importance of thermal equilibrium of defects formed during cooling at the grain boundaries. The sixth model was 'Hol-induced breakdown' [71]. The energy band diagram proposed by Blatter and Greuter [71 (c) (d)] is shown in *Fig 1.8*. According to their theory, the highly non-ohmic property is caused by lowering of potential barriers at the grain boundaries due to hole accumulation. The holes are created by accelerated electrons in the depletion region. The potential barriers depend both on the interface states and on bulk traps. The seventh model was the 'Bypass effect' [72] which represents the important role of the Bi_2O_3 rich intergranular layer in the small current region and supposed that parallel current paths though the heterojunctions. The eight model was 'induces space-charge current at the heterojunctions' composed of thin films of ZnO and Bi_2O_3 [73].

According to the current understanding, the hole-induced breakdown model seems to be consistent with the highly non-ohmic property, the high α values, the interface state effects, the bulk trap effects, the hole creation mechanism and the dynamic properties.

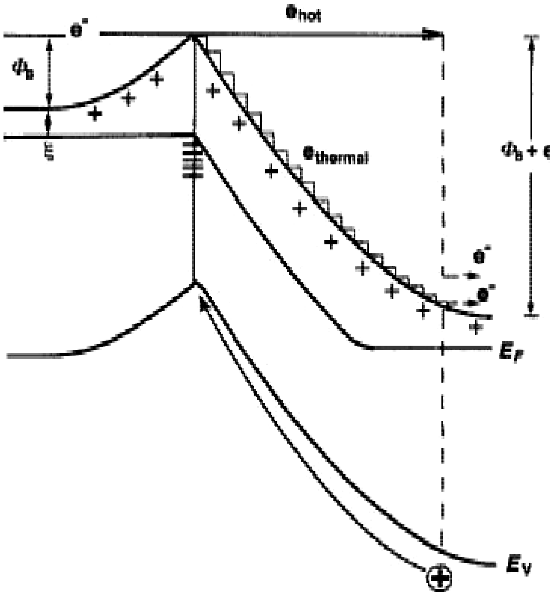

FIG. 1.8 Energy band diagram for a varistor grain boundary under an applied voltage, illustrating the process of interband impact ionization and the generation of holes. Holes are drawn to the grain boundary, where they compensate the trapped negative charge and lower the potential barrier [Ref. 71(c)].

The model of Mahan et al. [27(d)] and Blatter et al. [71 (d)] both associate the highly non-linear conduction with a triggered tunnelling mechanism involving hole creation. When the voltage exceeds a critical value of about 3 V per grain boundary, it is possible for some electrons, which have overcome the potential barrier, to absorb so much energy in the high potential field (F>10-6 V/cm), that holes are created by means of impact ionization. The positively charged holes drift to the negatively charged grain boundary, where they reduce the overall charge. The hole-current therefore reduces the height of the barrier. This sudden reduction of the barrier height explains the dramatic increase in current. The breakdown voltage per barrier does not depend on varistor composition or processing. Tunnelling is so far the only mechanism proposed, capable of qualitatively describing grain-to-grain conduction at breakdown.

1.7 Fabrication of varistors

The method of preparation, crystalline size and additive homogeneity are the critical parameters to produce a better varistor material [74]. Varistors with inhomogeneous microstructure can cause a large spread in current/voltage characteristics due to high local currents and this leads to the degradation of the varistor during electrical operation [74 (b) and (c), 75]. It is well documented that electrical and electronic characteristics can be altered by varying the microstructure at the grain boundaries [76], and careful control of the microstructure is required to produce a high performance varistor. A homogeneous distribution of composition is needed to control thermal stress arising form variations in resistance and thereby localized heat buildup. For achieving a uniform sintered microstructure, a uniform green microstructure of uniformly packed particles with a narrow size distribution is needed. Considerable amount of literature is available on preparation techniques of ZnO Varistor, few of techniques are discussed briefly below

Sol-gel process is describe by Hohenberger et al [77] wherein the varistor ceramics made from sol-gel powder can be sintered at lower temperature. The sol-gel prepared varistor exhibited a better non-linear characteristics compared to the ball milled samples. This is due to the fact that the sol-gel materials has more varistor active grain boundaries as result of more homogeneous distribution of dopants. Most importantly, these preparations yielded final grain sizes in the range 3-4 μm compare to 15-20 μm for the conventionally prepared ZnO varistor. The electrical breakdown and ability to withstand high powers enabled the researchers to manufacture small varistor. So these chemically prepared varistors are expected to play a major role in the production of chip-varistors, multilayer and surface modified device [78].

A smart technique given below proposes by Banerjee et al [79] for the fabrication of ZnO varistor. Homogeneously mixed ZnO powder can be prepared by coating ZnO powder with solutions of dopants. Varistors prepared from this powder exhibit higher non-linearity coefficient, higher low-voltage resistance and sharper change from ohmic to non-ohmic behavior than those prepared by the conventional oxide mixing route.

A novel technique for preparing ZnO varistor is proposed by Sinha et al [80]. It involves preparation of gel by adding citric acid to nitrate solution of varistor constituents. The gel on subsequent calcination forms submicron reactive varistor powder that exhibits the homogeneity and stoichiometric control associated with the chemical methods of preparation.

Modified citrate gel techniques [81], which enabled some control over the location of the minority components incorporated into the ZnO. By positioning these components according to their function, varistor pellets with higher nonlinear coefficients, higher characteristic voltages and slightly higher energy absorption abilities than those of the prepared by conventional mixed-oxide route.

There are other methods to produce uniform fine grained particles such as urea process [82], Colloidal suspension and centrifugal separation method [83] and Amine process [84]. All these processes gives rise to uniform, dense and nanosized particles having high surface, which can be sintered to near theoretical density at, lower sintering temperature and time.

1.8 Search for new varistor

In earlier section, it was explained how the surge arrestors/varistors have evolved from the gapless arrestors to SiC varistors and then to ZnO varistors. Since the discovery of ZnO-based varistors, there has been a steady search for alternative materials either to find varistors with superior properties or to circumvent patents. $SrTiO_3$ is relatively one of the new varistor materials, which exhibited relatively good varistor phenomena ($\alpha \approx 20$) used in micromotors [85]. ZnO varistors are used for high amplitude and low frequency voltage surges, such as transient voltage surges (i.e. transient line voltage and switching surges), $SrTiO_3$ varistors are used for medium amplitude and high frequency transient such as interface generated by electric motors.

ZnO varistor have an average breakdown voltage of 3.2 V per grain boundary. Hence for low voltage application, ZnO varistors are not preferred since there is a limit to the thickness that can be reduced for the sample. Lot of experimental work has been done to make thin film varistors [86] and multilayer varistors [87]

TiO_2 varistor has been studied since 1982 by Yan and Rhodes [88] reported (Nb, Ba)-doped TiO_2 ceramic have useful varistors properties with low non-linearity coefficients of α = 3-4. TiO_2 based varistors, first developed at Bell Laboratories and pentavalent ions such as Ta and Nb are used to control the grain resistivity and divalent ions with larger ionic radii such as Ba or Ca are added to segregate to the grain boundaries. There is considerable amount of literature is available on TiO_2 based varistor [89] with various dopants.

Similarly, SnO_2 is also a wide band gap semiconductor and this material was also investigated as a promising candidate for a good varistor material. Pianaro et. al. [90] tried to develop new varistor based on SnO_2. SnO_2 doped with Nb, Co and Cr were found to have relatively high non-linear coefficient ($\alpha \approx 40$) and also high breakdown field (4000 V cm^{-1}). These characteristics make these materials a potential candidate to replace ZnO varistor. Also the absence of any volatile dopants like Bi_2O_3 may give a new varistor with better degradation behavior than the ZnO varistor. Another low-voltage varistor was recently reported by Ezhilvalavav and Kutty [91] based on zinc antimony spinel ($Zn_7Sb_2O_{12}$) with breakdown voltages in the range of 3–20 V and nonlinearity coefficient α = 7–15. The varistor property is due to the formation of high ohmic potential barriers at the grain boundary regions on low-ohmic *n*-type grain interiors of the polycrystalline samples. The other varistor systems reported in the literature is WO_3 [92] as a low voltage varistor with α = 8. Recently reported $CaCu_3Ti_4O_{12}$ [93] with very high nonlinearity coefficient (α = 900), is even very greater that that of the ZnO based varistor materials.

1.9 SnO_2 based varistors

Tin oxide is a wide band gap (E_g = 3.6eV) material with many interesting electronic properties, crystallizing in the rutile structure (*Fig 1.9*) with space group D_{4h}^{14} ($P4_2/mnm$) [94]. Its unit cell contains two tin and four oxygen atoms. It has tetragonal symmetry with a quadratic basis of side a = b = 4.737 Å and c = 3.185 Å, The oxygen atoms are at position (±ua, ±ua, 0) respective to nearest tin atom with u = 0.307. Each tin atom is surrounded by a distorted octahedron of six oxygen atoms and each oxygen atom has three tin nearest neighbours at the corners of an almost equilateral triangle.

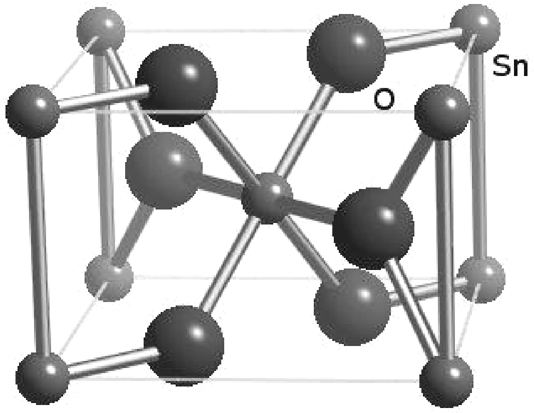

FIG. 1.9 Crystal structure of tetragonal rutile SnO_2.

Fig 1.10 shows a schematic representation of valence and conduction bands of SnO_2 [94]. The band located at –17 eV originates essentially from oxygen s states with a very small fraction of Sn s and Sn p admixture. Since it is separated by a 7 eV wide gap for the upper valence band, these states are only weakly coupled to the higher bands. The main valence band is 9 eV [95] and is divided into three parts of different orbital composition. The region between –9 to –5 eV results from the coupling of Sn s orbital to O p orbital. The latter have essentially a 'bonding p' character, i.e. they are directed along the nearest neighbour Sn-O axis and appreciably contribute to the chemical bonding. The bands in the region between –5 to –2 eV consist of oxygen bonding of p of orbital mixed with smaller fraction of Sn p orbitals. The region between –2 eV and the valence band edge (0 eV) consists mainly of O 2p lone pair orbitals which are directed perpendicularly to the Sn-O axis and contribute little to the chemical bonding. The band gap has a width of 3.6 eV. The Fermi level (E_f) lies near the middle of the band gap (assuming that tin oxide is stoichiometric). The bottom of the conduction band from 3.6 to 8 eV is made up of 90 % of the Sn s states and the top of the conduction band has a dominant Sn p character [96]. All states in the conduction band also contains a small admixture of O 2p bonding states. The wide band gap of tin oxide offers possibilities of n type of p type conduction depending on the dopant impurities. This type of doping leads to the formation of energy levels in the band gap.

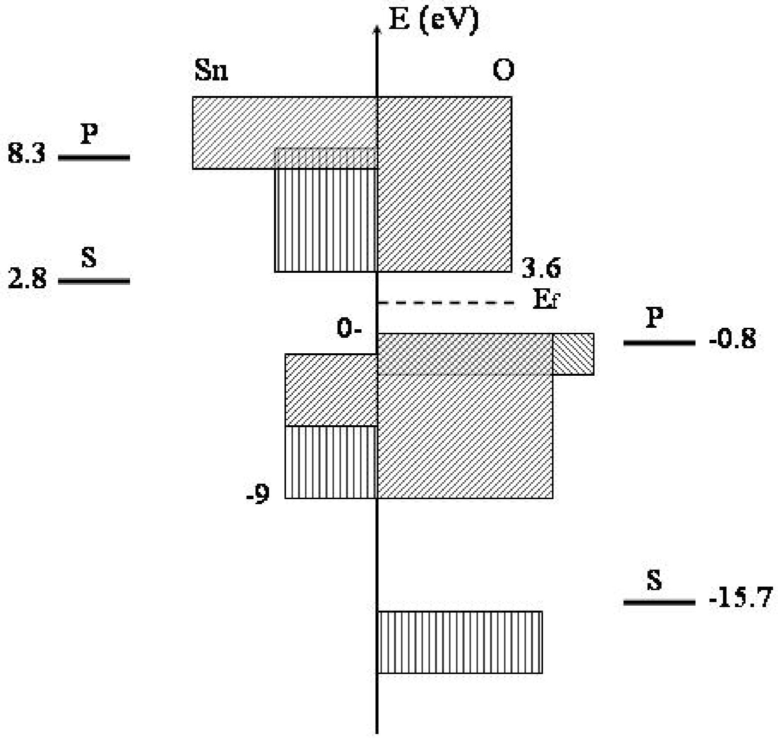

FIG. 1.10 Band diagram of tin oxide. The top of the valence band is 0 eV and the bottom of the condution band is 3.6 eV, Ef is the Fermi level [Ref. 94].

SnO_2 is material used in numerous technological applications, such as transparent electrodes [97], gas detectors [98], far-infrared detectors [99] and high efficiency solar cells [100]. The major application is its property of gas sensing arises due to its poor sinterability in air in pure form even at high temperatures [101]. It has been proven that negatively charged oxygen adsorbates, such as O^-, O^{2-}, etc., on the surface of SnO_2 grain boundaries (and/or grains), play an important role in detecting inflammable gases [102]. Hence oxygen vacancies and electronic states on SnO_2 surfaces have been studied in great details [103]. The most commonly accepted model for the operation of an n-type semiconductor gas sensor is bases on the variation in the potential barrier height at the grain boundary, induced by the change in the amount of oxygen adsorbates by reaction with an inflammable gas. However, nonlinear current-voltage (I-V) characteristics in porous SnO_2 ceramics are observed only above 250°C, because such high temperatures favor oxygen adsorbates, forming Schottky-like barrier between grains.

The addition of CoO and MnO_2 to SnO_2 produces high densification [104] allowing for development of other electronic devices, such as varistors [105] at room temperature.

Although most nonlinear electric behaviors of SnO_2 ceramics have appeared in SnO_2-CoO based systems [106]. Yongjun et al [107] and wang et al [108] demonstrated that ZnO can substitute CoO without significantly altering the nonlinear coefficient compare to the SnO_2-CoO based system. The first of such SnO2-based system, reported on in the literature by Pianaro et al [105(a)] Yongjun et al [109] also obtained non-ohmic properties in SnO_2-Bi_2O_3 based systems. Castro and Aldao [110] showed dopants such as Co_3O_4, CuO, MnO_2, Bi_2O_3 and Sb_2O_3 could influence the dielectric properties, microstructure and densification of SnO_2-based ceramics. The addition of different dopants, as well as several thermal treatments in oxidizing and inert atmospheres were found to influence the microstructure and electrical properties of SnO_2-based varistor ceramics [111]. Other authors reported that dense SnO_2 ceramics doped with CoO and small concentration of Nb_2O_5 and Cr_2O_3, [112] Al_2O_3 [113] display highly non-ohmic I-V characteristics at room temperature with electrical characteristics similar to commercial metal oxide varistors, which are also highly dense polycrystalline ceramics composed predominantly of ZnO, with additions of Bi_2O_3, Sb_2O_3 and other oxide constituents. As discussed above dense SnO_2-based systems present values of nonlinear coefficient α, breakdown field E_B, and barrier voltage per grain (V_b) equivalent to those of the traditional ZnO varistor. However, non-ohmic ZnO systems have a complex microstructure consisting of several crystalline phases, such as the Bi_2O_3-rich phases, spinel (nominally $Zn_7Sb_2O_{12}$) and pyrochlore (nominally $Zn_2Bi_3Sb_3O_{14}$). The presence of these crystalline phases in these systems is easily verified by x-ray diffraction (XRD) patterns and scanning electron microscopy (SEM). Unlike the ZnO-Bi_2O_3 based system a secondary phase is not detectable by XRD in SnO_2.CoO. This technique only allows for the detection of SnO_2 cassiterite phase in SnO_2 bases varistor systems. SEM analysis show that non-ohmic SnO_2-CoO polycrystalline systems have a simpler homogeneous microstructure that that of ZnO-Bi_2O_3. It has recently been found that the nature of potential barriers in SnO_2-based varistors is Schottky like, as is that observed in ZnO-based systems [114].

1.10 Application of varistors

The varistor is mainly used as a surge suppresser. Usually they are connected in parallel to the electronic circuit that is to be protected as shown in *Fig 1.11* Varistors are selected in such a way that their breakdown voltage is just below the limiting voltage of the electronic component. At ordinary working voltage of the circuit (load), the varistor is in its pre-breakdown or low-current region. Hence it acts as high resistor. When the voltage spike occurs, the varistor conducts heavily since the varistor is now in its non-linear region. The surge is bypassed through the varistor and the circuit components are saved from the voltage surge.

For many years, the varistor have been in use to regulate transient voltage surges, initially selenium rectifiers were used as varistor. These were later replaced by single crystal silicon devices or avalanche Zener diodes for low voltage applications and SiC and ZnO varistors for high voltage applications. ZnO varistors are the most commonly used varistors. They account for 80% of the market value. $SrTiO_3$ is the new varistor in this group, and has been produced in a large scale commercially.

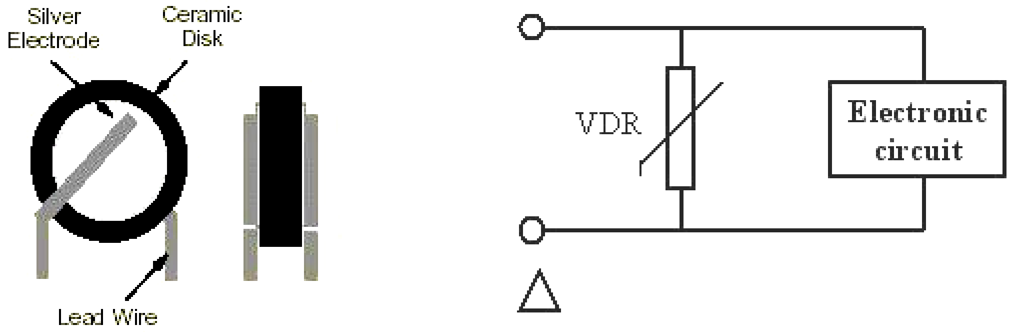

(a) (b)

FIG 1.11 (a) Front and side view of varistor disc (b) Varistor connected in circuit.

Varistors offer cost savings and performance advantages over crowbar-type surge protectors and Zener diode clamp devices in a wide range of applications. Enhanced materials and optimized component design particularly in the field of Zinc Oxide varistors have opened up new applications for varistors, especially those requiring low protective level and a low standby current. In line with the industry's overriding drive toward miniaturization and surface-mount technology, VDRs in a single-layer SMD package are emerging to satisfy medium energy handling capabilities within a relatively small volume. Also, where disc-type varistors occupy relatively large space within an enclosure, new low-profile varistors reduce the maximum height above the board for such a device, while maintaining equivalent current handling capabilities. In addition to these, ultrahigh surge varistors are also more widely used in the market, capable of offering an improved surge current/size ratio and allowing replacement of large components by smaller devices with similar performance and reliability. Some of recent application of varistors are described in literature [26 (b) & (c), 115] *Fig 1.12* shows the application of varistor in various fields.

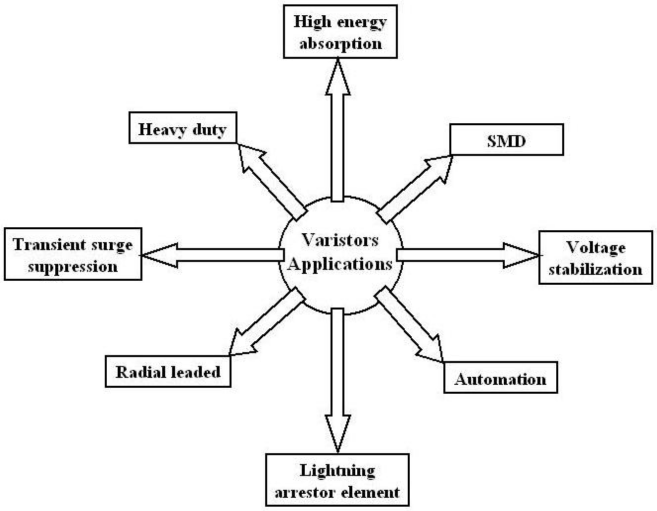

FIG 1.12 Application of varistor in various field.

1.11 Varistor research and Market analysis

Many groups worldwide are currently doing extensive research on preparation characterization and development of ZnO based and other new varistor materials. Industries like General Electric, Matsushita, Siemens, Thompson, NEC etc. are the major global player producing varistors commercially and pursuing basic research on varistor phenomena.

IISc Banglore, RRL Trivnedram, BARC Mumbai, IIT Mumbai and IIT Delhi are few institutions working in this area other than NCL Pune. Phillips India, Elpro, Crompton switchgears are few industries which are commercially producing varistors. According to the Electronic Materials Manufacturers Association of Japan, the production value of varistors totaled $ 86 million in

2003. Demand for varistors will reach over 10.5 billion units worldwide by end 2005. Mobile phones, PDAs, digital cameras, notebook PCs and A/V equipment mainly drive the demand.

References

1. Shackelford J K, *Encyclopedia of Applied Physics* Vol. **3,** Edited by Trigg G L (New York, VCH) 169 (1992)
2. Segal D, Chemical synthesis of advanced ceramic materials, *Chemistry of solid state materials*, Vol. **1**, Edited by West A R and Axter H B, Cambridge University press (1989)
3. Zhan G D, Kuntz J D, Garay J E and Mukherjee A K, *Appl. Phys. Lett.* **83**, (6) 1228 (2003)
4. *Advanced ceramics*, edited by S. Saito Oxfored university press, (1988)
5. Spencer E G, Lenzo P V and Ballam A A, *Proceedings IEEE* **55**, 2074 (1967)

6 **(a)** Reynolds T G and Buchanan R C, Ferrite (magnetic) Ceramics, *Ceramic Materials for Electronics,* 2nd edition, Edited by Bhuchanan R C, Marcel Dekker Inc., New York **(b)** Sugimoto M, *J. Am. Ceram. Soc.* **82**, 269 (1999)

7. Hench L L, *J. Am. Ceram. Soc.* **81**, 1705 (1998)
8. Schoonman J, *Solid State Ionics* **157**, 319 (2003)
9. Minh N Q, *J. Am. Ceram. Soc.* **78**, 563 (1993)
10. Barsoum M W, *Fundamentals of ceramics*, McGraw Hill, Singapore (1997)
11. Bigij P, Stanpinski T, Jonas S and Walasek E, *XXIV Conference of International Microelectronics and Packaging Society – Poland*, IMAPS Poland (2000)
12. Rouxel J, Tourhoux M, Brec R, Soft chemistry routes to new materials; CHEMIE DOUCE*, Materials Science Forum V*, **152-153**, Trans Tech Publication ltd. Switzerland (1994)
13. **(a)** Jaffe H, *J. Am. Ceram. Soc.* **41,** 494 (1958) **(b)** Jaffe B, Cook W R Jr., and Jaffe H, *piezoelectric ceramic*, Academic press, New york, (1971)
14. **(a)** Uchino K, *Amer. Ceram. Soc. Bull.* **65,** 647 (1986) **(b)** Huybrechts B, Ishizaki K and Takata M, *J. Mater. Sci.* **30** 2463 (1995) **(c)** Duran P and Moure C, *J. Mater. Sci.*, **20** 827 (1985) **(d)** Amin A, *J. Amer. Ceram. Soc.* **72**, 369 (1989) **(e)**

Newnham R E, *Rep. Prog. Phys.* **52,** 123 (1989) **(f)** Uchino K, *Mat. Res. Soc. Bull.* **XVIII**, 42 (1993)

15. Haertling G H, *J. Am. Ceram. Soc.* **82,** 797 (1999)
16. Yoon, D –S, and Roh J S, *Critical Rev. Solid State Mat. Sci.* **27**, 143 (2002)
17. **(a)** Maurice A K and Buchanan R C, *Ferroelctrics* **74**, 61 (1987) **(b)** Scott J F and Raz de Aranjo C A, *Scicence*, **246,** 1400 (1989) **(c)** Werring W, Schnoller M and Wahl H, *Ferroelctrics*, **68,** 145 (1986) **(d)** Heywang W, *J. Mater. Sci.*, **6,** 1214 (1971) **(e)** Park S M and Payne D A, *Amer. Ceram. Soc. Bull.* **58**, 732 (1979)
18. **(a)** Okazaki K and Hagata K, *J. Am. Ceram. Soc.* **56**, 82 (1973) **(b)** Haertling G H, Photoelectronic effect in PLZT ceramics, *Ceramic Transactions* Vol. **14** Electrooptics and nonlinear optic materials, Edited by Bhalla A, Vigel E and Nair K, American Ceramic Society, Westervulle OH. (1990) **(c)** Cascales C and Zaldo C, *J. Solid State Chem.* **171,** 262 (2003) **(d)** Mendez-B A, Rico M, Volkov V, Zaldo C and Cascales C, *Mol. Phys.* **101,** 941 (2003)
19. Carlson D E and Wronski C R, *Appl. Phys. Lett.* **28**, 671 (1976)
20. Cava R J, *J. Am. Ceram. Soc.* **83**, 5 (2000)
21. Ichinose N, *Advanced Ceramics*, Edited by S. Saito, Oxford university press and Ohmsha Ltd. (1988)
22. Ura M, 'Ceramic substrates', in *Fine Ceramic*, Edited by S. Saito, Elsevier, New York, (1988)
23. **(a)** Frosch C J, *Bell Lab. Rec.*, **32**, 336 (1954) **(b)** Dienel H F, *Bell Lab. Rec.* **34**, 407 (1956)
24. Matsuoka M, Masuyama T, and Iida Y, *Jpn. J. Appl. Phys.*, **8**, 1275 (1969)
25. Matsuoka M, *Jpn. J. Appl. Phys.* **10,** 736 (1971)
26. **(a)** Levinson L M and Philipp H R, *Ceram. Bull.* **65**, 639 (1986) **(b)** Gupta T K, *J. Amer. Ceram. Soc.*, **73,** 1817 (1990) **(c)** Kharat D K, Date S K, *J. Scientific and industrial Research* **50,** 596 (1991) **(d)** Clarke D R, *J. Amer. Ceram. Soc.*, **82,** 485 (1999)

27. **(a)** Bartkowiak M, Comber M G and Mahan G D, *J. Appl. Phys.*, **79,** 8629 (1996) **(b)** Einzinger R, *Annu. Rev. Mater. Sci.*, **17,** 299 (1987) **(c)** Levinson L M and Philipp H R *J. Appl. Phys.*, **46,** 1332 (1975) **(d)** Mahan G D, Levinson L M and Philipp H R, *J. Appl. Phys.*, **50,** 2799 (1979) **(e)** Santhanam A T, Gupta T K and Carlson W G, *J. Appl. Phys.*, **50**, 852 (1979)

28. **(a)** Levine J O, CRC Crit. Rev., *Solid State Sci.* **5,** 597 (1975) **(b)** Greuter F, Blatter G, Stucki F, and Rossineli M 'Advances in varistor technology', *Ceramic Transactions*, Vol. **3** edited by L M Levinson (American Ceramic Society Inc., Columbus, Ohio, USA) (1989)

29. **(a)** Phillipp H R and Levinson L M, *J. Appl. Phys.* **50,** 383 (1979) **(b)** Gupta T K, Mathur M P and Carlson W G, *J. Electron. Mater.* **6,** 483 (1977) **(c)** Tso M, Ai B, Dorlanne O and Loubiere A, *J. Appl. Phys*. **61,** 1562 (1987) **(d)** Van Kemenada T C and Eijnthoven R K, *J. Appl. Phys.* **50,** 938 (1979) **(e)** Gupta T K, *Proceedings of 1984 conference on electrical insulation and Dielectric phenomena*, IEEE Electrical insulation society, IEEE service center, Piscataway, NJ, (1984) **(f)** Sweetana A, Radford K C, Johnson R G and Hensley S P, *Ceramic transactions*, **3**, edited by Levinson L M, Amer. Ceram. Soc., Westerville, OH, (1989) **(g)** Chen Q, He J, Tan K, Chen S, Yan M and Tang J, *Science in China, Series E: Technological Sciences*, **45,** 337 (2002) **(h)** Hung N T, Quang N D and Bernik S, *J. Mater. Res.* **16,** 2817 (200) **(i)** Ott J, Lorenz A, Harrer M, Preissner E A, Hesse C, Feltz A, Whitehead A, H, Schreiber M, *J. Electroceram.* **6,** 135 (2001) **(j)** Bartkowiak M, Comber M G, and Mahan G D, *IEEE Trans. Power Delivery*, **14,** 152 (1999) **(k)** Karim A N M, Puyane R, El-Baradie M A, Hashmi M S J, *Adv. Powder Metall. Part. Mater.* **3,** 8/23 (1996) **(l)** Karim A N M, Puyane R, El-Baradie M A, Hashmi M S J, *Adv. Powder Metall. Part. Mater.* **4,** 13/123 (1996) **(m)** He J L, Han S W, Cho H G, *Annu. Rep. - Conf. Electr. Insul. Dielectr. Phenom.* **2,** 568 (1998) **(n)** He J L, Han S W, Cho, H G, Kang H B, *Korean J. Ceram.* **4,** 47 (1998)

30. **(a)** Olsson E, Falk I K L, Dunlop G E and Osterlund R, *J. Mater. Sci.* **20,** 4091 (1985) **(b)** Asokan T, Iyenger G N K and Nagabhushana G R, *J. Amer. Ceram. Soc.* **70,** 643 (1987) **(c)** Wong J and Morris W G, *Amer. Ceram. Soc. Bull.*, **53,** 816 (1974) **(d)** Gupta T K, *Tailoring multiphase and composite ceramics*, Edited by Tressler R E, Murray G L, Pantino C G, and Newhman R E, Plenum, New York (1986) **(e)** Gupta T K *Ceram. Trans.*, **15** (Mater. Processes Microelectron. Syst.), 711 (1990) **(f)** Peigney A, Carles V and Rousset A, *Mater. Res. Bull.* **31,** 503 (1996) **(g)** Haskell B A, Souri S J, Helfand M A, *J. Am. Ceram Soc.* **82,** 2106 (1999) **(h)** He J, Zeng R, Chen Q, Chen S, Guan Z, Han S W, Cho H G, *IEEE Transactions on Power Delivery*, **19,** 138 (2004) **(i)** Bradt C, Burkett S L, *Ceram. Microstruct: Control At. Level, [Proc. Int. Mater. Symp.], Meeting Date 1996,* 339. Edited by Tomsia A P, Glaeser A M, Plenum, New York, (1998)
31. Gupta T K, *J. Mater. Res.* 7, 3280 (1992)
32. **(a)** Carlson W G and Gupta T K, *J. Appl. Phys.* **53,** 5746 (1982) **(b)** Takemura T and Kobayashi M, *Advances in Ceramics,* Vol. **1,** grain boundary phenomena in electronic ceramics, edited by Levinson L M and Hill D, Amer. Ceram. Soc. Columbus, OH (1981) **(c)** Miyoshi T, Maeda K, Takahashi K and Yamazaki T, *Advances in Ceramics,* Edited by Levinson L M, Amer. Ceram. Soc. Westerville, OH (1981) **(d)** Gupta T K, Straub W D, Ramanchalam M S, Schaffer J P and Rohatgi A, *J. Appl. Phys.* **66,** 6132 (1989)
33. **(a)** Ezhilvalavan S and Kutty T R N, *J. Mater. Sci; Materials in Electronics* **7,** 137 (1996) **(b)** Yano Y, Takai Y and Morooka H, *J. Mater. Res.* **9,** 12 (1994)
34. Smith A, Smith D S and Abelard P, *Mater. Lett.* **19,** 159 (1994)
35. Inada M, *Jpn. J. Appl. Phys.***19,** 409 (1980)
36. Pinaro S A, Pereira E C, Bulhoes L O S, Longo E and Varela J, *J. Mater. Sci.* **30,**133 (1995)
37. **(a)** Kim E D, Kim C H and Oh M H, *J. Appl. Phys.* **58,** 3231 (1985) **(b)** Kusy A and kleinpennin T G M, *J. Appl. Phys.* **54,** 2900 (1983)

38. Eda K, *IEEE Electr. Insulation* **5,** 28 (1989)

39. **(a)** Matsioka M, Masuyama T and Lida Y, *Jpn. J. Appl. Phys.* **8,** 1275 (1969) **(b)** Wong J, *J Appl. Phys.* **46,** 1653 (1975) **(d)** Tsai J K and Wu T B, *J. Appl. Phys.* **76,** 4817 (1994) **(d)** Williams P, Krivanek O L, Thomas G and Yodagawa M, *J. Appl. Phys.* **51,** 3930 (1980) **(e)** Kutty T R N, and Raghu N, *J. Appl. Phys.* **54,** 1796 (1989) **(f)** Fan J and Freer R, *J. Appl. Phys.* **77,** 4795 (1995) **(g)** Gilbert I and Freer R, *J. Phys.: Condens Matter* **14** 945 (2002) **(h)** Anastasiou A, Lee M H J, Leach C and Freer R, *J. Euro. Ceram. Soc.* **24,** 1171 (2004) **(i)** Hng H H and Chan P L, *Mater. Chem. Phys.* **75,** 61 (2002) **(j)** Kim C H and Kim J H, *J. Euro. Ceram. Soc.* **24,** 2537 (2004) **(k)** Pfeiffer H and Knowles K M, *J. Euro. Ceram. Soc.* **24,** 1199 (2004) **(l)** Hng H H and Knowles K M, *J. Am. Ceram. Soc.,* **83,** 2455 (2000) **(m)** Kutty T R N and Ezhilvalavan S, *Jpn. J. Appl. Phys.* **34**, 3125 (1995) **(n)** Kutty T R N and Ezhilvalavan S, *J. Phys. D: Appl. Phys.* **29**, 809 (2996)

40. **(a)** Kutty T R N and Ezhilvalavan S, *Mater. Chem. Phys.* 38, 267 (1994) **(b)** Metz R, Delalu H, Vignalou J R Achard N, and Eilkhatib M, *Mater. Chem. Phys.* 63, 157 (2000)

41. **(a)** Mukae K, Tsuda K and Nagasawa I, *Jpn. J. Appl. Phys.* **16,** 1361 (1977) **(b)** Mukae K, *Am. Ceram. Soc. Bull.* **66,** 1329 (1987)

42. **(a)** Nahm C W, Shin B C, *Mater. Lett.* **57,** 1322 (2003) **(b)** Nahm C W, Shin B C and Min B H, *Mater. Chem. Phys.* **82,** 157 (2003) **(c)** Nahm C W, *J. Euro. Ceram. Soc.* **23,** 1345 (2003)

43. **(a)** kharat D K, Dhami G S and Date S K, *Solid State Commun.* **84,** 375 (1992) **(b)** Sung G Y, Kim C H and Oh M H, *Adv. Ceram. Mater.* **2,** 841 (1987) **(c)** Smith A, Gasgnier G and Abelard P, *J. Amer. Ceram. Soc.* **73,** 1098 (1990)

44. **(a)** Nuns S I and Bradt R C, *J. Amer. Ceram. Soc.* **78,** 2469 (1995) **(b)** Kanai H and Imai M, *J. Mater. Sci.* **23,** 4379 (1988)

45. Yong S G, and Kim C H, *Adv. Ceram. Mater.* **3,** 604 (1998)

46. Jaroch U, Murbe J, Hilarius V, and Buhling D, ‘Ceramics Today-Tomarrows Ceramics’, *Mater. Sci. Monographs.* **66C,** Edited by Vincenzini P, Elsevier, Amsterdam (1991)
47. Pike G E, ‘Semiconducting polycrystalline ceramics’, in *Materials Science and Technology*, Vol. **11,** Edited by Swain M V, VCH, Weinheim, Germany, (1994)
48. Blatter G and Greuter F, *Semicond. Sci. Technol.* **5,** 111 (1990)
49. Sze S M, *Physics of semiconductor devices*, Wiley, New York, (1969)
50. Seto J Y W, *J. Apply. Phy.* **46,** 5347 (1975)
51. Werner J H and Guttler H H, *J. Appl. Phys.* **69,** 1522 (1991)
52. Gambino J P, Kingery W D, Pike G E, Philipp H R and Levinson L M, *J. Appl. Phys.* **61,** 2571 (1974)
53. Lang D V, *J. Appl. Phys.* **45,** 3023 (1974)
54. Maeda T, Meguro S and Takata M, *Jpn. J. Appl. Phys.* **28,** L714 (1989)
55. Tuda K and Mukae K, *IECEJ, Tech. Rep.* **CPM 86-29**, 27 (1986)
56. Yano Y, Shirkawa Y and Morooka H, *Jpn. J. Appl. Phys.* **31,** L719 (1992)
57. **(a)** Stucki F, Bruesch P and Grueter F, *Surf. Sci.* **189/190,** 2941 (1987) **(b)** Hayashi M, Kuramoto M and Hayashi M, *Ceramic Transcations*, **3,** 364 (1988)
58. **(a)** Cordaro J F, Shim Y and May J E, *J. Appl. Phys.* **60,** 4186 (1986) **(b)** Shim Y and Cordaro J F, *J. Appl. Phys.* **64,** 3994 (1988) **(c)** Tnaka S, Takahashi K, Sekiguchi T, Sumino K and Tanaka J, *J. Appl. Phys.* **77,** 4022 (1995)
59. Seager C H, *Ann. Rev. mater. Sci.* **15,** 271 (1985)
60. Alles A B and Burdick V L, *J. Appl. Phys.* **70,** 6883 (1991)
61. Stucki F and Grueter F, *Appl. Phys. Lett.* **57,** 446 (1990)
62. Tanaka S, Akita C, Ohashi N, Kanai J, Haneda H and Tanaka J, *J. Solid State Chem.* **105,** 36 (1993)
63. **(a)** Eda K, Iga A and Matsuoka M, *Jpn. J. Appl. Phys.* **18,** 997 (1979) **(b)** Shirley C G and Paulson W M, *J. Appl. Phys.* **50,** 5782 (1979) **(c)** Eda K, Iga A and Matsuoka M, *J. Appl. Phys.* **51,** 2678-84 (1980) **(d)** Gupta T K, Carlson W G and

Hower P L, *J. Appl. Phys.* **52,** 4104 (1981) **(e)** Moldenhauer W, Bather K H, Bruckner W, Hinz D and Buhling D, *Phys. Status Solidi A* **67,** 533 (1981) **(f)** Hayashi M, Haba M, Hirano S, Okamoto M and Watanbe M, *J. Appl. Phys.* **53,** 5754 (1982) **(g)** Philipp H R and Leninson L M, 'Degradation phenomena in ZnO varistor; A review', in *Advances on ceramics,* Vol. **7,** Additives and interfaces in Electronic Ceramics, Edited by Yan M R and Heuer A H, Am. Ceram. Soc. Columbus, Oh, (1983)

64. Bruckner W, Moldenhauer W and Hinz D, *Phys. Status Solidi A*, **59,** 713 (1980)
65. Sato K and Takada Y, *J. Appl. Phys.* **53,** 8819 (1982)
66. **(a)** Gupta T K and Carlson W G, *J. Mater. Sci.*, **20,** 3487 (1985) **(b)** Gupta T K and Miller A C, *J. Mater. Res.*, **3,** 745 (1988) **(c)** Rmanachalam M S, Rohatgi A, Schaffer J P and Gupta T K, *J. Appl. Phys.* **69,** 8380 (1991) **(d)** Ramanchalam M S, Rohatgi A, Carter W B, Schaffer J P and Gupta T K, *J. electron. Mater.* **24,** 413 (1995)
67. **(a)** Ivon A I, Glot A B, Mozharovskii L A, Chernenko I. M, *Inorg. Mater.* **34,** 1285 (1998) **(b)** Zhou D, Zhang C, Gong S, *Mater. Sci. Eng. B* **99,** 412 (2003) **(c)** Chen W P, Chan, Helen L. W., *J. Am. Ceram. Soc.*, **85,** 1625 (2002) **(d)** Takanori I and Shinzo Y, *Key Engineering Materials*, **216** (Electroceramics in Japan IV), 77 (2002) **(e)** Chen C S, Kuo C T, Lin I N, *J. Mater. Res.* **13,** 1560 (1998) **(f)** Asokan T, Freer R, *J. Eur. Ceram. Soc.* **11,** 545 (1993) **(g)** Masasuke T, *Am. Ceram. Soc. Bull.* **72,** 119 (1993) **(h)** Lee W I, Young R L, *Appl. Phys. Lett.* **69,** 526 (1996) **(i)** Castro M S and Aldao C M, *Ceram. Int.* **22,** 39 (1996) **(j)** Leite E R, Varela J A and Longo E, *J. Mater. Sci.* **27**, 5325 (1992) **(k)** Binks D J, Grimes R W, *J. Am. Ceram. Soc.* **76**, 2370 (1993)
68. **(a)** Levine J O, *CRC Crit. Rev. Solid State Sci.* **5,** 597 (1975) **(b)** Morris W G, *J. Vac. Sci. Technol.* **13,** 296 (1976) **(c)** Bernasconi J, Strassler S, Knecht B, Klein H P and Menth A, *Solid State Commun.* **21,** 867 (1877) **(d)** Hower P L and Gupta T K, *J. Appl. Phys.* **50,** 4847 (1979)

69. **(a)** Emtage P R, *J. Appl. Phys.* **48,** 4372 (1977) **(b)** Eda K, *J. Appl. Phys.* **49,** 2964 (1978)

70. **(a)** Enzinger R, *Appl. Surf. Sci.* **1,** 329 (1978) **(b)** Einzinger R, *Appl. Surf. Sci.* **3,** 390 (1979)

71. **(a)** Pike G E, *Mater. Res. Soc. Proc.* **5,** 369 (1982) **(b)** Pike G E, *Phys. Rev. B* **30,** 795 (1984) **(c)** Blatter G and Greuter F, *Phys. Rev. B* **33,** 3952 (1986) **(d)** Blatter G and Greuter F, *Phys. Rev. B* **34,** 8555 (1986)

72. **(a)** Eda K, *Materials Research Society Symposia proceedings: Grain boundaries in Semiconductors,* Edited by Leamy H J, Pike G E and Seager C H, New york, Elsevier, (1982) **(b)** Philipp H R, Mahan G D and Levinson L M, 'Advanced Metal Oxide varistor concepts' *Final Report* ORNL/Sub/84-17457/1 (1984)

73. Suzuoki Y, Ohki A, Mizutani T and Ieda T, *J. Phys. D*, **20,** 511 (1987)

74. (a) Pillai S C, Kelly J M, McCormack D E, O'Brien P and Ramesh R, *J. Mater. Chem.* **13,** 2586 (2003) **(b)** Duran P, Capel F, Tartaj J and Moure C, *J. Am. Ceram. Soc.,* **84,** 1661 (2001) **(c)** Haile S M, Johnson D W Jr., Wiseman G H and Bowen H K, *J. Am. Ceram. Soc.* **72,** 2004 (1989) **(d)** Kutty T R N, Raghu N, *J. Euro. Ceram. Soc.* 11, 161 (1993)

75. Hingorani S, Pillai V, Kumar P, Multani M S and Shah D O, *Mater. Res. Bull.* **28,** 1303 (1993)

76. **(a)** Jimenez-Gonzalez A E, Urueta J A S and Suarez-Parra R, *J. Cryst. Growth* **192,** 430 (1998) **(b)** West A R, *Solid State Chemistry and Its Applications*, John Wiley & Sons, London, (1984) **(c)** Reverchon E, Porta G D, Sannino D and Ciambelli P, *Powder Technol.* **102,** 127 (1999)

77. Hohenberger G and Tomandl G, *J. Mater. Res.* **7,** 546 (1992)

78. **(a)** Amiji N, Tanno Y, Okuma H and Kan M, *Adv. Ceram. Mater.* **1,** 232 (1986) **(b)** Dosch R G, Tuttle B A and Brooks R A, *J. Mater. Res.* **1,** 90 (1986) **(c)** Matier G H, Hutchins C E and Ross S D, *Amer. Ceram. Soc. Bull.* **72,** 73 (1993) **(d)**

Huang Y, Liu M, Zeng Y, Li C, Xia D and Liu S, *Mater. Sci. Eng. B* **86,** 232 (2001)

79. Banerjee A, Ramamohan T R and Patni M J, *Mater. Res. Bull.* **36,** 1259 (2001)
80. Sinha A, Sharma B P, *Mater. Res. Bull.* **32,** 1571 (1997)
81. Lorenz A, Ott J, Harrer M, Preissner E A, Whitehead A H, Schreiber M, *J. Electroceram.* **6,** 55 (2001)
82. Sonder E, Zuhr R A and Martinelli J R, *Mater. Res. Soc. Symp.* **60,** 365 (1986)
83. Viswanath R N, Ramasamy S, Ramamoorthy R, Jayavel P and Nagarajan T, *Nanostructured Mataials* **6,** 993 (1995)
84. Hishita S, Yao Y and Shirasaki S I, *J. Am. Ceram. Soc.* 72, 338 (1989)
85. **(a)** Nakano Y and Ichinose N, *J. Mater. Res.* **5,** 2910 (1990) **(b)** Kutty T R N and Ravi V, *Appl. Phys. Lett.* **59,** 2691 (1991) **(c)** Zhou L and Yu C, *J. Mater. Sci.* **29,** 6055 (1994)
86. **(a)** Shohata N, Nakanishi M and Utsumi K, *Advances in varistor technology*, Vol **3** *Ceramic Transaction*, Edited by Levinson L M, Amer. Ceram. Soc. Westerville, OH (1989) **(b)** Ling H C, Yan M F and Rhodes W W, *J. Am. Ceram. Soc.* **72,** 1274 (1989) **(c)** Huang Y, Liu M, Jiang S, Zeng Y, Li C, Liu S, Zhou D, *Microelectronic Engineering* **66**, 760 (2003) **(d)** Gould R D, Hassan A K, Mahmood F S, *Int. J. Electron.* **76,** 895 (1994)
87. **(a)** Lee Y S and Tseng T Y, *J. Mater. Sci.; Materials in Electronics,* **6**, 90 (1995) **(b)** Puyane R, *J. Mats. Pro. Tech.* **55,** 268 (1995)
88. Yan M F and Rhodes W W, *Appl. Phys. Lett.* **40,** 536 (1982)
89. **(a)** Pennewiss J and Hoffmann B, *Mater. Lett.* **9,** 219 (1990) **(b)** Yang S L and Wu J M, *J. Mater. Res.* **10,** 345 (1995) **(c)** Bueno P R, Camargo E, Longo E, Leite E, Pianaro S A, Varela J A, *J. Mater. Sci. Lett.* **15,** 2048 (1996) **(d)** Sousa V C, Leite E R and Longo E, *J. Euro. Ceram. Soc.* **22,** 1277 (2002)
90. Pianaro S A, Bueno P R, Longo E and Varela J A, *J. Mater. Sci. Lett.* **14**, 692 (1995)

91. Ezhilvalavav S and Kutty T R N, *Appl. Phy. Lett.* **68,** 2693 (1996)

92. Makarov V and Trontelj M, *J. Mater. Sci. Lett.* **13,** 937 (1994)

93. Chung S Y, Kim I D and Kang S J L, *Nature Materials* **3**, 774 (2004)

94. Munnix M and Schmeits, *Phys. Rev. B* **27**, 7624 (1983)

95. Robertson J, *J. Phys. C Solid State Phys.* **12**, 4767 (1979)

96. Sherwood P M A, *Phys. Rev. B* **41**, 10151 (1990)

97. Peaker A R and Horsley B, *Rev. Sci. Instrum.* **42**, 1825 (1971)

98. **(a)** Oyabu T, *J. Appl. Phys.* **53**, 2785 (1982) **(b)** Fagan F G, Amararakoon V R W, *J. Am. Ceram. Soc.* **72**, 119 (1993) **(c)** Jarzebski Z M and Marton J P, *J. Elecrochem. Soc.* **123**, 299C (1976)

99. Ortenberg M V, Link J and Helbig R, *J. Opt. Soc. Am.* **67**, 968 (1977)

100. Ghosh A K, Fishman C, Feng T, *J. Appl. Phys.* **49**, 3490 (1978)

101. P.T. Moseley, *Meas. Sci. Technol.* **8,** 223 (1997)

102. Jarzebski Z M and Marton J P, *J. Elecrochem. Soc.* **123**, 299C (1976)

103. **(a)** Cox D F, Fruberger T B and Semancik S, *Phys. Rev. B* **38**, 2072 (1988) **(b)** Egashira M, Shimizu Y, Takao Y and Sako S, *Sens. Actuators B* **35-36**, 62 (1996)

104. **(a)** Cerri J A, Leite E R, Gouvea D and Longo E, *J. Am. Ceram. Soc.* **79**, 799 (1996) **(c)** Orlandi M O, Bueno P R, Leite E R and Longo E, *Materials Research* **6**, 279 (2003)

105. **(a)** S.A. Pianaro, P.R. Bueno E. Longo and J.A. Varela *J. Mater. Sci. Lett.* **14** (1995) 692 **(b)** Antunes A C, Antunes S R M, Pianaro S A, Rocha M R, Longo E and Varela J A, *J. Mater. Sci. Lett.* **17**, 577 (1998) **(c)** Pinaro S A, Bueno P R, Longo E, Varela J A, *Ceram. Int.* **25**, 1 (1998) **(d)** Oliveira M M, Bueno P R, Olivi P and Longo E, *J. Eur. Ceram Soc.* **21**, 1179 (1999) **(e)** Kale A S, Seal S, Date S K, Santhosh P N, Barve R N, *J. Vac. Sci. Technol. A* **17**, 1196 (1999) **(f)** Leite E R, Nascimento A M, Bueno P R, Longo E and Varela J A, *J. Mater. Sci.: Mater. Electon.* **10**, 321 (1999) **(g)** Bueno P R, Cassia-Santos M R, Leite E

R, Longo E, Bisquert J, Gracia-Belmonte G and Fabregat-Santiago F, *J. Appl. Phys.* **88**, 6545 (2000) **(h)** Li C, Wang J, Su W, Chen H, Wang W, Zhuang D, *Physica B Condensed Matter*, **307**, 1 (2001) **(i)** Skuratovsky I A and Glot A B, *Functional Material* **10**, 314 (2003) **(j)** Wang W X, Wang J F, Chen H C, Su W B, Jiang B Z, Guo Z, Wang C M and Qi P, *Journal of Physics D: Applied Physics*, **36**, 1040 (2003) **(k)** R. Parra, J.A. Varela, C.M. Aldao, M.S. Castro, *Ceram. Int.* **31**, 737 (2005) **(l)** Wang J F, Su W B, Chen H C, Wang W X, Zang G Z, Li C P and Bodde S, *J. Am. Ceram. Soc.* **88**, 331 (2005)

106. Varela J A, Cerri J A, Leite E R, Longo E, Shamsuzzoha M, Bradt R C, *Ceram. Int.* **25**, 253 (1999)
107. Yongjun W, Jinfeng W, Hongeun C, Weilie Z, Peilin Z, Houmin D and Lianyi Z, *J. Phys. D* **33**, 96 (2000)
108. Wang J F, Wang Y J, Su W B, Chen H C, Wang W X, *Mater. Sci. Eng. B* **96**, 8 (2002)
109. Yongjun W, Jinfeng W, Hongeun C, Weilie Z, Peilin Z, Houmin D and Lianyi Z, *Eur. Phys. J.: Appl. Phys.* **11**, 155 (2000)
110. Castro M S and Aldao C M, *J. Eur. Ceram. Soc.* **18**, 2233 (1998)
111. Cassia-Santos M R, Sousa V C, Oliveira M M, Sensato F R, Bacelar W K, Gomes J W, Longo E, Leite E R and Varela J A, *Mater. Chem. Phys.* **90**, 1 (2005)
112. **(a)** Bueno P R, Pianaro S A, Pereira E C, Bulhoes L O S and Longo E, *J. Appl. Phys.* **84**, 3700 (1998) **(b)** Menegotto G F, Pianaro S A, Zara A J, Antunes S R M and Antunes A C, *J. Mater. Sci.: Mater. Electron.* **13**, 253 (2002) **(c)** Pianaro S A, Bueno P R, Olivi P, Longo E and Varela J A, *J. Mater. Sci.: Mater. Electron.* **9**, 158 (1998)
113. Santhosh P N, Potdar H S and Date S K, *J. Mater. Res.* **12**, 326 (1997)
114. Bueno P R, Oliveira M M, Bacelar-Junior W K, Leite E R and Longo E, *J. Appl. Phys.* **91**, 6007 (2002)

115. **(a)** Raghavendra R, Bellew P, McLoughlin N, Stojanovic G, Damnjanovic M, Desnica V and Zivanov L, *IEEE Electron Device Letters* **25**, 778 (2004) **(b)** Kim C H and Kim J H, *J. Euro. Ceram. Soc.* **24**, 2537 (2004) **(c)** Padmini P, Pulikkathara M, Wilkins R and Pandey R K, Appl. Phys. Lett. **82**, 586 (2003)

Chapter 2

Experimental

The experimental work has been carried out for the synthesis of the SnO_2 based varistor materials, pure SnO_2 and TiO_2. The characterization of the compounds and the evaluation of their electrical properties can be grouped into different categories: Synthesis methods, physico-chemical characterization and synthesis of fine SnO_2 & TiO_2 powders. Different type of techniques used for the characterization and evaluation of the properties of materials, the details discussed under the section of instrumental methods. The synthesis of phase pure SnO_2 and TiO_2 by reflux digestion method and by citrate gel method is discussed in last two sections. Further, these powders were used for the preparation of varistor ceramics.

2.1 Introduction

There are different synthesis methods available for the synthesis of oxide ceramic materials [1]. The most common method is ceramic method. In the present work, different SnO_2 based varistor ceramic materials were synthesized by conventional ceramic and by wet chemical method. The other steps involved in making final products such as pelletizing, sintering, lapping, electroding and curing are also described.

Physico-chemical characterization comprises of density measurement, phase analysis by powder X-ray diffraction, sintering properties by thermal mechanical analyzer and microstructure analysis by scanning electron microscopy. Electrical characterization comprises of current–voltage (I-V) measurements at room temperature and ac impedance analysis at various temperatures, between room temperature and 300 °C.

2.2 Methods of synthesis for varistor samples

2.2.1 Ceramic method

The SnO_2 and SnO_2-TiO_2 solid solution based varistor system with different additives used in this study were prepared by conventional ceramic method. In the ceramic method, the constituent oxides and/or carbonates in the stoichiometric ratio were taken and mixed thoroughly in an agate pestle & mortar with acetone as grinding medium. All the chemicals used were of AR grade. After thorough mixing, the ground dry powders were calcined at high temperature. After the first calcination, the powders were again thoroughly ground and heated at higher temperatures with repeated intermediate grinding. The temperature of processing, the duration and the number of grinding for a given material are discussed in respective chapters. The powders were then pelletized using a steel die (15 mm die) and hydraulic press (Carver laboratory press) under a uniform pressure of 3-4 metric tons. These pellets were then directly sintered at various temperatures for different durations in an electric furnace (Nabertherm, High temperature furnace LHT08), which contains heating element of molybdenum disilicide and PtRh-Pt thermocouple.

2.2.2 Chemical synthesis method

Chemical synthesis method used here was modified coprecipitation method. $SnCl_4$ was diluted using ice-cold distilled water and content of SnO_2 was estimated gravimetrically. The other constituents were in the nitrate, chloride and fluoride salts were mixed together in a stoichiometric ratio and finally whole solution was stirred continuously for thorough mixing. To this mixture, ammonium hydroxide was added drop wise with constant stirring as a precipitating agent. This precipitate was stirred continuously for 1 hrs. Since there was possibility of losing of some soluble components of the dopants during filtration, the whole mixture was dried on water bath and the dried powder was preheated at 600 °C. Direct sintering of the pellets was avoided since the evolution of nitrous fumes and other gases could lead to the crumbling of pellets. Few drops of 2 wt. % poly vinyl alcohol (PVA) was added to the calcined powder as a binder similar to the ceramic method. The samples were then sintered in furnace at 1300 °C for different durations. These sintered pellet/pellets were characterized by various physico-chemical characterization techniques.

2.3 Physico-chemical characterizations

2.3.1 Density

Density of the sintered pellets was measured to understand the effect of sintering temperature. The sintered pellets were lapped to uniform thickness with help of 400 and 600 mesh carborundum powder. The weight of the pallet was measured accurately using a microbalance and the thickness & diameter of the pellets were measured using a Vernier caliper. The density was calculated on 3 samples of a given batch and an average value was taken. The density was also measured by Archimedes method.

2.3.2 Thermal analysis (TGA/DTA)

The measurement of change in any property as a material is being heated (or cooled) at a constant rate is called thermal analysis. Weight (Thermogravimetry) & heat content (Differential thermal analysis) are examples of such properties, and come under the broad category of thermal analysis. Both TGA and DTA were done on the as dried powders using a Rheometric Scientific STA 1500+ thermal analyzer between room temperature and 900 °C at a rate of 10 °C per min.

2.3.3 Thermal mechanical analyzer

To study the linear shrinkage and rate of linear shrinkage as a function of temperature, Perkin Elmer Instrument, Pyris diamond TMA (Thermal Mechanical Analyzer) with high temperature system, temperature range of RT-1500 °C (heating rate 10 °C per min) with sample tube, probe - Alumina with R thermocouple was used. *Fig 2.1* shows the schematic block diagram for the TMA measurement principle.

The palletized sample was kept inside the sample tube on an alumina plate and constant force of 100 mN was applied to it. An independently connected linear voltage differential transformer (LVDT) and core detected the resulting change in sample length as a function of temperature.

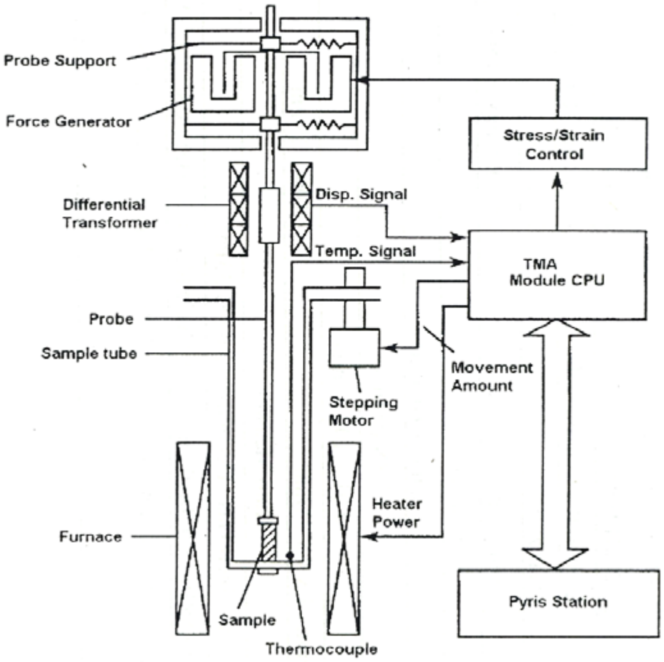

FIG. 2.1 Schematic block diagram for the TMA principle.

2.3.4 Powder X-ray diffraction

X-ray diffraction is useful nondestructive method of structure analysis. When an electromagnetic wave enters a crystal they get scattered by the electrons inside. But due to the periodicity associated with the arrangement of atoms of a crystal for certain angles of incidence (θ), there will be constructive interference between the different scatterers (plane of atoms). Nevertheless for most of the angles, destructive interferences leads to the cancellation of the differenced beam. With knowledge of the wavelength (λ) of the radiation and by measuring the angles at which the constructive interference occur (called Bragg angle θ_B). It is possible to understand the geometrical ordering of the atoms inside the crystal. The relation of the crystal structure with above two parameters is expressed by Bragg equation as given below:

$n \lambda = 2d \sin \theta$

where the integer n is the order of the diffracted beam, λ is the wavelength of the incident X-ray beam, d is the distance between adjacent planes of atoms (the d-spacings), and θ is the angle of incidence of the X-ray beam [2].

Whenever constructive interference occurs for a given set of plane, the angles of incidence θ is taken as θ_B of that planes. Bragg equation puts a limit to the maximum wavelength that can be used for diffraction as $\lambda \leq 2d$. This is the reason for using X-ray for crystal structure studies as the d values are typically in the range of few angstroms. Crystallite size measurement were calculated from X-ray diffraction pattern, using Scherrer formula [2(a)] given in *equation 2.1*

$$D = \lambda K / \beta \cos \theta \qquad 2.1$$

where, D is crystallite size, λ is wavelength of x-ray radiation, θ is the Braggs angle of the line profile, β is the half intensity full width (FWHM) if the line profile measurement in radians and K is constant whose value is taken to 0.9 for spherical particles.

Powder X-ray diffraction (XRD) patterns were recorded on a Philips PW 1839 diffractometer. The X-ray source of this diffractometer emits CuK_{α} radiation with wavelength of 1.5418 Å. The diffractometer is calibrated with reference to standard oriented Si wafer. For usual structural phase analysis a scan rate of 4 ° per min was used.

For determination of lattice parameter by least squares method form powder diffraction data, different computer programs were used viz. Lazy pulveriz (Yvon K, Jeitschko W and Perthe E) Powder diffreaction package 1.1 (Colligaris M and Geremia S) and Powder cell 2.3 (Kraus W and Nolze G).

2.3.5 Scanning electron Microscopy

The scanning electron microscope (SEM) is an incredible tool for seeing the unseen worlds of micro space. Conventional light microscopes use a series of glass lenses to bend light waves and create a magnified image. The scanning electron microscope creates the magnified images by using electrons instead of light waves. The SEM shows very detailed 3-dimensional images at much higher magnifications than that of possible with a light microscope. The images created without light waves are rendered black and white [3]. *Fig 2.2* shows the schematic block diagram of scanning electron microscope.

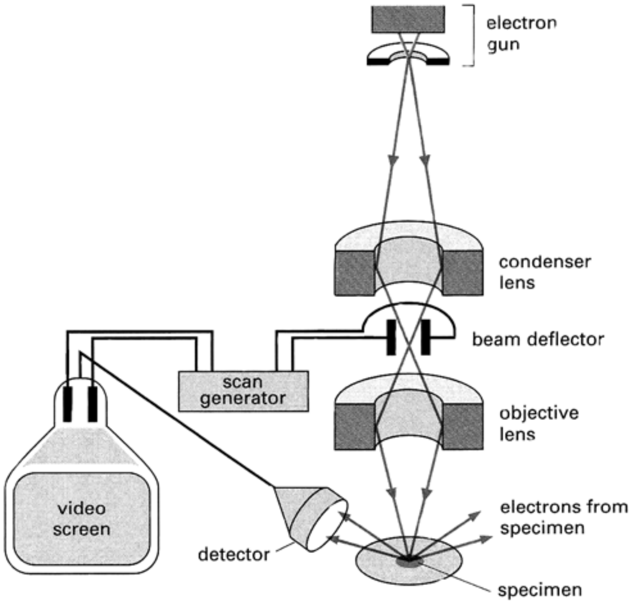

FIG. 2.2 Schematic block diagram of Scanning Electron Microscope.

In this work, the microstructural features of samples were obtained using a scanning electron microscope (Leica Cambridge 440). The sintered pellets were fractured to expose the inner portion and mounted on specimen mounting stub. Silver paste was used to stick the sample to the stub and a thin layer of gold was coated on surface of sample using an ion beam sputtering system (Poloran equipment ltd., SEM coating unit E5000) to avoid charging the specimen. Counting the number of grains intercepted by line of known length and taking the average of 3-4 measurements made across a given micrograph found the grain size. The task was made easy with the in built ability of the SEM system by which one can measure the grain size by moving the cursor across the grain.

2.3.6 Transmission Electron Microscopy

Based on similar principles of the conventional light microscope, the transmission electron microscope (TEM) is capable of magnification of 100,000 times an extreme resolution, far beyond the possibilities afforded by visible light. Unlike the scanning electron microscope, which uses reflected electrons, the TEM uses electrons passing through a very thin slice of the specimen. Magnetic lenses focus the electron beam and project the highly magnified image onto a phosphor screen or special photographic film. TEM is especially useful in studying the structure of cells, and in crystallography. TEM uses the electrons as light source and their much lower wavelength makes it possible to get a resolution a thousand times better than with a light microscope [4]. The possibility for high magnifications has made the TEM a valuable tool in medical, biological and materials research. TEM is a complementary tool to conventional crystallographic methods such as X-ray diffraction.

A crystalline material interacts with the electron beam mostly by diffraction rather than absorption. If the planes of atoms in a crystal are aligned at certain angles to the electron beam, the beam is transmitted strongly; while at other angles, the beam is diffracted, sending electrons in another direction. In the TEM, the specimen holder allows the user to rotate the specimen to any angle in order to establish the desired diffraction conditions; while an aperture placed below the specimen allows the user to select electrons diffracted in a particular direction. The resulting image shows strong diffraction contrast, which highlights the faults in the crystal structure very clearly. This is very important in materials science. Faults in crystals affect both the mechanical as well as electronic properties of materials, so understanding how they behave gives a powerful insight.

The samples for TEM were prepared by drop coating on to a carbon coated copper TEM grid. TEM micrographs and selected area diffraction patterns were obtained on a JEOL, 1200 EX instrument operated at an accelerating voltage of 100 kV.

2.4 Electrical characterization

2.4.1 Electroding

For electrical measurement the samples were given electrical contacts using silver paint. First the samples were lapped to required thickness and the thickness was accurately measured using Vernier caliper. Then circular contacts of known diameter were given to the pellets using silver paint and cured at 600 ^{o}C for 30 minutes.

2.4.2 DC Current-voltage characterization

The I-V characteristics were measured by using Kiethley electrometer 6517A, high resistance meter. It also contains a built in one-kilovolt dc power supply so that there was no need of external power supply in the circuit. *Fig 2.3* represents the circuit for I-V characteristic measurements. The measurement was carried out up to a maximum current of 1 mA since at high currents the chances of thermal breakdown were high (above this region, the characteristics are generally measured using pulse voltage method). At each voltage point a certain time lag was given for the current to stabilize.

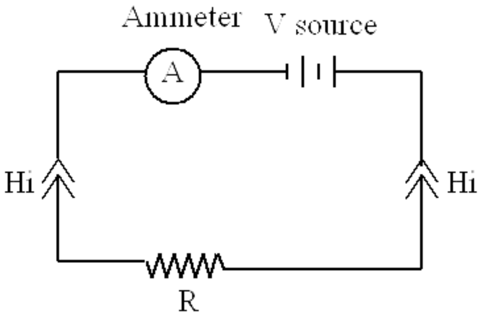

FIG. 2.3 Circuit for I-V characteristic measurements.

The current-voltage relation of a varistor is given by the *equation 2.2*,

$$J= (E/C)^{\alpha} \tag{2.2}$$

where, J is the current density, E is the applied field, C the proportionality constant and α is the nonlinear coefficient. The current-voltage curves were plotted on log - log scale, from which the slope of the curves gives the value of α. The important parameter, breakdown filed (E_B) was taken as the field applied when current flowing through the varistor is 1 mA. Since Schottky type grain boundary barriers are present in the present samples the current density in ohmic region of varistor is related to the electric field and the temperature given by *equation 2.3* [7].

$$J = AT^2 \exp [(\beta E^{1/2}-\Phi_B)/kT] \tag{2.3}$$

where A, equal to $4\rho emk^2/h^3$, is Richardson's constant, ρ = 6.95 gm cm^{-3} (density of tin oxide), e is electron charge, m is electron mass, K_B is Boltzmann's constant, h is Planck's constant, Φ_B is interface barrier height, and β is constant related to the relationship [4] given in *equation 2.4*

$$\beta \propto 1/(r\omega) \tag{2.4}$$

where r is grain number per unit length and ω is the barrier width. Measuring the current density in ohmic region and keeping the temperature of the tested varistor constant, for two different applied fields the *equations 2.5* and *2.6* are,

$J_1 = AT^2 \exp [(\beta E_1^{1/2}-\Phi_B)/K_BT]$ 2.5

$J_2 = AT^2 \exp [(\beta E_2^{1/2}-\Phi_B)/ K_BT]$ 2.6

The values of Φ_B and β can be calculated from above equations.

2.4.3 AC Impedance analysis

Impedance spectroscopy is a valuable technique used for the characterization of inhomogeneous (insulating, electrical and magnetic) materials exhibiting granular structures. To differentiate between the varying contributions from grains and grain boundaries, intergranular layers and electrode interface, ac impedance spectra are often used with great success. Most common method of impedance analysis is to measure impedance directly in the frequency domain by applying a single frequency voltage to the interface and measuring the phase shift and amplitude (real and imaginary parts) of the resulting current at that frequency. This way the measurements was done in a large range of frequency (few Hz to Giga Hz)

In the impedance spectroscopy, a time dependent voltage $E(\omega) = \delta E \sin(\omega t)$ is applied across the ceramic sample. A sinusoidal current with the same angular frequency will then flow through the sample and the response is characterizes by complex impedance Z. Z will be a function of ω. The real and imaginary parts of their complex impedance Z (Z′ and Z″) can be recorded for a large range of frequencies using the impedance analyzer. When the data points are plotted in complex impedance plane (Z′ and Z″), are usually along the arc of circles. An equivalent circuit based on a serial assembly of parallel resistances and capacitances can be then used to simulate the electrical behavior. Usually the values of the resistance and capacitance of each cell and therefore each arc can be assigned to a specific part of the ceramic sample: the grain interiors, grain boundaries, metal-ceramic interfaces etc. The chord of each arc of a circle is the resistance of that individual part of the ceramic. The time constant, Γ corresponding to each arc obeys the relation $\omega^*\Gamma = 1$, where ω^* corresponds to the top of the semicircular arc. The time constant corresponding to grains, grain boundaries, interfaces differ by one order of magnitude and hence well distinguished arcs corresponding to each part of the ceramic are usually obtained. A careful selection of the electrode is necessary to avoid the presence of an arc of a circle in the impedance spectrum, which can interfere with the grain-grain-boundary contributions.

The lumped-parameter/complex plane analysis have been found to be an important technique to study a heterogeneous system [5]. Another important parameter is the depression angle θ. Its presence indicates non-Debye (non-ideal) relaxation. A depression angle is defined when the center of semicircular relaxation lies below the X-axis instead of on the X-axis. The depression angle θ observed in the Z plane is related to the degree of uniformity/non-uniformity in reactance for the associated relaxation resulting in an average time constant. Alim *et al*. and others [6] have done extensive work on impedance analysis of ZnO varistors.

For ac impedance measurements, a sintered pellet of 12.5 mm diameter and 2 mm thickness were used after applying electrical contacts as explained in *section 2.4.1*. The impedance measurements were made with Impedance/gain-phase analyzer (Solartron model S1 1260) using frequency ranging from 0.1 Hz to 1 MHz with an ac amplitude voltage of 100 mV. The sample was kept between platinum electrodes in a sample holder Probostat test cell (Norweigian electro ceramic made) heated in furnace. The ac impedance data was recorded in the temperature range of 25 ºC to 300 ºC over the frequency range given above.

2.5 Synthesis of nanocrystalline SnO_2 and TiO_2 powders by reflux digestion method

The synthesis of phase pure nanocrystalline SnO_2 and TiO_2 powders is given in this section. A simple gel to crystal conversion method has been followed for the preparation of SnO_2 and TiO_2 at 80–100 ºC under refluxing conditions. Freshly prepared tin or titanium hydroxide gel was allowed to crystallize under refluxing and stirring conditions for 6–12 hrs. Formation of nanocrystallites of SnO_2, anatase TiO_2 and rutile TiO_2 after further heating was confirmed by X-ray diffraction (XRD) study and crystallite size study was confirmed by TEM. These powders have been used to prepare varistor disc subsequently.

2.5.1 Introduction

To prepare active nanocrystalline powders, several chemical techniques have been investigated and reported in the literature. Among the various methods of preparing nanostructured SnO_2, co-precipitation, sol–gel, spray pyrolysis, hydrothermal methods, freeze–drying, etc. are popular. Recently, gel combustion methods using a variety of organic fuels like urea, hydrazine, citric acid and others have been reported to be promising methods to prepare a variety of oxides including nanocrystalline SnO_2 [8]. Though the combustion methods are fairly simple, higher calcination temperatures have been reported and the method requires an oxidizing agent and necessarily a fuel in the reaction mixture [8]. The method of gel to crystalline conversion is reported in the literature for the preparation of multicomponent oxides such as perovskites and spinels [9]. But this method is not yet found in the literature for the preparation of SnO_2. Here, this simple method of digestion of amorphous stannic hydroxide gel under refluxing conditions at 100 °C for the preparation of nanocrystalline SnO_2 is given. It differs from traditional sol-gel technique (i) no calcinations is required for final product (ii) no expensive alkoxides are used.

2.5.2 Experimental

$SnCl_4$ was diluted with ice-cold distilled water to form $SnOCl_2$ solution. To this solution ammonium hydroxide was added drop wise to precipitate tin as hydroxide. The hydrated stannic hydroxide gel was thoroughly washed free of anions and transferred to flask fitted with a water condenser. The gel was continuously stirred for 6 hrs and temperature was maintained around 80–100 °C. The solid mass after refluxing was found to be crystalline and free flowing. The crystalline powder formed was filtered and oven dried. The same procedure was repeated for the preparation of TiO_2 powder and the precursor used was $TiCl_4$. These fine powders obtained by this simple gel to crystalline method are potential candidates for gas sensors and varistor applications.

Various techniques such as Powder x-ray diffraction (XRD), BET surface area measurements (Nova 1200 instrument) and transmission electron microscopy (TEM) were employed to characterize these powders. The Raman scattering experiments were performed in the region 100 - 700 cm^{-1} in the back scattering mode using SPEX 1403 reflection grating type double spectrometer to confirm rutile and anatase phases of TiO_2.

2.5.3 Results and discussion

2.5.3.1 SnO_2

Fig 2.4 shows the X-ray diffraction pattern for the samples before and after refluxing at 100 °C. The sample was X-ray amorphous for the former and no distinct peaks were observed. The powders after digestion showed the crystalline pattern and the observed *d*-lines match the reported values for the rutile SnO_2 phase (JCPDS No. 21-1250). The calculated lattice parameters are $a = 4.738$ Å and $c = 3.188$ Å. It was noted that the molarity of the solution should be > 0.15 M of SnO_2 to obtain crystallization in this method. Otherwise it requires long durations to form a crystalline product at 100 °C. It was also noted that crystalline SnO_2 was found to formed from the hydroxide precipitate without refluxing, when calcined at 400 °C for 12 hrs. This shows the advantage of the present method.

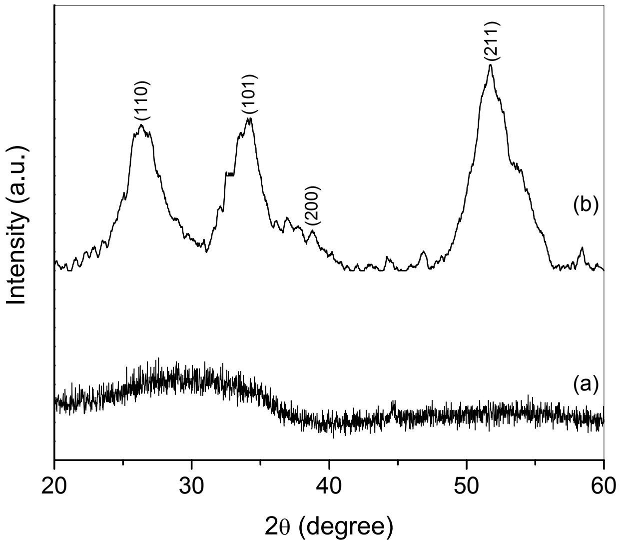

FIG. 2.4 X-ray diffraction patterns of (a) freshly prepared tin hydroxide precipitate before refluxing and (b) after refluxing for 6 hrs at 100 °C.

The average particle size was found to be 30 nm and the particles were observed agglomerated (*Fig 2.5a*). The selected area diffraction pattern for the SnO_2 nanocrystals is given in *Fig 2.5b*, it was in good agreement with the X-ray diffraction pattern. The surface area of this powder was found to be 70 $m^2\ g^{-1}$. The crystallite size measurements were also carried out using the Scherrer equation, the average particle size obtained from X-ray diffraction data was 40 nm.

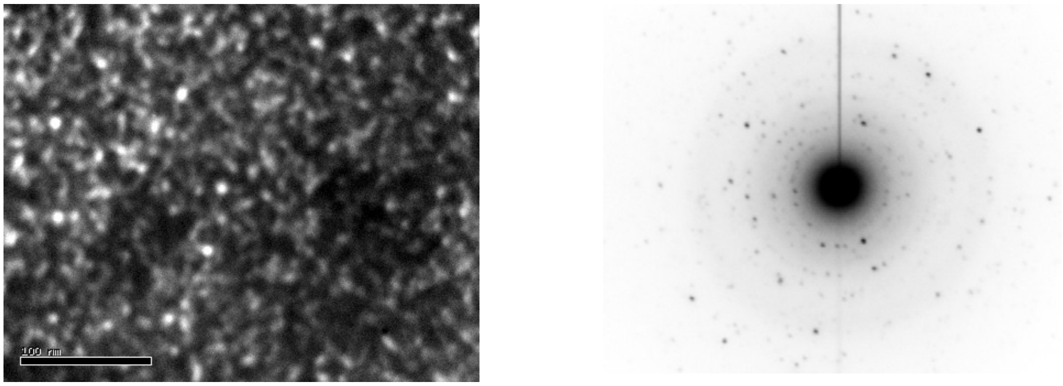

(a) (b)

FIG. 2.5 (a) TEM micrograph (b) selected area diffraction pattern of tin oxide powder prepared at 100 °C.

2.5.3.2. TiO_2

Fig. 2.6 shows the X-ray diffraction patterns for the samples before and after refluxing at 100 °C. The sample was X-ray amorphous for the former and no distinct peaks were observed. The powder after digestion showed the crystalline pattern and the observed d-lines match with the reported values for the anatase phase (JCPDS No. 21-1272). The calculated lattice parameters for anatase were, a = 3.772 Å and c = 9.505 Å. It was noted that the molarity of the solution should be > 0.15 M of TiO_2 to obtain crystallization in this method. Otherwise, it requires long durations to form a crystalline product at 100 °C. Calcining the sample at 700 °C for 12 hrs results in rutile phase (JCPDS No. 21-1276). The calculated lattice parameters for rutile were a = 4.565 Å and c = 2.945 Å. The surface area of the anatase powders was found to be 60 m^2 g^{-1}.

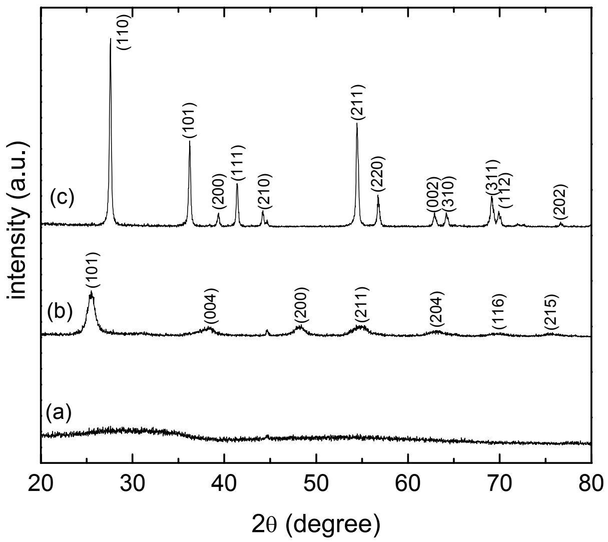

FIG. 2.6 X-ray diffraction patterns of (a) as dried gel, (b) after digestion at 100 °C for 6 hrs (anatase) and (c) after annealing the powder at 700 °C for 12 hrs (rutile).

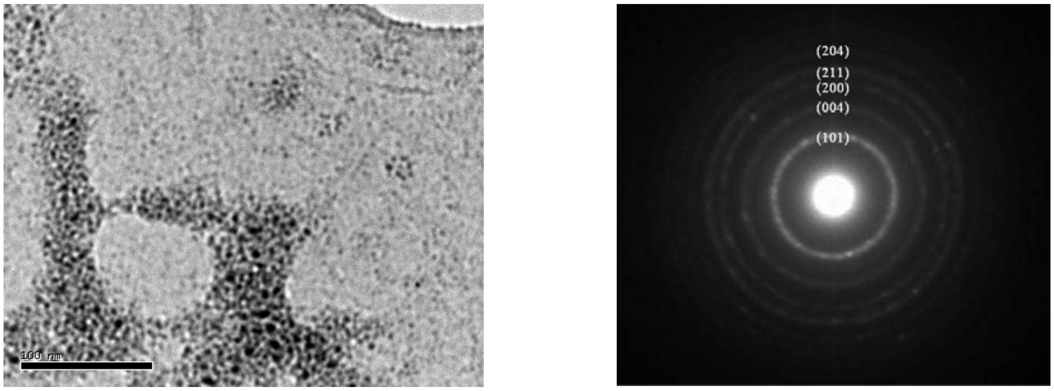

(a)

(b)

FIG. 2.7 (a) TEM micrograph (b) selected area diffraction pattern of anatase titanium oxide powder prepared at 100 °C.

The average particle size of anatase phase was found to be 10 nm and the particles were observed agglomerated (*Fig. 2.7a*). The crystallite size measurements were also carried out using the Scherrer equation, the average crystallite size obtained for anatase and rutile phases from X-ray diffraction data were 15 and 40 nm respectively. *Fig 2.7b* shows the electron diffraction pattern with indexed diffraction rings for the anatase phase. *Fig 2.8 (a)* and *(b)* shows the TEM micrograph and indexed selected area diffraction pattern of the rutile TiO_2 respectively. The Raman spectrum of TiO_2 has been studied extensively, but the investigation of the Raman spectrum of nanocrystalline TiO_2 is limited. *Fig 2.9* shows the Raman spectrum of TiO_2 powders in both phases namely anatase and rutile. The band near 608 cm^{-1} was identified as A1g mode, the band near 446 cm^{-1} as the Eg mode for the rutile phase [10]. The small differences in assigning peak wave numbers from the literature are considered to be arising out of intragrain defects present in the sample. The Raman bands for anatase phase also are similar to that reported in the literature [10].

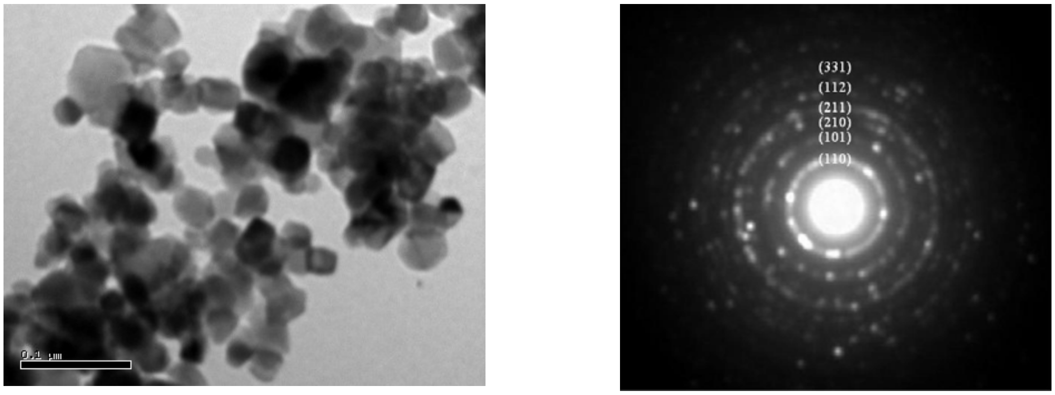

(a) (b)

FIG. 2.8 (a) TEM micrograph (b) selected area diffraction pattern of rutile titanium oxide powder calcined at 700 °C.

It is well known that both anatase and rutile TiO_2 can grow from TiO_6 octahedra and that the phase transition proceeds by the rearrangement of the octahedra. Arrangement of octahedra through face sharing initiates the anatase phase while the edge sharing leads to the rutile phase. In aqueous medium, protonated surfaces of TiO_6 octahedra easily combine with -OH groups of other TiO_6 octahedra to form Ti–O–Ti oxygen bridge bonds by elimination water molecule. The protonation followed by the possible face-sharing TiO_6 octahedra would result in formation of anatase phase while edge sharing leads to rutile phase. Crystalline rutile TiO_2 with particle size <10 nm were prepared by the homogeneous precipitation method by heating and stirring aqueous $TiOCl_2$ solution at room temperature to 150 °C under one atmospheric pressure [11]. Metal hydroxide gels are in general polymeric chains forming an entangled network in which solvent is entrapped. It was proposed that with increasing pH within the gel, desolation of the bridging groups such as Ti–O–Ti takes places leading formation of TiO_6 octahedra as given below:

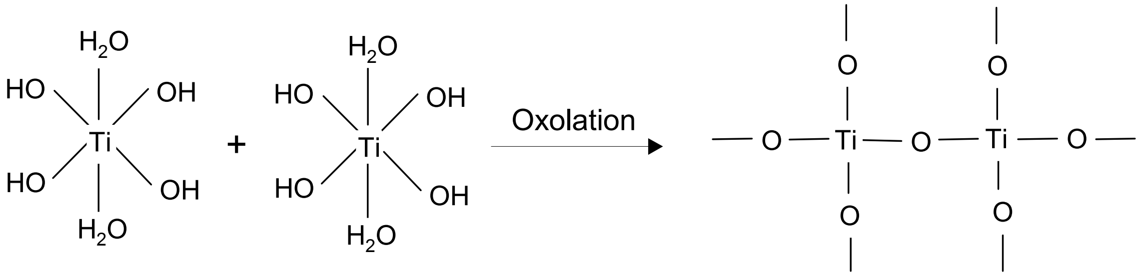

Metal hydroxide gels are in general polymeric chains forming an entangled network in which solvent is entrapped. It is the osmotic pressure, which is the sum of rubber elasticity, polymer–polymer affinity and hydrogen ion pressure that contributes to stability of the gel. If any one of the factors altered, the gel collapses irreversibly. The continuous influx of solvent breaks the gel network and small crystalline regions were created. This crystallization was favored because of reduction in the free energy. Thus possibly SnO_2 and anatase TiO_2 phase formed at 100 °C.

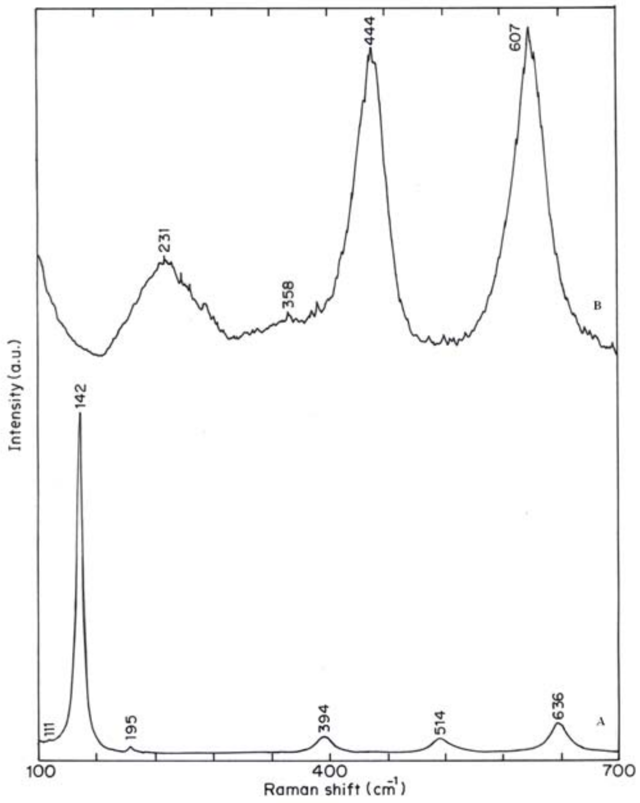

FIG. 2.9 Raman shift in (A) anatase and (B) rutile powders.

2.6 Synthesis of nanocrystalline TiO_2 powder by citrate gel method

A gel was formed when a mixture of $TiOCl_2$ and citric acid was heated on a water bath. An ultrafine powder of TiO_2 in the anatase phase was formed, when the gel was decomposed at 350 °C. The anatase phase was converted into rutile phase on annealing at higher temperatures >500 °C. These powders were characterized by X-ray diffraction (XRD), transmission electron microscopy (TEM) and surface area measurements. The average particle size obtained for anatase phase was 3.5 nm whereas it was 45 nm for rutile phase.

2.6.1 Introduction

The three crystalline polymorphs of TiO_2 are anatase, rutile and brookite. Ultrafine powder of rutile is widely used as a pigment in paints because of its maximum light scattering with virtually no absorption, whereas the anatase phase is reported to show improved performance for photocatalysis and photon-electron transfer [12]. TiO_2 also finds application as a dielectric material due to its high dielectric constant [13]. A large number of preparation methods of TiO_2 have been investigated and reported in the literature. Nanocrystalline anatase is generally synthesized by hydrothermal methods with $TiCl_4$ [14], amorphous TiO_2 [15] or $TiOCl_2$ aqueous solution [11] and sol-gel methods using titanium alkoxides [16]. Vapour phase decomposition of titanium alkoxide or $TiCl_4$ in an oxygen atmosphere at 100 °C is reported to yield particles [17]. Synthesis of spherical particles of TiO_2 has been reported by the hydrolysis of a dilute alcoholic solution of titanium alkoxide [18]. A mixture of anatase and rutile were produced by evaporation of Ti metal in a helium atmosphere, followed by the collection and subsequent oxidation of the Ti clusters thus formed [19]. Ultrafine particles of anatase and rutile TiO_2 were produced by a simple citrate method are presented here. This method has not been reported in the literature. The citrate gel method offers a number of advantages for the preparation of fine powders of many complex oxides as quoted in the literature [20].

2.6.2 Experimental

$TiCl_4$ and citric acid used for the preparation of TiO_2 were of AR grade. $TiCl_4$ was diluted with ice-cold distilled water and mixed with citric acid in a 1:1 molar ratio and heated on a water bath. Since there was no precipitation during mixing, the pH of the solution was not varied. On heating on a water bath at 100 °C a light yellowish gel was formed after evaporation of water. Subsequently, the gel was decomposed at various temperatures ranging from 200 °C to 900 °C. The gel initially started to swell and filled the beaker producing a foamy precursor. This foam consists of very light and homogeneous flakes of very small particle size.

Various techniques such as X-ray diffraction (XRD), thermogravimetric analysis (TGA/DTA), BET surface area measurements and Transmission electron microscopy (TEM) were employed to characterize these powders.

2.6.3 Results and discussion

The citric acid added acts as a complexing agent. The mixture of citric acid and $TiOCl_2$ solution forms a gel on heating on a water bath which decomposes at higher temperatures >150 °C. During calcinations, a black fluffy mass (foam like) was formed which occupies large volumes of the furnace. As the temperature increases, the black mass turns to white in colour with the removal of carbon. Samples calcined at 500 °C for 15 min shows less than 1 % of carbon. At higher temperatures of calcinations no carbon was found to present. *Fig 2.10* show the X-ray diffraction patterns for the samples heated at three different temperatures. The sample is X-ray amorphous until 200 °C and no distinct peaks were observed. However on increasing temperature to 350 °C, anatase phase was found to form. The observed d-lines match the reported values for the anatase phase. The calculated lattice parameters for anatase are a = 3.778 Å and c = 9.508 Å. Further, rise in temperature to 500 °C leads to beginning of the conversion of anatase phase into rutile phase. X-ray diffraction patterns shows the presence of both anatase and rutile phases. At 800 °C the conversion was complete and single phase rutile was formed. The calculated lattice parameters for rutile were a = 4.568 Å and c = 2.949 Å.

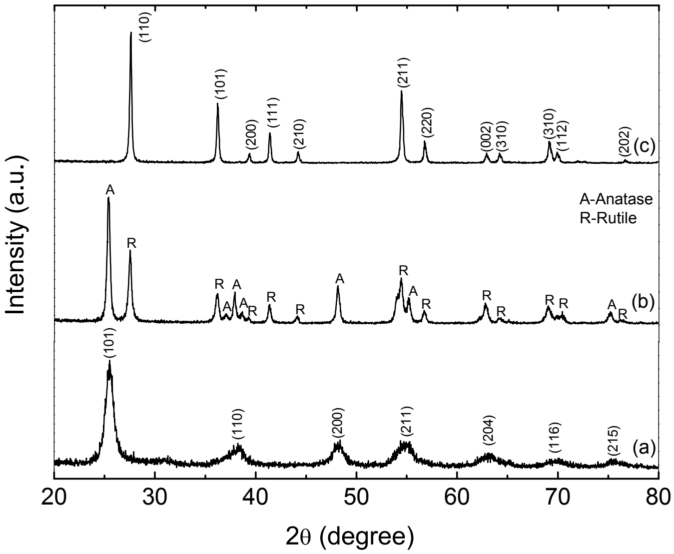

FIG. 2.10 X-ray diffraction patterns of sample calcined at (a) 350 °C anatase phase, (b) 500 °C mixture of anatase and rutile and (c) 800 °C rutile phase.

The DTA/TGA curve recorded at a rate of 10 °C per min in air for the powder heated at 150 °C is depicted in *Fig 2.11*. The exotherm at 500 °C shows the formation of rutile phase. The surface area of the anatase powders calcined at 350 °C was found to 60 m^2 g^{-1}. The average particle size of anatase phase was found to 3.5 nm and the particles of rutile phase were observed agglomerated with average particle size of 35 nm (*Fig 2.12*). The particle did not grow much (~45 nm) after annealing at 900 °C for 12 hrs. The crystallite size measurements were also carried out using the Scherrer equation, $D = \lambda K/ \beta \cos \theta$ where, D is the crystallite size, k is a constant (0.9 assuming that the particles are spherical), λ is the wavelength of the X-ray radiation, β is the line width (obtained after correction for the instrumental broadening) and θ is the angle of diffraction. The average crystallite size obtained for anatase and rutile phases from X-ray diffraction data are 5 and 40 nm, respectively. It is well known that both anatase and rutile TiO_2 can grow from TiO_6 octahedra and that the phase transition proceeds by the rearrangement of the octahedra. Arrangement of octahedra through face sharing initiates the anatase phase while the edge sharing leads to the rutile phase. For pH <3.5, the protonated surfaces of TiO_6 octahedra easily combine with -OH groups of other TiO_6 octahedra to form Ti–O–Ti oxygen bridge bonds by elimination of water molecule. In the presence of citric acid, the protonation followed by the possible face-sharing TiO_6 octahedra will result in formation of anatase phase.

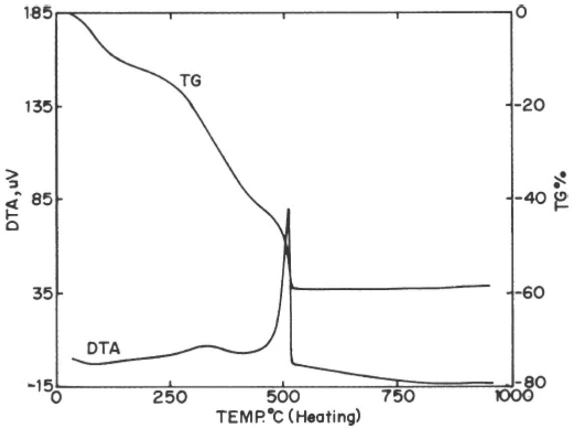

FIG. 2.11 DTA/TGA curve for the sample calcined at 423 K.

Under hydrothermal conditions [21], the initial amorphous TiO_2 converts into rutile phase in the presence of citric acid, whereas in the present case the addition of citric acid into $TiOCl_2$ leads to anatase on calcining at 350 °C. In hydrothermal conditions [14(b)], the obtained average particle size of rutile is 20 nm whereas for anatase, it is 10 nm. It is also reported [14(b)] that the presence of NaCl and $SnCl_2$ as mineralizers are essential for the formation of rutile phase. Anatase powders prepared from hydrolysis of tetra-2- propoxide consists of ~200 nm sized particles [16(b)] when calcined at 600 °C. Crystalline rutile TiO_2 with particle size < 10 nm were prepared by the homogeneous precipitation method by heating and stirring aqueous $TiOCl_2$ solution at room temperature to 150 °C under one atmospheric pressure [11].

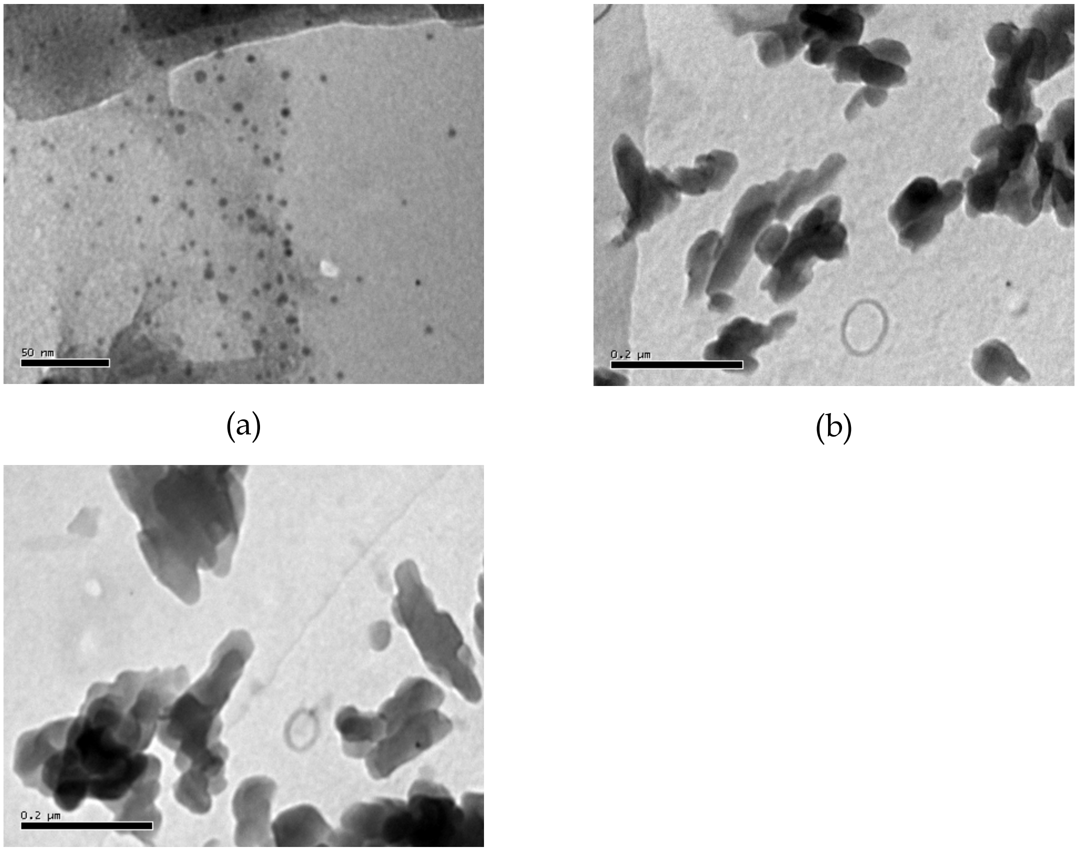

(a)

(b)

(c)

FIG. 2.12 TEM pictures of (a) anatase, (b) rutile and (c) sample annealed at 900°C for 12 hrs.

References

1. Rao C N R, *Chemical approaches to the synthesis of inorganic materials*, Wiley Eastern Ltd. New Delhi (1994)
2. **(a)** Klug H P and Alexander L E, *X-ray diffraction procedures*, John weley and sons New York (1954) **(b)** Cullity B D, *Elements of X-ray diffraction*, Addison Wesley publishing company, Inc. Massachusetts (1956)
3. Goldstein J I, Newbury D E, Echlin P, Joy D C, Romig Jr A D, Lyman C E, Fiori C and Lifshin E, *Scanning Electron Microscopy and X-ray microanalysis*, Plenum Publishing corporation, New York (1992)
4. Fryer J R, *Chemical application of Transmission Electron Microscopy*, Academic press, San Diego (1979)
5. Macdonald J R, *Impedance spectroscopy (Emphasizing on solid materials and systems)* A Wiley Interscience publication (1987)
6. **(a)** Alim M A, Seitz M A and Hirthe R A, *J. Amer. Ceram. Soc.* **71**, C52 (1988) **(b)** Alim M A and Seitz M A, *J. Amer. Ceram. Soc.* **71**, C246 (1988) **(c)** Alim M A, *J. Amer. Ceram. Soc.* 72, 28 (1989) (d) Alim M A, Seitz M A and Hirthe R A, *J. Appl. Phys.* **63**, 2337 (1988)
7. Pianaro S A, Bueno P R, Olivi P, Longo E, Varela J A, *J. Mater. Sci. lett.* **16**, 634 (1997)
8. Bhagwat M, Shah P and Ramaswamy V, *Mater. Lett.* **57,** 1604 (2003)
9. **(a)** Kutty T R N and Padmini P, *Mater. Chem. Phys.* **39,** 200 (1995) **(b)** Padmini P and Kutty T R N, *J. Mater. Chem.* **4,** 1875 (1994)
10. Cheng H, Ma J, Zhao Z and Qi L., *Chem. Mater.* 7, 663 (1995)
11. Kim S J, Park S D, Jeong Y H and Park S, *J. Am. Cerm. Soc.* **82**, 927 (1999)
12. **(a)** Moritz T, Reiss J, Diesner K, Su D and Chernseddine A, *J. Phys. Chem. B* **101**, 8052 (1997) **(b)** Fox M A and Dula M T, *Chem. Rev.* **93,** 341 (1993)

13. Hoffman M R, Martin S T, Choi W and Bahnemann D W, *Chem. Rev.* **95**, 69 (1995)

14. **(a)** Moser J and Gratzel M, *J. Am. Chem. Soc.* **105,** 6574 (1983) **(b)** Cheng H, Ma J, Zhao Z and Qi L, *Chem. Mater.* **7**, 663 (1995)

15. Yanagisawa K and Ovenstone J, *J. Phys. Chem. B* **103**, 7781 (1999)

16. **(a)** Ding X, Qi Z. and He Y., J. *Mater. Sci. Lett.* **14**, 21 (1995) **(b)** Nishimoto S, Ohtani B, Kojiwara H and Kagiya T, *J. Chem. Soc. Faraday Trans.* **81,** 61 (1985)

17. Suyama Y and Kato A, *J. Am. Ceram. Soc.* **68**, C-154 (1985)

18. Barringer E A and Bowen H K, *J. Am. Ceram. Soc.* **65**, C-199 (1982)

19. Parker J C, Singel R W, *Appl. Phys. Lett.* **57**, 943 (1990)

20. **(a)** Wang C C, Ying J Y, *Chem. Mater.* **11**, 3113 (1999) **(b)** Stathates E, Lianes P, Del Monte F, Levy D, Tsiourvas D, *Langmuir* **13**, 4295 (1997)

21. Yin H, Wada Y, Kitamura T, Kambe S, Mursawa S, Mori H, Sakata T and Yanagida S, *J. Mater. Chem.* **11,** 1694 (2001)

Chapter 3

Influence of various donors

This chapter deals with the influence of different donors: Sb_2O_3, Ta_2O_5, Nb_2O_5 and V_2O_5 on non-linear current (I) - voltage (V) relations of tin oxide ceramics. The influence of Sb_2O_3, Ta_2O_5, Nb_2O_5 and V_2O_5 is separately discussed in four different sections. The room-temperature resistivity (ρ), non-linear coefficient (α), breakdown electric field (E_B) and barrier height (Φ_B) were calculated as a function of donor content. The present system contains fewer additives as compared to ZnO varistor wherein small quantities of variety of metal oxides are added. Optimum doping of Sb-doped samples showed the promising behavior for low-voltage varistor applications. The pentavalent impurity added acts as donor and increases the electronic conductivity. The observed non-linear coefficient (α) was in the range of 3 - 36 and the breakdown field varies from 110 to 4925 V cm^{-1}.

3.1 Introduction

It is postulated in literature [1] that at least two additives should be introduced into metal oxide varistor in order to obtain good non-linear characteristic. Dopant with higher valency acts as donor when dissolves into SnO_2 lattice, thus decreases the lattice resistivity of the SnO_2. In contrast, dopant having lower valency will increase the grain boundary resistivity by behaving as an acceptor and locally compensating donors. Therefore, the defect induced potential barriers forms. Pentavalent additive can be one of the varistor forming oxide. CoO is an additive reported [2] for SnO_2 to get sinter-densities above 94 %. The substitution of the Sn by Co leads to the formation of oxygen vacancies and these vacancies control the rate of diffusion resulting in higher densification. The Co^{2+} ion having lower valence than Sn^{4+} creates oxygen vacancies in tin oxide lattice and species Co'_{Sn} and Co''_{Sn} can segregate at grain boundaries. The presence of pentavalent impurity, which has a greater valency than Sn^{4+} leads to an increase of electronic conductivity in the SnO_2 lattice [3]. There are few reports found in the literature for Nb_2O_5 [4], Ta_2O_5 [5] and Sb_2O_3 [6] as pentavalent additives in the SnO_2 varistor ceramics.

3.2 Experimental

Samples were prepared by conventional ceramic method and modified coprecipitation method. All the chemicals used were of AR grade. SnO_2, CoO, Sb_2O_3, Ta_2O_5, Nb_2O_5 and V_2O_5 were weighed in required ratio (99-x) SnO_2+1 CoO+ x D (where, D = Sb_2O_3, Ta_2O_5, Nb_2O_5 & V_2O_5 and x = 0.01, 0.05, 0.1 and 0.5 all in at. %), mixed well with acetone and ground for several hours with agate mortar & pestle. The powder samples were mixed with few drops of a binder (2 wt % of poly vinyl alcohol) and pelletized (15 mm diameter, 2 mm thickness). The green pellets were sintered at 1300 °C for 4 and 24 hrs. The densities of the pellets were measured by mass volume and Archimedes methods. The sintered pellets were polished and low temperature curing silver paint was applied on their surfaces of known area. The pellets were cured at 600 °C for 30 minutes. The samples were identified as SCX-1, SCX-2, SCX-3 and SCX-4 for 0.01, 0.05, 0.1 and 0.5 at. % X-oxide (where, X=A, Ta, N and V for Sb_2O_3, Ta_2O_5, Nb_2O_5 and V_2O_5 respectively).

3.3 Sb_2O_3 doped series

3.3.1 I-V characteristics

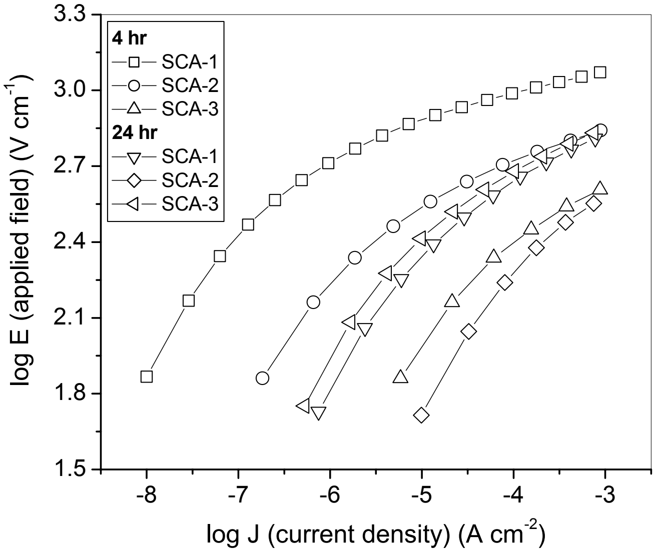

FIG. 3.1a I-V characteristic plots for the samples: SCA-1, SCA-2 and SCA-3 sintered at 1300 ºC for 4 and 24 hrs.

A typical current-voltage characteristic was measured for the Sb_2O_3 doped samples. *Fig 3.1a* shows the current density (J) versus applied field (E) (I-V characteristic) plots on log scale for the samples: SCA-1, SCA-2 and SCA-3 sintered at 1300 ºC for 4 and 24 hrs. The non-linear coefficients (α) calculated from the slopes of the curves in the non-linear regions for the samples sintered for 4 hrs were found to be 19, 14, 9 and 3 for SCA-1, SCA-2, SCA-3 and SCA-4 respectively. The values of non-linear coefficients calculated for the samples sintered for 24 hrs were 12, 8 and 9 for SCA-1, SCA-2 and SCA-3 respectively and the SCA-4 was conducting. The other performance parameters: breakdown field (E_B), density (ρ) and barrier height (Φ_B) are given in *Table I*. The leakage current (I_l) range for Sb_2O_3 doped series was between 0.044 to 12.4 nA. The non-linear coefficient and breakdown field both decrease with the increase concentration of Sb_2O_3. Decrease in non-linear coefficient and breakdown field was also observed for the increase in sintering duration from 4 to 24 hrs. When the content of Sb was between 0.1 and 0.5 at. %, the room temperature resistivity decreases tremendously and the sample behaves as good conductor at high concentration of Sb, mainly when sintering duration was long (*Table I*).

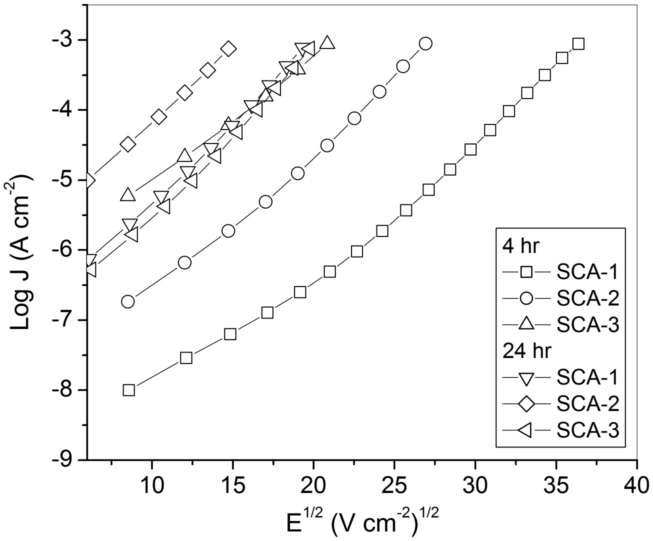

FIG. 3.1b Characteristic plots of log J against $E^{1/2}$ for the samples: SCA-1, SCA-2 and SCA-3 sintered at 1300 °C for 4 and 24 hrs.

The decrease in breakdown field with increase in the duration of sintering was due to the grain growth that occurs in these ceramics. By considering the Schottky type conduction model, characteristic plots of log J against $E^{1/2}$ as shown in *Fig 3.1b* could be built up to determine the values for β and Φ_B using Richardson's formula (discussed in *chapter 2*). Since Richardson's constant depends on the density of the sample and varies from material to material, the values calculated for Sb_2O_3 doped samples was of the order of 1.794 x 10^6. The values for barrier height (Φ_B) are given in *Table I*.

Table I. Characteristic parameters for the samples: SCA-1, SCA-2 SCA-3 and SCA-4.

Sample identification	Sb_2O_3 (at. %)	α	E_B, V cm^{-1}	Density, gm cm^{-3}	Relative density, %	Φ_B, eV	Average grain size, μm
Sintering time 4 hr							
SCA-1	0.01	19	1325	6.50	93.5	0.424	4
SCA-2	0.05	14	725	6.58	94.7	0.377	4
SCA-3	0.1	9	435	6.37	91.7	0.309	5
SCA-4	0.5	3	110	6.35	91.4	0.242	6
Sintering time 24 hr							
SCA-1	0.01	12	375	6.42	92.3	0.339	6
SCA-2	0.05	8	220	6.35	91.4	0.299	5
SCA-3	0.1	9	390	6.40	92.1	0.344	6
SCA-4	0.5	C[a]	--	6.28	94.5	--	8

[a]Conducting

3.3.2 Sintering behavior

Fig 3.2 shows the linear shrinkage ($\Delta L/L_0$) and the rate of linear shrinkage ($d(\Delta L/L_0)/dT$) (inset) as a function of temperature for the samples: SC (0 % Sb_2O_3), SCA-1, SCA-2, SCA-3 and SCA-4. From the linear shrinkage curves it was observed that the shrinkage starts at a temperature around 975 °C and completed at the maximum temperature around 1250 °C for the samples SC, SCA-1, SCA-2 and SCA-3. For the sample SCA-4 it starts at around 1050 °C and ends at around

1300 ºC. The maximum shrinkage rate temperature (T_M) was taken from the linear shrinkage rate against temperature plots. There was slight increase in T_M with the concentration of Sb_2O_3. However, not much difference in T_M values was found at lower concentration of Sb_2O_3. It abruptly increases for the higher concentration of Sb_2O_3 (*Table II*). The sample SC showed a clear densification of SnO_2 at the temperature above 1200 °C.

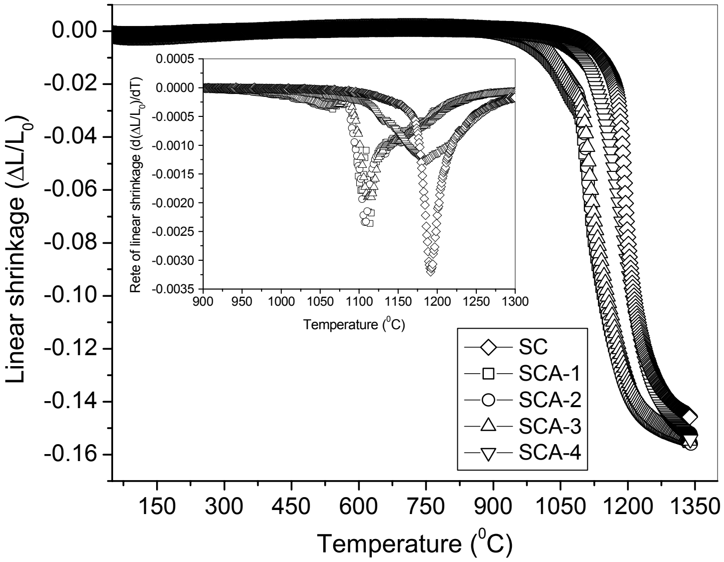

FIG. 3.2 Plots for the linear shrinkage ($\Delta L/L_0$) and rate of linear shrinkage ($d(\Delta L/L_0)/dT$) (inset) as a function of temperature for the samples: SC, SCA-1, SCA-2, SCA-3 and SCA-4.

Table II. Maximum shrinkage rate temperature for Sb_2O_3 doped series.

Sample Identification	T_M (ºC)
SC	1191
SCA-1	1112
SCA-2	1109
SCA-3	1113
SCA-4	1187

3.3.3 X-ray powder diffraction

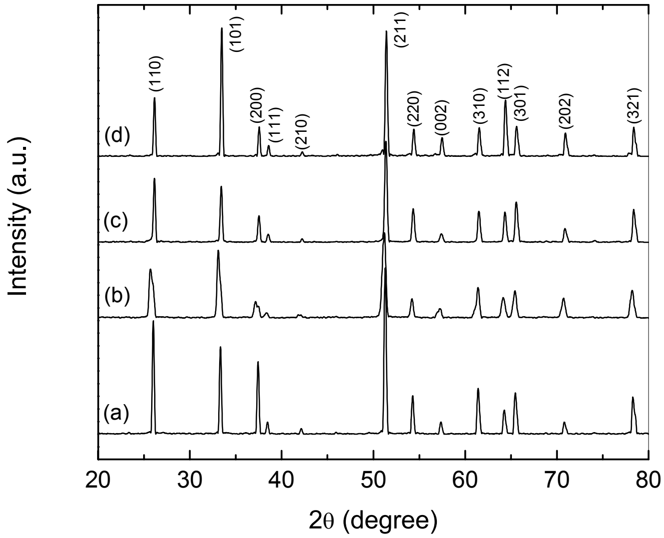

FIG. 3.3 X-ray powder diffraction patterns of sintered samples: (a) SCA-1, (b) SCA-2, (c) SCA-3 and (d) SCA-4.

Fig 3.3 shows the X-ray diffraction patterns (XRD) recorded for the samples: (a) SCA-1, (b) SCA-2, (c) SCA-3, and (d) SCA-4. Apparently, no other phases were found and all the d-lines corresponding to tetragonal rutile SnO_2 phase were observed. It may be due to the smaller concentrations of dopants added, which were undetectable by X-ray diffraction. The lattice parameters calculated by least squares method are given in *Table III*.

Table III. Lattice parameters for Sb_2O_3 doped series.

Lattice parameter (Å)	Sample identification			
	SCA-1	SCA-2	SCA-3	SCA-4
a	4.725	4.721	4.729	4.728
c	3.177	3.179	3.182	3.178

3.3.4 Scanning electron microscopy

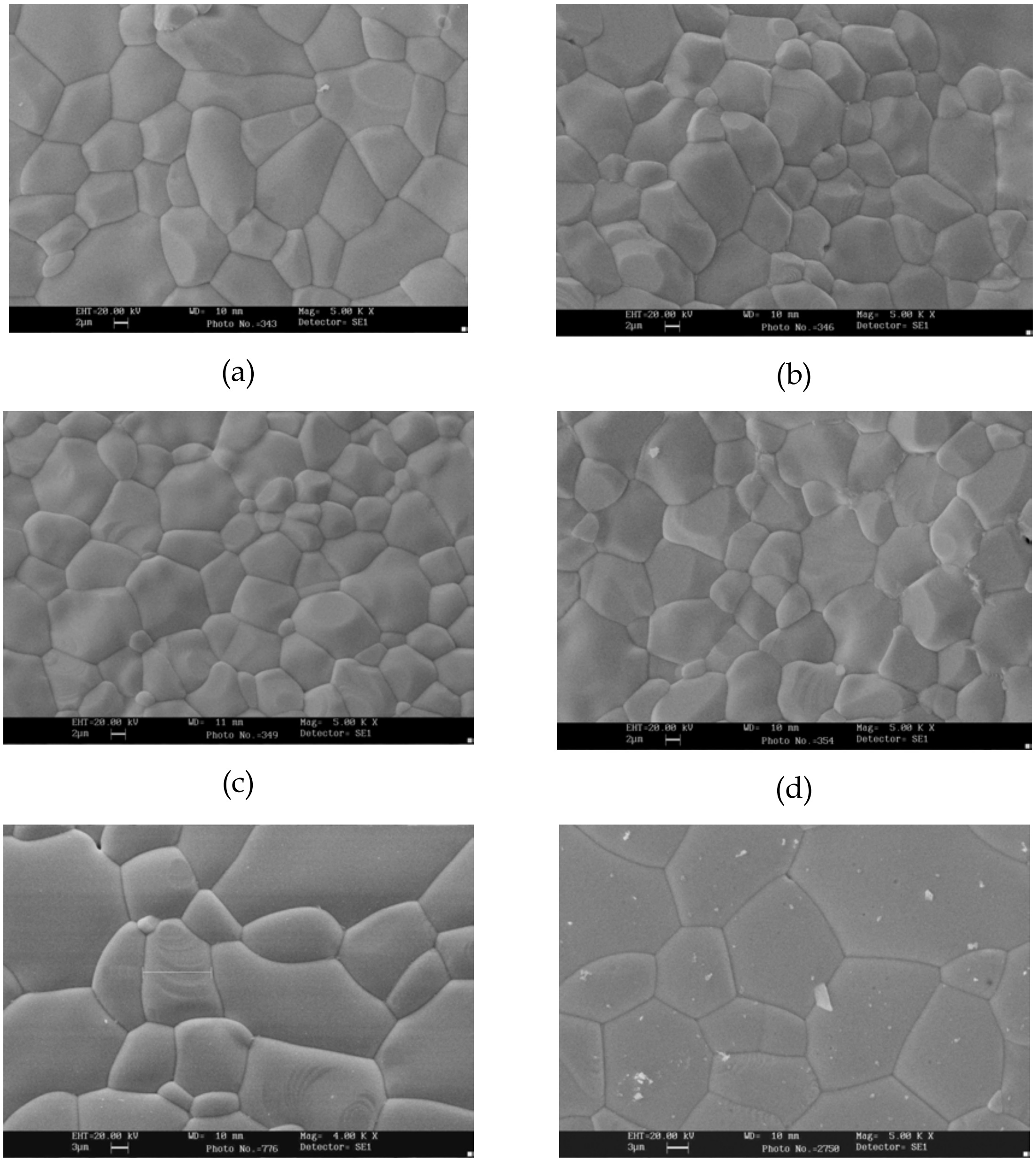

(a) (b)

(c) (d)

(e) (f)

FIG. 3.4 Scanning electron micrographs of the fractured surfaces for the samples: (a) SCA-1, (b) SCA-2, (c) SCA-3 & (d) SCA-4 (all sintered at 1300 °C for 4 hrs) and (e) SCA-1 & (f) SCA-2 (both sintered at 1300 °C for 24 hrs).

To understand the grain-grain boundary microstructure and determine the grain size, the scanning electron micrographs of the fractured surfaces of the pellets were taken after gold coating on the surface. The micrographs for the samples: (a) SCA-1, (b) SCA-2, (c) SCA-3 & (d) SCA-4 (all sintered at 1300 °C /4 hrs) and (e) SCA-1 & (f) SCA-2 (both sintered at 1300°C/24 hrs) are shown in *Fig 3.4*. The values of average grain sizes were found to be 4, 4, 5 and 6 μm for the samples SCA-1, SCA-2, SCA-3 and SCA-4 (all sintered for 4 hrs) respectively (*Table I*). The values of average grain sizes were found to be 6, 5, 6 and 8 μm for the samples: SCA-1 SCA-2 SCA-3 and SCA-4 (all sintered for 4 hrs) respectively (*Table I*). The Grain coarsening was observed for longer sintering duration. The grain size has a clear effect on the current-voltage characteristics of the varistor. The breakdown field decreases with increase in grain size. Even though no grain boundary phase was found in the micrograph, the contribution from the grain boundary to the conduction phenomena was confirmed by impedance analysis as discussed in *section 3.7*.

3.4 Ta_2O_5 doped series

3.4.1 I-V characteristics

Fig 3.5a shows the current density (J) versus applied field (E) (I-V characteristic) plots on log scale for the samples: SCTa-1, SCTa-2, SCTa-3 & SCTa-4 sintered at 1300 °C for the 4 and 24 hrs. The values of non-linear coefficient (α) were observed to be 21, 18, 18 and 36 for the samples: SCTa-1, SCTa-2, SCTa-3 and SCTa-4 (all sintered for 4 hrs) respectively. The values of non-linear coefficient (α) were observed to be 12, 13, 13 and 16 for SCTa-1, SCTa-2, SCTa-3 & SCTa-4 (all sintered for 24 hrs) respectively. The other parameters: breakdown field (E_B), density (ρ) and barrier height (Φ_B) are given in *Table IV*. The large value of non-linear coefficient (almost doubled) was obtained for the higher concentration of Ta_2O_5. Breakdown field increases with the concentration of Ta_2O_5. Decrease in both non-linear coefficient as well as breakdown field were observed for the increase in sintering duration from 4 to 24 hr for the respective samples.

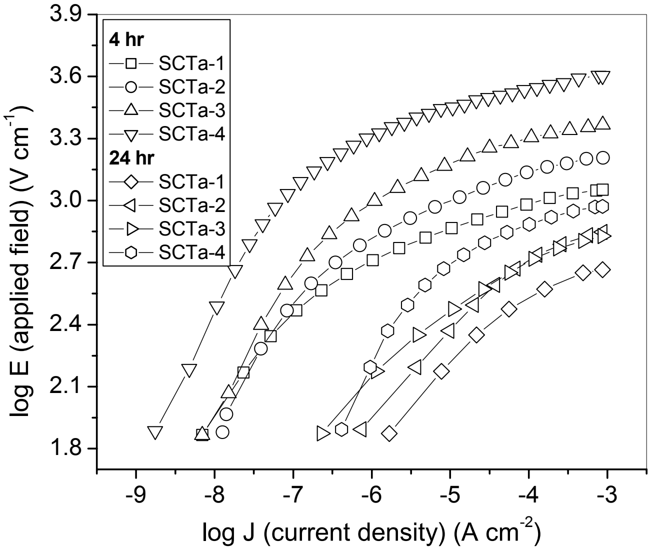

FIG. 3.5a I-V characteristic plots for the samples: SCTa-1, SCTa-2, SCTa-3 & SCTa-4 sintered at 1300°C for 4 and 24 hrs.

In contrast to Sb doped samples, the conductivity did not increase with the increase in Ta concentration. The incorporation of Ta probably might have charge compensated by electrons at lower concentrations. The decrease in breakdown field with increase in sintering duration was due to the grain growth that occurred in these ceramics. Considering the Schottky type conduction model, plots of log J against $E^{1/2}$ (*Fig 3.5b*) could be built up to determine value for β and Φ_B from the Richardson's formula. The Richardson's constant values calculated for Ta_2O_5 doped samples was of the order of 1.839 x 10^6. The values for barrier height (Φ_B) are given in *Table IV*.

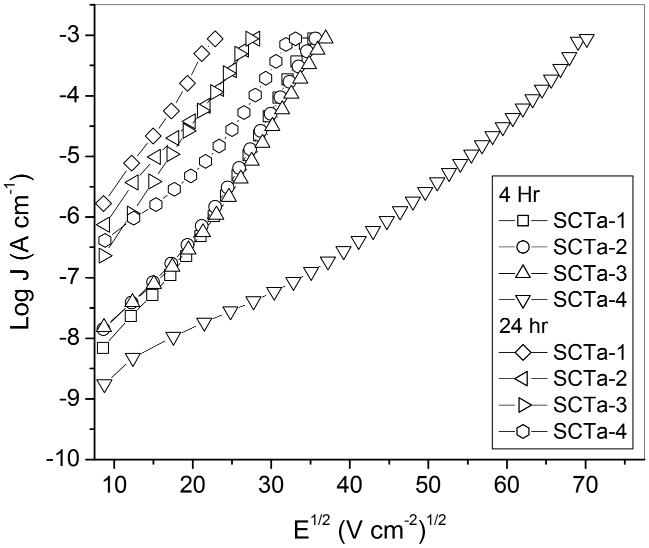

FIG. 3.5b Characteristic plots of log J against $E^{1/2}$ for the samples: SCTa-1, SCTa-2 SCTa-3 & SCTa-4 sintered at 1300 °C for 4 and 24 hr.

Table IV. Characteristic parameters of the samples: SCTa-1, SCTa-2 SCTa-3 and SCTa-4

Sample identification	Ta_2O_5 (at. %)	α	E_B, V cm^{-1}	Density, gm cm^{-3}	Relative density, %	Φ_B, eV	Average grain size, μm
Sintering time 4 hr							
SCTa-1	0.01	21	1250	6.68	96.1	0.448	2
SCTa-2	0.05	18	1270	6.60	94.9	0.414	2
SCTa-3	0.1	18	1365	6.65	95.7	0.413	2
SCTa-4	0.5	36	4925	6.73	96.8	0.627	2
Sintering time 24 hr							
SCTa-1	0.01	12	520	6.64	95.5	0.356	4
SCTa-2	0.05	13	780	6.71	96.5	0.362	3
SCTa-3	0.1	13	745	6.71	96.5	0.358	3
SCTa-4	0.5	16	1095	6.68	91.1	0.389	4

3.4.2 Sintering behavior

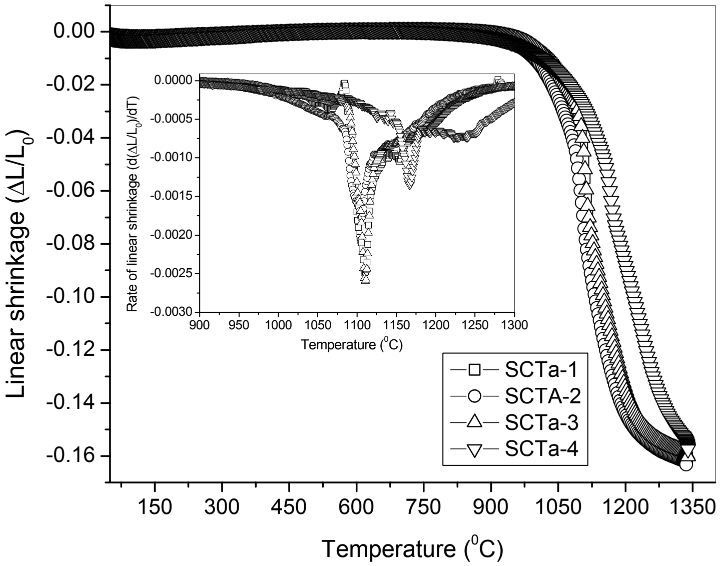

FIG. 3.6 Plots for the linear shrinkage ($\Delta L/L_0$) and rate of linear shrinkage ($d(\Delta L/L_0)/dT$) (inset) as a function of temperature for the samples: SCTa-1, SCTa-2, SCTa-3 and SCTa-4

Fig 3.6 shows the linear shrinkage ($\Delta L/L_0$) and the rate of linear shrinkage ($d(\Delta L/L_0)/dT$) (inset) as a function of temperature for the samples: SCTa-1, SCTa-2, SCTa-3 and SCTa-4. From the linear shrinkage curves it was observed that the shrinkage starts at the temperature around 950 °C and completed at the maximum temperature of 1250 °C for all the samples except for the SCTa-4 it starts at 1000 °C and ends at around 1300 °C. The maximum shrinkage rate temperature (T_M) was taken from the linear shrinkage rate against temperature plots. However, not much difference was found in T_M values at the lower concentration of Ta_2O_5. It abruptly increased for the higher concentration of Ta_2O_5 (*Table V*).

Table V. Maximum shrinkage rate temperature for Ta_2O_5 doped series.

Sample identification	T_M (ºC)
SCTa-1	1108
SCTa-2	1106
SCTa-3	1110
SCTa-4	1166

3.4.3 X-ray powder diffraction

Fig 3.7 shows the X-ray diffraction patterns (XRD) recorded for the samples: (a) SCTa-1, (b) SCTa-2, (c) SCTa-3 and (d) SCTa-4. Apparently, no other phases were found and all the peaks corresponding to only tetragonal rutile SnO_2 phase were observed. The absence of other phases may be due to the lower concentration of additives. The lattice parameters calculated by least squares method are given in *Table VI*.

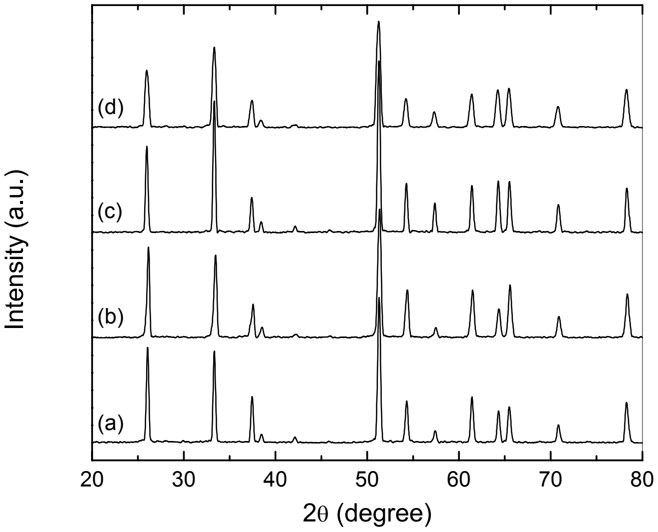

FIG. 3.7 X-ray powder diffraction patterns for sintered samples: (a) SCTa-1, (b) SCTa-2, (c) SCTa-3 and (d) SCTa-4.

Table VI. Lattice parameters for Ta_2O_5 doped series.

Lattice parameter (Å)	Sample identification			
	SCTa-1	SCTa-2	SCTa-3	SCTa-4
a	4.726	4.732	4.724	4.725
c	3.180	3.181	3.175	3.178

3.4.4 Scanning electron microscopy

To understand the grain-grain boundary microstructure and determine the grain size, the scanning electron micrographs of the fractured surfaces of the pellets were taken. The micrographs for the samples: (a) SCTa-1, (b) SCTa-2, (c) SCTa-3 & (d) SCTa-4 (all sintered at 1300 °C for 4 hrs) and (e) SCTa-1 & (f) SCTa-4 (both sintered at 1300 °C for 24 hrs) are shown in *Fig 3.8*. The average grain size for the samples sintered for 4 hrs was found to be 2 µm for SCTa-1, SCTa-2, SCTa-3 and SCTa-4 (*Table IV*). The average grain sizes for the samples sintered for 24 hrs were found to be 4, 3, 3 and 4 µm for SCTa-1, SCTa-2, SCTa-3 and SCTa-4 respectively (*Table IV*). The grain growth was observed for longer sintering duration (e.g. SCTa-1 / SCTa-4 sintered for 4 and 24 hrs). The grain size has a clear effect on the current-voltage characteristics of the varistor. The breakdown field decreases with increase in grain size. No grain boundary phase was found in the micrograph.

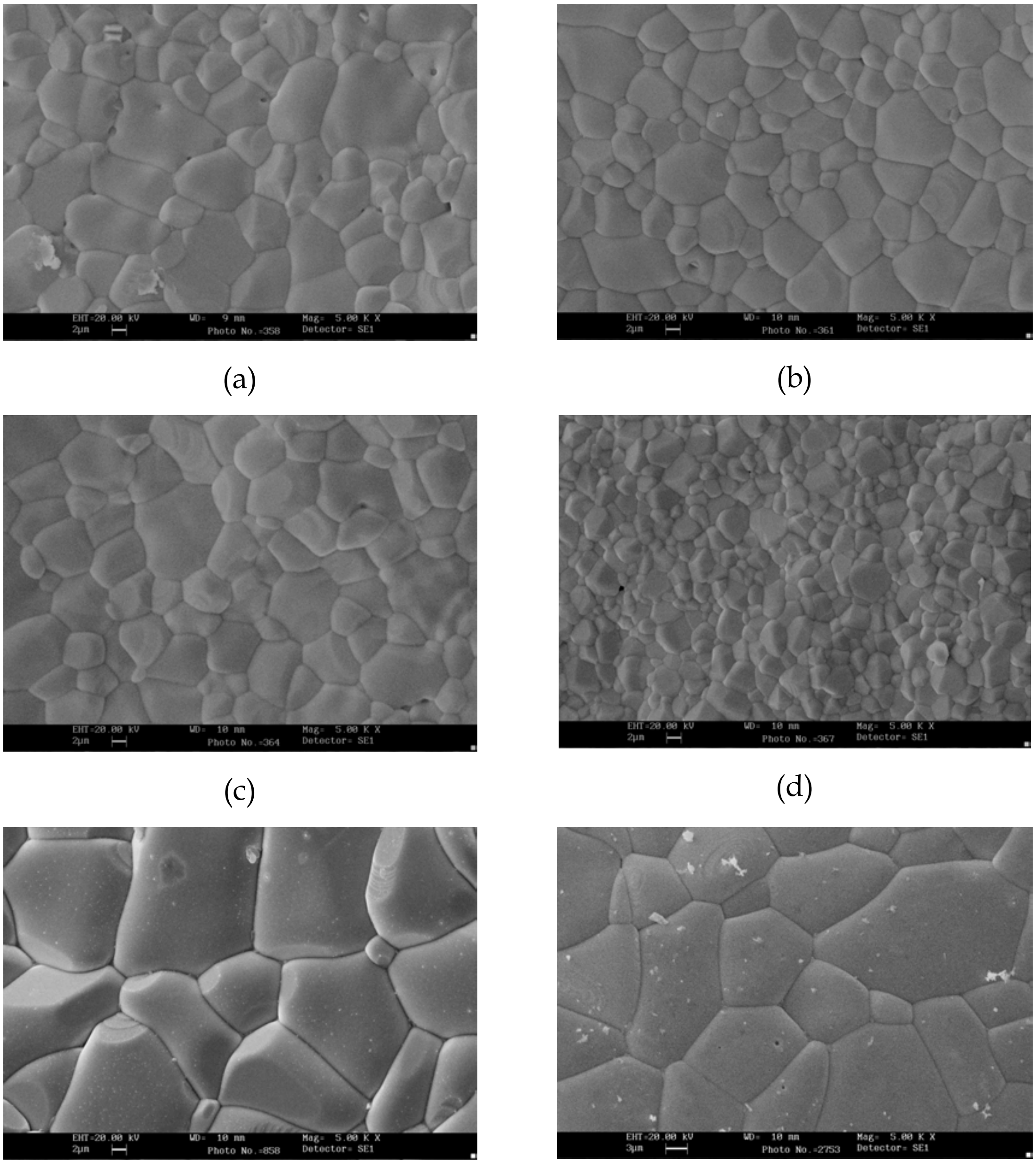

(a) (b)

(c) (d)

(e) (f)

FIG. 3.8 Scanning electron micrographs of the fractured surfaces for the samples: (a) SCTa-1, (b) SCTa-2, (c) SCTa-3 & (d) SCTa-4 (all sintered at 1300 ºC for 4 hrs) and (e) SCTa-1 & (f) SCTa-4 (Both sintered at 1300 ºC for 24 hrs).

3.5 Nb_2O_5 Series

3.5.1 I-V Characteristic

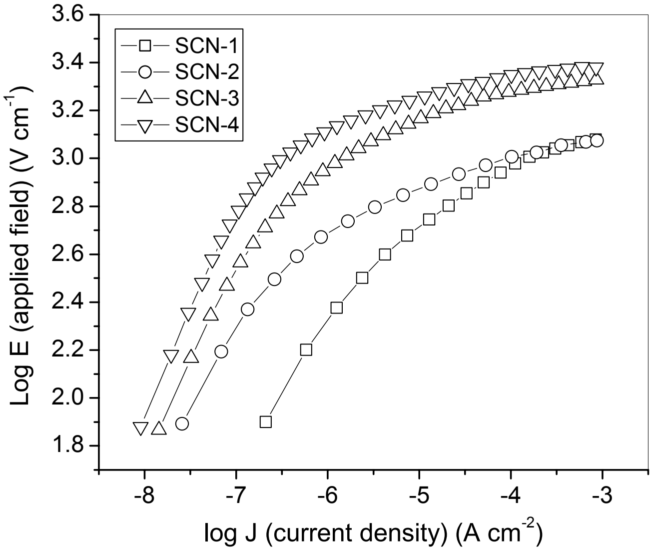

FIG. 3.9a I-V characteristic plots for the samples: SCN-1, SCN-2, SCN-3 and SCN-4 sintered at 1300 °C for 4 hrs.

Fig 3.9a shows the current density (J) versus applied field (E) (I-V characteristic) plots on log scale for the samples: SCN-1, SCN-2, SCN-3 and SCN-4 sintered at 1300 °C for 4 hrs. The values of non-linear coefficient (α) calculated from the slopes of the curves in the non-linear region for the samples sintered for 4 hrs were observed as 22, 23, 24 and 28 for SCN-1, SCN-2 SCN-3 and SCN-4 respectively. The other performance parameters: breakdown field (E_B), density (ρ) and barrier height (Φ_B) are given in *Table VII*. The non-linear coefficient increases slightly for the lower concentration of Nb (up to 0.1 at. %). At higher concentration (0.5 at. %) it showed remarkable increase in non-linear coefficient. Breakdown field increases with the concentration of Nb_2O_5. The conductivity did not increase with Nb concentration. At lower concentration, the incorporation of Nb was probably charge compensated by electrons. Considering the Schottky type conduction model, plots of log J against $E^{1/2}$ (*Fig 3.9b*) were built up to determine the values for β and Φ_B using Richardson's formula. The values calculated for Richardson's constant for Nb_2O_5 doped samples was of the order of 1.839 x 10^6. The values for barrier height (Φ_B) are given in *Table VII*.

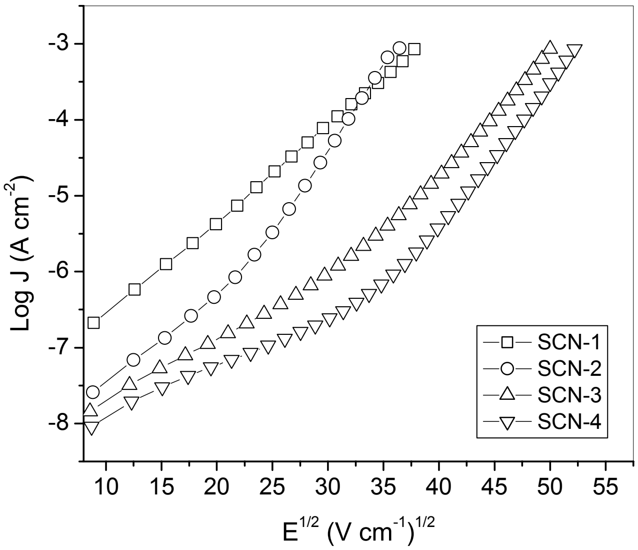

FIG. 3.9b Characteristics plots of log J against $E^{1/2}$ for the samples: SCN-1, SCN-2, SCN-3 and SCN-4.

Table VII. Characteristic parameters for the samples: SCN-1, SCN-2, SCN-3 and SCN-4.

Sample identification	Nb_2O_5 (at. %)	α	E_B, V cm^{-1}	Density, gm cm^{-3}	Relative density, %	Φ_B, eV	Average grain size, μm
SCN-1	0.01	22	1425	6.49	93.4	0.448	5
SCN-2	0.05	24	1330	6.51	93.7	0.449	4
SCN-3	0.1	23	2500	6.63	95.4	0.427	4
SCN-4	0.5	28	2725	6.55	94.2	0.492	3

3.5.2 Sintering behavior

Fig 3.10 shows the linear shrinkage ($\Delta L/L_0$) and the rate of linear shrinkage ($d(\Delta L/L_0)/dT$) (inset) as a function of temperature for the samples:

SCN-1, SCN-2, SCN-3 and SCN-4. From the linear shrinkage curves it was observed that the shrinkage starts at the temperature around 950 ºC and completes at the maximum temperature of around 1250 ºC for all the samples. The maximum shrinkage rate temperature (T_M) was taken from the linear shrinkage rate against temperature plot and not much difference in the variation of T_M with lower concentration of Nb was observed. However, it abruptly increased for the higher concentration (0.5 at %) of Nb (*Table VIII*).

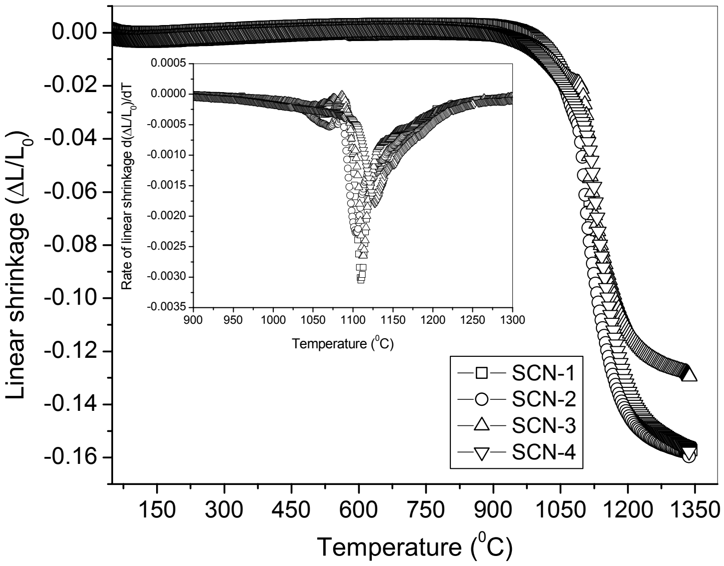

FIG. 3.10 Plots for linear shrinkage ($\Delta L/L_0$) and rate of linear shrinkage ($d(\Delta L/L_0)/dT$) (inset) as a function of temperature for the samples: SCN-1, SCN-2, SCN-3 and SCN-4.

Table VIII. Maximum shrinkage rate temperature for Nb_2O_5 doped series.

Sample identification	T_M (ºC)
SCN-1	1109
SCN-2	1105
SCN-3	1112
SCN-4	1128

3.5.3 X-ray powder diffraction

Fig 3.11 shows the X-ray diffraction patterns (XRD) recorded for the samples: (a) SCN-1, (b) SCN-2, (c) SCN-3 and (d) SCN-4. All the reflections corresponding to only tetragonal rutile SnO_2 phase were observed. The lattice parameters calculated by least squares method are given in *Table IX*.

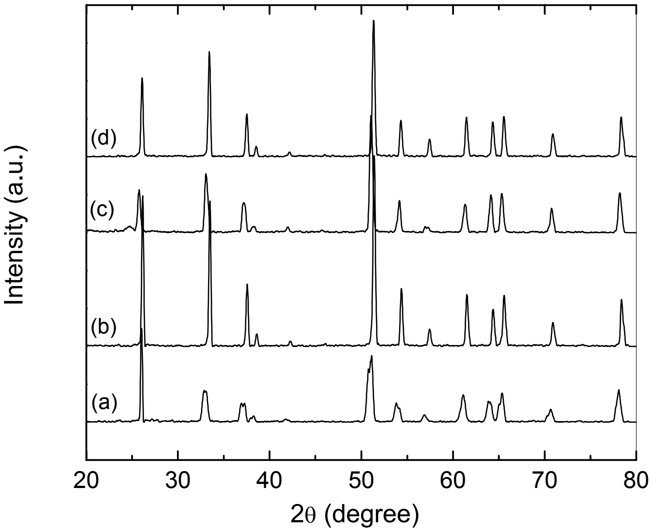

FIG. 3.11 X-ray powder diffraction patterns of sintered samples: (a) SCN-1, (b) SCN-2, (c) SCN-3 and (d) SCN-4.

Table IX. Lattice parameters for Nb_2O_5 doped series.

Lattice parameter (Å)	Sample identification			
	SCN-1	SCN-2	SCN-3	SCN-4
a	4.737	4.734	4.725	4.729
c	3.182	3.180	3.170	3.179

3.5.4 Scanning electron microscopy

To study the grain-grain boundary microstructure and calculate the grain size, the scanning electron micrographs of the fractured surfaces were taken. The micrographs for the samples: (a) SCN-1, (b) SCN-2, (c) SCN-3 and (d) SCN-4 sintered at 1300 ºC for 4 hrs are shown in *Fig 3.12*. The average grain size obtained from the micrographs for the samples SCN-1, SCN-2, SCN-3 and SCN-4 are 5, 4, 4 and 3 µm respectively (*Table VII*). The grain size has a clear effect on the current-voltage characteristics of the varistor. The breakdown field decreases with increase in grain size. In this case, the grain size decreases with increase in concentration of Nb_2O_5, which confirms the increase in breakdown field. No grain boundary phase seen in the micrograph.

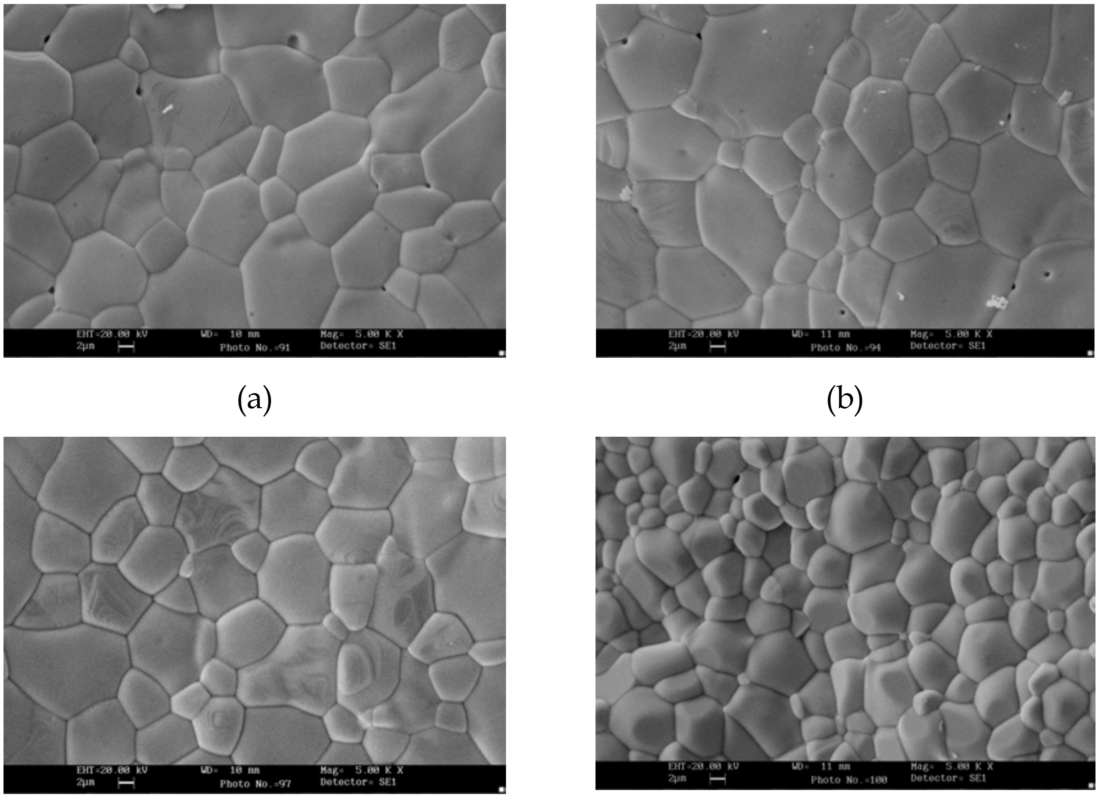

(a) (b)

(c) (d)

FIG. 3.12 Scanning electron micrographs of the fractured surfaces for the samples: (a) SCN-1, (b) SCN-2, (c) SCN-3 and (d) SCN-4 sintered at 1300 ºC for 4 hrs.

3.6 V_2O_5 Series

3.6.1 I-V characteristics

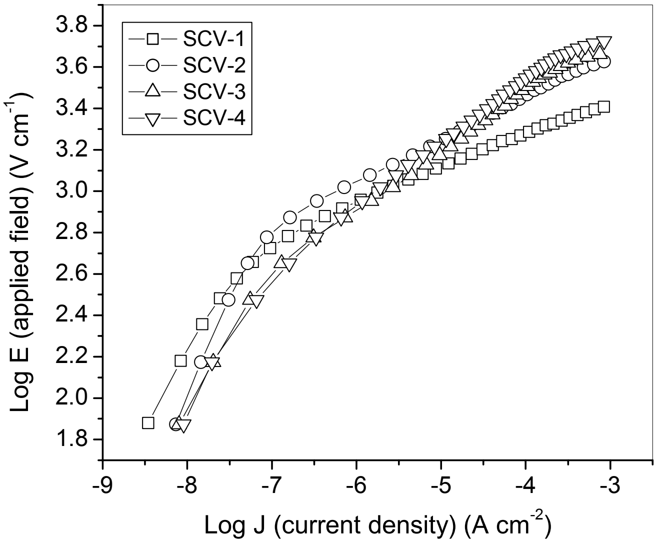

FIG. 3.13a I-V characteristic plots for the samples: SCV-1, SCV-2, SCV-3 and SCV-4 sintered at 1300 °C for 4 hr.

Fig 3.13a shows the current density (J) versus applied field (E) (I-V characteristic) plots on log scale for the samples: SCV-1, SCV-2, SCV-3 and SCV-4 sintered at 1300 °C for 4 hr. The non-linear coefficient (α) calculated from the slopes of the curves in the non-linear regions for the samples: SCV-1, SCV-2, SCV-3 and SCV-4 were found as 15, 16, 19 and 10 respectively. The other parameters: breakdown field (E_B), density (ρ) and barrier height (Φ_B) are given in *Table X*. The non-linear coefficient increased slightly for the lower concentration of V_2O_5 (up to 0.1 at. %), whereas it showed the lower value at higher concentration of V_2O_5 (0.5 at. %). However, the breakdown field increased with the concentration of V_2O_5. The conductivity did not increase with the increase in V concentration. The incorporation of V in SnO_2 lattice was probably charge compensated by electrons at its lower concentrations. Considering the Schottky type conduction model, plots of log J against $E^{1/2}$ (*Fig 3.13b*) could be built up to determine value for β and Φ_B from the Richardson's formula. The values calculated for Richardson's constant for V_2O_5 doped samples was of the order of 1.839 x 10^6. The values for barrier height (Φ_B) are given in *Table X*.

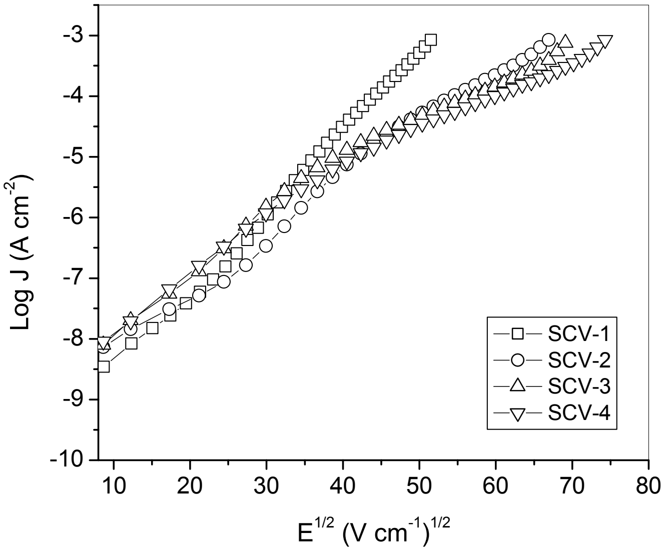

FIG. 3.13b Characteristic plots of log J against $E^{1/2}$ for the samples: SCV-1, SCV-2, SCV-3 and SCV-4.

Table X. Characteristic parameters for SCV-1, SCV-2, SCV-3 and SCV-4.

Sample identification	V_2O_5 (at. %)	α	E_B, V cm^{-1}	Density, gm cm^{-3}	Relative density, %	Φ_B, eV	Average grain size, μm
SCV-1	0.01	15	2510	6.37	91.6	0.385	6
SCV-2	0.05	16	4262	6.39	91.9	0.387	5
SCV-3	0.1	19	4535	6.33	91.2	0.437	5
SCV-4	0.5	10	4859	6.28	90.3	0.492	4

3.6.2 Sintering behavior

Fig. 3.14 shows the linear shrinkage ($\Delta L/L_0$) and the rate of linear shrinkage ($d(\Delta L/L_0)/dT$) (inset) as a function of temperature for the samples:

SCV-1, SCV-2, SCV-3 and SCV-4. From the linear shrinkage curves it was observed that the shrinkage starts at the temperature around 1000 °C and completes at the maximum temperature of 1250 °C for all the samples, except for the samples SCV-4. The maximum shrinkage rate temperature (T_M) was taken from the linear shrinkage rate against temperature plot and not much difference in T_M variation with lower concentration of V was observed. However it decreased abruptly for higher concentration of V_2O_5 (0.5 at %) as given in *Table XI*. The density of SCV-4 sample was comparably low; hence the higher concentration of V inhibits the shrinkage.

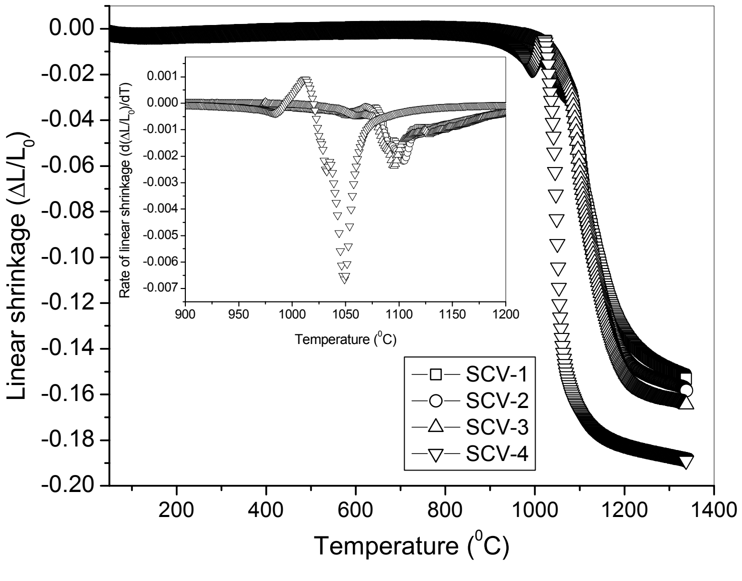

FIG. 3.14 Plots for linear shrinkage ($\Delta L/L_0$) and rate of linear shrinkage ($d(\Delta L/L_0)/dT$) as a function of temperature (inset) for the samples: SCV-1, SCV-2, SCV-3 and SCV-4.

Table XI. Maximum shrinkage rate temperature for V_2O_5 doped series.

Sample Identification	T_M (ºC)
SCV-1	1109
SCV-2	1105
SCV-3	1096
SCV-4	1051

3.6.3 X-ray powder diffraction

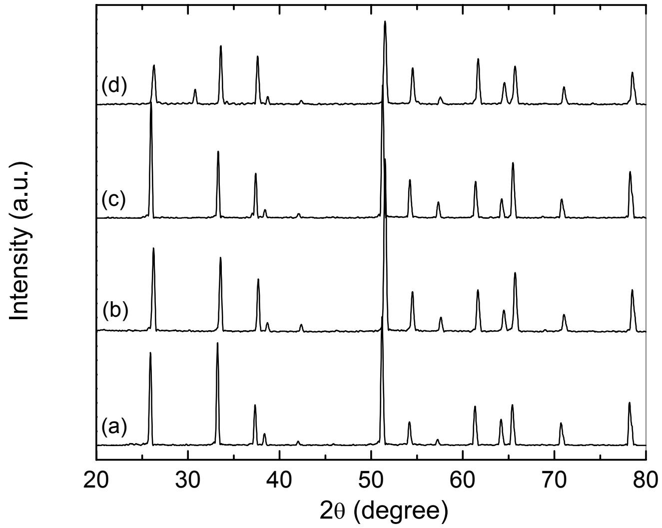

FIG. 3.15 X-ray powder diffraction patterns of sintered samples: (a) SCV-1, (b) SCV-2, (c) SCV-3 and (d) SCV-4.

Fig 3.15 shows the X-ray diffraction patterns (XRD) recorded for the samples: (a) SCV-1, (b) SCV-2, (c) SCV-3 and (d) SCV-4. Only lines corresponding to SnO_2 tetragonal rutile phase were observed. The other phases due to the additives were not observed because of their lower concentrations. The lattice parameters calculated least squares method are given in *Table XII*.

Table XII. Lattice parameters for V_2O_5 doped series

Lattice parameter (Å)	Sample Identification			
	SCV-1	SCV-2	SCV-3	SCV-4
a	4.723	4.721	4.725	4.728
c	3.177	3.176	3.177	3.179

3.6.4 Scanning electron microscopy

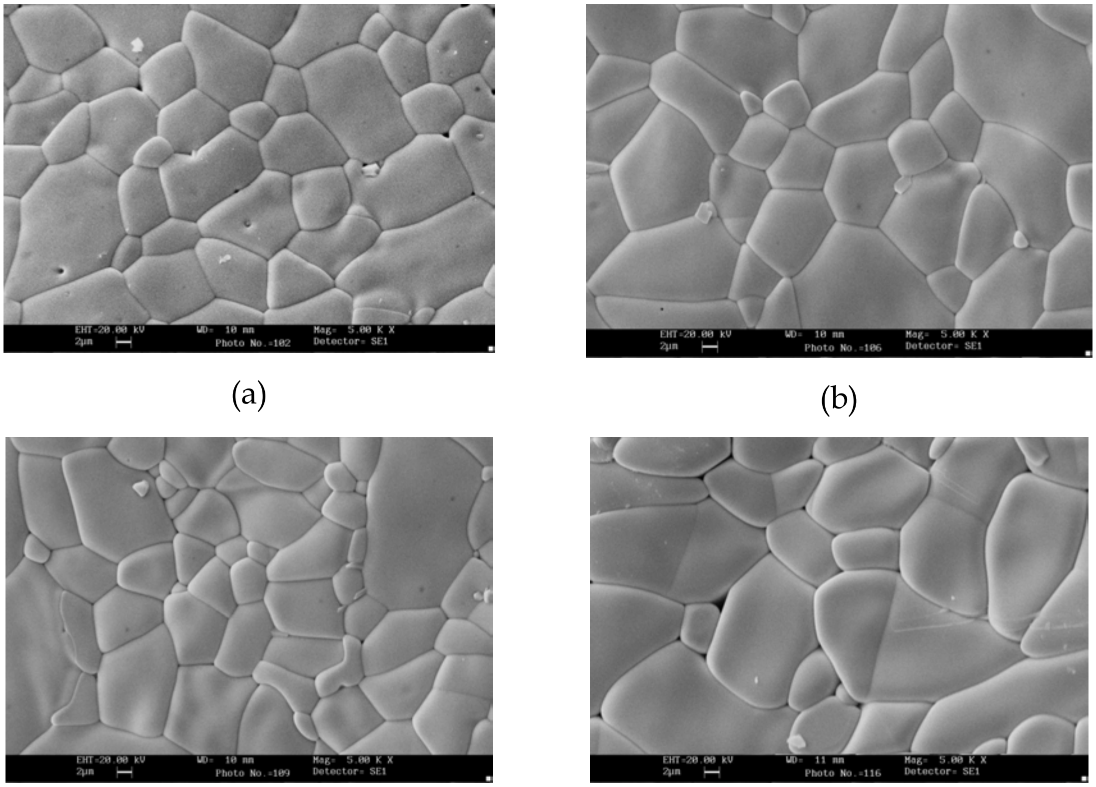

(a) (b)

(c) (d)

FIG. 3.16 Scanning electron micrographs of the fractured surfaces of the samples: (a) SCV-1, (b) SCV-2, (c) SCV-3 and (d) SCV-4 sintered at 1300 °C / 4 hrs

The scanning electron micrographs for the samples (a) SCV-1, (b) SCV-2, (c) SCV-3 and (d) SCV-4 are shown in *Fig 3.16*. The average grain size obtained from the micrographs for SCV-1, SCV-2, SCV-3 and SCV-4 were 6, 5, 5 and 4 μm respectively (*Table X*). The grain size has a clear effect on the current-voltage characteristics of the varistor. The breakdown field decreases with increase in grain size. In this case the grain size decreases with increase in V_2O_5 concentration, which conforms the increase in breakdown field. Even though no grain boundary phase found in the micrograph, the contribution from grain boundary phase to the non-linear electrical characteristic was confirmed by impedance analysis, as discussed in *section 3.7*

3.7 Impedance analysis

3.7.1 Nyquist plot

The ac impedance analysis of the samples: SCA-2, SCTa-3, SCN-3 and SCV-2 was done in the frequency range of 0.1 Hz to 1 MHz with an ac amplitude voltage of 100 mV. *Fig 3.17 (a), (b), (c)* and *(d)* represent the impedance plots of real (Z') versus imaginary (Z") resistance (Nyquist plot) measured at different temperatures for the samples: SCA-2, SCTa-3, SCN-3 and SCV-2 respectively.

The room temperature measurement lacks a proper semicircular nature and thereby making it difficult to distinguish between the grain and grain boundary contributions. Hence, the impedance spectra were recorded at higher temperatures up to 300 °C. As the measurement temperature was increased, clear semicircles were emerged due to decrease in total resistance. The decrease in resistance was due to the fact that the material was highly semiconducting. A full semicircle was seen at temperatures greater than 135, 200, 140 and 130 °C for the samples SCA-2, SCTa-3, SCN-3 and SCV-2 respectively (*Fig 3.17*). But these curves failed to give an expected semicircular nature corresponding to the grains at higher frequency side. It was due to the fact that the grain boundary contribution to the total resistance was very large compared to that of grain. Hence, the semicircle corresponding to grain was submerged in the circle representing the grain boundaries. Therefore, separating out the individual component by fitting the semicircle was not possible. However, the semicircular fit of this curve can give the contribution from each part approximately. Further, the low and high frequency intercepts of the real part represent the grain boundary and grain contribution at the measurement temperature.

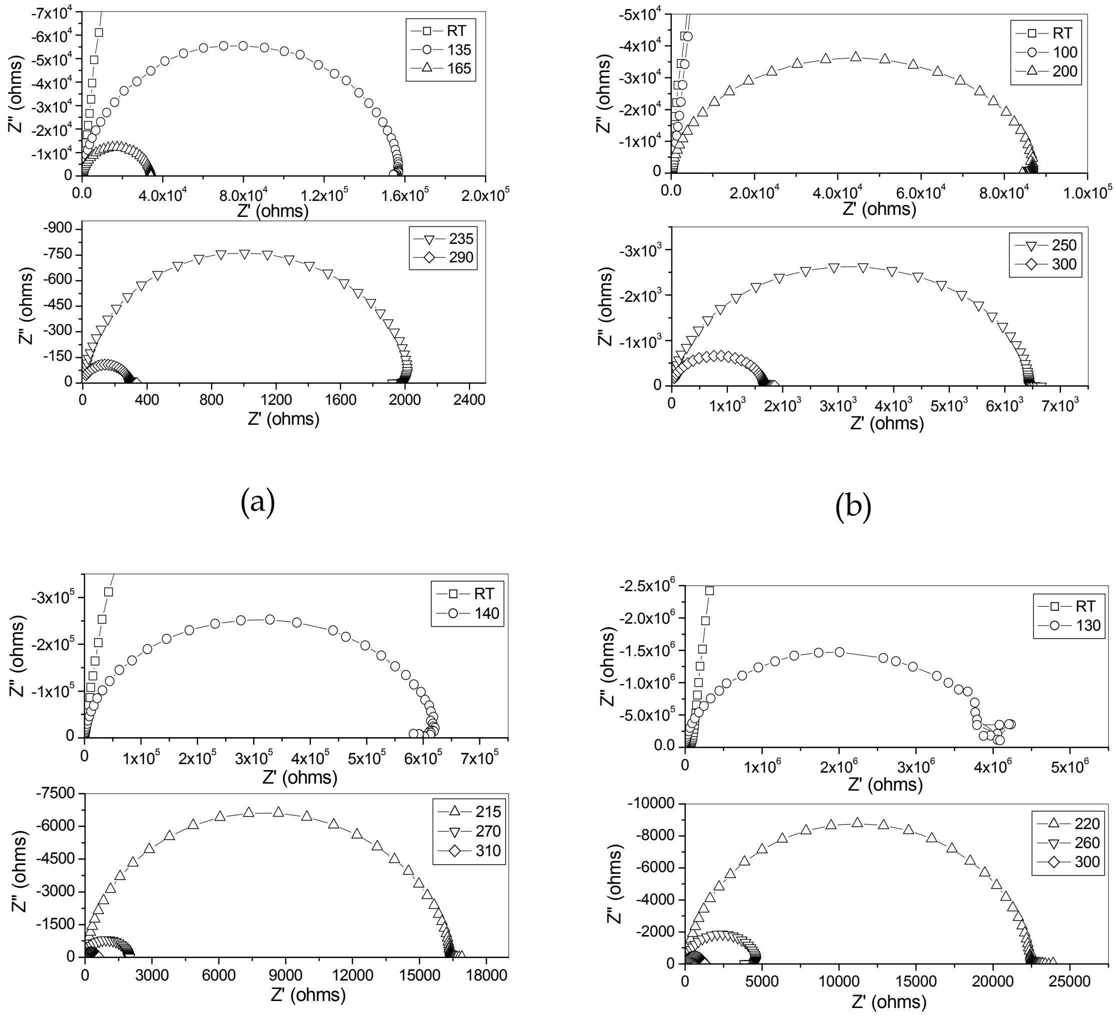

(a) (b)

(c) (d)

FIG. 3.17 Impedance plots (Z' versus Z'') for the samples: (a) SCA-2, (b) SCTa-3, (c) SCN-3 and (d) SCV-2 at different temperatures.

Since the semicircle were not well defined at room temperature and in some cases up to 200 ºC, the estimation of different contribution to the total resistance of the samples was not possible (e.g. above impedance plots). The semicircles correspond to the contribution from the grains were not seen even at higher measuring temperatures of 300 ºC. Hence, the analysis of the different contributions could be done using Bode plots.

3.7.2 Bode plot

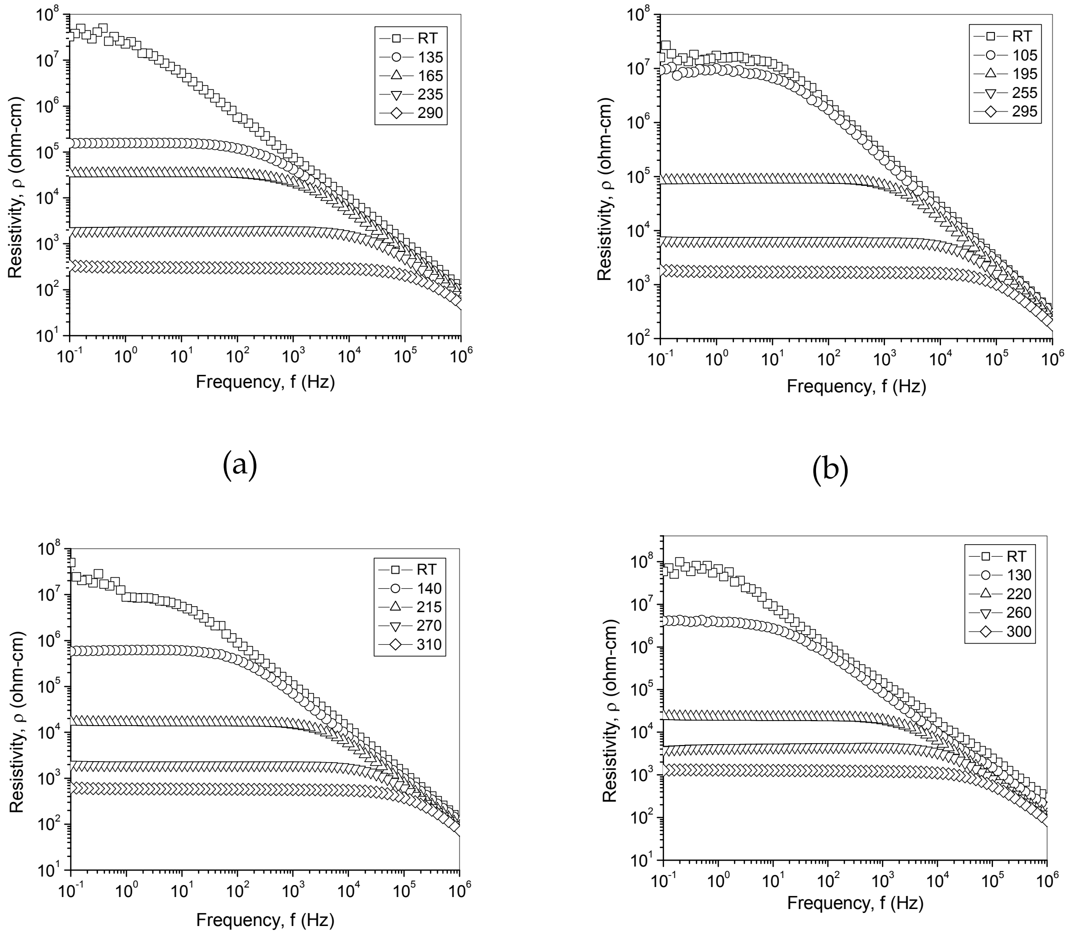

(a) (b)

(c) (d)

FIG. 3.18 Bode plots of log resistivity (ρ) against log frequency for the samples: (a) SCA-2, (b) SCTa-3, (c) SCN-3 and (d) SCV-2 at different temperatures.

Bode plot is the curve for log of resistivity against the log frequency. Since the measurement frequency range was large (0.1 Hz to 1 MHz) & the impedance also changes over 10^8 to 100 ohm-cm, the plots made on log scale for the samples SCA-2, SCTa-3, SCN-3 and SCV-2 at different temperature are shown in *Fig 3.18 (a), (b), (c)* and *(d)* respectively. To find the grain and grain boundary contributions from the Bode plots the approximation given in *equation 3.1* and *3.2* were employed.

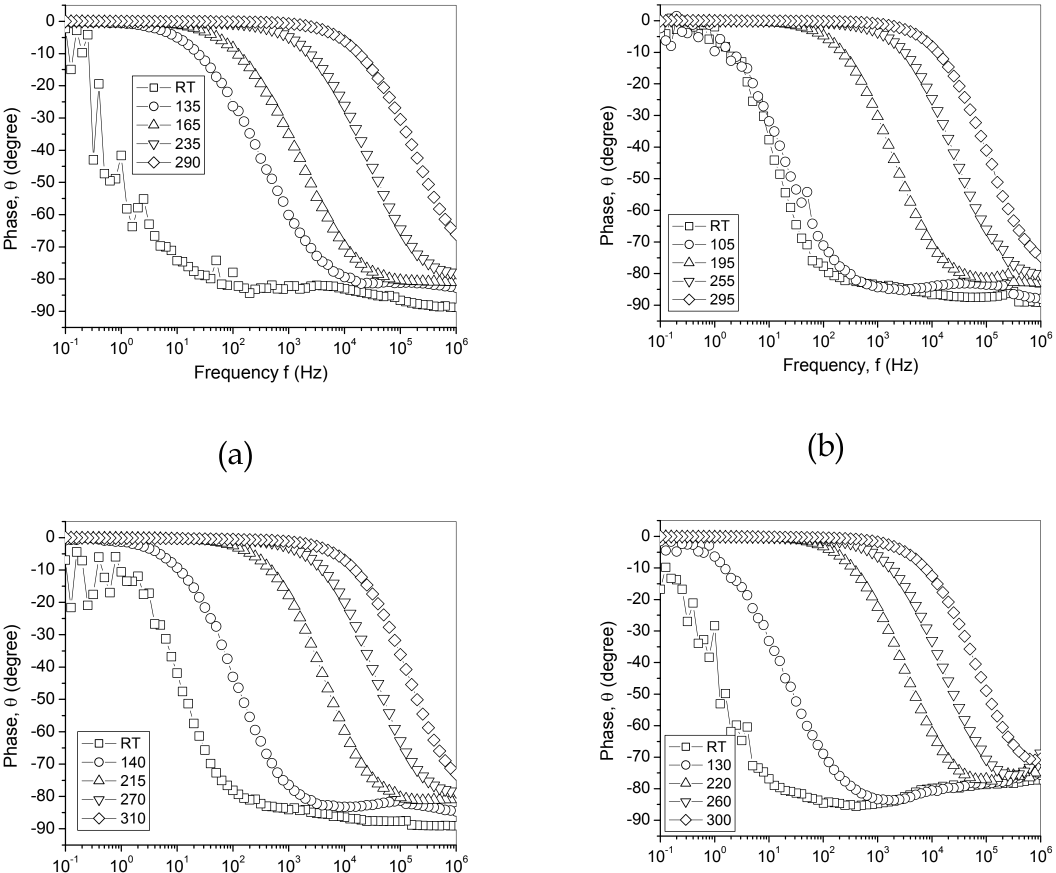

(a) (b)

(c) (d)

FIG. 3.19 Bode plots of phase (θ) against log frequency for the samples: (a) SCA-2, (b) SCTa-3, (c) SCN-3 and (d) SCV-2 at different temperatures.

$$\log_{f\to 0}(|\rho|) = \log_{f\to 0}(|\rho_{gb}|+|\rho_g|) = \log_{f\to 0}(\rho_{gb}), \quad \rho_{gb} >> \rho_g \qquad 3.1$$

$$\log_{f\to\infty}(|\rho|) = \log(\rho_g) \qquad 3.2$$

Fig 3.18 showed the drastic drop in resistivity values with increase in frequency. This itself was the evidence for the presence of grain boundary phase between the grains. At low frequency the sample exhibited capacitor like behavior due to grain-grain boundary-grain structure giving high resistance to current flow. As the frequency increases, the resistance drastically decreases (i.e. the capacitive impedance; $X_c = 1/\omega c$). At the highest frequency the impedance corresponding to grain boundary was negligible (i.e. X_c decreases) and the total resistivity was controlled by the change in phase with frequency as shown in *Fig 3.19 (a), (b), (c)* and *(d)* for the samples SCA-2, SCTa-3, SCN-3 and SCV-2 respectively. The phase angle was 0° at low frequency but at the highest frequency point it has changed to 90°. The phase angle dependence of frequency for different temperature indicated the presence of capacitive like behavior.

All the samples have nearly similar values for initial resistivity at lower frequency. This can be seen from *Table XIII*, which gives the grain and grain boundary resistivity values at different temperatures for the samples: SCA-2, SCTa-3, SCN-3 and SCV-2. The corresponding grain boundary capacitance was found from the relation given in *equation 3.3.*

$$C_{gb} = 1/(\rho_{gb} \cdot \omega) \text{ for } \tan(\theta) = 1 \qquad 3.3$$

where, $\omega = 2\pi f$, f is frequency at which θ becomes 45°

From this analysis, we can build at an equivalent circuit having R_g in series with the parallel connection of R_{gb} and C_{gb}.

3.7.3 Relaxation time

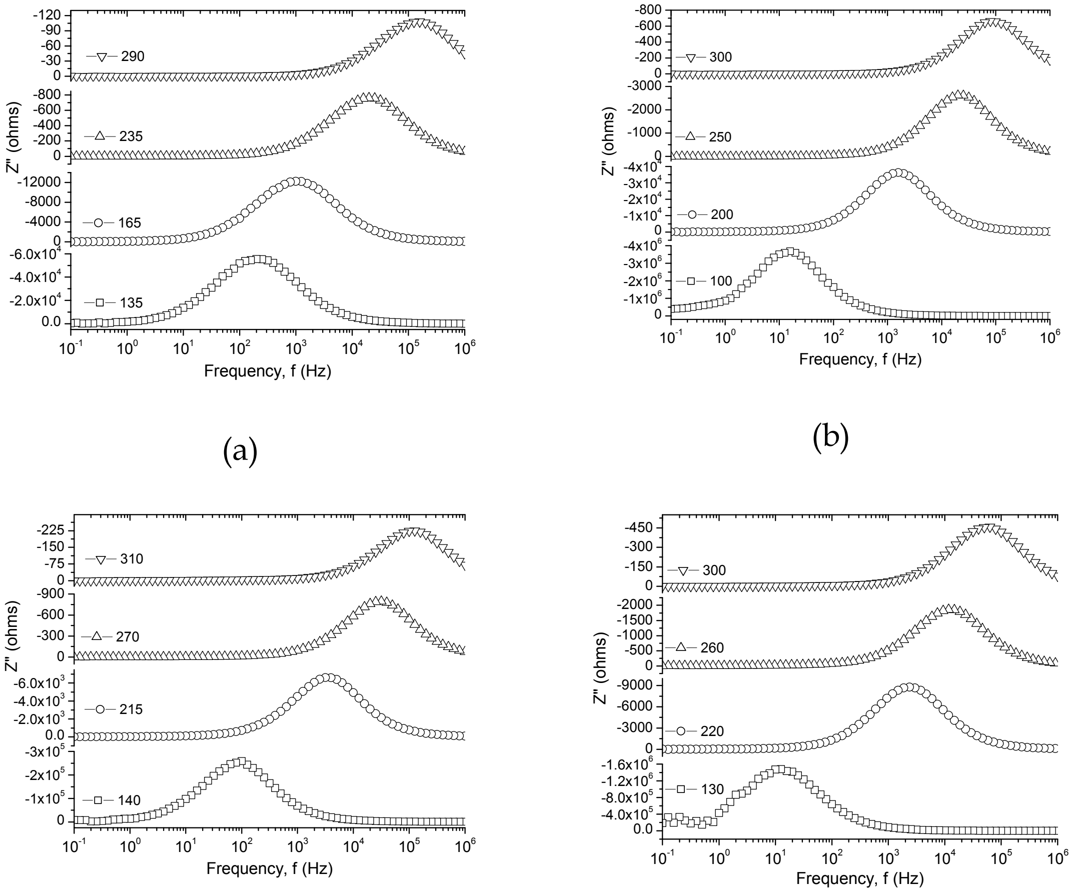

(a)

(b)

(c)

(d)

FIG. 3.20 Z" against log frequency plots for the samples: (a) SCA-2, (b) SCTa-3, (c) SCN-3 and (d) SCV-2 at different temperatures.

Fig. 3.20 (a), (b), (c) and *(d)* represent the Z" (Imaginary resistance) against log frequency plots for the samples: SCA-2, SCTa-3, SCN-3 and SCV-2 respectively. This representation was most suitable to evaluate the relaxation frequency of the most resistive contribution. The f_{max} was taken from the plot and relaxation time was calculated by using the relation, $\Gamma = 1/2\pi f_{max}$ and are given in *Table XIII*. The relaxation time found to vary from 10^{-6} to 10^{-2} s depending upon the compositions indicating the presence of temperature dependent relaxing defects in the sample. The shift of f_{max} towards higher frequency side with temperature indicated the presence of space charge effect in the samples.

Table XIII. Grain resistivity (ρ_g), grain boundary resistivity (ρ_{gb}), capacitance (C) and relaxation time (Γ) for the samples: SCA-2, SCTa-3, SCN-3 and SCV-2 at various temperatures

Sample	Temperature (°C)	ρ_g (ohm-cm)	ρ_{gb} (ohm-cm)	C (Farad)	Γ (second)
SCA-2	RT	104.32	3.24×10^{7}	--	--
	135	87.24	1.54×10^{5}	4.42×10^{-9}	7.98×10^{-4}
	165	78.16	3.41×10^{4}	3.97×10^{-9}	1.26×10^{-4}
	235	61.72	1.92×10^{3}	3.69×10^{-9}	7.98×10^{-6}
	290	49.21	3.32×10^{2}	3.36×10^{-9}	1.04×10^{-6}
SCTa-3	RT	294.05	1.41×10^{7}	--	--
	105	287.45	9.29×10^{6}	1.01×10^{-9}	1.07×10^{-2}
	195	238.37	8.43×10^{4}	1.07×10^{-9}	1.04×10^{-4}
	255	199.19	6.66×10^{3}	1.07×10^{-9}	6.34×10^{-6}
	295	178.69	1.85×10^{3}	9.87×10^{-10}	1.59×10^{-6}
SCN-3	RT	125.74	1.14×10^{7}	--	--
	140	113.74	5.83×10^{5}	2.88×10^{-9}	1.59×10^{-3}
	215	90.53	1.69×10^{4}	2.70×10^{-9}	4.00×10^{-5}
	270	76.25	2.01×10^{3}	2.63×10^{-9}	5.03×10^{-6}
	310	74.23	6.23×10^{2}	2.33×10^{-9}	1.26×10^{-6}
SCV-2	RT	189.92	5.89×10^{7}	--	--
	130	172.26	4.09×10^{6}	2.66×10^{-9}	1.26×10^{-2}
	220	117.25	2.39×10^{4}	2.61×10^{-9}	6.34×10^{-5}
	260	96.82	3.87×10^{3}	2.38×10^{-9}	1.26×10^{-5}
	300	84.92	1.28×10^{3}	2.27×10^{-9}	2.52×10^{-6}

3.8 Arrhenius plot

The grain boundary resistivity and temperature are related by the Arrhenius equation given in *equation 3.4*.

$$\rho_{gb} = \rho_{gb0} \exp(-E_A/K_BT) \qquad 3.4$$

The slope of the curve log (ρ_{gb}) versus 1000/T (*Fig 3.21*) gives the value corresponding to E_A/K. The activation energy was calculated from the slope of the curve. The values of activation energies thus calculated were 0.128, 0.129, 0.129 and 0.123 eV for the sample SCA-2, SCTa-3, SCN-3 and SCV-2 respectively. This was similar to the variation in non-linear coefficient values measured from I-V characteristics. Hence the large value of grain boundary activation energy indicates a better intergranular grain boundary region leading to superior current-voltage characteristic.

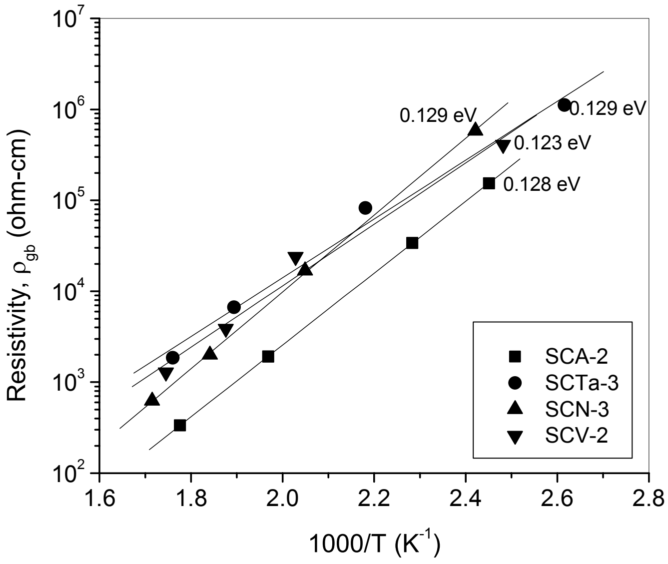

FIG 3.21 Arrhenius plots (resistivity versus 1000/T) for the samples SCA-2, SCTa-3, SCN-3 and SCV-2

3.9 Discussion

The addition of small quantities of transition metal oxides such as CoO to tin oxide helps in its densification. For example with 1 mol % CoO, the densification is > 94% when sintering is done at 1300 °C for one hour [2]. At low temperature, the CoO may take up oxygen and at high temperatures CoO is the stable phase releasing oxygen to its environment as given in *equations 3.5 and 3.6*.

$$2CoO + \frac{1}{2}O_2 \xrightarrow{500\text{-}680\ ^\circ C} Co_2O_3 \tag{3.5}$$

$$Co_2O_3 \xrightarrow{950°C} 2CoO + \tfrac{1}{2}O_2 \qquad 3.6$$

It was confirmed from the linear shrinkage studies that 1 at. % CoO was giving highest density of SnO_2 and the maximum shrinkage rate temperature was at 1190°C, which was very high than any other donor doped composition. The varistor action observed in polycrystalline ZnO ceramics is explained by considering the Schottky type energy barrier at the grain boundaries. In case of ZnO varistors Al_2O_3 is used as donor [14]. In the present case, the acceptor like surface states formed by CoO may lead to formation of energy barrier at the grain boundaries. The Co^{2+} ion having lower valence creates oxygen vacancies in tin oxide lattice, which is a rate-determining step for sintering. The densification of tin oxide ceramics has been attributed to the above-mentioned effect of Co in the SnO_2 lattice leading to the formation of oxygen vacancies according to the *equations 3.7* and *3.8.*

$$CoO \xrightarrow{SnO_2} Co''_{Sn} + V_o^{\bullet\bullet} + O_o^x \qquad 3.7$$

$$Co_2O_3 \xrightarrow{SnO_2} 2\,Co'_{Sn} + V_o^{\bullet\bullet} + 3\,O_o^x \qquad 3.8$$

The incorporation of donor increases the electronic conductivity, if donor is compensated by electron as given in *equation 3.9* or the resistivity will increase if donor is dominantly compensated by the cation vacancies as described by the following defect reaction in *equation 3.10.*

$$D_2O_5 \xrightarrow{SnO_2} 2D^{\bullet}_{Sn} + 2e' + 4\,O_o^x + 1/2O_2\,(g) \qquad 3.9$$

$$2D_2O_5 \xrightarrow{SnO_2} 4D^{\bullet}_{Sn} + V''''_{Sn} + 10O_o^x \qquad 3.10$$

Where, D = Sb, Ta, Nb and V

This was similar to donor doped $BaTiO_3$, wherein semiconductivity is introduced only at specific concentration of the donor [8]. The functional parameters α, Φ_B, and E_B decrease continuously with increase in the content for Sb doped samples, whereas these parameters change irregularly with the concentration for other donors. *Fig 3.22 (a)* and *(b)* shows the variation of nonlinear coefficient (α) and breakdown field (E_B) respectively with respect to donor concentration. Unlike Ta and Nb, Sb having multiple valency (3+ and 5+) changes the resistivity. *Fig 3.23* represents the plots for the room temperature resistivity as function of temperature for Sb_2O_3, Ta_2O_5, Nb_2O_5 and V_2O_5 doped series. In general, when breakdown field is high, the values of α and Φ_B increase and vice versa although this need not be always hold good. Since, the ionic radii of the donors used were (assuming they are in pentavalent state) being similar to that of Sn^{4+} (effective ionic radius 0.74 Å) ion, it was expected that they would substitute in Sn^{4+} site. In the case of Nb and V doped samples, the room temperature resistivity decreases by a smaller margin. The obtained barrier height values for the present systems were much lower than that reported for ZnO varistor [9].

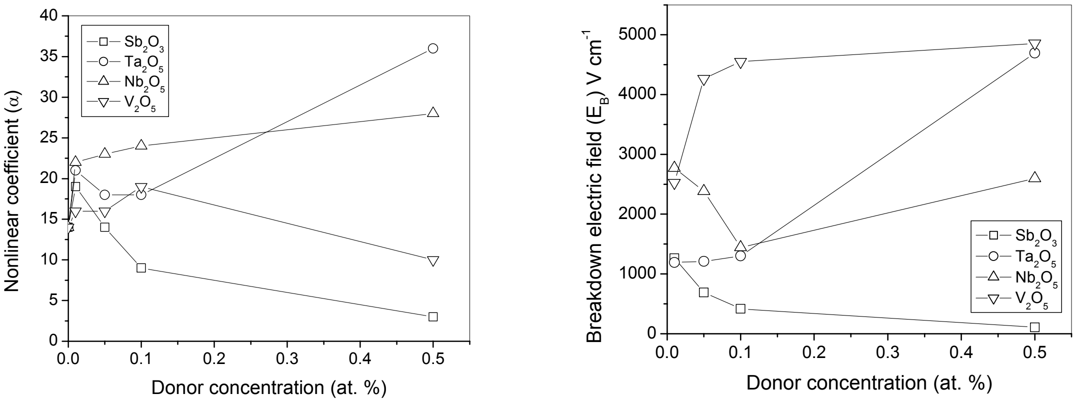

(a) (b)

FIG. 3.22 Plots of variation of (a) non-linear coefficient and (b) breakdown field with respect to donor concentration

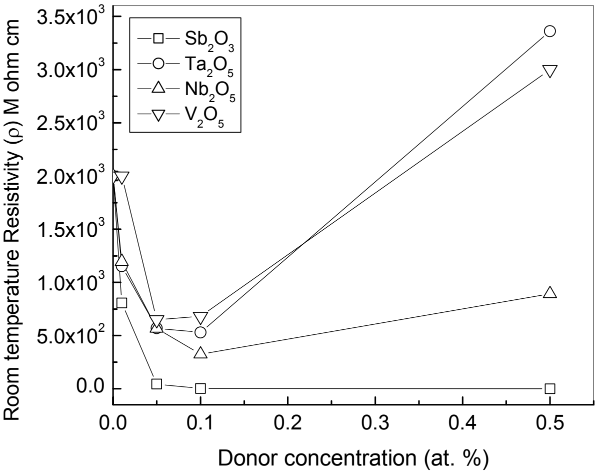

FIG. 3.23 Plots for room temperature resistivity as a function of donor concentration for Sb_2O_3, Ta_2O_5, Nb_2O_5 and V_2O_5 -doped series

The conductivity did not increase with increase in the Ta concentration. The incorporation of Ta was probably charge compensated by electrons at lower concentrations and by cation vacancies at higher concentrations. Smaller amount of Ta_2O_5 were added to SnO_2 ceramics to promote the substitution of Sn^{4+} for Ta^{5+} (effective ionic radius 0.69 Å) leading to an increase of electronic conductivity in the SnO_2 lattice according to *equation 3.9*. The barrier height calculated for Ta_2O_5 doped samples was in the range of 0.356 to 0.627 eV.

Sb_2O_5 is the stable up to 970 °C, but Sb_2O_3 is more stable at higher temperature. However, the Sb^{5+}/Sb^{3+} ratio will depend both on the temperature and on the concentration of ambient oxygen [10]. Then the transformation of Sb^{3+} into Sb^{5+} (effective ionic radius 0.60 Å) is possible during the cooling process. At lower concentrations, Sb is pentavalent acting as a donor (*equation 3.9*) and the probable defect equation for the Sb_2O_3 is given in *equation 3.11*. The barrier height calculated for Sb_2O_3 doped samples was in the range of 0.242 to 0.424 eV.

$$Sb_2O_3 \xrightarrow{SnO_2} 2Sb'_{Sn} + V_o^{\cdot\cdot} + 3\,O_o^{x} \qquad 3.11$$

As discussed in the literature [11], the dopant Nb (5+ valence) having an ionic radius 0.69 Å nearly similar to that of Sn^{4+}, acts as donor, which dissolves into the SnO_2 lattice. The substitution of Sn by Nb leads to increasing the concentration of electron, and thus decreases the lattice resistivity of the SnO_2 according to *equation 3.9* [12]. The reaction given in *equation 3.10* was also possible. Barrier height calculated for Nb_2O_5 doped samples was in the range of 0.247 to 0.429 eV.

The dopant V with 5+ valence (effective ionic radius 0.54 Å) at low concentration was expected to dissolve into the SnO_2 lattice this leads to increase the concentration of electrons according to *equation 3.9*. However, there was also a possibility of V with 4+ valence isovalent to Sn^{4+} responsible for increase in lattice resistivity of the SnO_2. Amongst the donors discussed here, the Nb_2O_5 and Ta_2O_5 do not show variable valance state even at higher temperatures. Both were in 5+ states and expected to increase electronic conductivity. However, Sb_2O_3 and V_2O_5 having variation in valance state with temperature were responsible to affect the electronic conductivity. Oxygen released due to donor incorporation according to *equation 3.9* will be partly absorbed at SnO_2 grain boundaries by *equation 3.12*.

$$O_2 \longrightarrow O_2^{x}(ad) \qquad 3.12$$

These absorbed oxygen easily capture the electrons to become negatively charged ions by *equations 3.13 and 3.14*.

$$O_2^{x}(ad) + e' \longrightarrow O'(ad) \qquad 3.13$$

$$O_2^{x}{}_{(ad)} + 2e' \longrightarrow O''_{(ad)} \qquad 3.14$$

The role of the absorbed oxygen in the formation of boundary barriers is addressed in the literature [13]. The grain boundary resistivity at room temperature calculated from Bode plots for Sb_2O_3, Ta_2O_5, Nb_2O_5 and V_2O_5 doped samples were of the order of 3.24 x 10^7, 1.41 x 10^7, 1.14 x 10^7 and 5.89 x 10^7 ohm-cm respectively. *Fig 3.24* shows a schematic grain boundary barrier diagram, wherein possible negative surface states are also given. The positively charged donors extending from the both sides of grain boundary are compensated by the negatively charged acceptors at the grain boundary interface. The electric transport occurs by tunneling across the barrier and is responsible for the electrical non-linearity.

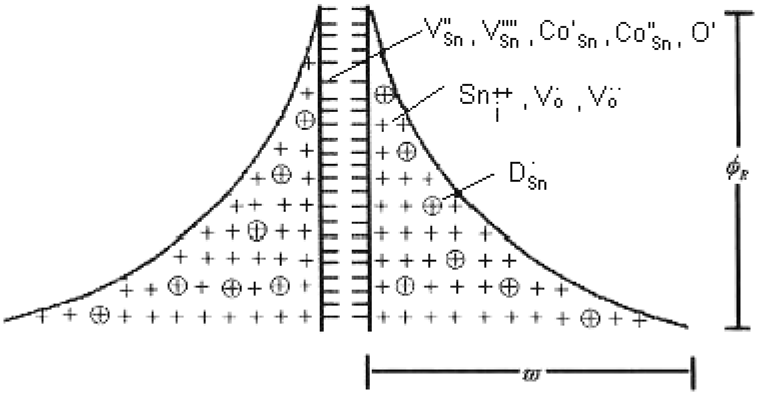

FIG 3.24 Schematic Schottky type grain boundary barrier diagram

3.10 Summary and conclusions

The non-linear coefficient values were dependent on both composition and processing parameter. Under the optimum conditions i.e. at longer durations of sintering low voltage varistors were realized.

Sb and Nb doped samples show promising results for the low voltage varistor applications, whereas V doped samples shows reasonable non-linearity with higher breakdown field.

The maximum α (= 36) observed among all the donors was for Ta-doped sample at a concentration of 0.5 at. %. The advantage of the present varistor systems was that it contains less number of additives as compared to ZnO ceramics, wherein a variety of metal oxides are added in smaller quantities to achieve the optimum properties.

Impedance plot and bode plots are supporting for the constituents from second phase segregation at the grain boundaries and responsible for the Schottky type energy barrier at the grain boundary in the conduction phenomena. The oxygen adsorbed at grain boundaries was due to the donor incorporation leading to non-linear varistor behavior.

References

1. Gupta T K, *J. Mater. Res.* **7**, 3280 (1992)
2. Cerri J A, Leite E R, Gouvea D and Longo E, *J. Am. Ceram. Soc.* **79**, 799 (1996)
3. Pianaro S A, Bueno P R, Longo E and Varela J A, *J. Mater. Sci. Lett.* **14**, 692 (1995)
4. Wang Y J, Wang J F, Li C P, Chen H C, Su W B, Zhnag W L, Zhang P L, Zhao L Y, *J. Mater. Sci. Lett.* **20**, 19 (2001)
5. Antunes A C, Antunes S R M, Pianaro S A, Roha M R, Longo E, Varela J A, *J. Mater. Sci. Lett.* **17**, 577 (1998)
6. Fayat J, Castro M S, *J. Euro. Ceram. Soc.* **23**, 1585 (2003)
7. Bueno P R, Pianaro S A, Pereira E C, Bulhoes L O S, Longo E and Varela J A, *J. Appl. Phys.* **84**, 3700 (1998)
8. Ravi V and Kutty T R N, *J. Amer. Ceram. Soc.* **75,** 203 (1992)
9. Clarke D R, *J. Am. Ceram. Soc.* **82**, 485 (1999)
10. Ovenston A, Sprinceana D, Walls J R and Caldararu M, *J. Mater. Sci.* **29,** 4946 (1994)
11. Pianaro S A, Bueno P R, olivi P, Longo E, Varela J A, *J. Mater. Sci. Lett.* **16,** (1997) 364
12. Bueno P R, Pianaro S A, Pereira E C, Bulholes L O S, Longo E and Varela J A *J. Appl. Phys.* **84**, 3700 (1998)
13. **(a)** Leite E R, Nascimento A M, Bueno P R, Longo E, Varela J A, *J. Mater. Sci. Mate. Electr.* **10,** 321 (1999) **(b)** Santos M R C, Bueno P R, Longo E and Varela J A, *J. Eur. Ceram. Soc.* **21** 161, (2001) **(c)** Stucki F and Greuter F, *Appl. Phys. Lett.* **57,** 446 (1990) **(d)** Bueno P R, Leite E R, Oliveira M M, Orlandi M O and Longo E, *Appl. Phys. Lett.* **79,** 48 (2001)
14. Fiwei F and Freer R, *J. Appl. Phys.* **77**, 4798 (1995)

Chapter 4

(Sn, Ti)O_2 solid solution

This chapter describes the influence of isovalent ion, Ti^{4+} on the I-V characteristics of doped SnO_2 in detail. The non-linear coefficient (α), breakdown electric field (E_B) and barrier height (Φ_B) were calculated as a function of donor content. Different compositions were prepared with respect to each donor. 5 mole % of TiO_2 was substituted for SnO_2 in each case. The series of compositions were (94-x) SnO_2 + 5 TiO_2 + 1 CoO + x D (where x = 0.01, 0.05, 0.1 & 0.5 at. % and D = Sb_2O_3, Ta_2O_5, & Nb_2O_5). The studies have showed the high voltage non-linear I-V electrical response for Sb doped (Sn, Ti)O_2 based polycrystalline ceramics. All these systems are potentially promising for varistor applications.

4.1 Introduction

As in the case of SnO_2, TiO_2 in the rutile phase is an electrically insulating material with a tetragonal crystalline structure. It is being investigated for the applications in electrocatalysis, photo electrochemistry and as counter electrode in smart windows [1]. The good stability of SnO_2 sensor properties for reducing gases, combined with good chemical stability of TiO_2 at low temperature is strong motivation for investigations into SnO_2-TiO_2 solid solution for ceramic sensor applications [2]. Studies have shown that binary systems such as SnO_2-TiO_2 solid solutions can also display a varistor like behavior in addition to sensor properties. Control of electrical and sensor properties as well as sinterability of some semiconducting oxides is mainly exerted by the use of additives (as dopants). This control is crucial to obtain the high performance materials such as varistors, resistors, capacitors or sensors ceramics.

Yan and Rhodes [3] first reported that (Nb, Ba)-doped TiO_2 ceramics have useful varistor properties with non-linear coefficients (α) in the range of 3 to 4, wherein an oxidizing atmosphere during cooling is necessary. Yang and Wu [4] reported a (Ba, Bi, Nb)-doped TiO_2 ceramic with a non-linear coefficient (α) of 9.5 without an oxidizing agent. Fully dense TiO_2 displays high non-ohmic properties as compare to SnO_2. However, a much lower breakdown field allows its use in the low-voltage varistor [3] and humidity sensor [5] applications. TiO_2 differs from SnO_2 during sintering, because unlike SnO_2 it requires no dopants to densify. Hence, the non-ohmic properties of TiO_2 based ceramics can be obtained using the same types and concentrations of dopants as those used in SnO_2 based varistors [6].

The basic characteristics of varistors are: (i) host material must be perfectly insulating, (ii) type of impurity doping and (iii) grain boundary segregation. The three crystalline polymorphs of TiO_2 are anatase, rutile and brookite. Anatase, rutile and brookite are low temperature, high temperature and high pressure phases respectively. Amongst these, the high temperature rutile phase is more stable and used for doping.

High densification can be achieved by the addition of CoO [7]. Thermal treatments in an O_2 atmosphere on (Ti, Sn)O_2 matrix provide better varistor response with increase in the non-linearity [8].

The dopants used in TiO_2 and SnO_2 were different and both show non-linear I-V characteristics having rutile (tetragonal) structure. Further, SnO_2 has a slightly higher breakdown field (E_B) values compared to TiO_2. Hence we have attempted to prepare a solid solution with common additives to get an optimum E_B value. The results are presented here from the investigations carried out on (Sn, Ti)O_2 doped system. The goal of this work was to show the possibility of combining the features of SnO_2 and TiO_2 based ceramics in an oxide matrix of (Sn, Ti)O_2. This helped to obtain the ceramics with non-ohmic properties similar to those of pure components, in view of the fact that SnO_2 and TiO_2 share a common structure and hence common oxygen sublattice.

4.2 Experimental

SnO_2 containing additives were prepared by the standard ceramic method as well as chemical method. SnO_2, along with dopants such as TiO_2, CoO and Sb_2O_5/Ta_2O_5/Nb_2O_5 in the stoichiometric ratio were mixed, ground well and calcined at 1200 °C for 24 hrs. The calcined powders were again ground and fired at 1200 °C for another 24 hrs. Three compositions were prepared with respect to each donor and 5 mole % of TiO_2 was substituted for SnO_2 in each case. The molar compositions were (94-x)% SnO_2 + 5% TiO_2 + 1% CoO + x %D (i.e. STCD where x = 0.01, 0.05, 0.1 & 0.5 at. % and D = Sb_2O_5, Ta_2O_5 & Nb_2O_5). The calcined powders were mixed with a binder (2 wt. % poly vinyl alcohol) and pelletized

(15 mm dia, 1 mm thick) at a pressure of 2-3 metric tons. The pellets were sintered at 1300 °C for two different durations: 4 and 24 hrs. The density of the pellet was calculated using mass volume and Archimedes methods. The sintered pellets were polished and ohmic silver contacts were obtained by curing Ag-paste at 600 °C for 30 minutes. The samples were identified as STCX-1, STCX-2, STCX-3 and STCX-4 for 0.01, 0.05, 0.1 and 0.5 at. % X-oxide (where, X=A, Ta & N for Sb_2O_3, Ta_2O_5, and Nb_2O_5 respectively).

4.3 Sb_2O_3 doped series

4.3.1 I-V characteristics

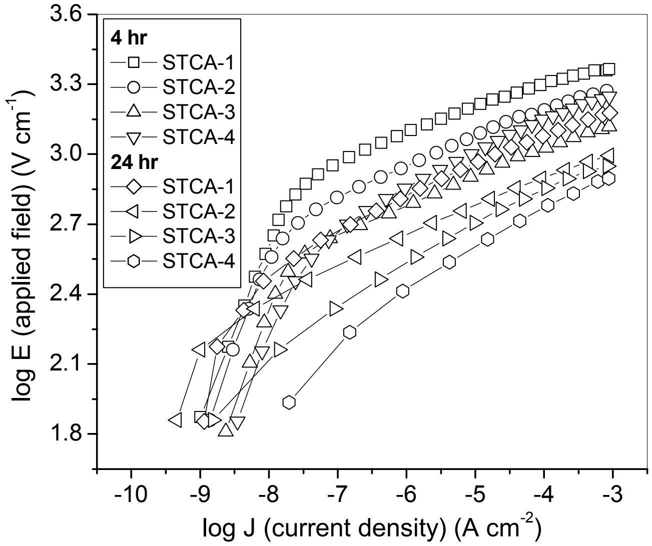

FIG. 4.1a I-V characteristic plots for the samples: STCA-1, STCA-2, STCA-3 and STCA-4 sintered at 1300 ºC for 4 and 24 hrs.

Fig 4.1a shows the current density (J) versus applied field (E) (I-V characteristic) plots on log scale for the samples: STCA-1, STCA-2, STCA-3 and STCA-4 sintered at 1300 ºC for 4 & 24 hrs. The non-linear coefficients (α) calculated from the slopes of the curves in the non-linear regions for the samples sintered for 4 hrs were 26, 24, 20 & 17 for STCA-1, STCA-2, STCA-3 and STCA-4 respectively. The values for non-linear coefficients calculated for samples sintered at 1300 °C for 24 hrs were 20, 19, 16 & 14 for STCA-1, STCA-2, STCA-3 and SCA-4 respectively. The other performance parameters: breakdown field (E_B), density (ρ) and barrier height (Φ_B) are given in *Table I.* Both the non-linear coefficient and breakdown field decrease with the concentration of Sb_2O_3. The leakage current (I_l) range for Sb_2O_3 doped series was between 1.25 to 86 nA. Decrease in non-linear coefficient and breakdown field were observed for the increase in sintering duration from 4 to 24 hrs. When the content of Sb was between 0.1 and 0.5 at. %, the room temperature resistivity decreases tremendously. Hence, for the high concentration of Sb the breakdown field was low particularly when sintering duration was long (*Table I*).

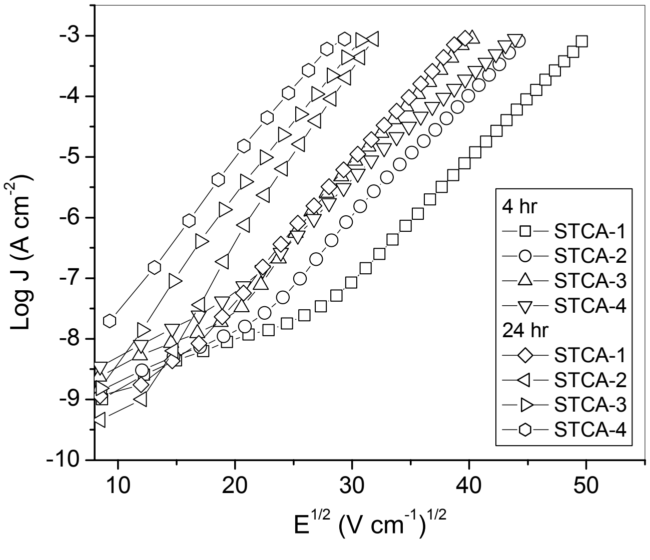

FIG. 4.1b Characteristic plots of log J against $E^{1/2}$ for the samples: STCA-1, STCA-2, STCA-3 and STCA-4 sintered at 1300 °C for 4 and 24 hrs.

The grain growth due to the increase in the duration of sintering causes the decrease in breakdown field. By considering the Schottky type grain boundary barriers responsible for conduction phenomena, characteristic plots of log J against $E^{1/2}$ as shown in *Fig 4.1b* could be built up to determine the values for β and Φ_B using Richardson's formula (as discussed in *chapter 2*). Since Richardson's constant depends on the density of the sample and varies from material to material, the values calculated for Sb_2O_3 doped samples were of the order of 1.808×10^6. The values for the barrier height (Φ_B) are given in *Table I*.

Table I. Characteristic parameters for the samples: STCA-1, STCA-2, STCA-3 and STCA-4.

Sample identification	Sb_2O_3 (at. %)	α	E_B, V cm^{-1}	Density, gm cm^{-3}	Relative density, %	Φ_B, eV	Average grain size, µm
Sintering time 4 hr							
STCA-1	0.01	26	2540	6.67	96.0	0.498	6
STCA-2	0.05	24	1960	6.47	93.1	0.406	7
STCA-3	0.1	20	1620	6.41	92.2	0.436	7
STCA-4	0.5	17	1930	6.42	92.4	0.400	8
Sintering time 24 hr							
STCA-1	0.01	20	1570	6.47	93.1	0.434	10
STCA-2	0.05	19	1015	6.45	92.8	0.433	9
STCA-3	0.1	16	940	6.68	96.1	0.393	10
STCA-4	0.5	14	860	6.47	93.1	0.368	9

4.3.2 Sintering behavior

Fig 4.2 shows the linear shrinkage ($\Delta L/L_0$) and the rate of linear shrinkage ($d(\Delta L/L_0)/dT$) (inset) as a function of temperature for the samples: STCA-1, STCA-2, STCA-3 and STCA-4. From the linear shrinkage curves it was observed that the shrinkage starts at the temperature around 1040 °C and completed at the maximum temperature of 1250 °C for all the samples. The maximum shrinkage rate temperature (T_M) was taken from the linear shrinkage rate against temperature plot and it was found that the T_M increases with increasing concentration of Sb_2O_3 (*Table II*). The density of all the samples was greater than 92 %as given in *Table I*.

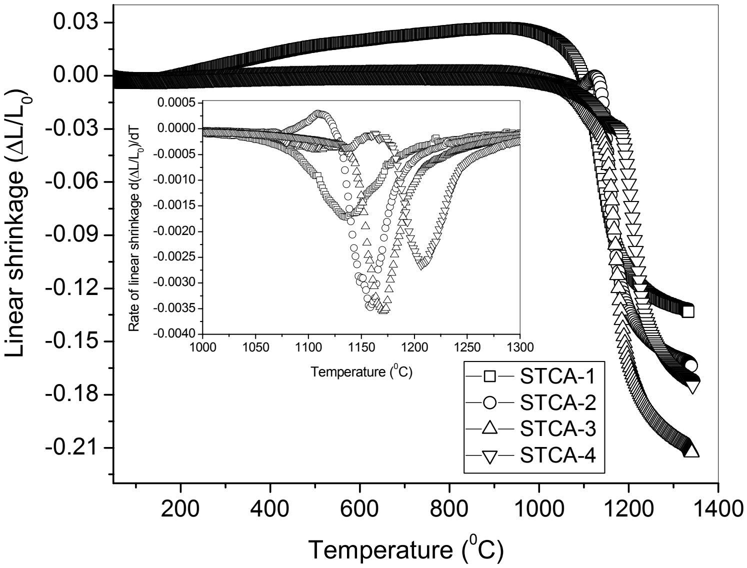

FIG. 4.2 Plots for the linear shrinkage ($\Delta L/L_0$) and rate of linear shrinkage ($d(\Delta L/L_0)/dT$) (inset) as a function of temperature for the samples: STCA-1, STCA-2, STCA-3 and STCA-4.

Table II. Maximum shrinkage rate temperature for Sb_2O_3 doped series.

Sample identification	T_M (°C)
STCA-1	1133
STCA-2	1157
STCA-3	1170
STCA-4	1207

4.3.3 X-ray powder diffraction

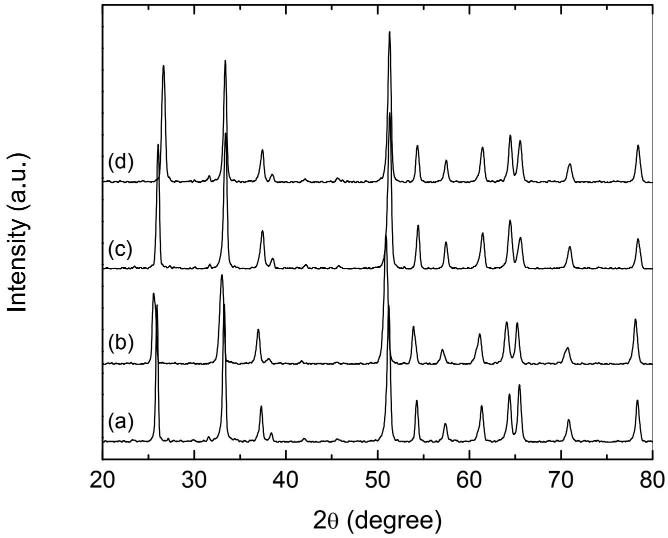

FIG. 4.3 X-ray powder diffraction patterns of sintered samples: (a) STCA-1, (b) STCA-2, (c) STCA-3 and (d) STCA-4.

Fig 4.3 shows the X-ray diffraction patterns (XRD) recorded for the samples: (a) STCA-1, (b) STCA-2, (c) STCA-3 and (d) STCA-4. Apparently no second phases were found, since all the diffraction patterns showed only the peaks corresponding to SnO_2 rutile structure. No peaks corresponding to any other secondary phases were seen. It was also noted that the concentrations of dopants added were too small to be detected by X-ray diffraction. The lattice parameters calculated by least squares method are given in *Table III*.

Table III. Lattice parameters for Sb_2O_3 doped series.

Lattice parameter (Å)	Sample identification			
	STCA-1	STCA-2	STCA-3	STCA-4
a	4.722	4.726	4.726	4.727
c	3.172	3.173	3.173	3.274

4.3.4 Scanning electron microscopy

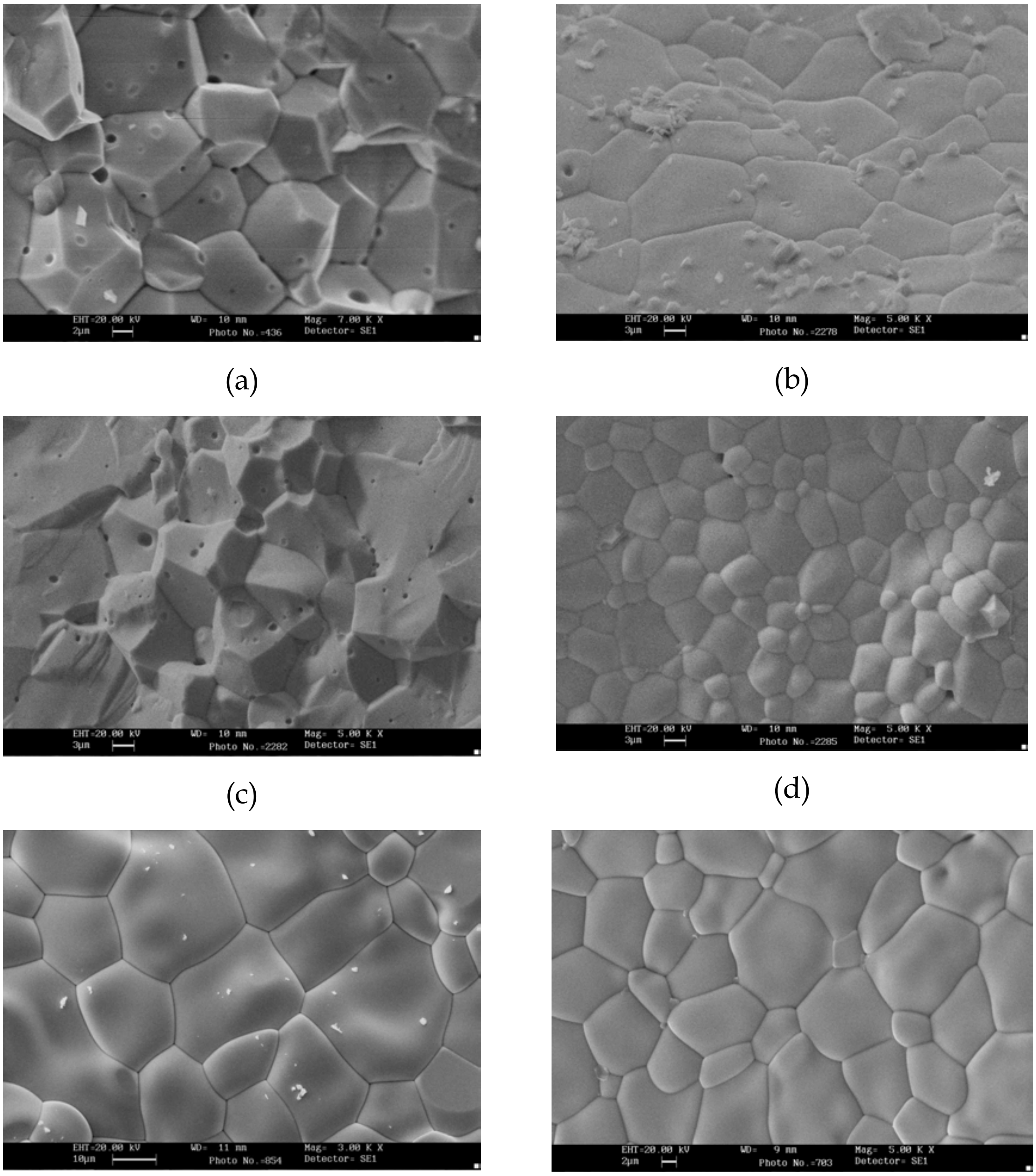

(a) (b)

(c) (d)

(e) (f)

FIG. 4.4 Scanning electron micrographs of the fractured surfaces for the samples: (a) STCA-1, (b) STCA-2, (c) STCA-3 & (d) STCA-4 (all sintered at 1300 ºC for 4 hrs) and (e) STCA-1 & (f) STCA-3 (both sintered at 1300 ºC for 24 hrs).

To understand the grain-grain boundary microstructure and determine the grain size, the scanning electron micrographs of the fractured surfaces of the pellets were taken after gold coating on the surface. The micrographs for the samples: (a) STCA-1, (b) STCA-2, (c) STCA-3 & (d) STCA-4 (all sintered at 1300 ^{o}C/4 hrs) and (e) STCA-1 and (f) STCA-2 (both sintered at 1300 ^{o}C/24 hrs) are shown in *Fig 4.4*. The average grain sizes for the samples: STCA-1, STCA-2, STCA-3 and STCA-4 sintered for 4 hrs were found to be 6, 7, 7 & 8 μm respectively and the average grain sizes for the respective samples sintered for 24 hrs were 10, 9, 10 and 9 μm (*Table I*). Grain growth was observed when sintering duration was long. With increasing the sintering duration, the grain size was increased e.g. samples: STCA-1 and STCA-2 as shown in *Fig 4.4 (e)* and *(f)* respectively. Voids were also seen at certain sections of the samples. Densities calculated for these samples were more than 92 %with respect to theoretical density as given in *Table I*.

The grain size has a clear effect on the current-voltage characteristics of the varistor. The breakdown field decreases with increase in grain size. Even though no grain boundary phase from the added constituents were found in the micrograph, the grain boundary phase responsible for conduction phenomena was confirmed by the impedance analysis, as discussed in *section 4.6*.

4.4 Ta_2O_5 doped series

4.4.1 I-V characteristics

Fig 4.5a shows the current density (J) versus applied field (E) (I-V characteristic) plots on log scale for the samples: STCTa-1, STCTa-2, STCTa-3 and STCTa-4 sintered at 1300 ^{o}C for 4 and 24 hrs. The non-linear coefficients (α) were calculated from the slopes of the curves in the non-linear regions. The values for the non-linear coefficients were found to be 32, 28 and 17 for the samples: STCTa-

1, STCTa-2 & STCTa-3 (all sintered for 4 hrs) whereas the sample STCTa-4 was insulating. The non-linear coefficients calculated for samples sintered for 24 hrs were 26, 24, 24 & 34 for STCTa-1, STCTa-2, STCTa-3 and STCTa-4 respectively. The other performance parameters: breakdown field (E_B), density (ρ) and barrier height (Φ_B) are given in *Table IV*. Both the non-linear coefficient and breakdown field decrease with increase in the concentration of Ta_2O_5. Decrease in non-linear coefficient as well as breakdown field was observed for the increase in sintering duration from 4 to 24 hrs. The decrease in breakdown field with increase in the duration of sintering was a direct consequence from the corresponding increase in grain size. As the duration of sintering increases, both α and E_B decrease as can be seen from the *Table IV*. Considering the Schottky type conduction model, plots of log J against $E^{1/2}$ (*Fig 4.5b*) could be built up to determine value for β and Φ_B using Richardson's formula. The Richardson's constant values calculated for Ta_2O_5 doped samples were of the order of 1.79 x 10^6. The values for barrier height (Φ_B) are given in *Table IV*.

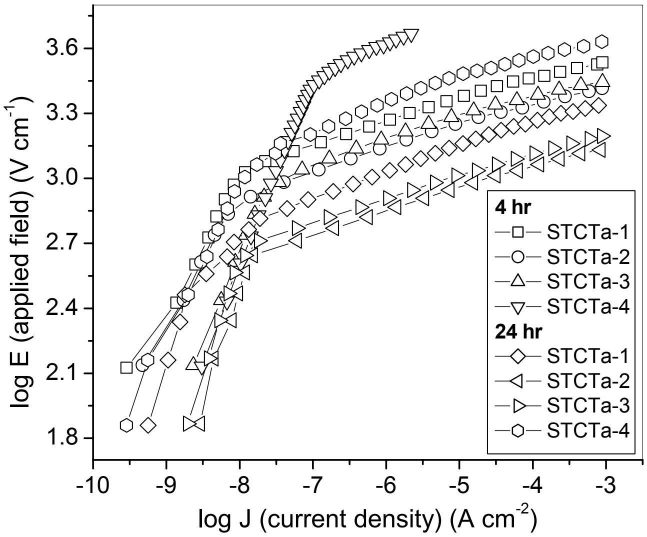

FIG. 4.5a I-V characteristic plots for the samples: STCTa-1, STCTa-2, STCTa-3 and STCTa-4 sintered at 1300 °C for 4 and 24 hr.

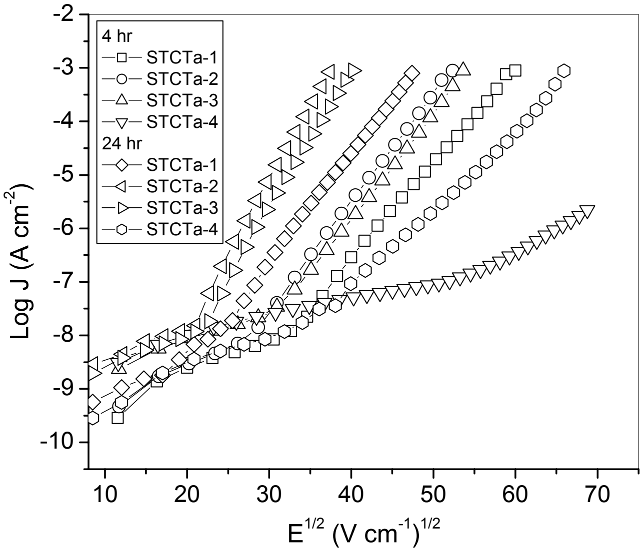

FIG. 4.5b Characteristic plots of log J against $E^{1/2}$ for the samples: STCTa-1, STCTa-2, STCTa-3 & STCTa-4 sintered at 1300 °C for 4 and 24 hrs.

Table IV. Characteristic parameters for the samples: STCTa-1, STCTa-2, STCTa-3 and STCTa-4.

Sample identification	Ta_2O_5 (at. %)	α	E_B, V cm^{-1}	Density, gm cm^{-3}	Relative density, %	Φ_B, eV	Average grain size, µm
Sintering time 4 hr							
STCTa-1	0.01	32	3600	6.35	91.3	0.569	5
STCTa-2	0.05	28	2740	6.40	91.1	0.526	6
STCTa-3	0.1	27	2880	6.40	92.1	0.516	6
STCTa-4	0.5	I[a]	-	6.26	90.1	-	4
Sintering time 24 hr							
STCTa-1	0.01	26	2245	6.61	95.1	0.469	10
STCTa-2	0.05	24	1400	6.56	94.4	0.469	9
STCTa-3	0.1	24	1615	6.69	96.2	0.478	9
STCTa-4	0.5	34	4350	6.58	94.7	0.597	10

[a] Insulating

4.4.2 Sintering behavior

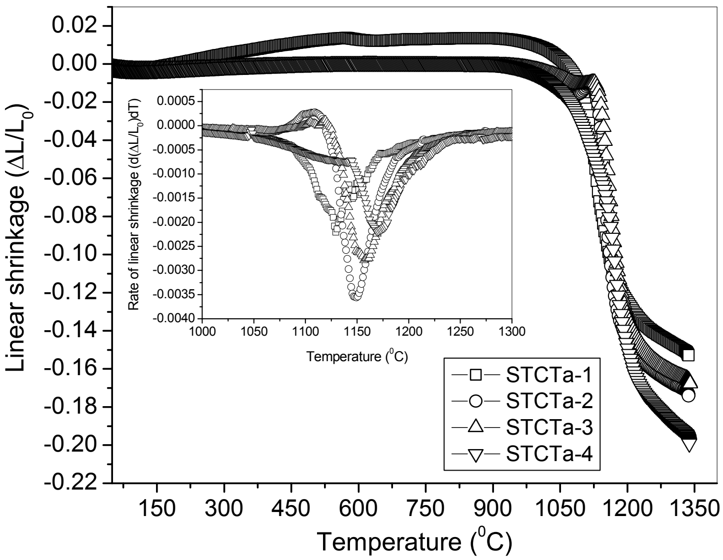

FIG. 4.6 Plots for the linear shrinkage ($\Delta L/L_0$) and rate of linear shrinkage ($d(\Delta L/L_0)/dT$) (inset) as a function of temperature for the samples: STCTa-1, STCTa-2, STCTa-3 and STCTa-4.

Table V. Maximum shrinkage rate temperature for Ta_2O_5 doped series.

Sample identification	T_M (°C)
STCTa-1	1129
STCTa-2	1146
STCTa-3	1158
STCTa-4	1169

Fig 4.6 shows the linear shrinkage ($\Delta L/L_0$) and the rate of linear shrinkage ($d(\Delta L/L_0)/dT$) (inset) as a function of temperature for the samples: STCTa-1, STCTa-2, STCTa-3 and STCTa-4. From the linear shrinkage curves, it was observed that the shrinkage starts at the temperature around 1015 °C and completed at the maximum temperature of 1235 °C for all the samples. The

densities of all the samples were found to be greater than 90 % as given in *Table IV*. The maximum shrinkage rate temperature (T_M) was taken from the linear shrinkage rate against temperature plot. Increase in T_M was observed with the increase in concentration of Ta_2O_5 as given in *Table V*.

4.4.3 X-ray powder diffraction

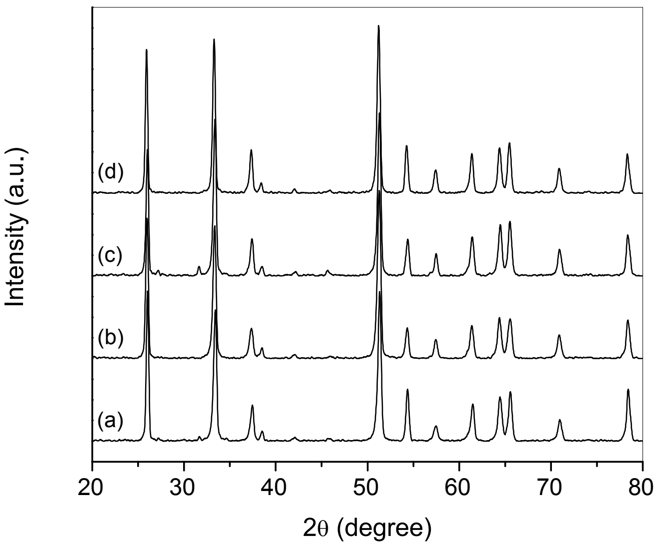

FIG. 4.7 X-ray powder diffraction patterns for sintered samples: (a) STCTa-1, (b) STCTa-2, (c) STCTa-3 and (d) STCTa-4.

Table VI. Lattice parameters for Ta_2O_5 doped series.

Lattice parameter (Å)	Sample identification			
	STCTa-1	STCTa-2	STCTa-3	STCTa-4
a	4.725	4.722	4.725	4.721
c	3.171	3.170	3.171	3.170

Fig 4.7 shows the X-ray diffraction patterns (XRD) recorded for the samples: (a) STCTa-1, (b) STCTa-2, (c) STCTa-3 and (d) STCTa-4. The XRD patterns of all the samples did not show any additional peaks corresponding to

secondary phases, which were expected to develop during sintering process. This may be due to the fact that concentrations of dopants added were too small to be detected by X-ray diffraction. All the lines were correspond to the tetragonal rutile SnO_2 phase. The lattice parameters calculated by least squares method are given in *Table VI*.

4.4.4 Scanning electron microscopy

The scanning electron micrographs of the fracture surfaces of the samples: (a) STCTa-1, (b) STCTa-2, (c) STCTa-3 & (d) STCTa-4 sintered at 1300 °C for 4 hrs and (e) STCTa-1 & (f) STCTa-2 sintered at 1300 °C for 24 hrs are shown in *Fig 4.8*. The average grain sizes for the samples: STCTa-1, STCTa-2, STCTa-3 and STCTa-4 (all sintered for 4 hrs) obtained from the microstructures were 5, 6, 6 and 4 µm respectively. Grain growth was observed when sintering duration was long. The average grain sizes for the respective samples sintered for 24 hrs were 10, 9, 9 and 10 µm as given in *Table IV*. The grain size has a clear effect on the current-voltage characteristics of the varistor. The increase in grain size for the samples STCTa-1 and STCTa-2 are shown in *Fig 4.8 (e)* and *(f)* respectively. The breakdown field decreases with increase in grain size. No grain boundary phase due to added constituents was found in the micrograph. The contribution of the grain boundary to the electrical conduction was confirmed by the impedance analysis, as discussed in *section 4.6*

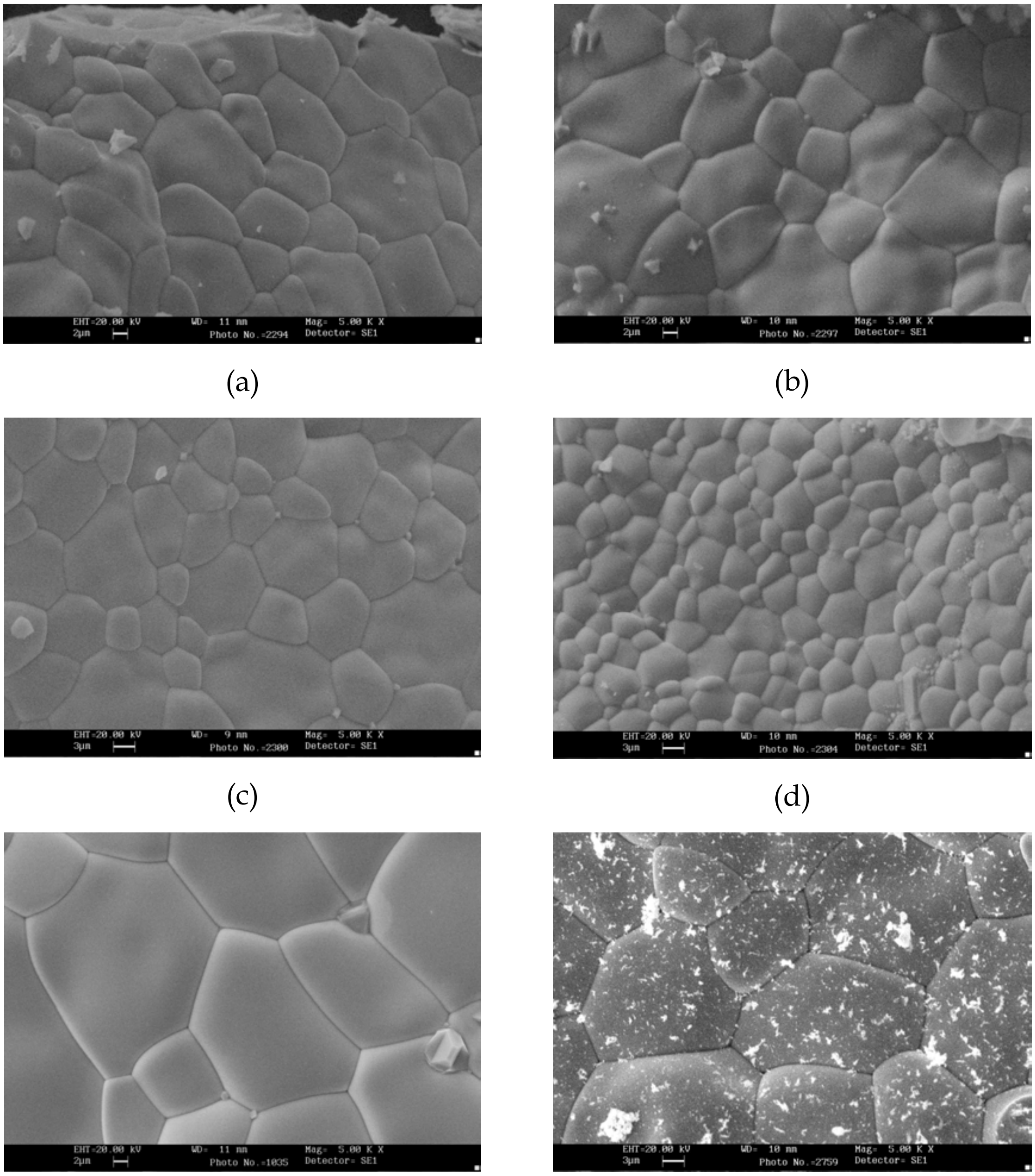

(a) (b)

(c) (d)

(d) (e)

FIG. 4.8 Scanning electron micrographs of the fractured surfaces for the samples: (a) STCTa-1, (b) STCTa-2, (c) STCTa-3 & (d) STCTa-4 (all sintered at 1300 °C for 4 hrs) and (e) STCTa-1 & (f) STCTa-2 (both sintered at 1300 °C for 24 hrs).

4.5 Nb_2O_5 doped series

4.5.1 I-V characteristics

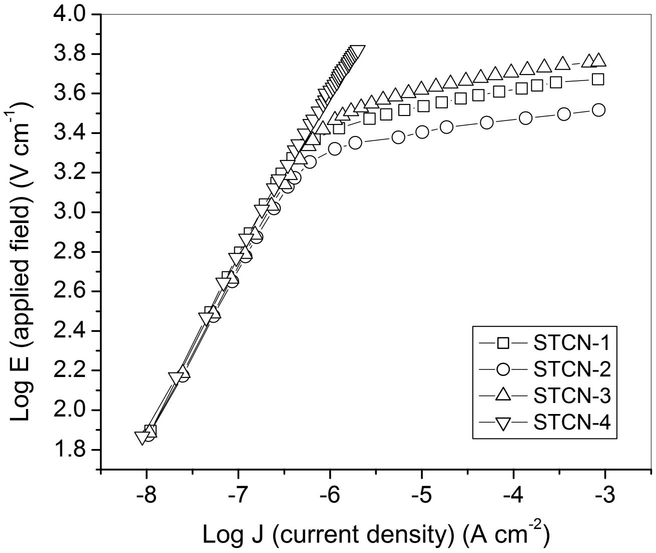

FIG. 4.9a I-V characteristic plots for the samples: STCN-1, STCN-2, STCN-3 and STCN-4 sintered at 1300 °C for 4 hrs.

Fig 4.9a shows the current density (J) against applied field (E) (I-V characteristics) plots on log scale for the samples: STCN-1, STCN-2, STCN-3 and STCN-4 sintered at 1300 °C for 4 hrs. The non-linear coefficient (α) calculated from the slopes of the curves in the non-linear regions for the samples: STCN-1, STCN-2 and STCN-3 were 36, 26 and 31 respectively. Sample STCN-4 was insulating. The other parameters: breakdown field (E_B), density (ρ) and barrier height (Φ_B) are given in *Table VII*. The decrease in both non-linear coefficient and breakdown field was observed for the 0.05 at. % Nb_2O_5. However, at higher concentration of Nb_2O_5 (0.1 at. %) both the parameters decrease. Further at the higher concentration, the sample (0.5 at. %) became insulating that means the conductivity did not increase with the increase in Nb concentration. The incorporation of Nb was probably might have charge compensated by the electrons and cation vacancies (which increases the resistivity) at its lower and higher concentrations respectively. The leakage current (I_l) range for all Nb_2O_5 doped samples was 0.02 to 0.13 nA. Considering the Schottky type conduction model, plots of log J against $E^{1/2}$ (*Fig 4.9b*) were built up to determine the values for β and Φ_B using Richardson's formula. The values calculated for Richardson's constant for Nb_2O_5 doped samples were of the order of 1.794 x 10^6. The values for the barrier heights (Φ_B) are given in *Table VII*.

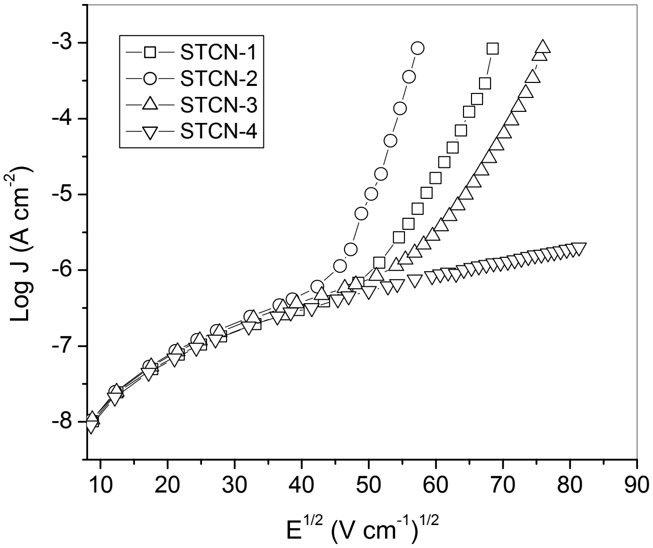

FIG. 4.9b Characteristics plots of log J against $E^{1/2}$ for the samples: STCN-1, STCN-2, STCN-3 and STCN-4.

Table VII. Characteristic parameters for the samples: STCN-1, STCN-2, STCN-3 and STCN-4.

Sample identification	Nb_2O_5 (at. %)	α	E_B, V cm^{-1}	Density, gm cm^{-3}	Relative density, %	Φ_B, eV	Average grain size, µm
STCN-1	0.01	36	4690	6.42	92.3	0.498	6
STCN-2	0.05	26	3480	6.36	91.6	0.406	7
STCN-3	0.1	31	5770	6.42	92.5	0.436	7
STCN-4	0.5	I[a]	--	6.44	92.7	--	8

[a]Insulating

4.5.2 sintering behavior

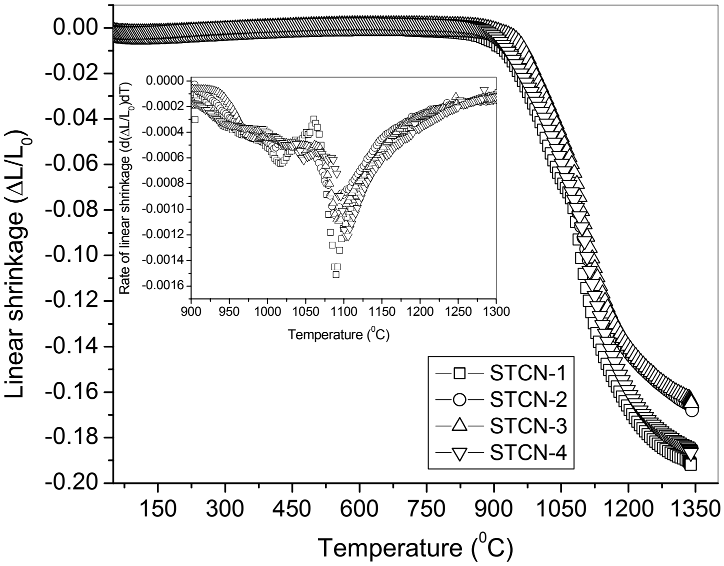

FIG. 4.10 Plots for the linear shrinkage (ΔL/L$_0$) and rate of linear shrinkage (d(ΔL/L$_0$)/dT) (inset) as a function of temperature for the samples: STCN-1, STCN-2, STCN-3 and STCN-4.

Table VIII. Maximum shrinkage rate temperature for Nb_2O_5 doped series.

Sample identification	T_M (ºC)
STCN-1	1089
STCN-2	1092
STCN-3	1097
STCN-4	1103

Fig 4.10 shows the linear shrinkage (ΔL/L$_0$) and the rate of linear shrinkage (d(ΔL/L$_0$)/dT) (inset) as a function of temperature for the samples: STCN-1, STCN-2, STCN-3 and STCN-4. From the linear shrinkage curves it was observed that the shrinkage starts at the temperature around 900 ºC and completed at the maximum temperature of 1220 ºC for all the samples. The

maximum shrinkage rate temperature (T_M) was taken from the linear shrinkage rate against temperature plot. Small increase in T_M values was observed with increase in concentration of Nb_2O_5 as given in *Table VIII*.

4.5.3 X-ray powder diffraction

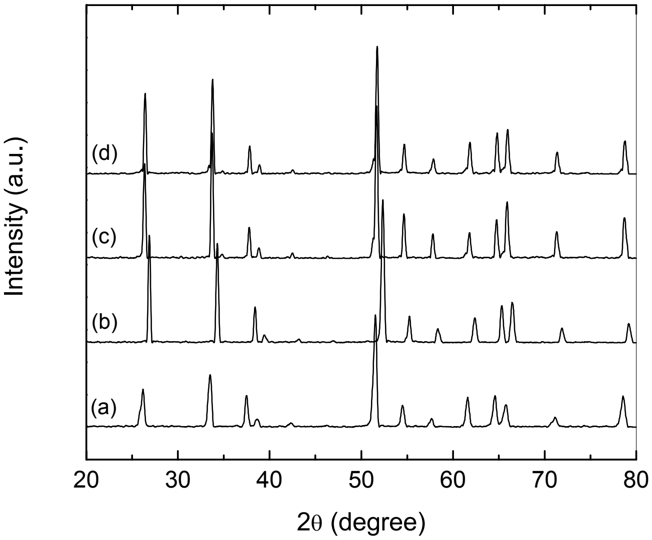

FIG. 4.11 X-ray powder diffraction patterns of sintered samples: (a) STCN-1, (b) STCN-2, (c) STCN-3 and (d) STCN-4.

Table IX. Lattice parameters for Nb_2O_5 doped series.

Lattice parameter (Å)	Sample identification			
	STCN-1	STCN-2	STCN-3	STCN-4
a	4.721	4.716	4.723	4.725
c	3.171	3.166	3.170	3.172

Fig 4.11 shows the X-ray diffraction patterns (XRD) recorded for the samples: (a) STCN-1, (b) STCN-2, (c) STCN-3 and (d) STCN-4. All the lines were correspond to tetragonal rutile SnO_2 phase. The concentrations of dopants added

were too small to be detected by X-rays. No additional peaks due to added constituents were seen in the diffraction patterns. The lattice parameters calculated by least squares method are given in *Table IX*. The ionic radius of the dopant Nb^{5+} (0.69 Å) added is smaller than that of Sn^{4+} (0.74 Å) and hence Nb^{5+} ions occupy the lattice positions. Since no liquid phase forming materials were added (like Bi), no separate phases were formed.

4.5.4 Scanning electron microscopy

The scanning electron micrographs of the fracture surfaces for the samples (a) STCN-1, (b) STCN-2, (c) STCN-3 and (d) STCN-4 sintered at 1300 °C for 4 hr are shown in *Fig 4.12*. The average grain sizes obtained from the micrographs for the samples STCN-1, STCN-2, STCN-3 and STCN-4 were 8, 7, 8 and 6 µm respectively (*Table VII*). The grain size has a clear effect on the current-voltage characteristics of the varistor. The breakdown field decreases with increase in grain size. In this case, the grain size decreases with increase in Nb concentration, which was confirmed from the increase in breakdown field. Clear separations of individual grains were observed and no voids were seen in the micrographs resulting in higher density of the materials. Even though no grain boundary phase from the added constituent was found in the micrograph, the grain boundary phase was conformed by the impedance analysis, as discussed in *section 4.6*

In typical ZnO and TiO_2 varistors, the grain boundary phases are generally observed in the micrographs. But in this SnO_2 varistor, no clear grain boundary phases were seen. This may be due to the absence of low temperature melting dopants like Bi_2O_3 and the known effect of liquid phase sintering.

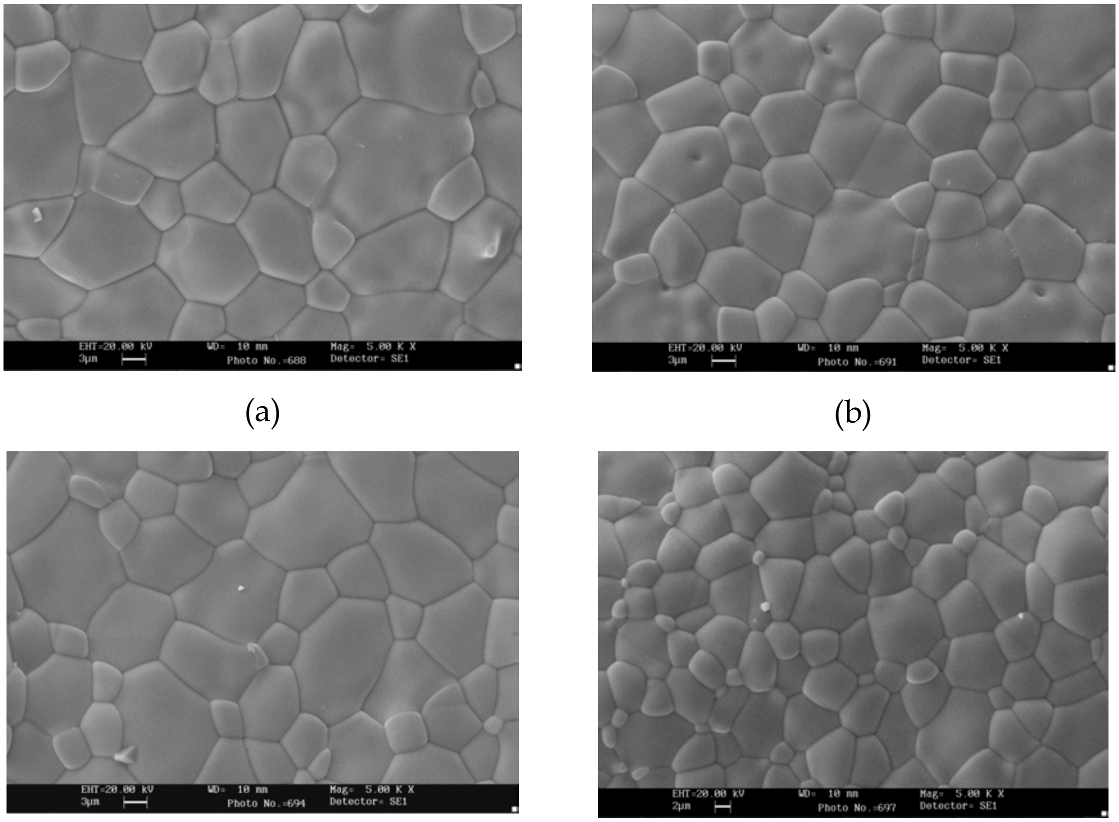

(a) (b)

(c) (d)

FIG. 4.12 Scanning electron micrographs of the fractured surfaces for the samples: (a) STCN-1, (b) STCN-2, (c) STCN-3 and (d) STCN-4 sintered at 1300 °C for 4 hrs.

4.6 Impedance analysis

4.6.1 Nyquist plot

The ac impedance analysis of the samples: STCA-2, STCTa-2 and STCN-3 were done in the frequency range of 0.1 Hz to 1 MHz with an ac amplitude voltage of 100 mV. *Fig 4.13 (a), (b)* and *(c)* represent the impedance Nyquist plots Z' (real resistance) Vs. Z'' (imaginary resistance) for the samples: STCA-2, STCTa-2 and STCN-3 respectively recorded at various temperatures. It was difficult to distinguish between the grain and grain boundary contributions because the room temperature measurements lack a proper semicircular nature. Hence, the impedance spectra were recorded up to temperatures 300 °C. As the measurement temperature increases, a clear semicircle emerges due to the decrease in total resistance.

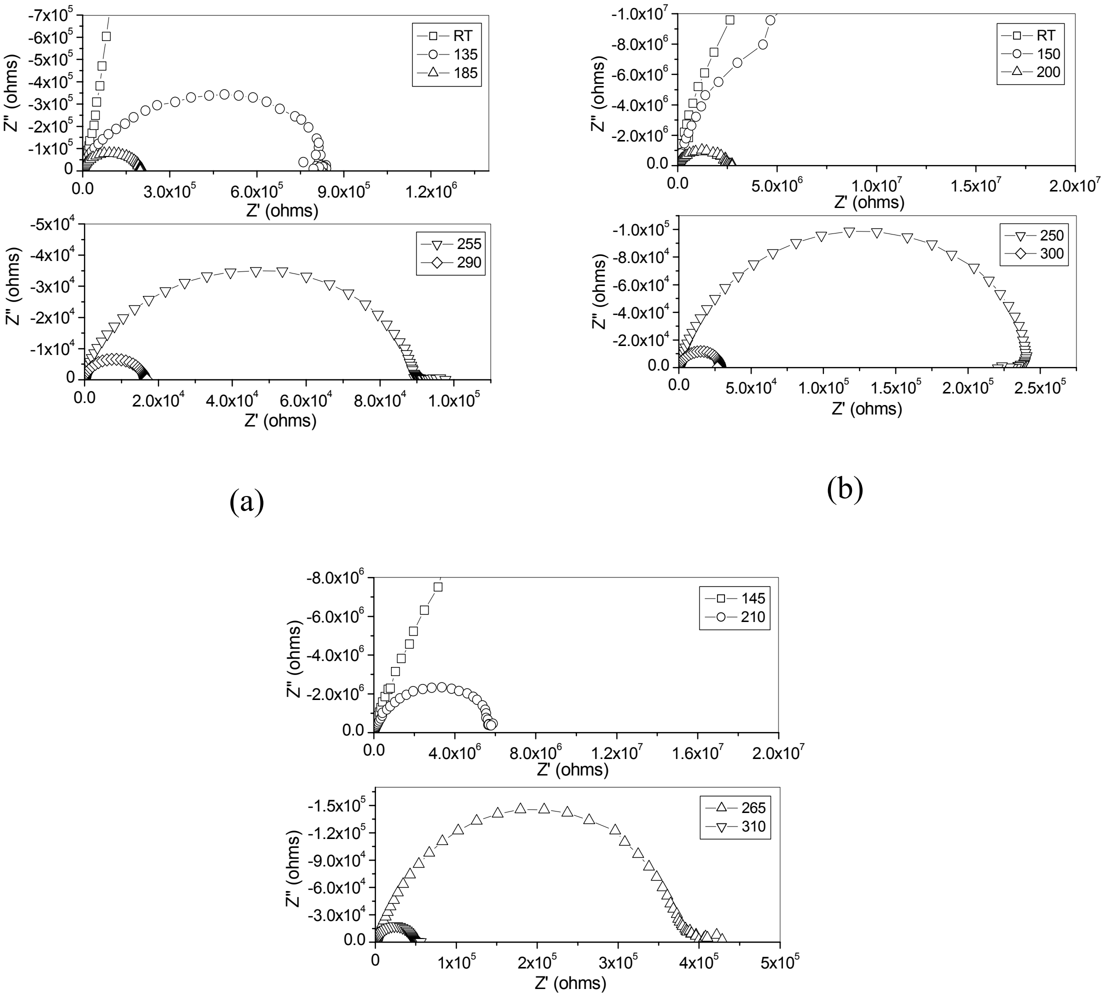

(a)

(b)

(c)

FIG. 4.13 Impedance plots (Z' versus Z") for the samples: (a) STCA-2, (b) STCTa-2 and (c) STCN-3 at different temperatures.

A full semicircle was seen at a temperature greater than 135, 200 and 210 °C for the samples: STCA-2, STCTa-2 and STCN-3 respectively. But these curves failed to give an expected semicircular nature corresponding to the grains at higher frequency side. This was due to the fact that the grain boundary contribution to the total resistance was very large compared to that of grain. Hence, the semicircle corresponding to grain was submerged in the circle representing the grain boundaries. Therefore, separating out the individual components by fitting the semicircle was not possible and the Bode diagrams were plotted to analyze the above data.

4.6.2 Bode plot

Bode plot represents the log of resistivity (ρ) against log frequency (f) for the sample STCA-2, STCTa-2 and STCN-3 in *Fig 4.14 (a), (b)* and *(c)* respectively. To separate out the grain and grain boundary contributions the approximation used by Longo *et al.* [9] was applied. The lowest frequency point was taken as the grain boundary resistivity (ρ_{gb}) and the highest frequency point as grain resistivity (ρ_g), are given in *Table X*. The decrease in grain boundary resistance with increase in temperature was the indication for second phase at the grain boundary. The grain and grain boundary resistivity values are given in *Table X*.

Fig 4.14 shows drastic drop in resistivity values with increase in frequency. This itself was evidence for the presence of grain boundary phase between the grains. At low frequency, the sample exhibits a capacitor like behavior; grain-grain boundary-grain structure giving high resistance to current flow. As the frequency increases, the resistance drastically decreases i.e. the capacitive impedance. Generally, at the higher frequency, the impedance corresponding to grain boundary is negligible and the total resistivity is controlled by the change in phase with frequency. This observation was also noted from the *Fig 4.15 (a), (b)* and *(c)* for the samples STCA-2, STCTa-2 and STCN-3 respectively. The phase angle was 0 ° at low frequency, but at the highest frequency point it has changed to 90 °. This was also an indication for a capacitance like behavior. The phase angle dependence of frequency was justified the conclusion of the formation of the grain boundary.

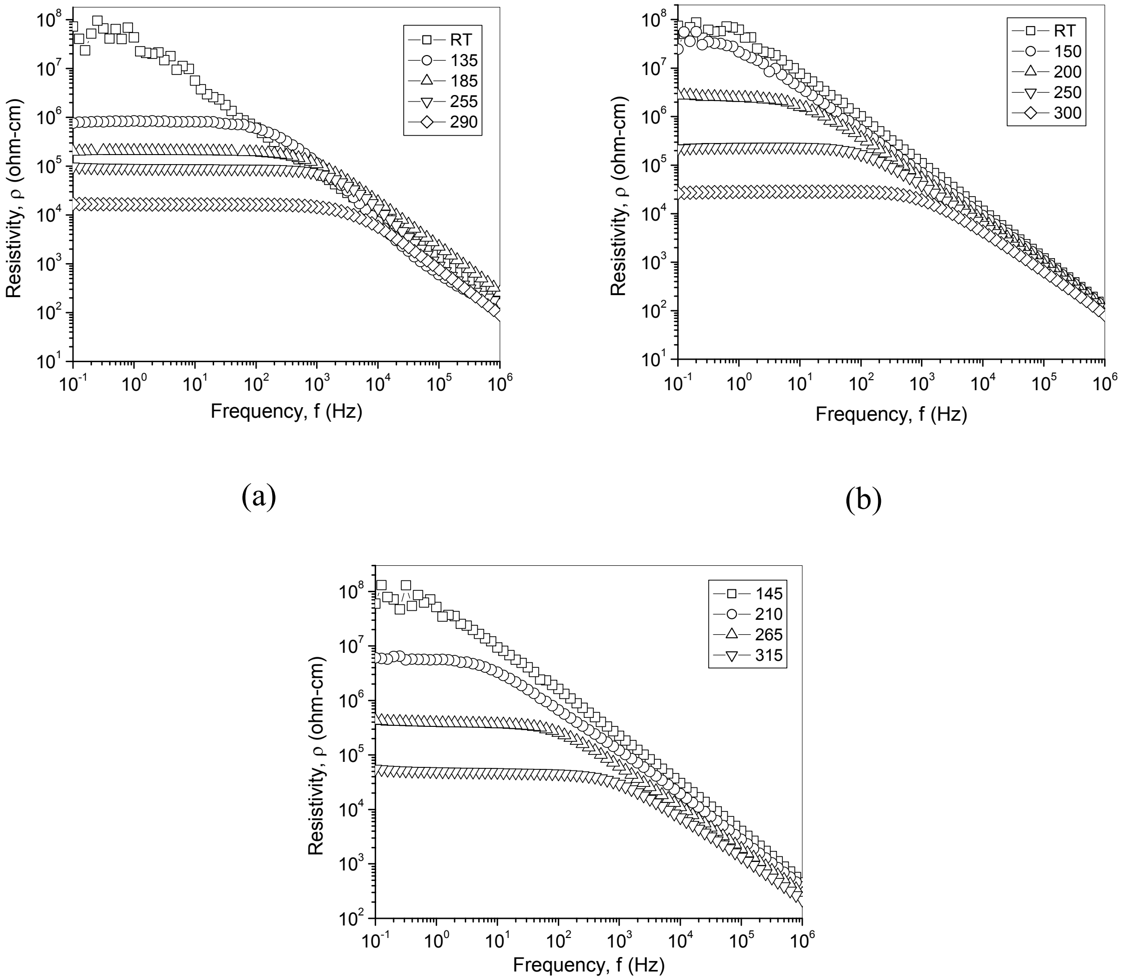

(a)

(b)

(c)

FIG. 4.14 Bode plots of log resistivity against log frequency for the samples: (a) STCA-2, (b) STCTa-2 and (c) STCN-3 at different temperatures.

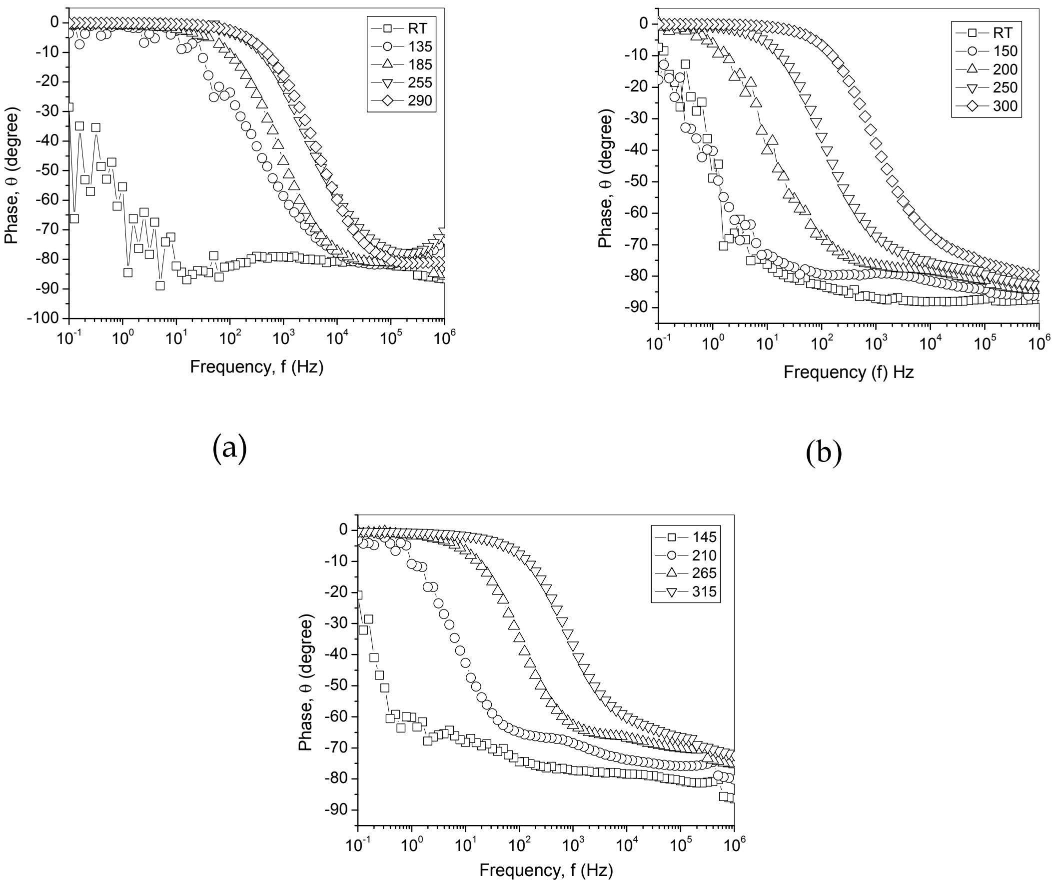

(a)

(b)

(c)

FIG. 4.15 Bode plots of phase (θ) against frequency for the samples: (a) STCA-2, (b) STCTa-2 and (c) STCN-3 at different temperatures.

4.6.3 Relaxation time

Fig 4.16 (a), (b) and *(c)* show the Z" (imaginary resistance) against frequency for the samples: STCA-2, STCTa-2 and STCN-3 respectively. The f_{max} was taken from the plots and relaxation time was calculated by using the relation, $\Gamma = 1/2\pi f_{max}$ (*Table X*). The relaxation time was found to vary from 10^{-5} to 10^{-2} s depending upon compositions, indicating the presence of temperature dependent relaxing defects in the sample. The shift of f_{max} towards the high frequency side with temperature indicated the presence of space charge effect in the samples.

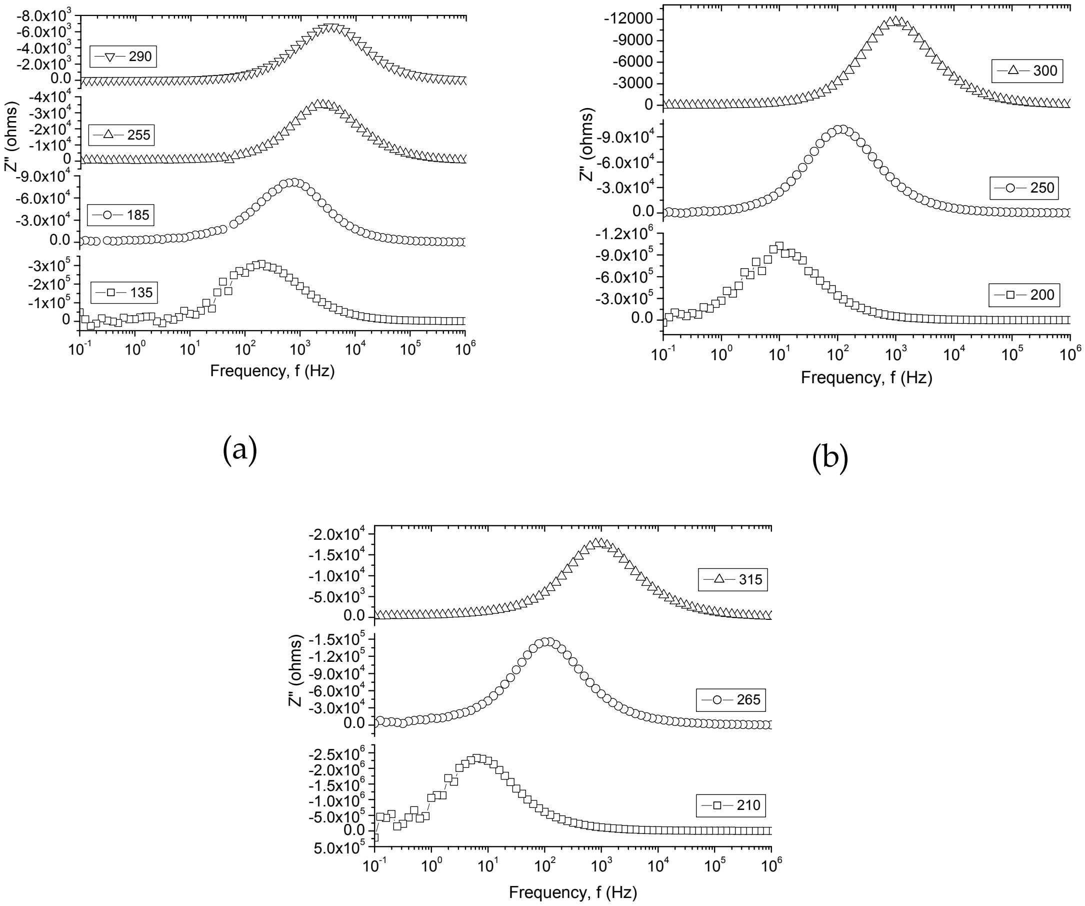

(a)

(b)

(c)

FIG. 4.16 Z" against frequency plots for the samples: (a) STCA-2, (b) STCTa-2 and (c) STCN-3 at different temperatures.

4.7 Arrhenius plot

The grain boundary resistivity and temperature are related by the Arrhenius equation. The slope of the curve log grain boundary resistivity (ρ) versus 1000/T gave the value corresponding to E_A/K and hence the activation energy was calculated. The values of activation energies thus calculated from *Fig 4.17* were 0.156, 0.192 and 0.198 eV for the samples: STCA-2, STCTa-2 and STCN-

3 respectively. This was similar to the variation in non-linear coefficient values measured from I-V characteristics. Hence, the large value of grain boundary activation energy pointed out that a better intergranular grain boundary region leads to superior current-voltage characteristics.

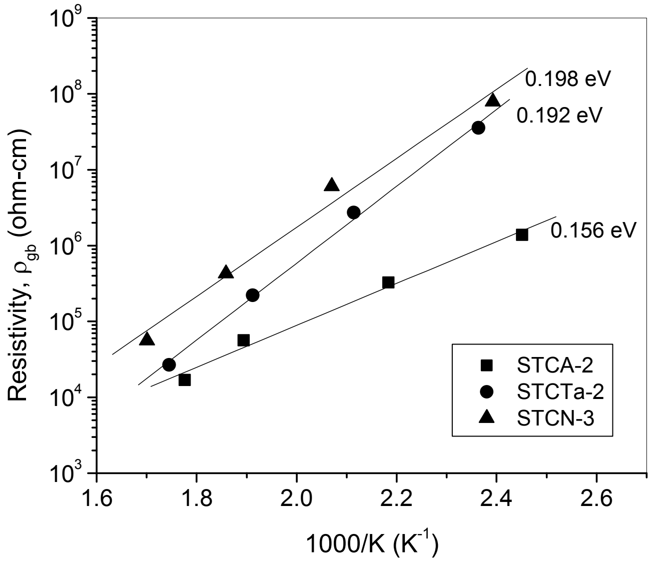

FIG. 4.17 Arrhenius plots (resistivity versus 1000/T) for the samples: STCA-2, STCTa-2 and STCN-3.

Table X. Grain resistivity (ρ_g), grain boundary resistivity (ρ_{gb}), capacitance (C) and relaxation time (Γ) for the samples: STCA-2, STCTa-2 and STCN-3 at various temperatures.

Sample	Temperature (°C)	ρ_g (ohm-cm)	ρ_{gb} (ohm-cm)	C (Farad)	Γ (second)
STCA-2	RT	137.79	4.04×10^7	--	--
	135	136.46	7.60×10^5	6.97×10^{-9}	7.98×10^{-4}
	185	129.23	1.98×10^5	7.08×10^{-9}	2.01×10^{-4}
	255	118.85	9.77×10^4	6.71×10^{-9}	6.34×10^{-5}
	290	90.53	1.69×10^4	5.62×10^{-9}	3.99×10^{-5}
STCTa-2	RT	120.24	5.06×10^7	--	--
	150	113.14	3.58×10^7	--	--
	200	103.59	2.73×10^6	6.48×10^{-9}	1.26×10^{-2}
	250	94.27	2.21×10^5	5.41×10^{-9}	1.26×10^{-3}
	300	82.39	2.67×10^4	5.32×10^{-9}	1.59×10^{-4}
STCN-3	145	456.88	7.87×10^7	--	--
	210	375.97	6.07×10^6	3.62×10^{-9}	2.50×10^{-2}
	265	282.55	4.29×10^5	3.65×10^{-9}	1.26×10^{-3}
	315	219.32	5.61×10^4	3.42×10^{-9}	2.01×10^{-4}

4.8 Discussion

Santos *et al.* [10] recently produced the materials with various electric and microstructural features based on the $Sn_xTi_{1-x}O_2$ polycrystalline system with and without doping. Sousa *et al.* [8] successfully produced $Sn_xTi_{1-x}O_2$-based system with non-linear characteristics of low voltage varistor by doping this binary system with only 0.05 mole % Nb_2O_5.

Both the cell parameters of tetragonal rutile structure decrease with increase in TiO_2 content. This was in accordance with decrease in ionic radius as Sn^{4+} was substituted by Ti^{4+}, when less than 25 % rutile TiO_2 segregates as second phase as reveled by XRD. The solubility of Ti^{4+} in SnO_2 is up to 25 mole % [11]. The dopants added in small quantities do not show as second phases in XRD.

The dopant, D_2O_5 (D = Sb, Ta and Nb) acts as a donor both in SnO_2 and TiO_2. The D^{5+} added in small quantities dissolves in the lattice, replaces Ti^{4+} or

Sn^{4+} to give an extra electron to the conduction process. This increases electronic conductivity if donor was compensated by electron as given in *equation 4.1* or the resistivity will increase if donor was dominantly compensated by the cation vacancies as described by reaction in *equation 4.2*

$$\mathrm{D_2O_5 + SnO_2\ (TiO_2) \longrightarrow 2D^{\cdot}_{Ti}\ (2D^{\cdot}_{Sn}) + 2e' + 4O^{x}_{0} + 1/2O_2(g)} \qquad 4.1$$

$$\mathrm{2D_2O_5 + SnO_2\ (TiO_2) \longrightarrow 4D^{\cdot}_{Sn}\ (4D^{\cdot}_{Ti}) + V''''_{Sn}\ (V''''_{Ti}) + 10O^{x}_{o}} \qquad 4.2$$

During the sintering and cooling processes, the diffusion of molecular oxygen through the grain boundary may occur (*equation 4.3*) and then it can be adsorbed at the interfaces and react with V_{Sn}'''' (V_{Ti}'''') according to *equations 4.4* and *4.6*

$$\mathrm{1/2O_2 \longrightarrow O^{x}_{ad}} \qquad 4.3$$

$$\mathrm{2\,O^{x}_{ad} + V''''_{Sn}\ (V''''_{Ti}) \longrightarrow 2O' + V''_{Sn}\ (V''_{Ti})} \qquad 4.4$$

$$\mathrm{V''_{Sn}\ (V''_{Ti}) + 4O' \longrightarrow 4O'' + V^{x}_{Sn}\ (V^{x}_{Ti})} \qquad 4.5$$

The presence of D_2O_5 generated abundant molecular oxygen, which was adsorbed at the interface and became O' or O'' according to *equations 4.4 and 4.5.* The D^{5+} ions were also expected to increase the conductivity in solid solution. The role of donors (Sb, Ta and Nb) and acceptor (Co) is already discussed in *chapter 3*.

The comparison between with and without TiO_2 (*chapter 3*) showed the noticeable improvement in performance parameters with 5 at. % TiO_2 introduced in SnO_2 matrix. The non-linear coefficient, breakdown field, barrier height and average grain size all the parameters were found to be increased when 5 at. % of TiO_2 is incorporated in SnO_2 matrix. This may be due to slight increase in resistivity by incorporation of 5 at. % TiO_2 in SnO_2 matrix. These parameters are found to be decrease when the sample was sintered for 24 hrs. This was due to increase in grain size with sintering duration from 4 to 24 hrs. The barrier height calculated for the Sb_2O_3 doped samples was in the range of 0.386 to 0.498 eV. The grain boundary resistivity values obtained from impedance data were 4.04×10^7 and 1.69×10^4 ohm-cm at room temperature and 290 °C respectively. These values were higher than that of the corresponding values obtained for the samples having 0 % of TiO_2 (*chapter 3*). The same kind of behavior was also observed in Ta_2O_5 and Nb_2O_5 doped series. Few compositions in the miscibility gap have relative densities > 94 % with respect to the theoretical value due to the Ti atoms present in the SnO_2 matrix. From the above discussion, a certain influence of isovalent Ti^{4+} ions on the performance of SnO_2 based varistor matrix was resolved. The non-linear behavior of I-V plots of this $Ti_{0.05}Sn_{0.95}O_2$ based compositions was assumed to be related to the presence of segregated phase between grains that was undetectable by X-ray diffraction and scanning electron microscopy. It was assumed that the presence of this segregated phase was caused by the beginning of spinodal decomposition as discussed by Bueno *et al.* [12]. The impedance results indicated that the addition of Ti^{4+} to the SnO_2 matrix contributes to the formation of potential barrier acting to increase the concentration of effective barriers and thus leading to the improvement in non-linear properties and the breakdown electric field.

4.8 Summary and conclusions

Depending on the concentration of donor introduced in the matrix and the nature of dopants, this varistor matrix gives rise to better characteristics of high voltage varistor. The non-ohmic properties of this system derived from the presence of D_2O_5 (D = Sb, Ta and Nb probably responsible for the grain conductivity) are analogous to that of the SnO_2 based varistor system.

The impedance analysis revealed the second phase segregation in the grain boundary region. It was also pointed out that, similar to the SnO_2 based varistor system, a high non-ohmic behavior could be obtained in the $Ti_{0.05}Sn_{0.95}O_2$ based varistor system.

References

1. Jarzebski Z M and Marton J P, *J. Electrochem. Soc.* **129**, 299C (1976)
2. **(a)** Zakrzewska K, Radecka M and Rekas M, *Thin Solid Films* **310**, 161 (1997) **(b)** Radecka M, Zakrzewska K and Relas M, *Sensors Actuators B* **47**, 194 (1998)
3. Yan M F and Rhodes W W, *Appl. Phys. Lett.* **40**, 536 (1982)
4. Yang S L and Wu J M, *J. Am. Ceram. Soc.* **76**, 145 (1993)
5. Gopel W and Shierbaum K D, *Sensors and Actuators B*, **26**, 1 (1995)
6. Bueno P R, Camargo E, Longo E, Leite E, Pianaro S S and Varela J A, *J. Mater. Sci. Lett.* **15**, 2048 (1996)
7. **(a)** Castro M S and Aldao C M, *J. Eur. Ceram. Soc.* **18**, 2233 (1998) **(b)** Cerri J A, Leite E R, Gouvea D and Longo E, *J. Am. Ceram. Soc.* **79**, 799 (1996)
8. Sousa V C, Santos M R C, Barrado C M, Bomio M R D, Leite E R, Varela J A and Longo E, *J. Mater. Sci. Mater. Electron.* **15**, 665 (2004)
9. Bueno P R, Pianaro S R, Pereira E C, Bulhoes L O S, Longo E and Varela J A, *J. Appl. Phys.* **84**, 3710 (1998)
10. Santos M R C, Bueno P R, Longo E and Varela J A, *J. Am. Ceram Soc.* **83**, 282 (2002)
11. Ravi V and Date S K, *Bull. Mater. Sci.* **24**, 483 (2001)
12. Bueno P R, Santos M R C, Simoes L G P, Gomes J W, Longo E and Varela J A, *J. Am. Ceram. Soc.* **85**, 282 (2002)

Chapter 5

Influence of rare earth

The variation in the non-linear current (I)- voltage (V) characteristic of the system (98.95% SnO_2 + 1% CoO + 0.05% Ta_2O_5) (all in at. %) due to the incorporation of a rare earth oxide such as Y_2O_3, La_2O_3 and CeO_2 in small quantities (0.05 to 0.5 at. %) is investigated thoroughly in this chapter. It was proposed that due to ionic radius mismatch from stannic ion, rare earth ion would segregate to grain boundaries. The presence of rare earth ion at the grain boundaries leads to the formation of grain boundary defect. The change in grain size and grain boundary barrier height (Φ_B) was studied as a function of the quantity of the rare earth introduced. X-ray powder diffraction (XRD), thermal mechanical analyzer (TMA) and scanning electron microscopy (SEM) were used for physico-chemical characterizations of samples. Impedance analysis was done to reveal the grain boundary phase contributions to the electrical properties of the samples.

5.1 Introduction

The basic varistor system with various donors has been dealt in the previous chapter. Since the varistor property originates from grain boundary modulation, the modifications of grain boundaries will alter the final non-linear electrical properties. There are two ways to incorporate additives into grain boundaries. The first one is by use glass form in system such as SiO_2. The second method is to introduce large ionic radii elements into bulk, so that it segregates due to size misfit. The influence of large ionic radius element such as rare earth ion is studied thoroughly in this chapter. Since the ionic radius of rare earth ion is much larger than Sn^{4+}, it would prefer the grain boundary site, thereby modifying grain boundary acceptor states. The donors will substitute for Sn ions, which leads to increase in electronic conductivity as discussed in *chapter 3* and modify grain boundaries by oxygen absorptions and occupy the bulk lattice.

It is clearly established that diffusion and mass transport are more rapid along grain boundaries and that grain boundaries generally act as diffusion short circuit. The diffusivity of grain boundaries is greater than that of lattice. Such feature makes possible the enrichment of grain boundaries with oxygen species as was demonstrated mainly in SnO_2 based varistor system [1]. Such enrichment of grain boundaries controls the non-ohmic properties and it is believed to be dependant of grain boundary segregation and/or phase precipitation [2].

The varistor action observed in polycrystalline ZnO ceramics is explained by the presence of Schottky type energy barrier at the grain boundaries. In the present case the acceptor like surface states formed by CoO will lead to formation of energy barrier at the grain boundaries. Small amount of Ta_2O_5 was added to SnO_2 ceramics to promote the substitution of Sn^{4+} for Ta^{5+} leading to an increase of electronic conductivity in the SnO_2 lattice. Antunes *et al.* [3] and Leite *et al.* [4] reported that the oxide dopants with +3 metal valency appear to be more effective to increase the non-linear properties. Oxide dopants with +3 metal valency appears to exert on influence on the microstructure similar to that observed when Bi_2O_3 [5], Cr_2O_3 [6] Al_2O_3 [7] is added to the SnO_2-CoO-Nb_2O_5 system. Al_2O_3 was also used as donor in ZnO varistor [8]. Very few reports on the rare earth elements like La, Ce, Pr, Nd on SnO_2 varistor are available in literature [9].

5.2 Experimental results and analysis

SnO_2 containing additives was prepared by the ceramic method as well as by modified coprecipitation method. The SnO_2 along with dopants such as CoO, Ta_2O_5, Y_2O_3, La_2O_3 and CeO_2 in the stoichiometric ratio were mixed, ground well and calcined at 1200 ^oC for 24 hrs. The calcined powders were again ground and fired at 1200 ^oC for another 24 hrs. The series of compositions were prepared of SnO_2 with respect to concentration of rare earth to study the influence of it. The prepared molar compositions were, series (SCTaY); (98.95-x)% SnO_2 + 1% CoO + 0.05% Ta_2O_5 + x% Y_2O_3, series (SCTaL); (98.95-x)% SnO_2 + 1% CoO + 0.05% Ta_2O_5 + x% La_2O_3 and series (SCTaCe); (98.95-x)% SnO_2 + 1% CoO + 0.05% Ta_2O_5 + x% CeO_2 where x = 0.05, 0.1 and 0.5 at. %. The calcined powders were mixed with a binder, 2 wt. % poly vinyl alcohol and pelletized (15 mm dia, 1 mm thick) at 2-3 metric tons. The pellets were sintered at 1300 ^oC for 4 hrs. The sintered pellets were polished and ohmic silver contacts were obtained by Ag-paste and annealed at 600 ^oC for 30 minutes. The samples were identified as SCTaX-05, SCTaX-1 and SCTaX-5 for 0.05, 0.1 and 0.5 at. % X-oxide respectively (where, X= Y, La and Ce for Y_2O_3, La_2O_3 and CeO_2 respectively).

5.3 Y_2O_3 doped series

5.3.1 I-V Characteristics

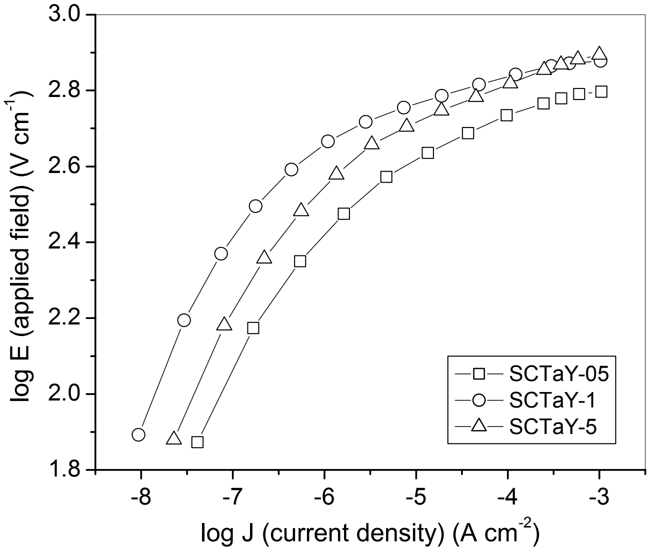

FIG. 5.1a I-V characteristic plots for the samples: SCTaY-05, SCTaY-1 and SCTaY-5 sintered at 1300 °C.

A typical current-voltage characteristic measured on SnO_2 Pellets/compacts. *Fig. 5.1a* shows the current density (J) versus applied field (E) (I-V characteristic) plots for the samples: SCTaY-05, SCTaY-1 and SCTaY-5. The non-linear coefficient (α) calculated from the slopes of the curves in the non-linear region for the samples: SCTaY-05, SCTaY-1 and SCTaY-5 were found to be 16, 21 and 20 respectively. The other performance parameters viz. breakdown field (E_B), density (ρ) and barrier height (Φ_B) of theses SnO_2 compacts are given in *Table I*. The Y_2O_3 as a dopant did not seem to have much impact on the non-linear coefficient. The α value increases by small extent but the breakdown field decreases with the concentration of Y_2O_3 compared to without Y_2O_3 doping. The decrease in breakdown field was in correlation with that of the increase in grain size. The barrier height was slightly changed with breakdown field for different concentration of Y_2O_3. The addition of Y_2O_3 (effective ionic radius [10] of Y^{3+} is 0.9 Å) to the SnO_2-CoO-Ta_2O_5 was expected to segregate at grain boundary. The leakage current for Y_2O_3 doped samples was in the range of 11.7 to 51.6 nA.

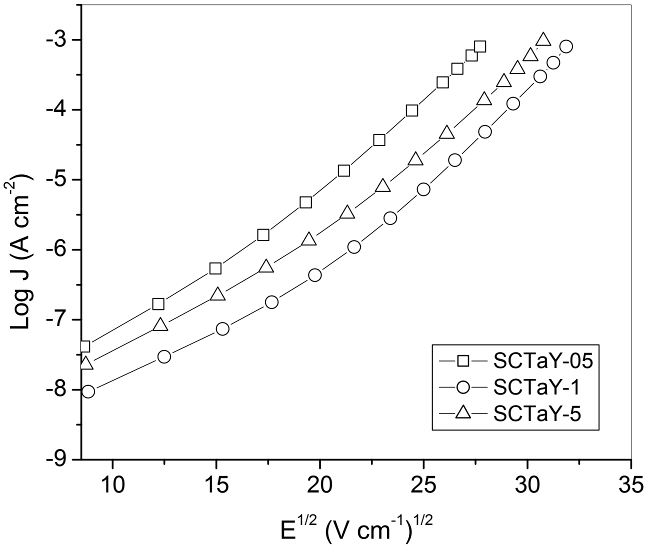

FIG. 5.1b Characteristic plots of log J against $E^{1/2}$ for the samples: SCTaY-05, SCTaY-1 and SCTaY-5 sintered at 1300 °C.

Table I. Characteristic parameters for the samples: SCTaY-05, SCTaY-1 and SCTaY-5

Sample identification	Y_2O_3 (at. %)	α	E_B, V cm^{-1}	Density, gm cm^{-3}	Relative density, %	Φ_B, eV	Average grain size, μm
SCTa	0	15	1270	6.60	94.9	0.414	2
SCTaY-05	0.05	16	769	6.45	92.8	0.409	3
SCTaY-1	0.10	21	1016	6.47	93.1	0.460	4
SCTaY-5	0.50	20	947	6.56	94.4	0.435	4

By considering the Schottky type conduction model, characteristic plots of log J against $E^{1/2}$ as shown in *Fig 5.1b* could be built up to determine the values for β and Φ_B using Richardson's formula (discussed in *chapter 2*). Since Richardson's constant depends on the density of the sample, it varies from material to material, the values calculated for Y_2O_3 doped samples were of the order of 1.808 x 10^6. The values for barrier height (Φ_B) are given in *Table I*.

5.3.2 Sintering behavior

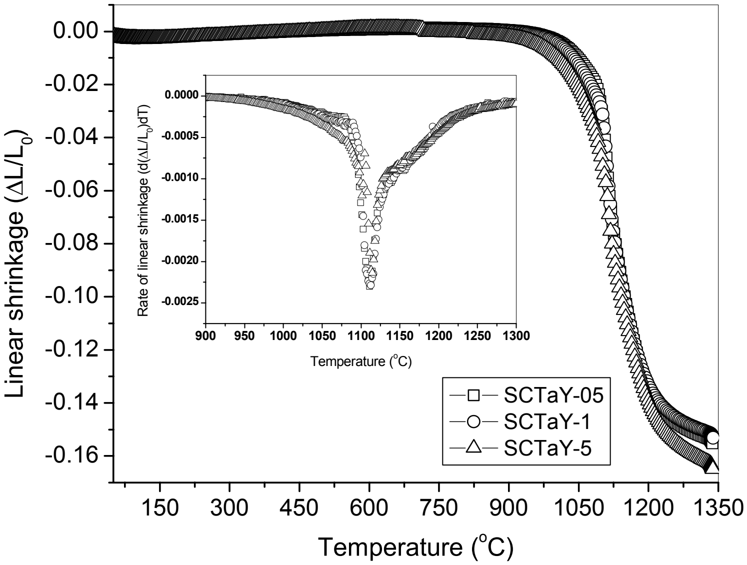

FIG. 5.2 Plots for linear shrinkage ($\Delta L/L_0$) and rate of linear shrinkage ($d(\Delta L/L_0)/dT$) (inset) as a function of temperature for the samples: SCTaY-05, SCTaY-1 and SCTaY-5.

Fig. 5.2 shows the linear shrinkage ($\Delta L/L_0$) and the rate of linear shrinkage ($d(\Delta L/L_0)/dT$) (inset) as a function of temperature for the samples: SCTaY-05, SCTaY-1 and SCTaY-5. From the linear shrinkage curve it was observed that the shrinkage starts at the temperature around 1000 °C and completed at the maximum temperature of 1250 °C. The density calculated for all the pellets was greater than 92 %, with respect to the theoretical density of SnO_2 (6.95 g cm^{-3}). The calculated density values for these pellets are given in *Table I.* The maximum shrinkage rate temperature (T_M) was taken from the linear shrinkage rate against temperature plot, comparatively not much difference was found in T_M values as given in *Table II*.

Table II. Maximum shrinkage rate temperature for Y_2O_3 doped series.

Sample identification	T_M (ºC)
SCTaY-05	1110
SCTaY-1	1111
SCTaY-5	1114

5.3.3 Powder x-ray diffraction

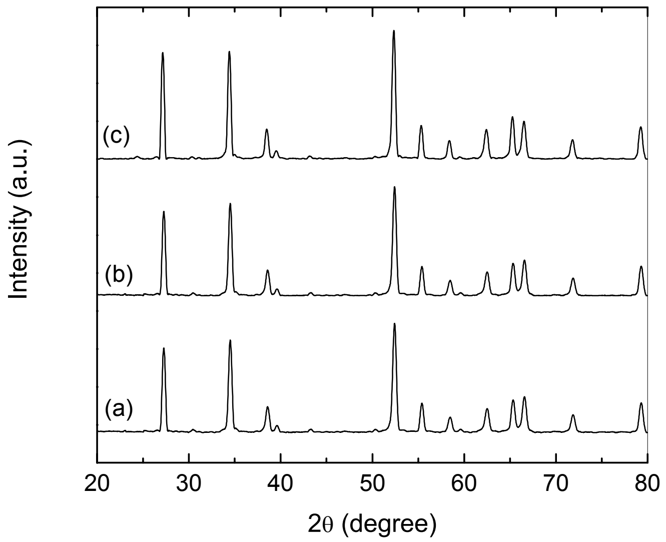

FIG. 5.3 X-ray powder diffraction pattern of sintered samples: (a) SCTaY-05, (b) SCTaY-1 and (c) SCTaY-5.

Fig. 5.3 shows the X-ray diffraction patters (XRD) recorded for the samples (a) SCTaY-05, (b) SCTaY-1 and (c) SCTaY-5. Apparently no second phases were found and all the peaks were correspond to SnO_2 tetragonal rutile phase. Since concentrations of Y_2O_3 and other dopants added were too small to be detected by

X-rays, the diffraction peaks correspond to them were not found. The lattice parameters calculated by least squares method are given in *Table III*.

Table III. Lattice parameters for Y_2O_3 doped series.

Lattice parameter (Å)	Sample identification		
	SCTaY-05	SCTaY-1	SCTaY-5
a	4.735	4.726	4.736
c	3.186	3.177	3.188

5.3.4 Scanning electron micrograph

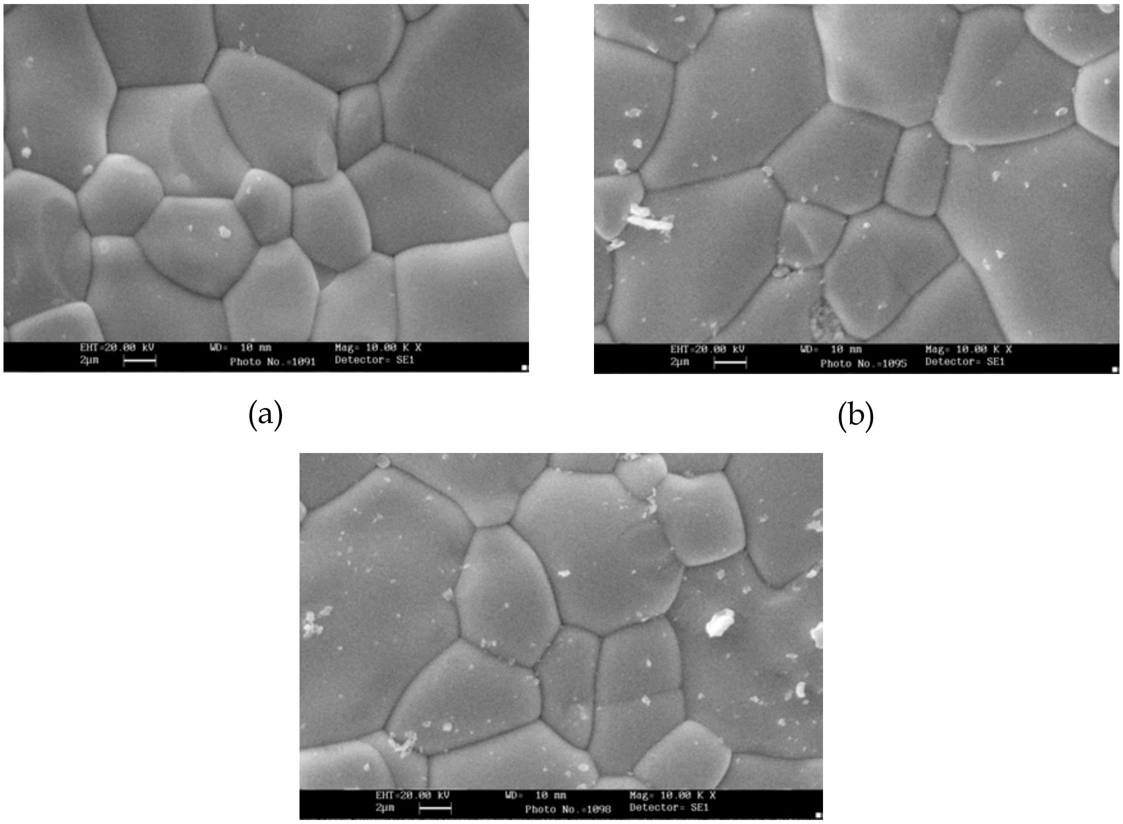

(a) (b)

(c)

FIG. 5.4 Scanning electron micrographs of the fractured surfaces for the samples: (a) SCTaY-05, (b) SCTaY-1 and (c) SCTaY-5 sintered at 1300 °C.

To understand the grain-grain boundary microstructure and to determine the grain size, the scanning electron micrographs of the fractured surfaces of the pellets were taken after gold coating on the surface. The micrographs for the samples: (a) SCTaY-05, (b) SCTaY-1 and (c) SCTaY-5 are shown in *Fig. 5.4*. The average grain sizes obtained from the micrographs were 3, 4 and 4 μm for the samples SCTaY-05, SCTaY-1 and SCTaY-5 respectively (*Table I*). The grain size has a clear effect on the current-voltage characteristic of the varistor. The breakdown voltage decreases with increase in grain size. No grain boundary phase from the added constituents was seen in the micrograph, but the contribution of the second phase to the electrical property was confirmed by the impedance analysis as discussed in *section 5.6*.

5.4 La_2O_3 doped series

5.4.1 I-V characteristics

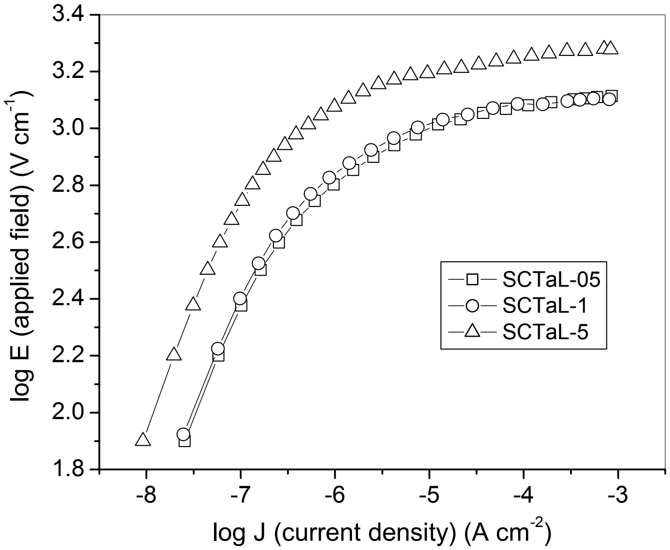

FIG. 5.5a I-V characteristic plots for the samples: SCTaL-05, SCTaL-1 and SCTaL-5 sintered at 1300 °C.

Fig. 5.5a shows the current density (J) versus applied field (E) (I-V characteristic) for the samples: SCTaL-05, SCTaL-1 and SCTaL-5. The non-linear coefficient (α) calculated from the slopes of the curves in the non-linear region for the samples: SCTaL-05, SCTaL-1 and SCTaL-5 were found to be 25, 27 and 30 respectively. The other performance parameters: breakdown field (E_B), density (ρ) and barrier height (Φ_B) are given in *Table IV*. The effective ionic radius [10] of La^{3+} (1.032 Å) is larger than that of Sn^{4+} (0.74 Å), hence it preferably segregates at grain boundary and enables to form grain boundary barriers, which was resulted into higher α value. The breakdown field as given in *Table IV*, was higher for all the La_2O_3 doped samples, if compare to the original sample with 0 at. % La_2O_3 (1270 V cm^{-1}). The leakage current (I_l) for La_2O_3 doped samples was in the range of 11.6 to 31.3 nA. Considering the Schottky type conduction model, plots of log J against $E^{1/2}$ (*Fig. 5.5b*) could be built up to determine value for β and Φ_B using Richardson's formula. The value for Richardson's constant for La_2O_3 doped samples was of the order of 1.819 x 10^6. The values for barrier height (Φ_B) are given in *Table IV*.

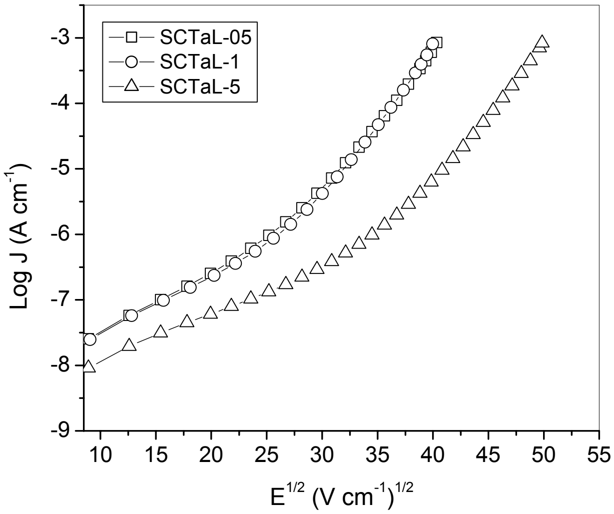

FIG. 5.5b Characteristic plots of log J against $E^{1/2}$ for the samples: SCTaL-05, SCTaL-1 and SCTaL-5 sintered at 1300 °C.

Table IV. Characteristic parameters for the samples: SCTaL-05, SCTaL-1 and SCTaL-5

Sample identification	La_2O_3 (at. %)	α	E_B, V cm^{-1}	Density, gm cm^{-3}	Relative density, %	Φ_B, eV	Average grain size, μm
SCTaL-05	0.05	25	1598	6.57	94.6	0.462	2
SCTaL-1	0.10	27	1627	6.51	93.7	0.483	2
SCTaL-5	0.50	30	2484	6.53	94.0	0.5022	2

5.4.2 Thermal Mechanical Analysis

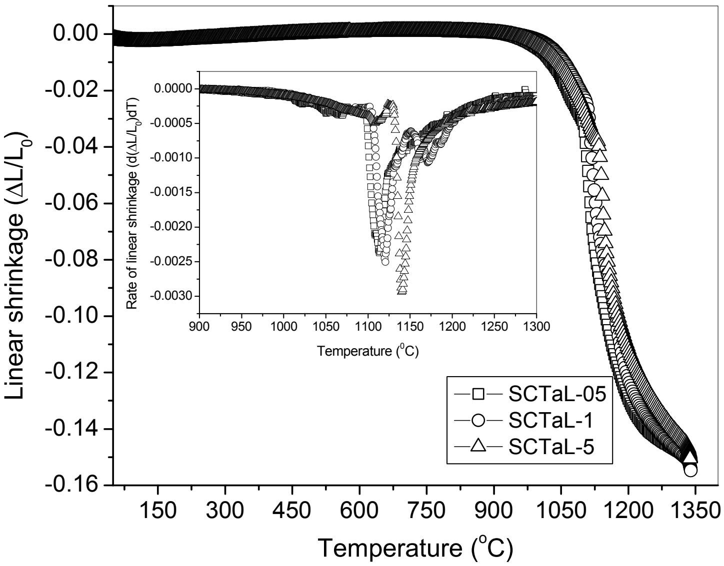

FIG. 5.6 Plots for linear shrinkage ($\Delta L/L_0$) and rate of linear shrinkage ($d(\Delta L/L_0)/dT$) (inset) as a function of temperature for the samples: SCTaL-05, SCTaL-1 and SCTaL-5.

Fig. 5.6 shows the plots for the linear shrinkage ($\Delta L/L_0$) and the rate of linear shrinkage ($d(\Delta L/L_0)/dT$) (inset) as a function of temperature for the samples: SCTaL-05, SCTaL-1 and SCTaL-5. The complete densification can be seen from the curves for all the samples. From the linear shrinkage curve it was observed that the shrinkage starts at the temperature around 1000 °C and completed at the maximum temperature of 1250 °C. The density for the La_2O_3 added compacts was high as given in *Table IV*. The maximum shrinkage rate temperature (T_M) was taken from the linear shrinkage rate against temperature plots. Increase in T_M was observes with the increase in concentration of La_2O_3 values as given in *Table V*.

Table V. Maximum shrinkage rate temperature for La_2O_3 doped series.

Sample Identification	T_M (°C)
SCTaL-05	1114
SCTaL-1	1121
SCTaL-5	1141

5.4.3 Powder x-ray diffraction

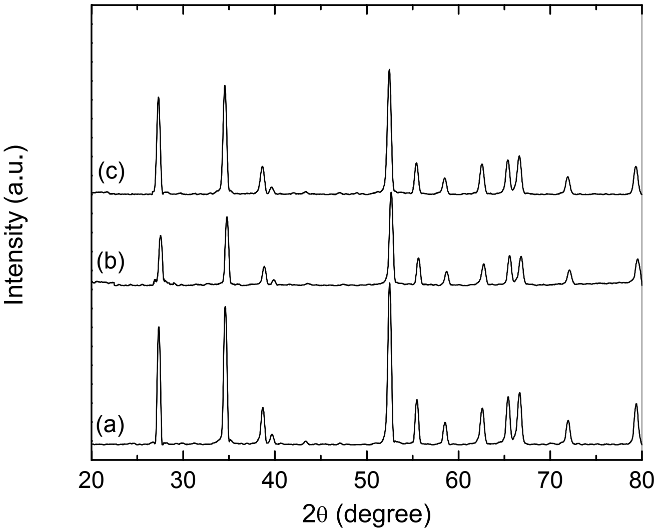

FIG. 5.7 X-ray powder diffraction patterns for sintered samples: (a) SCTaL-05, (b) SCTaL-1 and (c) SCTaL-5.

Fig. 5.7 shows the X-ray diffraction patters (XRD) recorded for the samples: (a) SCTaL-05, (b) SCTaL-1 and (c) SCTaL-5. Apparently no second phases were found and all the lines were correspond to SnO_2 tetragonal rutile phase. It was also to be noted that the concentrations of all the dopants including La_2O_3, added were too small to be detected by X-rays. The lattice parameters calculated by least squares method are given in *Table VI*.

Table VI. Lattice parameters for La_2O_3 doped series.

Lattice parameter (Å)	Sample identification		
	SCTaL-05	SCTaL-1	SCTaL-5
a	4.742	4.744	4.740
c	3.192	3.193	3.193

5.4.4 Scanning electron micrograph

To understand the grain-grain boundary microstructure and the grain size determination, scanning electron micrographs of the fractured surface of the pellets were taken. The micrographs for the samples: (a) SCTaL-05, (b) SCTaL-1 and (c) SCTaL-5 are shown in *Fig. 5.8*. The average grain size obtained from the micrographs was 2 μm for all the samples (*Table IV*). A clear separation of individual grains was observed and few abnormally large grains were also seen. The grain size has a clear effect on the current-voltage characteristic of the varistor. The breakdown voltage decreases with increase in grain size. As for La_2O_3 doped samples the average grain is 2 μm for all the samples, hence the grain size had not have any influence on the change in breakdown field. The increase in breakdown field was may be due to the change in resistivity with concentration of La_2O_3. No grain boundary phase from the added constituents found in the micrograph, but the second phase contribution was confirmed by the impedance analysis as discussed in *section 5.6*.

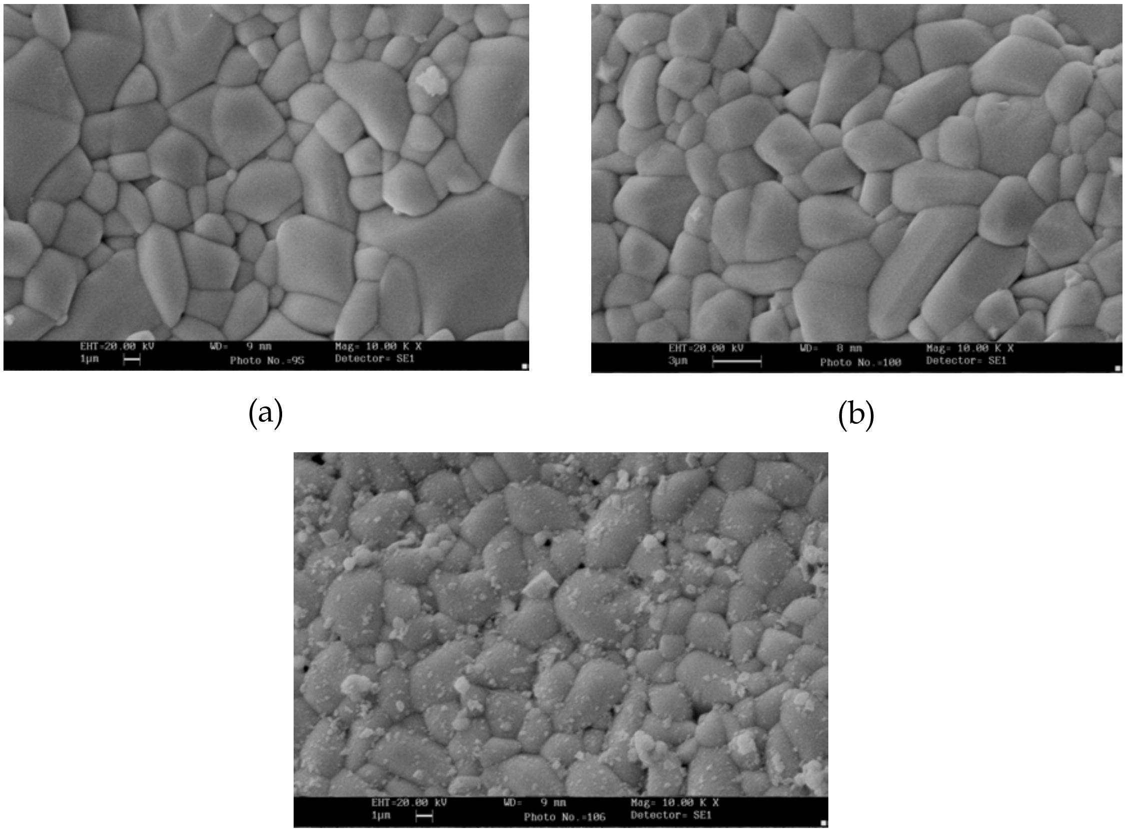

(a) (b)

(c)

FIG. 5.8 Scanning electron micrographs of the fractured surfaces for the samples: (a) SCTaL-05, (b) SCTaL-1 and (c) SCTaL-5 sintered at 1300 °C.

5.5 CeO_2 doped series

5.5.1 I-V characteristics

Fig. 5.9a shows the current density (J) versus applied field (E) (I-V characteristic) plots for the samples: SCTaCe-05, SCTaCe-1 and SCTaCe-5. The non-linear coefficients (α) calculated from the slopes of the curves in the non-linear region for the samples: SCTaCe-05, SCTaCe-1 and SCTaCe-5 were found to be 6, 8 and 18 respectively. The other performance parameters: breakdown field (E_B), density (ρ) and barrier height (Φ_B) are given in *Table VII*. CeO_2 as a dopant has no significant influence on the non-linear values, as compare to Y_2O_3 and La_2O_3. The parameters α and E_B decrease with the increase in concentration of CeO_2. The barrier height was also very low for all the CeO_2 doped samples. This may be due to reason that CeO_2 (effective ionic radius of Ce^{3+} & Ce^{4+} 1.01 Å and 0.87 Å respectively) probably forms a solid solution with SnO_2 in the grain and sufficiently segregates at the grain boundaries but fails to create energy barriers at grain boundaries. For the samples SCTaCe-05 and SCTaCe-1 decrease in resistivity was observed. This may be due to CeO_2 forming solid solution with SnO_2 at lower concentration. The leakage current range for samples SCTaCe-05 and SCTaCe-1 were 22 μA and for the sample SCTaCe-5 it was in the range of 20.8 nA. Considering the Schottky type conduction model, plots of log J against $E^{1/2}$ (*Fig. 5.9b*) can be built up to determine value for β and Φ_B using Richardson's formula. The value for Richardson's constant for CeO_2 doped samples was of the order of 1.830 x 10^6. The values for barrier height (Φ_B) are given in *Table VII*.

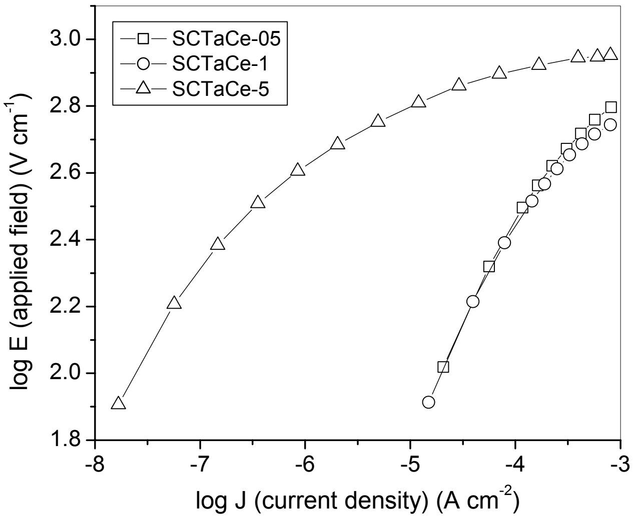

FIG. 5.9a I-V characteristic plots for the samples: SCTaCe-05, SCTaCe-1 and SCTaCe-5 sintered at 1300 °C.

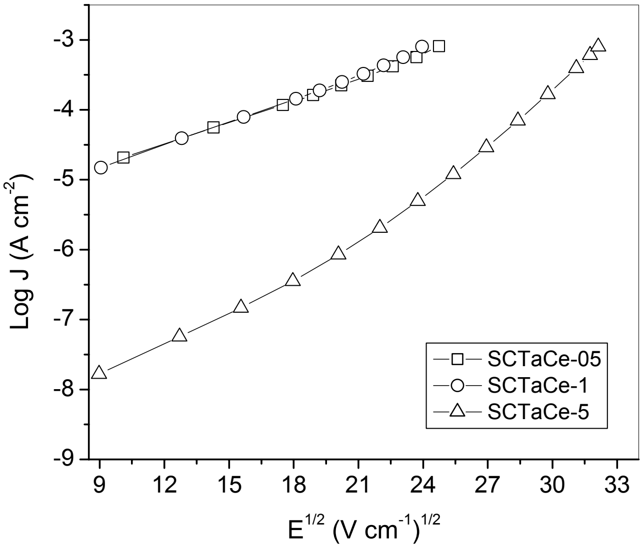

FIG. 5.9b Characteristic plots of log J against E$^{1/2}$ for the samples: SCTaCe-05, SCTaCe-1 and SCTaCe-5 sintered at 1300 °C.

Table VII. Characteristic parameters for the samples: SCTaCe-05, SCTaCe-1 and SCTaCe-5.

Sample identification	CeO_2 (at. %)	α	E_B, V cm^{-1}	Density, gm cm^{-3}	Relative density, %	Φ_B, eV	Average grain size, μm
SCTaCe-05	0.05	6	612	6.60	94.9	0.294	3
SCTaCe-1	0.10	8	574	6.48	93.3	0.287	4
SCTaCe-5	0.50	18	1032	6.55	94.3	0.445	5

5.5.2 sintering behavior

Fig. 5.10 show the plots of linear shrinkage ($\Delta L/L_0$) and the rate of linear shrinkage ($d(\Delta L/L_0)/dT$) (inset) as a function of temperature for the samples: SCTaCe-05, SCTaCe-1 and SCTaCe-5. Complete densification can be seen from the linear shrinkage curve for all the samples. From the linear shrinkage curve it was observed that the shrinkage starts at the temperature around 1000 °C and completed at the maximum temperature of 1250 °C. The density calculated for

CeO_2 doped compacts was greater than 93 % as given in *Table VII*. The maximum shrinkage rate temperature (T_M) was taken from the linear shrinkage rate against temperature plot, comparatively not much difference was found in T_M values as given in *Table VIII*.

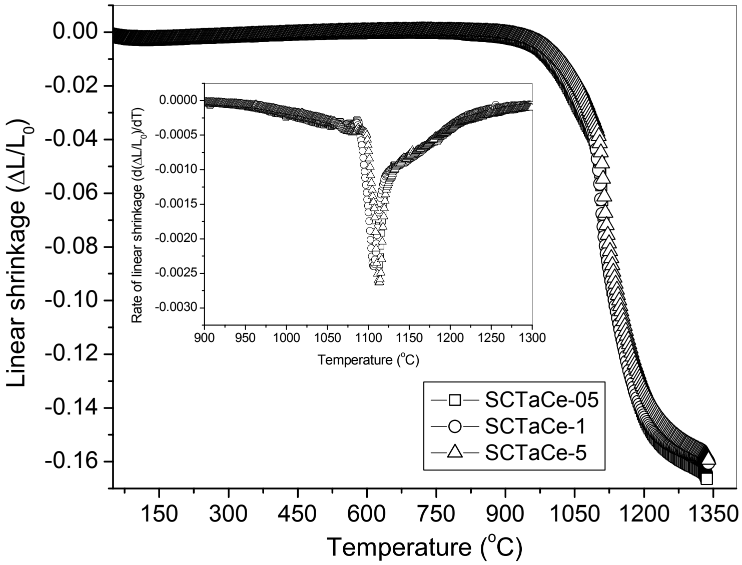

FIG. 5.10 Plots for the linear shrinkage ($\Delta L/L_0$) and rate of linear shrinkage ($d(\Delta L/L_0)/dT$) (inset) as a function of temperature for the samples: SCTaCe-05, SCTaCe-1 and SCTaCe-5.

Table VIII. Maximum shrinkage rate temperature for CeO_2 doped series.

Sample Identification	T_M (°C)
SCTaCe-05	1113
SCTaCe-1	1107
SCTaCe-5	1112

5.5.3 Powder X-ray diffraction

Fig. 5.11 shows the X-ray diffraction patters (XRD) recorded for the samples: (a) SCTaCe-05, (b) SCTaCe-1 and (c) SCTaCe-5. All the X-ray diffraction patterns show only the characteristic peaks corresponding to SnO_2 tetragonal rutile phase. Since the concentrations of dopants added were too small to be detected by X-rays, no peaks corresponding to any secondary phases were seen. Lattice parameters calculated by least squares method are given in *Table IX*.

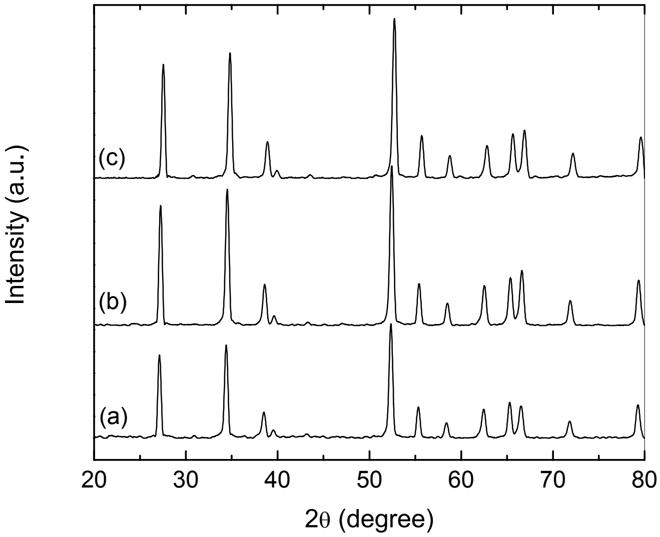

FIG. 5.11 X-ray powder diffraction patterns of sintered samples: (a) SCTaCe-05, (b) SCTaCe-1 and (c) SCTaCe-5.

Table IX. Lattice parameters for CeO_2 doped series.

Lattice parameter (Å)	Sample identification		
	SCTaCe-05	SCTaCe-1	SCTaCe-5
a	4.734	4.737	4.738
c	3.186	3.188	3.189

5.5.4 Scanning electron microscopy

The scanning electron micrographs for the samples: (a) SCTaCe-05, (b) SCTaCe-1 and (c) SCTaCe-5 are shown in *Fig. 5.12*. The average grain size obtained from the micrographs was found to be 3, 4 & 5 µm for SCTaCe-05, SCTaCe-1 and SCTaCe-5 respectively (*Table VII*). The grain size has a clear effect on the current-voltage characteristic of the varistor. The breakdown voltage decreases with increase in grain size. There was a small indication of phase between to separate grains in the micrograph, and this was also confirmed by the impedance analysis discussed in *section 5.6*. The second phase segregation observed in CeO_2 doped samples fails to create energy barriers at grain boundaries, which is playing crucial role in the non-linear current-voltage characteristic.

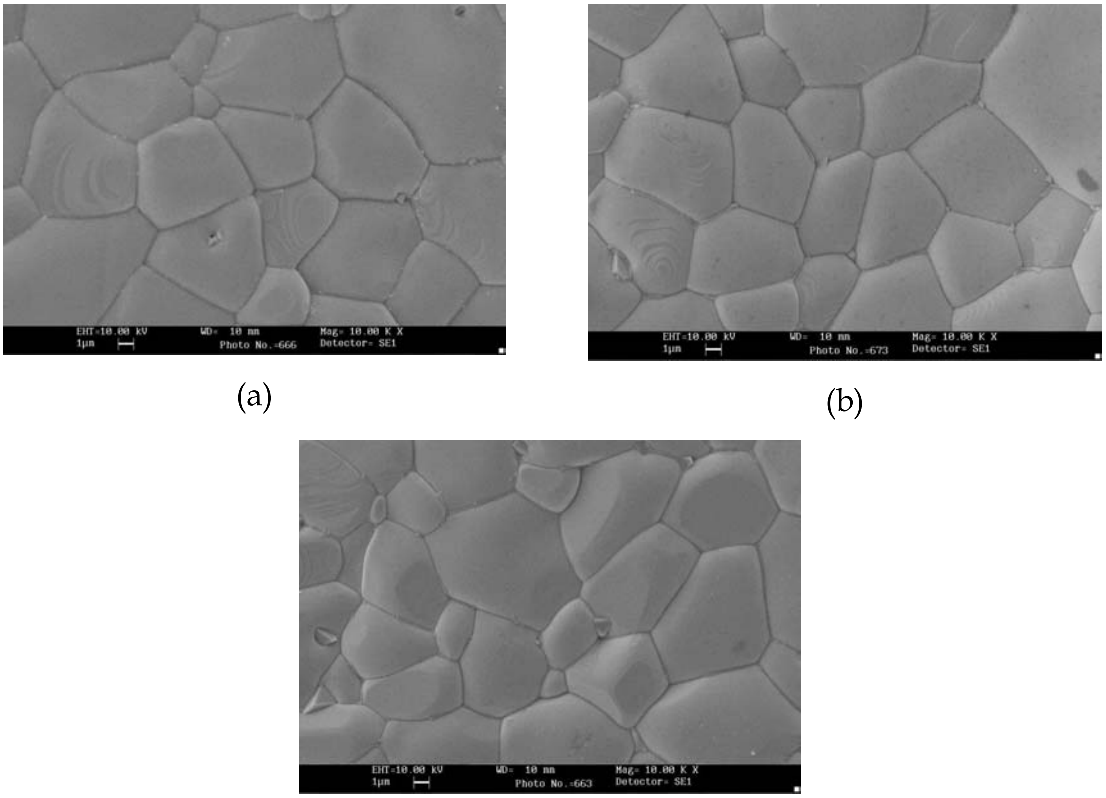

(a)

(b)

(c)

FIG. 5.12 Scanning electron micrographs of the fractured surfaces for the samples: (a) SCTaCe-05, (b) SCTaCe-1 and (c) SCTaCe-5 sintered at 1300 °C.

5.6 Impedance analysis

5.6.1 Nyquist plot

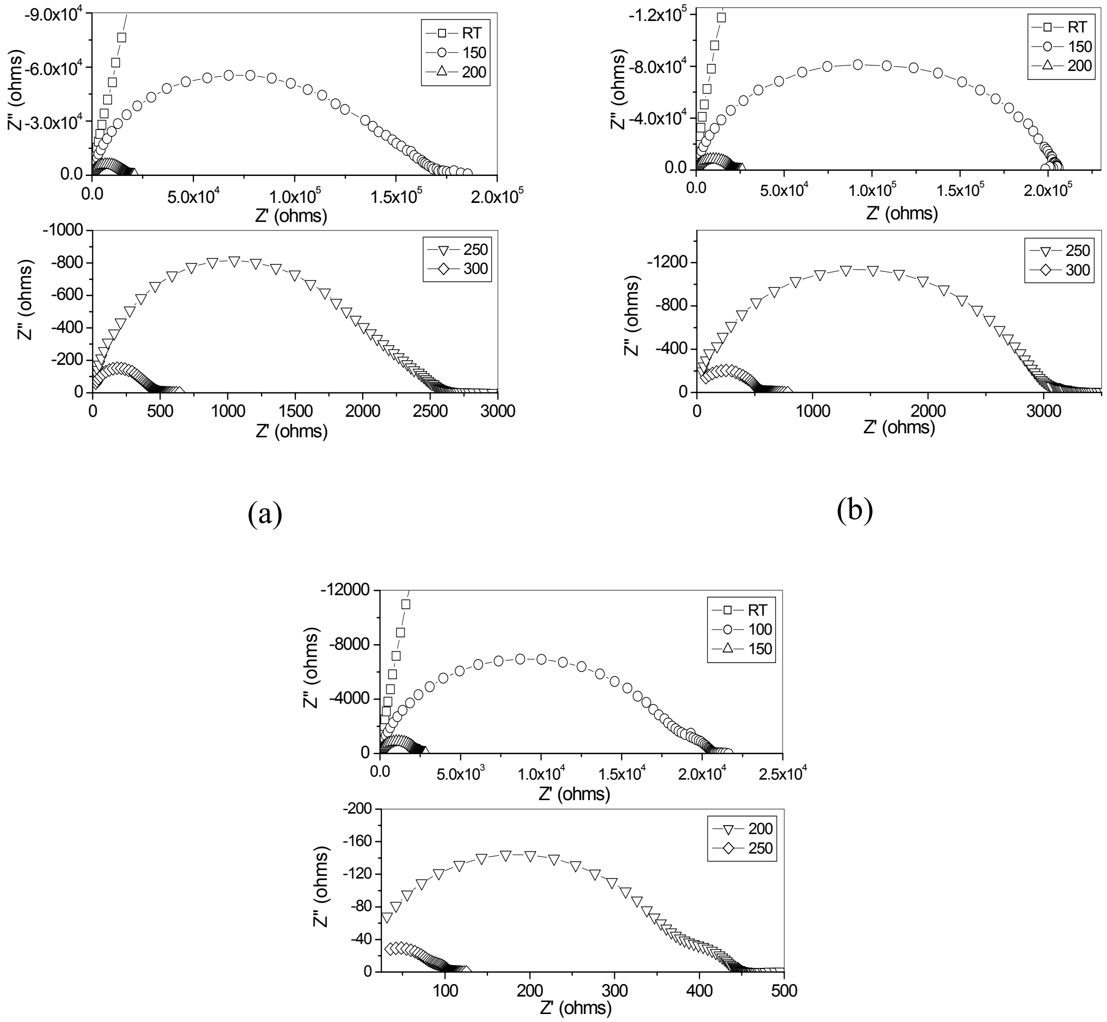

(a)

(b)

(c)

FIG. 5.13 Impedance plot (Z' versus Z") for the samples: (a) SCTaY-1, (b) SCTaL-5 and (c) SCTaCe-1 at various temperatures.

The ac impedance analysis of the samples: SCTaY-1, SCTaL-5 and SCTaCe-1 was done in the frequency range from 0.1 Hz to 1 MHz with an ac amplitude voltage of 100 mV. *Fig. 5.13 (a), (b)* & *(c)* represent the impedance plots

Z' (real resistance) versus Z" (imaginary resistance) at various temperatures for the samples: SCTaY-1, SCTaL-5 and SCTaCe-1 respectively. The room temperature measurement lack a proper semicircular nature and thereby making it difficult to distinguish between the grain and grain boundary contributions. Hence the impedance spectra were recorded at higher temperatures up to 300 ºC. As the measurement temperature increases, a clear semicircle emerges due to the decrease in total resistance. Since the materials were high resistance materials, it was observed that the grain boundary resistance decreases with increase in temperature. A full semicircle was seen at a temperature greater than 150 °C for the samples: SCTaY-1 & SCTaL-5 and 100 °C for SCTaCe-1. Even at high temperature a semicircular like nature at high frequency region represents the grain impedance was absent. This may be due to the considerable difference between grain (~100 ohm) and grain boundary (~10^7 ohm) impedance. Even at 300 °C the grain boundary impedance was considerably larger than that of the grain impedance so that the semicircle correspond to grain at high frequency region may be submerged in the circle represent the grain boundaries. Since the separation of the contribution from grain and grain boundaries was not possible from the above plot, the Bode diagram were plotted to analyze the above data.

5.6.2 Bode plot

Bode plot represent the resistivity (ρ) against frequency (f) on log scale for the samples: SCTaY-1, SCTaL-5 and SCTaCe-1 are shown in *Fig. 5.14 (a) (b)* and *(c)* respectively. The approximation given in *equation 5.1* was taken to separate out the grain and grain boundary contribution.

$\log_{f\to 0}(|\rho|) = \log_{f\to 0}(|\rho_{gb}| + |\rho_g|) = \log_{f\to 0}(\rho_{gb})$

Since $\rho_{gb} >> \rho_g$

$\log_{f\to\infty}(|\rho|) = \log(\rho_g)$ 5.1

The lowest frequency point was taken as the grain boundary resistivity (ρ_{gb}) and the highest frequency point as grain resistivity (ρ_g), the values are given in *Table X*. This was in accordance with the method used by Longo *et al.* [11]. The Bode plot between phase (θ) and log frequency (f) for the same samples: SCTaY-1, SCTaL-5 and SCTaCe-1 are shown in *Fig. 5.15 (a), (b)* and *(c)* respectively.

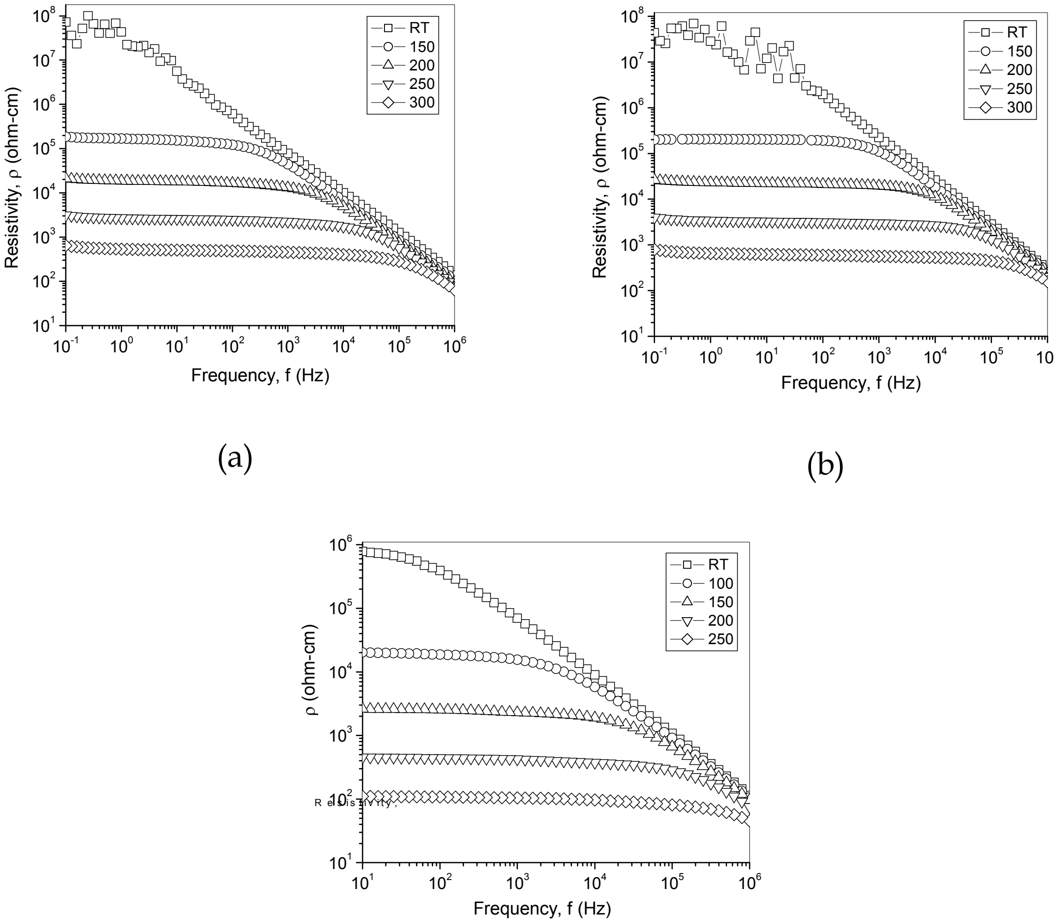

(a)

(b)

(c)

FIG. 5.14 Bode plot of log resistivity against log frequency for the samples: (a) SCTaY-1, (b) SCTaL-5 and (c) SCTaCe-1 at different temperatures.

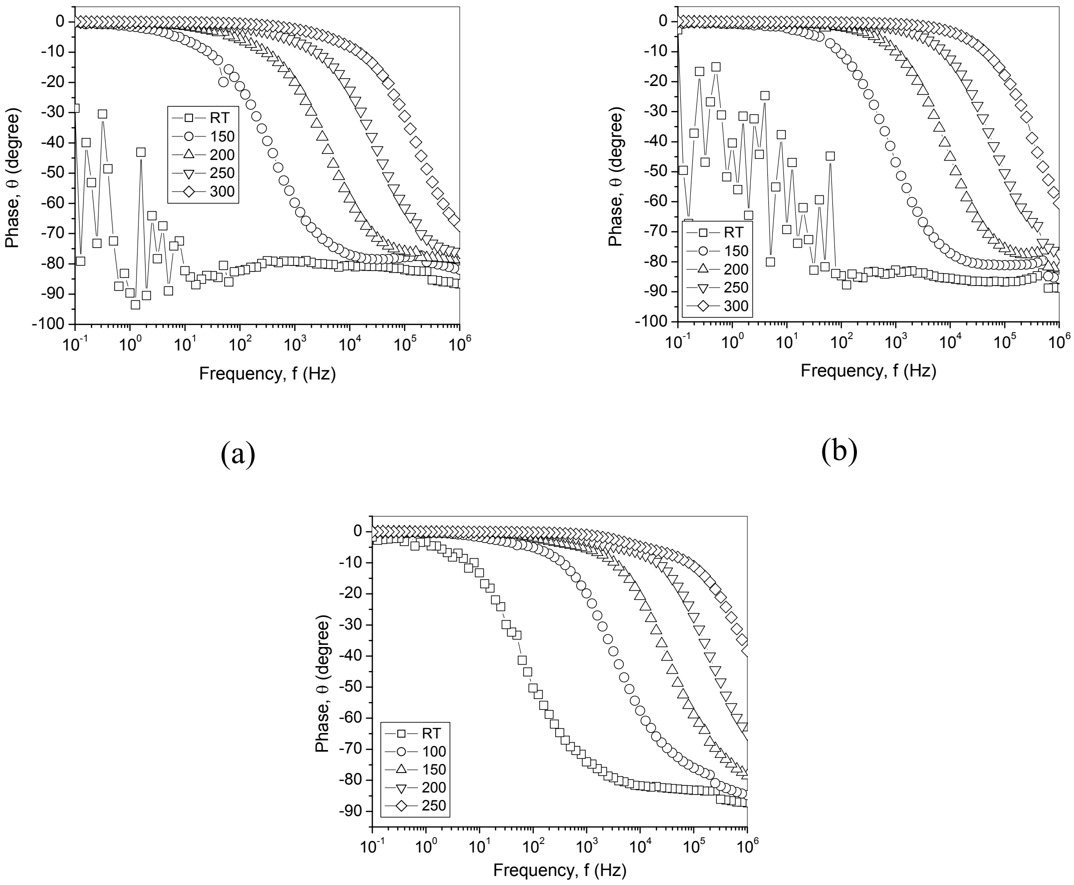

(a)

(b)

(c)

FIG. 5.15 Bode plot of phase (θ) against log frequency for the samples: (a) SCTaY-1, (b) SCTaL-5 and (c) SCTaCe-1 at different temperatures.

Since room temperature (RT) samples shows lots of fluctuating points, it was difficult to get well defined values of the grain boundary resistivity from these curves. Hence the average values for RT curves were taken. In *Fig. 5.14* the curves shows the drastic drop in resistivity values with respect to change in frequency indicating the grain-grain boundary structure in all the samples. At low frequency the sample exhibits capacitor like behavior, grain-grain boundary-grain structure giving high resistance to current flow. As the frequency increases, the resistance drastically decreases i.e. the capacitive impedance ($X_c = 1/\omega c$). At the highest frequency the impedance corresponding to grain boundary will be negligible and the total resistivity will be controlled by the change in phase with frequency shown in *Fig. 5.15(a), (b)* and *(c)* for the samples: SCTaY-1, SCTaL-5 and SCTaCe-1 respectively. The phase angle was 0 ° at low frequency but at the highest frequency point it has changes to 90 °. This indicates the presence of capacitive like behavior.

5.6.3 Relaxation time

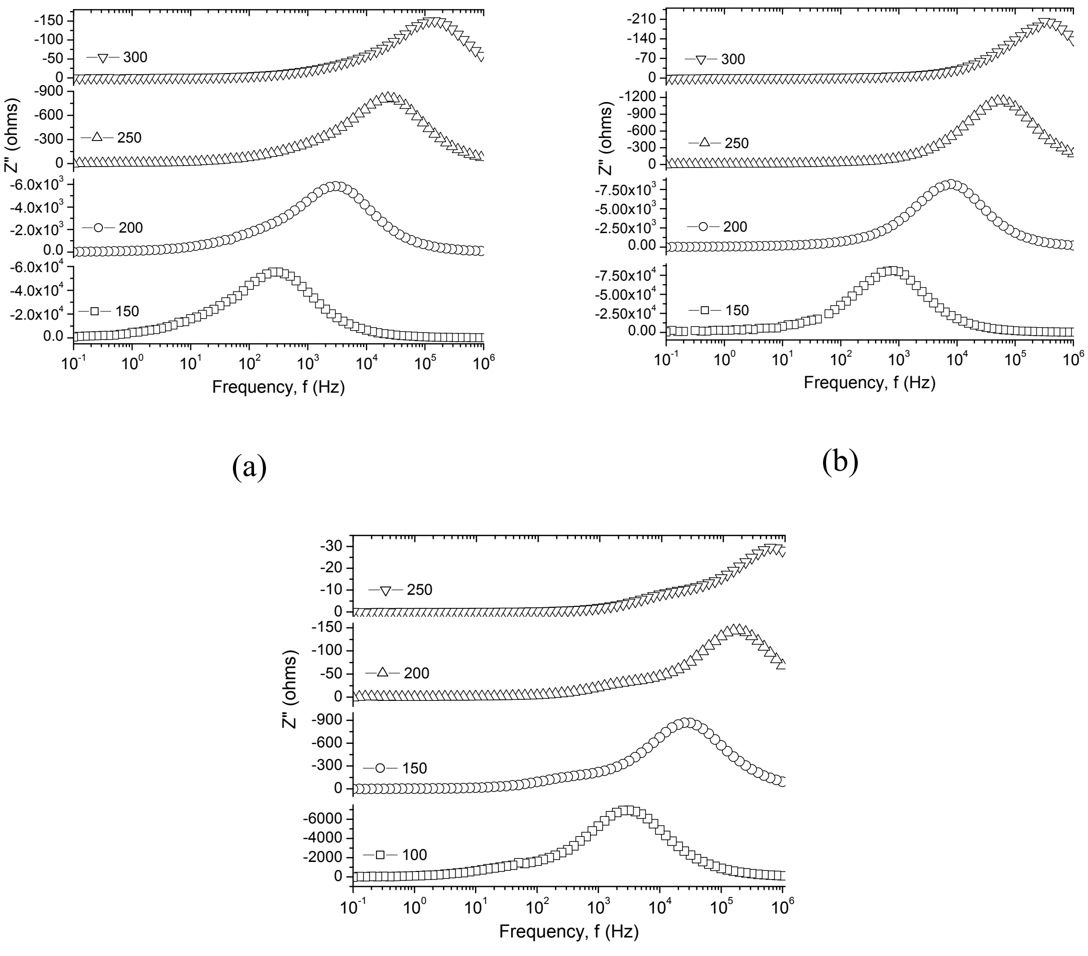

(a)

(b)

(c)

FIG. 5.16 Z" against log frequency plots of the samples: (a) SCTaY-1, (b) SCTaL-5 and (c) SCTaCe-1 at different temperatures.

Fig. 5.16 (a), (b) and *(c)* shows the plots of Z" (imaginary resistance) against log frequency for the samples: SCTaY-1, SCTaL-5 and SCTaCe-1 respectively. The f_{max} was taken from the plot and relaxation time was calculated by using the relation ($\Gamma = 1/2\pi f_{max}$), the values are given in *Table X*. The relaxation times found to vary from 10^{-7} to 10^{-4} s depending upon compositions indicating the presence of temperature dependent relaxing defects in the sample. The shift of f_{max} towards high frequency side with temperature indicates the presence of space charge effect in the samples.

Table X. Grain resistivity (ρ_g), grain boundary resistivity (ρ_{gb}), capacitance (C) and relaxation time (Γ) for the samples: SCTaY-1, SCTaL-5 and SCTaCe-1 at various temperatures.

Sample	Temperature (°C)	ρ_g (ohm-cm)	ρ_{gb} (ohm-cm)	C (Farad)	Γ (second)
SCTaY-1	RT	91.68	6.33×10^5	--	--
	150	107.65	1.85×10^5	3.44×10^{-9}	5.61×10^{-4}
	200	92.49	2.09×10^4	3.01×10^{-9}	5.04×10^{-5}
	250	77.54	3.12×10^3	2.67×10^{-9}	6.27×10^{-6}
	300	64.09	6.43×10^2	2.44×10^{-9}	1.12×10^{-6}
SCTaL-5	RT	288.29	4.38×10^7	--	--
	150	258.76	1.98×10^5	1.06×10^{-9}	2.01×10^{-4}
	200	231.07	2.62×10^4	9.84×10^{-10}	2.05×10^{-5}
	250	200.07	3.99×10^3	9.63×10^{-10}	2.84×10^{-6}
	300	156.68	7.85×10^2	7.85×10^{-10}	5.06×10^{-7}
SCTaCe-1	RT	113.46	8.86×10^5	--	--
	100	105.52	2.16×10^4	2.74×10^{-9}	5.41×10^{-5}
	150	95.63	2.84×10^3	2.42×10^{-9}	5.62×10^{-6}
	200	75.38	5.15×10^2	2.21×10^{-9}	8.36×10^{-7}
	250	45.40	1.25×10^2	2.06×10^{-9}	2.47×10^{-7}

5.7 Arrhenius plot

The grain boundary resistivity and temperature is related by the Arrhenius equation given in *equation 5.2*

$$\rho_{gb} = \rho_{gb0} \exp(-E_A/K_BT) \qquad 5.2$$

where K_B is the Boltzmann constant, E_A the activation energy, T is measuring temperature in °K, and ρ_{gb0} is the grain boundary resistivity at 0°K, from *equation 5.3*

$$\log(\rho_{gb}) = -E_A/K_B T \qquad 5.3$$

The slope of the curve log (ρ_{gb}) versus 1/T gives the value corresponding to E_A/K_B and hence the activation energy was calculated. The activation energy thus calculated from *Fig. 5.17* is given near corresponding curve. Hence the large value of grain boundary activation energy points at a better intergranular grain boundary region leading to superior current-voltage characteristic.

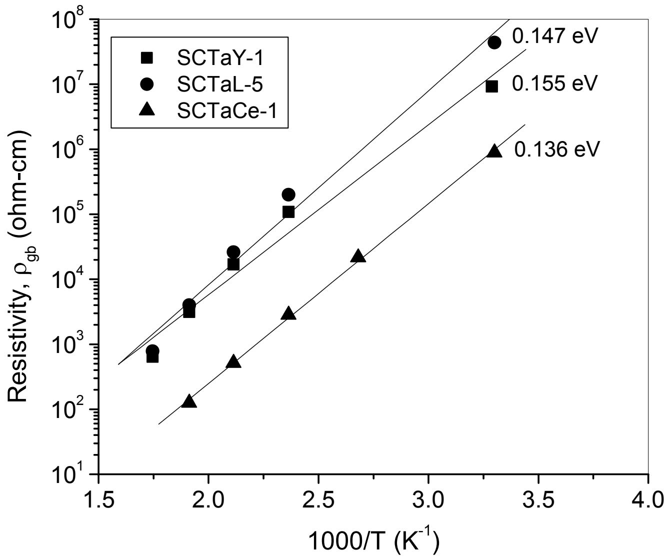

FIG. 5.17 Arrhenius plots (log resistivity Vs 1000/T) of the samples: SCTaY-1, SCTaL-5 and SCTaCe-1.

5.8 Discussion

The varistor property of polycrystalline ZnO ceramics originates from Schottky type grain boundaries. In the present case the acceptor like surface states were formed by rare earth ion, in addition CoO leads to formation of energy barrier at the grain boundaries is explained in earlier chapter. Small amount of Ta_2O_5 was added to SnO_2 ceramics to promote the substitution of Sn^{4+} for Ta^{5+}, this lead to an increase of electronic conductivity in the SnO_2 lattice, which is also explained in *Chapter 3*

Addition of Y_2O_3 (Effective ionic radius [10] of Y^{3+} 0.9 Å) to the SnO_2-CoO-Ta_2O_5 increases the non-linear coefficient to small extent but breakdown field was reduced. The average grain size for the samples: SCTaY-05, SCTaY-1 and SCTaY-5 was found to be 3, 4 and 4 μm respectively, and the breakdown field was comparably low despite the low porosity and high density (*Table I*). The relatively low breakdown field was due to enhanced grain size. Substitution of Sn ions by La was creating oxygen vacancies by the defect reaction given in *equation 5.4*. Higher values of barrier heights were responsible for good non-linear behavior. The barrier height values calculated for Y_2O_3 doped samples are given in *Table I*. The Rechardson's constant value varies from materials to materials. The calculated values for Y_2O_3, La_2O_3 and CeO_2 doped samples were of the order of 1.808×10^6, 1.825×10^6 and 1.830×10^6 respectively.

$$Ln_2O_3 \xrightarrow{SnO_2} 2\,Ln'_{Sn} + V_o^{\bullet\bullet} + 3\,O_o^x \qquad 5.4$$

where Ln = Y and La

The other tin dioxide system wherein the study of the influence of La_2O_3 on SnO_2-CoO-Nb_2O_5 system, the effective ionic radius [10] of La^{3+} (1.032 Å) is quite larger than the Sn^{4+} (0.74 Å) it preferably segregates at the grain boundaries this modification results in better α (30) and E_B (2484 V cm^{-1}) values. In the present case the defect reaction is represented by *equation 5.4*. The average grain size was of 2 μm for all the samples and the porosity was low for the La_2O_3 system. This was further confirmed by high relative density values for the La_2O_3

doped samples. The higher breakdown voltages for La_2O_3 doped samples were also supported by smaller average grain size as compared to other series.

CeO_2 as a dopant had no significant influence on the non-linear values, compare to Y_2O_3 and La_2O_3 and failed to alter the microstructural features of the system. It was also noted that second phase segregation at the grain boundary was observed. The average grain size is 3, 4 and 5 μm for the samples SCTaCe-05, SCTaCe-1 and SCTaCe-5 respectively, with higher density. This may be due to the fact that CeO_2 (effective ionic radius [10] of Ce^{3+} and Ce^{4+} 1.01 Å and 0.87 Å respectively) was probably formed a solid-solution with SnO_2 in the grain and sufficiently segregate at the grain boundaries but failed to create energy barriers at grain boundaries. This was illustrated by the defect reaction expressed in *equation 5.5* and *5.6.* The calculated lattice parameters for the CeO_2 doped samples is given in *table IX*

$$CeO_2 \xrightarrow{SnO_2} 2\,Ce_{Sn}^{x} + 2\,O_o^{x} \qquad 5.5$$

$$Ce_2O_3 \xrightarrow{SnO_2} 2\,Ce'_{Sn} + V_o^{\cdot\cdot} + 3\,O_o^{x} \qquad 5.6$$

Rare earth ions create oxygen vacancies according to *equations 5.4* and *5.6,* to promote adsorbed oxygen species defect formation, which was responsible for the barrier formation near the grain boundaries. The oxygen could also be responsible for Schottky barrier formation if we consider that oxygen can be adsorbed at the interface and react with negative defects (rare earth ions at the grain boundaries) according to the equations *equation 5.8, 5.9* and *5.10*

$$O_2 \longrightarrow O_2^{x}(ad) \qquad 5.7$$

$$Ln'_{Sn} + O_2^{x}(ad) \longrightarrow La_{Sn}^{x} + O'_2(ad) \qquad 5.8$$

$$Ln'_{Sn} + O'_2(ad) \longrightarrow La^{x}_{Sn} + 2O'(ad) \qquad 5.9$$

$$Ln'_{Sn} + O'(ad) \longrightarrow La^{x}_{Sn} + O'' \qquad 5.10$$

Therefore rare earth enhances oxygen adsorption, promotes the barrier formation and improves the non-linear characteristic. The barrier formed at grain boundaries in tin oxide was possibly like the description given below. The positive charges ($Sn_i^{\cdot\cdot\cdot\cdot}$, $V_o^{\cdot\cdot}$ and $Ta^{\cdot}_{Sn}$) extending from both side of the grain boundary were compensated by negative charges (Sn''_{Sn}, V''''_{Sn}, e', Co''_{Sn}, Ln'_{Sn} O' and O'') at the grain boundary interface. At the same time, the oxygen species adsorbed at the interface also were responsible for the Schottky barrier formation as shown in *equation 5.7, 5.8, 5.9* and *5.10*.

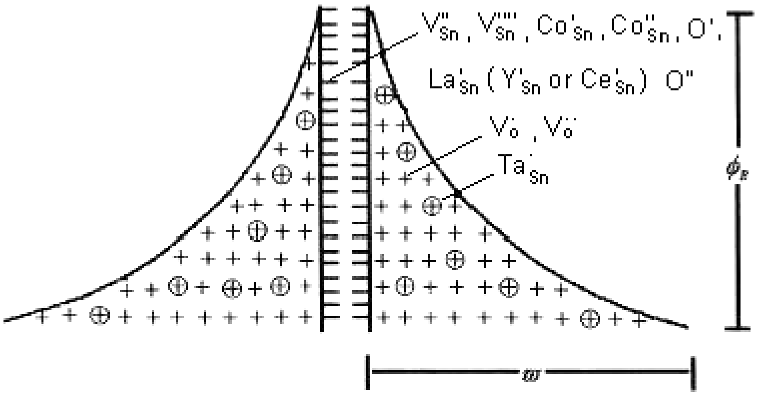

FIG. 5.18 Schematic Schottky type grain boundary barrier diagram

The electric transport occurs by tunneling across the barrier and was responsible for the electrical non-linearity. *Fig. 5.18* shows a schematic grain boundary barrier diagram wherein possible negative surface states are also given. The positively charged donors extending from both sides of grain boundary were compensated by negative charged acceptors at the grain boundary interface. The adsorbed oxygen at the grain boundary captures electrons from negatively charged defects at the grain boundary and stays at the interface [11]. Homogeneous segregation of Y'_{Sn}, La'_{Sn} and Ce'_{Sn} at grain the boundary was expected.

5.9 Summary and conclusions

The influence of a rare earth ion such as Y_2O_3, La_2O_3 or CeO_2 on SCTa system has been thoroughly studied. The Y_2O_3 doped series did not give much higher non-linear coefficients but breakdown field was low compared to other series. The relatively low breakdown field was due to enhanced grain size. La_2O_3 doped samples results in high non-linear coefficients with very high breakdown field whereas CeO_2 doped samples act as low voltage varistor with higher density.

The optimum temperature for the sintering in this rare earth dopes SnO_2 varistors was 1300 °C. Higher densification was necessary to have optimum grain-grain boundary contacts. The contributions from the grain boundary phase, due to incorporation of rare earth ion have been revealed by impedance analysis.

References

1. Santos M R C, Bueno P R, Longo E, Varela J A, *J. Euro. Ceram. Soc.* **21**, 161 (2001)
2. Bueno P R, Liete E R, Oliveira M M and Orlandi M O, *Appl. Phys. Lett.* **79**, 48 (2001)
3. Antunes A C, Antunes S R M, Pianaro S A, Rocha M R, Longo E, Varela J A, *J. Mater. Sci. Lett.* **17**, 577 (1998)
4. Leite E R, Nascimento A M, Bueno P R, Longo E, Varela J A, *J. Mater. Sci: Mater. Elctron.* **10**, 321 (1999)
5. Pianaro S A, Bueno P R, Olivi P, Longo E and Varela J A, *J. Mat. Sci. Lett.* **16,** 634 (1997)
6. Pinaro S A, Bueno P R, Olivi P, Longo E and Varela J A, *Ceram. Int.* **25**, 1 (1999)
7. Santhosh P N, Potdar H S and Date S K, *J. Mater. Res.* **12**, 326 (1997)
8. Fiwei F and Freer R, *J. Appl. Phys.* **77**, 4798 (1995)
9. **(a)** Dibb A, Tebcherani S M, Lacerda Jr. W, Clense M, Varela J A and Longo E, *J. Mater. Sci. Mater. Electron.* **13**, 567 (2002) **(b)** Oliveira M M, Soares Jr. P C, Bueno P R, Leite E R, Longo E, Varela J A, *J. Euro. Ceram. Soc.* **23**, 1875 (2003) **(c)** Wang C M, Wang J F, Chen H C, Su W B, Zang G Z, Qi P and Ming B Q, *Solid State Comm.* **132**, 163 (2004) **(d)** Bueno P R, Oliveira M M, Bacelar Jr. W K, Leite E R, Longo E, Garcia B G and Bisquert J, *J. Appl. Phys.* **91**, 6007 (2002) **(e)** Olivera M M, Bueno P R, Longo E and Varela J A, *Mater. Chem. Phys.* **74**, 150 (2002) **(f)** Antunes A C, Antunes S R, Pinaro S A, Longo E, Leite E R and Varela J A, *J. Mater. Sci. Mater. Electron.* **12**, **69** (2001) **(g)** Oliveira M M, Bueno P R, Santos M R C, Longo E and Varela J A, *J. Euro. Ceram. Soc.* **21**, 1179 (2001)
10. Shanon R D, *Acta. Cryst.* **B25,** 925 (1969)

11. Bueno P R, Pianaro S R, Pereira E C, Bulhoes L O S, Longo E and Varela J A, *J. Appl. Phys.* **84**, 3700 (1998)

Chapter 6

Role of alkali earth

The influence of an alkali earth (Ba/Sr) element in small quantities (< 1 at. %) on non-linear electrical properties of 98.5 % SnO_2 + 1 % CoO + 0.5 % Ta_2O_5 (all in at. %) varistor system has been investigated in this chapter. The non-linear coefficient increases from 33 to 52 whereas breakdown field strength varies 5025 to 6050 V cm^{-1} for the barium-doped samples. No increase in non-linear coefficient was found in strontium-doped samples whereas increase in breakdown field was observed. It was proposed that due to ionic size misfit, Ba and Sr segregates to grain boundaries thereby modifying their barriers properties. The contribution from grain boundary phase to the electrical property was confirmed by the impedance analysis.

6.1 Introduction

The influence of Ba and Sr as the only forming additives on ZnO based voltage-limiting resistors is studied in literature [1]. The non-linear behavior of SnO_2 varistor is directly related to the composition and to the microstructure development. The role of various dopants in the microstructural development is discussed in detail in earlier chapters. The addition of CoO creates oxygen vacancies and Co'_{Sn} and Co''_{Sn} which can segregates at grain boundaries. The addition of tantalum oxide creates $Ta^{\bullet}_{Sn}$ defect (donor) that increases the lattice conductivity of SnO_2 based ceramics. Among the additives it was proposed that the effective varistor forming ingredients were heavy elements with large ionic radii such as Bi, Ba, Sr, Pb etc., these heavy elements are able to segregate at grain boundary and form an electronic conduction barrier between n-type semiconductive SnO_2 grains. Alkali elements are heavy elements with larger ionic radii were expected to segregate at grain boundaries during the cooling from the sintering temperature and form energy barrier layers.

Grain boundary plays an important role in the electrical properties of ceramic materials. The influence of heavy elements with large ionic radii like effect of Bi addition on SnO_2 based varistor systems is reported in literature [2]. A non-linear electrical property of alkali element like Li on SnO2 based varistor is studied [3]. Wu *et al*. [4] studied effect of divalent Pb on tin oxide varistor. The influence of alkali earth elements like Ca, Sr and Ba on TiO_2 based varistor is also studied in detail in literature [5], but very few reports on alkali earth elements doped SnO_2 varistor are found in literature [6].

6.2 Experimental

SnO_2 containing additives was prepared by wet chemical method. The compositions were prepared by coprecipitation method as discussed in *Chapter 2*.

$SnCl_4$ was diluted using ice-cold distilled water and required quantity of $Co(NO_3)_2 \cdot 6H_2O$, TaF_5, and $BaCO_3$ (dissolved in dilute HCl) was mixed with it. The standard ammonia solution and ammonium oxalate were then added dropwise to the above solution with constant stirring until pH ~ 9. The precipitate then kept on water bath to evaporate the water content. The dried powders were calcined at 600 °C for 12 hrs. The calcined powders were mixed with a binder, poly vinyl alcohol 2 wt. %, and pelletized (15 mm dia, 1 mm thick) at 2-3 tons. The pellets were sintered at 1300 °C for 2 hrs. The densities of the pellets were measured by mass volume and Archimedes methods. The sintered pellets were polished and ohmic silver contacts were obtained by Ag-paste on the known area of surface, further annealed at 600 °C for 30 minutes. The series of compositions prepared were (98.5-x) % SnO_2 + 1 % CoO + 0.5 % Ta_2O_5 + x at. % $BaCO_3$ and (98.5-x) % SnO_2 + 1 % CoO + 0.5 % Ta_2O_5 + x at % $SrCO_3$ where x = 0.5 & 1 at. %. The sample identifications are SCTaB-05 & SCTaB-1 for 0.5 and 1 at. % $BaCO_3$ doped respectively; SCTaS-05 and SCTaS-1 for 0.5 at % and 1 at. % $SrCO_3$ respectively. The prepared samples were characterized by various physico-chemical characterization methods.

6.3 I-V characteristics

Fig 6.1a shows the current density (J) against applied field (E) (I-V characteristics) plots on log scale for samples: SCTaB-05, SCTaB-1, SCTaS-05 and SCTaS-1. The non-linear coefficient (α) calculated from the slopes of the curves in the non-linear region. The non-linear coefficient values for samples SCTaB-05 & SCTaB-1 were 52 and 41 with the breakdown field of 5025 and 6050 V cm^{-1} respectively as given in *Table I*. For Sr-doped samples, the non-linear coefficient values calculated for the samples: SCTaS-05 and SCTaS-1 were 31 and 36 with the breakdown field of 4965 and 5035 V cm^{-1} respectively (*Table I*).

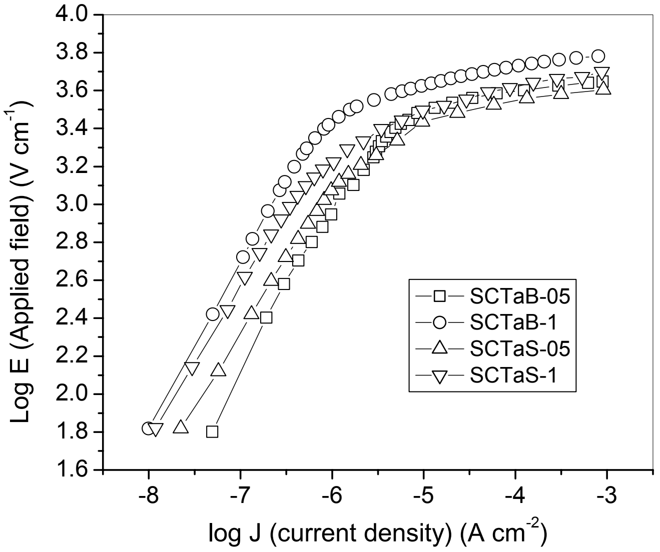

FIG. 6.1a I-V characteristic plots for the samples: SCTaB-05, SCTaB-1, SCTaS-05 and SCTaS-1 sintered at 1300 °C.

The prebreakdown region was analyzed because this region in the I-V curve, controlled entirely by the grain boundary impedance. Very small difference was observed in current density for both Ba and Sr doped samples in the prebreakdown region. The grain boundary resistances for both Ba and Sr-doped samples were rather high (~10^7 ohm-cm). The impact of Ba ions with larger ionic radii was seemed to be more effective than that of Sr ion. Ba ions segregate at grain boundary, which increases the non-linear coefficient, accompanied by the increase in breakdown voltage. However in case of Sr doped decrease in non-linear coefficient and increase in breakdown field with concentration of Sr was observed. The decrease in non-linear coefficient and increase in breakdown field was may be due to the small increase in resistance with the increase in concentration of Ba or Sr. By considering the Schottky type grain boundary barriers responsible for conduction phenomena, characteristic plots of log J against $E^{1/2}$ as shown in *Fig 6.1b* could be built up to determine the values for β and Φ_B using Richardson's formula (discussed in *chapter* 2). Since Richardson's constant depends on the density of the samples and varies from material to material, the values calculated for all Ba and Sr doped samples were of the order of 1.768 x 10^6. The values for barrier height (Φ_B) are given in *Table I*.

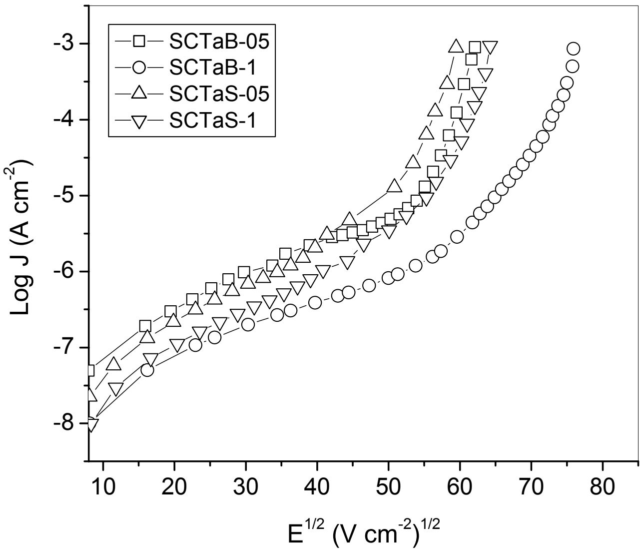

FIG. 6.1b Characteristic plots of log J against $E^{1/2}$ for the samples: SCTaB-05, SCTaB-1, SCTaS-05 and SCTaS-1 sintered at 1300 °C.

Table I. Characteristic parameters for the samples: SCTa, SCTaB-05, SCTaB-1, SCTaS-05 and SCTaS-1.

Sample identification	$BaCO_3$/ $SrCO_3$ (at. %)	α	E_B, V cm^{-1}	Density, gm cm^{-3}	Relative density, %	Φ_B, eV	Average grain size, μm
SCTa	0	33	4910	6.73	96.8	0.627	2
SCTaB-05	0.5	52	5025	6.29	90.6	0.749	1
SCTaB-1	1	41	6050	6.33	91.2	0.778	1.5
SCTaS-05	0.5	31	4965	6.35	91.4	0.575	1
SCTaS-1	1	36	5035	6.28	90.4	0.546	2

6.4 Sintering behavior

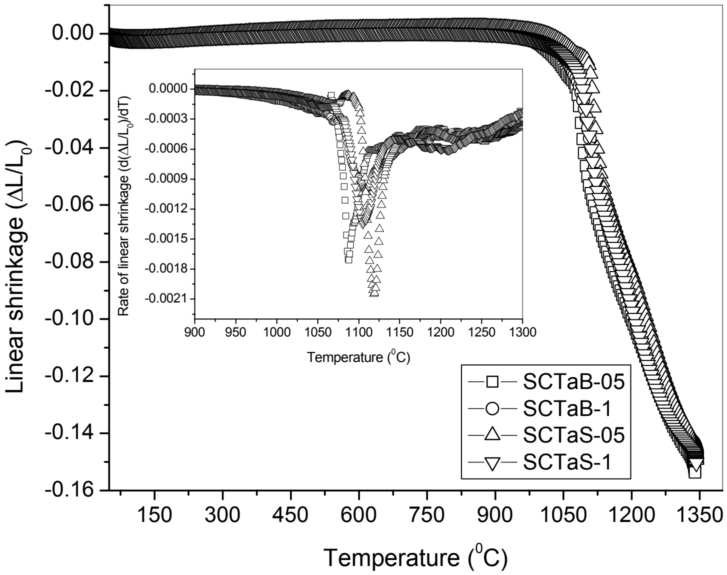

FIG. 6.2 Plots for linear shrinkage ($\Delta L/L_0$) and rate of linear shrinkage ($d(\Delta L/L_0)/dT$) (inset) as a function of temperature for the samples: SCTaB-05, SCTaB-1, SCTaS-05 and SCTaS-1.

Table II. Maximum shrinkage rate for Ba and Sr doped samples.

Sample identification	T_M (°C)
SCTaB-05	1087
SCTaB-1	1103
SCTaS-05	1118
SCTaS-1	1113

Fig 6.2 show the plots of linear shrinkage ($\Delta L/L_0$) and the rate of linear shrinkage ($d(\Delta L/L_0)/dT$) (inset) as a function of temperate for the samples: SCTaB-05, SCTaB-1, SCTaS-05 and SCTaS-1. From the linear shrinkage curve it was observed that the shrinkage starts at the temperature around 1000 °C and completed at the maximum temperature of 1250 °C for all the samples. The

density of the pellets calculated are given in *Table I.* The density for all the pellets was found to be greater than 90 %. The maximum shrinkage rate temperature (T_M) was taken from the linear shrinkage rate against temperature plot, slight increase in T_M was observed with increase in concentration of Ba but not much difference in T_M values was observed in Sr doped samples as given in *Table II*.

6.5 X-ray powder diffraction

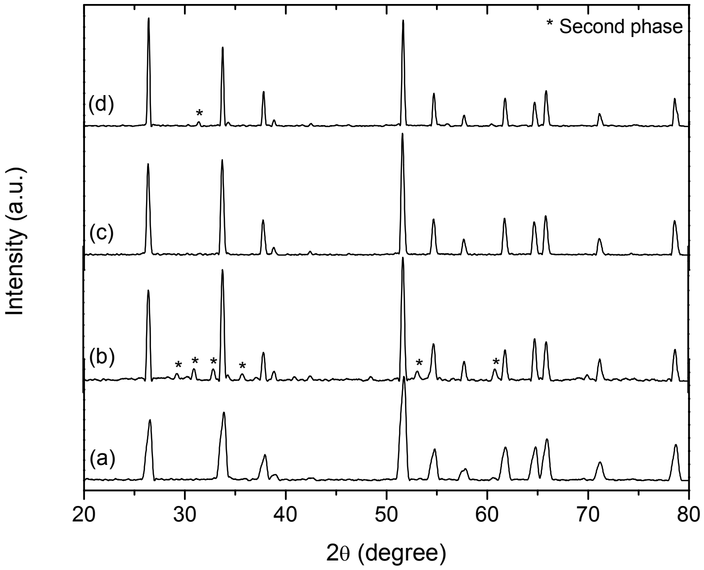

FIG. 6.3 X-ray powder diffraction pattern of sintered samples: (a) SCTaB-05, (b) SCTaB-1, (c) SCTaS-05 and (d) SCTaS-1 sintered at 1300 °C.

The samples were analyzed by X-ray diffraction to understand the phase evolved in the system as the concentration of alkali earth ions increased. *Fig 6.3* shows the X-ray diffraction pattern (XRD) recorded for the samples (a) SCTaB-05, (b) SCTaB-1, (c) SCTaS-05 and (d) SCTaS-1. Apparently X-ray diffraction patterns correspond to SnO_2 tetragonal rutile phase were observed. Small traces of impurity peaks were found for the 1 at % Ba and Sr doped samples as shown in *Fig 6.3(b)* and *(d)*. Additional peaks correspond to secondary phases, which were formed during the reaction between dopants with SnO_2. The peaks indicated by asterisk in *Fig. 6.3 (b)* were of $BaSnO_3$ formed during sintering. It was also noted that for the samples less than 0.5 at % Ba/Sr, the concentrations of dopants added were too small to be detected by X-rays (*Fig 6.3 (a)* and *(c)*). The lattice parameters calculated by least squares method are given in *Table III*. Since the maximum intense peaks corresponding to SnO_2 tetragonal rutile phase were very sharp, they must be representing SnO_2 grains and secondary phases of Ba and Sr were expected to segregate at the grain boundaries and thereby make a better intergranular layer.

Table III. Lattice parameters for Ba and Sr doped samples.

Lattice parameter (Å)	Sample identification			
	SCTaB-05	SCTaB-1	SCTaS-05	SCTaS-1
a	4.726	4.732	4.726	4.731
c	3.176	3.179	3.177	3.179

6.6 Scanning electron micrographs

To understand the grain-grain boundary microstructure and to determine grain size, the scanning electron micrographs of the fractured surfaces of the pellets were taken for all Ba and Sr doped samples. The micrographs for the samples: (a) SCTaB-05, (b) SCTaB-1, (c) SCTaS-05 and (d) SCTaS-1 are given in *Fig 6.4*. The average grain size obtained from the micrographs for the samples: SCTaB-05, SCTaB-1, SCTaS-05 and SCTaS-1 were 1, 1.5, 1 and 2 μm respectively as given in *Table I*. The grain size has a clear effect on the current-voltage characteristic of the varistor. The breakdown voltage decreases with increase in grain size. Clear separations of individual grains were observed and there were few voids seen in the micrographs, which resulted in slightly lower density. No grain boundary phase found in the micrograph, but the second phase was conformed by the impedance analysis as discussed in *section 6.7*.

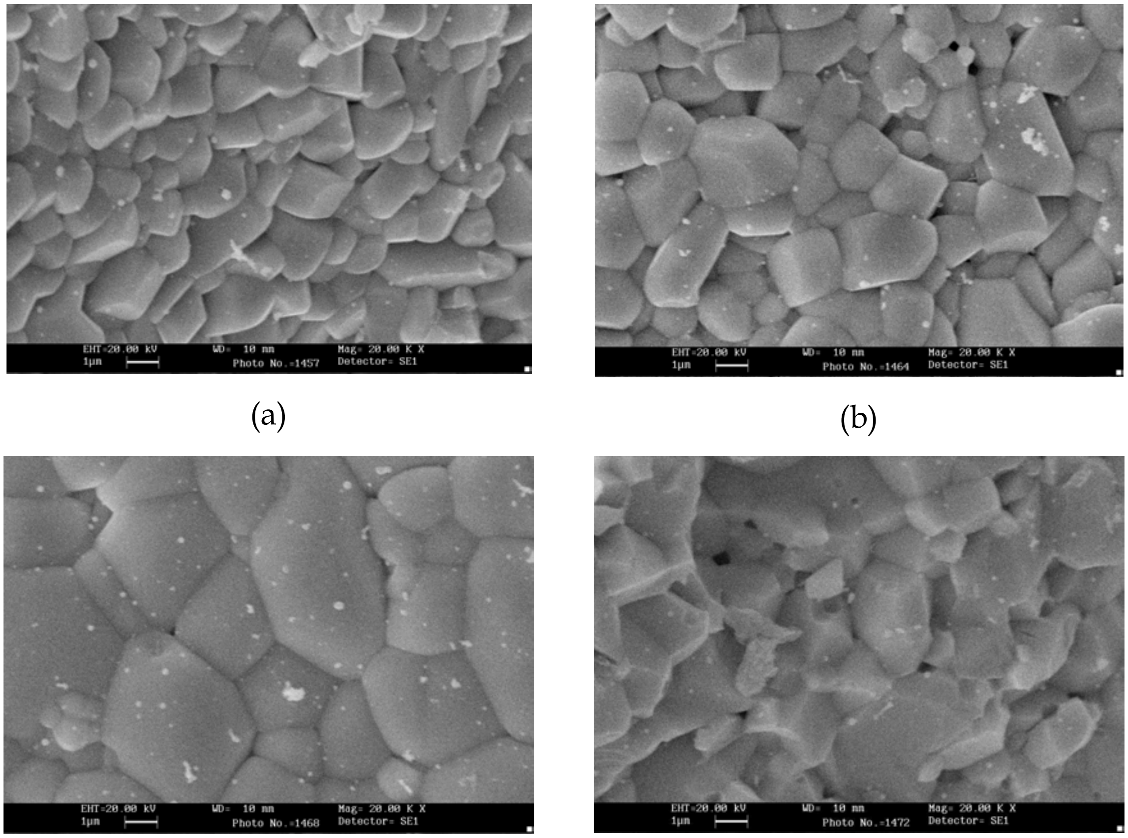

(a) (b)

(c) (d)

FIG. 6.4 Scanning electron micrographs of the fractured surfaces for the samples: (a) SCTaB-05, (b) SCTaB-1, (c) SCTaS-05 and (d) SCTaS-1 sintered at 1300 °C.

6.7 Impedance analysis

6.7.1 Nyquist plot

The ac impedance analysis of the samples: SCTaB-1 and SCTaS-05 was done in the frequency range from 0.1 Hz to 1 MHz with an ac amplitude voltage of 100 mV. *Fig 6.5 (a)* and *(b)* represent the impedance plots, real resistance (Z') versus imaginary resistance (Z") measured at various temperatures for the samples: SCTaB-1 and SCTaS-05 respectively.

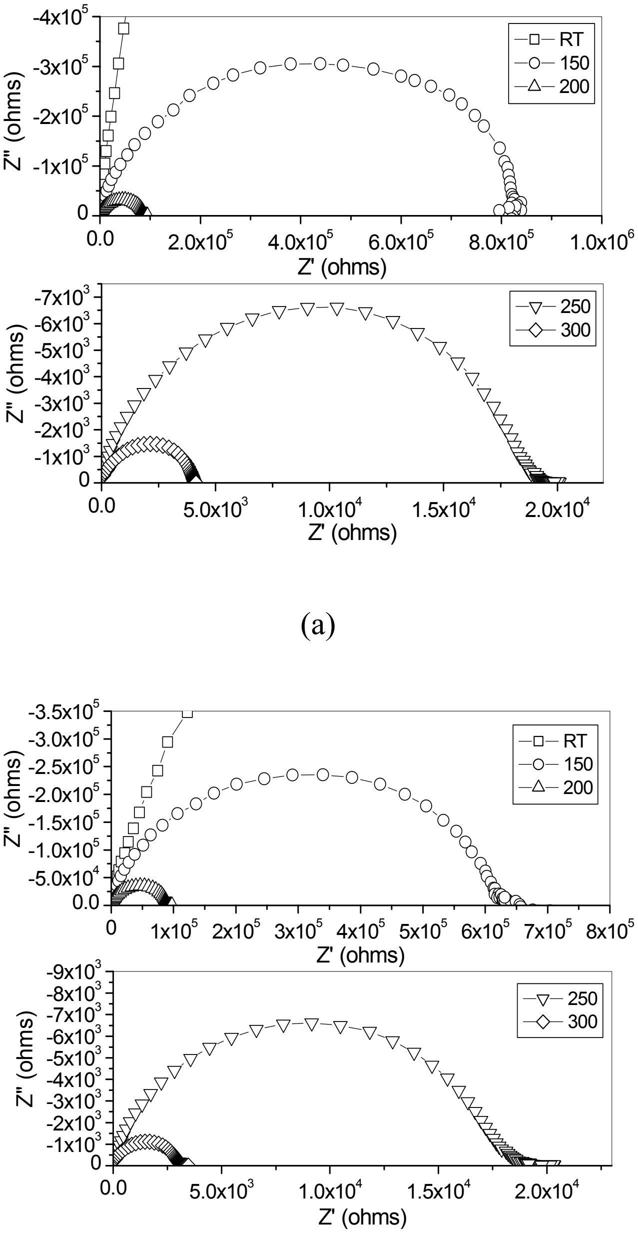

(a)

(b)

FIG. 6.5 Impedance plot (Z' versus Z") for the samples: (a) SCTaB-1 and (b) SCTaS-05 at various temperatures.

A room temperature curve shows a part of very large semicircle. This was because of very large resistance of samples (~ 10^9 ohm). Major contribution to this resistance was due to the grain boundary resistance. At a temperature greater than 150° C a full semicircle was seen for both the samples. As the grain boundary contribution to the total resistance was very large compare to that of the grain, these curves failed to give an expected semicircular nature corresponding to the grains at higher frequency side. The semicircles corresponding to grain were submerged in the circle representing the grain boundaries. Therefore separating out the individual component by fitting the semicircle was not possible. Since the separation of the contribution from grain and grain boundaries was not possible from the above plot, the Bode diagrams were plotted to analyze the above data.

6.7.2 Bode plot

Bode plot represent the resistivity (ρ) against frequency (f) on log scale for the samples: SCTaB-1 and SCTaS-05 at different temperatures (RT, 100, 150, 200, 250 300 °) as shown in *Fig 6.6 (a)* and *(b)* respectively. Since the measurement frequency range was large (0.1 Hz to 1 MHz) and the impedance also changes over a large range (10^8 to 100 ohm-cm), the plots were made on log scale. The lowest frequency point was taken as the grain boundary resistivity (ρ_{gb}) and the highest frequency point as grain resistivity (ρ_g), the values are given in *Table IV*. Since the room temperature (RT) measured samples shows a lot of fluctuating points, it was difficult to get well defined value of the grain boundary resistivity from this curve. The average value was taken for RT curve. This was in accordance with the method used by Bueno *et al.* [7]. The decrease in grain boundary resistance with increase in temperature was indication of second phase at the grain boundary. It was seen that there was a drastic drop in resistivity as the frequency changes from 0.1 Hz to 1 MHz. This was clear indication that a grain boundary like structure exists which leads to a capacitor like behavior. Decrease in grain boundary resistivity values with increase in temperature is given in *Table IV*.

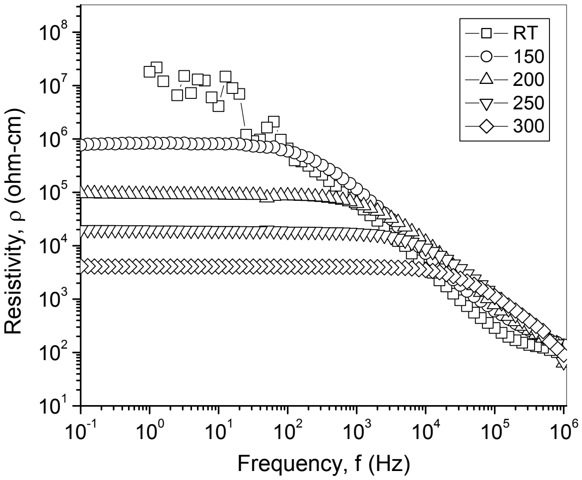

(a)

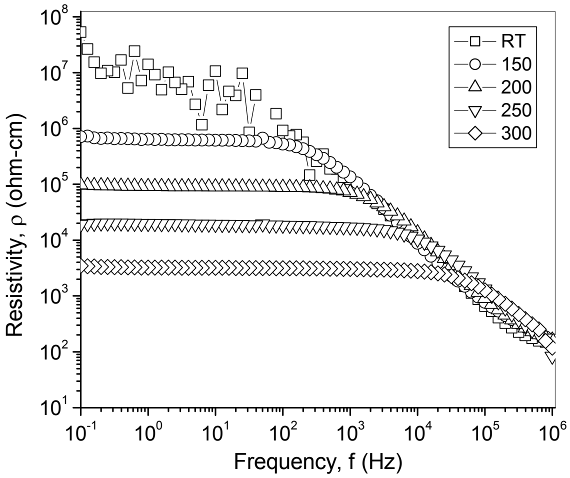

(b)

FIG. 6.6 Bode plot of log resistivity against log frequency for the samples: (a) SCTaB-1 and (b) SCTaS-05 at different temperatures.

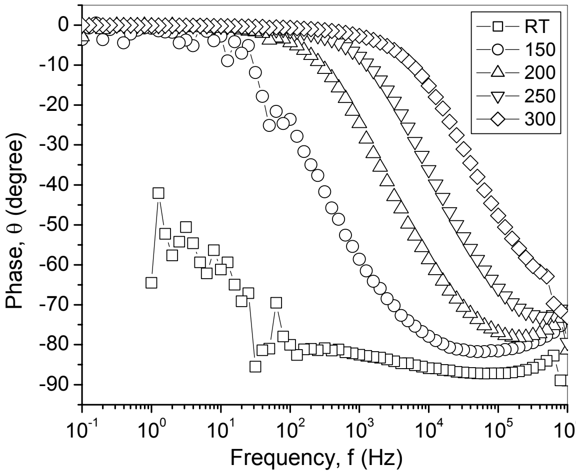

(a)

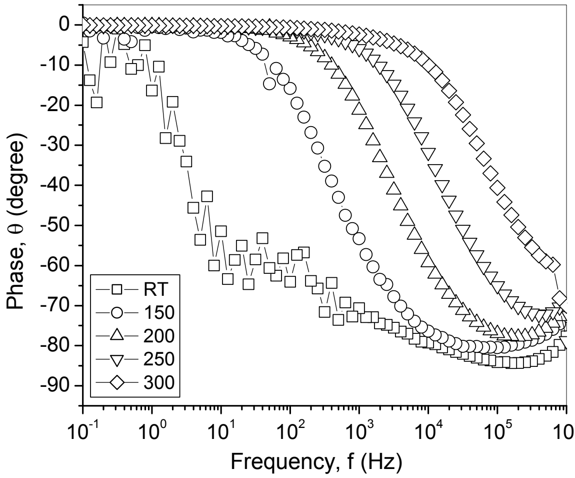

(b)

FIG. 6.7 Bode plot of phase versus log frequency for samples: (a) SCTaB-1 and (b) SCTaS-05 at different temperatures.

The capacitive like behavior was also justified when the phase was plotted at different frequencies. *Fig 6.7 (a)* and *(b)* represents the Bode plot of phase (θ) versus log frequency (f) at different temperatures for the samples: SCTaB-1 and SCTaS-05 respectively. The phase angle was 0 ° at low frequency but at the highest frequency point it has changed to 90°. This indicates the presence of capacitive like behavior. The capacitance values calculated for both the samples as given in *Table IV* was of nano Farad range this implies the contribution from the grain boundary. Hence it was conformed that a semiconductor-insulator-semiconductor (S-I-S) structure exists in these SnO_2 ceramics and it was the reason for the high non-linear behavior exhibits by these materials.

6.7.3 Relaxation time

Fig 6.8 (a) and *(b)* shows the Z" (imaginary resistance) against log frequency (f) plot for the same samples SCTaB-1 and SCTaS-05 respectively. The f_{max} was taken from the plot and relaxation time was calculated by using the relation, $\Gamma = 1/2\pi f_{max}$. The relaxation time was found to vary from 10^{-6} to 10^{-4} s as given in *Table IV*, for both Ba and Sr doped samples depending upon compositions indicating presence of temperature dependent relaxing defects in the sample. The shift of f_{max} towards high frequency side with temperature indicates the presence of space charge effect in the samples.

Table IV. Grain resistivity (ρ_g), grain boundary resistivity (ρ_{gb}), capacitance (C) and relaxation time (Γ) for the samples: SCTaB-1 and SCTaS-05.

Sample	Temperature (°C)	ρ_g (ohm-cm)	ρ_{gb} (ohm-cm)	C (Farad)	Γ (second)
SCTaB-1	RT	41.98	4.69×10^{7}	--	--
	150	38.46	8.33×10^{5}	8.06×10^{-10}	7.96×10^{-4}
	200	37.05	9.49×10^{4}	8.27×10^{-10}	7.98×10^{-5}
	250	35.87	1.99×10^{4}	8.23×10^{-10}	1.59×10^{-5}
	300	31.33	4.14×10^{4}	8.87×10^{-10}	3.99×10^{-6}
SCTaS-05	RT	71.55	1.11×10^{7}	--	--
	150	65.69	4.09×10^{5}	6.77×10^{-10}	5.03×10^{-4}
	200	61.88	9.77×10^{4}	6.47×10^{-10}	6.34×10^{-5}
	250	53.98	2.05×10^{4}	6.40×10^{-10}	1.26×10^{-5}
	300	38.56	3.43×10^{3}	6.99×10^{-10}	2.01×10^{-6}

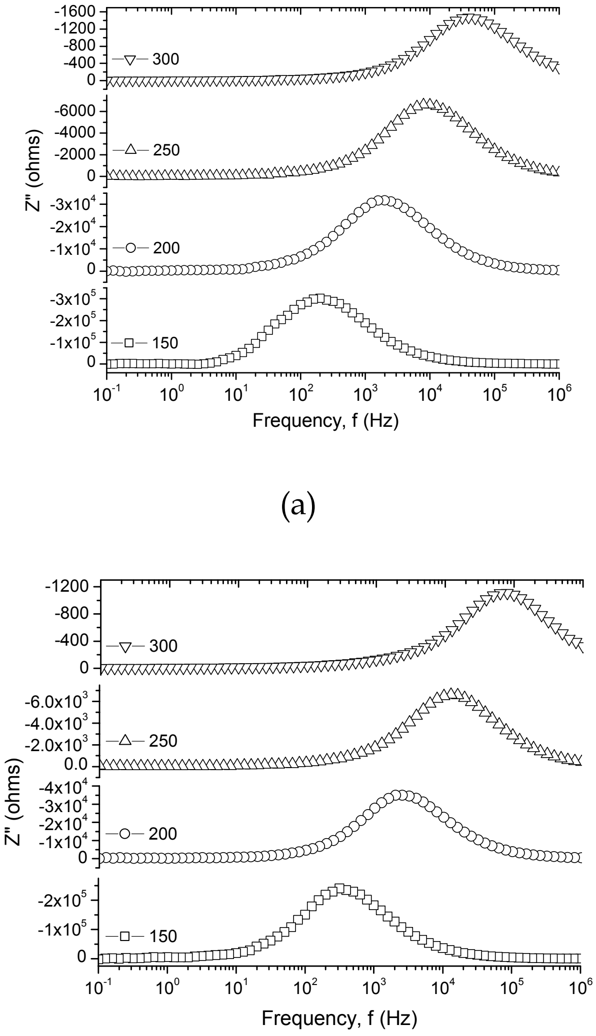

(a)

(b)

FIG. 6.8 Z'' versus log frequency for the samples: (a) SCTaB-1 and (b) SCTaS-05 at various temperatures.

6.8 Arrhenius plot

The grain boundary resistivity and temperature is related by the Arrhenius equation. The slope of the curve log (ρ_{gb}) Vs 1000/T (*Fig 6.9*) gives the value corresponding to E_A/K and hence the activation energy was calculated.

The activation energy thus calculated from *Fig 6.9* was found to be 0.171 eV and 0.161 eV for the sample SCTaB-1 and SCTaS-05 respectively. This is similar to the variation in non-linear coefficient values measured from I-V characteristics. Hence the large value of grain boundary activation energy points at a better intergranular grain boundary region leading to superior current-voltage characteristics.

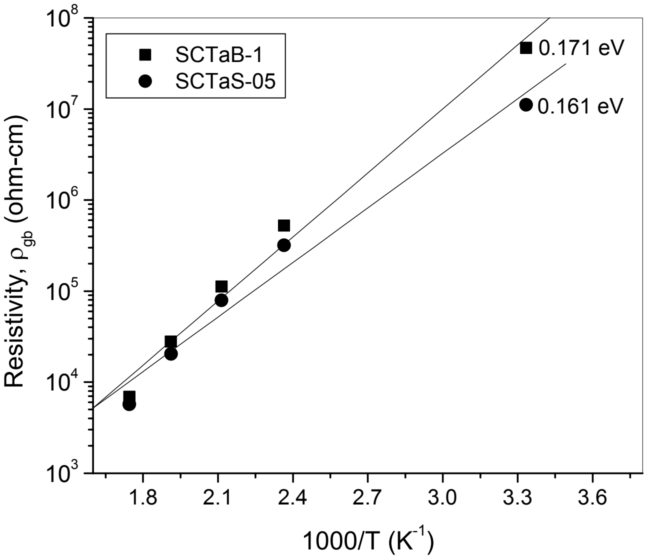

FIG. 6.9 Arrhenius plots (resistivity Vs 1000/T) for the samples SCTaB-1 and SCTaS-05

6.9 Discussion

Ba and Sr would segregate near SnO_2 grain boundary during cooling from the sintering temperature because the large elastic energy associated with Ba and Sr substitution in Sn sublattice can be relaxed by segregation at the grain boundary region. The segregation of Ba thus forms a grain boundary barrier layer for the motion of charge carrier. The formation of grain boundary barrier layer could be proved by the improvement in non-ohmic I-V behavior.

The addition of Ta_2O_5 in small amount to the SnO_2 ceramics causes the concentration of e' and V''''_{Sn}, boundaries, increase the electronic conductivity in the SnO_2 lattice and lead the semiconductivity of the grains is discussed in detail in previous chapters.

Alkali earth dopants with larger ionic radii and lower valence prefer to segregate at the grain boundary in order to relieve the large elastic energy caused by ionic radii misfit. These segregated ions act as acceptors, which locally compensate the donors, this resulting in increase in grain boundary resistivity.

The substitution of Ba (effective ionic radius for Ba^{2+} is 1.38 Å) in SnO_2 lattice creates oxygen vacancies according to the defect *equation 6.1* and the substitution of Sr (effective ionic radius for Sr^{2+} is 1.21 Å) also creates oxygen vacancies according to the defect reaction given in *equation 6.2*.

$$BaCO_3 \xrightarrow{SnO_2} Ba''_{Sn} + V_o^{\bullet\bullet} + O_o^{x} + CO_{2\,(g)} \qquad 6.1$$

$$SrCO_3 \xrightarrow{SnO_2} Sr''_{Sn} + V_o^{\bullet\bullet} + O_o^{x} + CO_{2\,(g)} \qquad 6.2$$

The oxygen vacancies ($V_o^{\bullet\bullet}$) are very important factor, which controls the sintering kinetics. It is well known that oxygen vacancies control grain growth. Hence Ba/Sr acts as grain growth enhancer at the same time addition of Ta leads to increase in oxygen partial pressure, which decreases the concentration of oxygen vacancies and inhibits grain growth. Hence Ta acts as donor as well as grain growth inhibitor. Ba/Sr acts as an acceptor and grain growth enhancer. Hence the oxygen vacancies can combine with tin vacancies according to the reaction given in *equation 6.3*.

$$2V_o^{\bullet\bullet} + V_{Sn}^{''''} \longrightarrow 2V_o^{\bullet} + V''_{Sn} \qquad 6.3$$

Moreover, the increase of the concentration of oxygen vacancies induced by the substitution of Sn^{4+} with Ba^{2+}/Sr^{2+}, will also play an important effect on the decrease of the grain resistivity because of an increased probability of electron hopping. Besides the substitution of Sn^{4+} with Ba^{2+}/Sr^{2+}, Ba^{2+}/Sr^{2+} also tends to segregate to grain boundary areas, especially during cooling. The segregation of Ba^{2+}/Sr^{2+} and the diffusion of oxygen vacancies would increase the acceptor concentration (density of surface states, Ns) and then give high values of Φ_B [8]. The barrier height values calculated for the Ba doped samples was in the range of 0.749 to 0.778 eV and for the Sr doped samples it was in the range of 0.546 to 0.575 eV.

The depletion layer comprising the barrier consists of positively charged ions includes $Ta^{\cdot}_{Sn}$, oxygen vacancies ($V^{\cdot}_{o}$ & $V^{\cdot\cdot}_{o}$) and tin interstitials. The positively charged ions extend from both sides of the grain boundary into adjacent grains were compensated by a layer of negatively charged ions of the acceptor ions (Ba''_{Sn}/Sr''_{Sn}) and the Sn vacancies. The negative charge grain boundary was compensated by the positive charge at the depletion layers and creates effective energy barriers to the conduction of electrons across the grain boundary. Both the intrinsic and the impurity controlled defects can produce an effective energy barrier at the grain boundary (Double Schottky barriers), this in turn will lead to non-linear behavior [9]. Greater the activation energy means more effective the grain boundary barrier layer. This is in agreement with the other work reported in the literature [5(a), 6(a)]. The activation energy calculated for the Ba doped samples was found to be 0.171 eV and for Sr doped samples it was 0.161 eV. Compositions prepared by the chemical route were not much improved in performance parameters, comparably similar value was found as that of the samples prepared by ceramic method. The density of the samples prepared by chemical method is slightly less than that of by ceramic method. The density of the samples is very important in determining the varistor characteristics. This has been found true in ZnO varistors also [10]. The impedance analysis also reveals the evidence of an insulating grain boundary phase which gives rise to a capacitor like structure. This capacitor like structure gives high impedance to conduction at low frequencies and its resistance becomes negligible at high frequencies. Hence the impedance analysis gives the evidence for a grain-brain boundary like structure existing in these SnO_2 ceramics.

6.10 Summary and conclusions

0.5 at. % $BaCO_3$ doped SnO_2 samples have non-linear coefficient value 52 with high breakdown field. Increase in Ba concentration was resulting in increase in resistivity, with low non-linear coefficient. There was very small increase in non-linear coefficient as well as breakdown field observed with the increase in Sr concentration.

Ba was segregating at grain boundaries and creating energy barriers, which was resulting in higher non-linear coefficient, whereas Sr was segregating at grain boundaries but may not be able to create energy barriers that was resulting not much increase in non-linear coefficients. Impedance analysis was worthful method to understand the grain-grain boundary phenomena. The activation energy calculated from the Arrhenius plot, which gave idea about the formation of energy barrier.

References

1. **(a)** Kutty T R N and Raghu N, *Mater. Sci. Eng. B* **13**, 181 (1992) **(b)** Raghu N, Ravi V and Kutty T R N, *Mater. Res. Bull.* **26**, 261 (1991)
2. **(a)** Bomio M R D, Sousa V C, Leite E R, Varela J A, Longo E, *Mater. Chem. Phys.* **85**, 96 (2004) **(b)** Pinaro S A, Bueno P R, Olivi P, Longo E and Varela J A, *J. Mater. Sci. Lett.* **16**, 634 (1997) **(c)** Anastasiou A, Lee M H J, Leach C, Freer R, *J. Euro. Ceram. Soc.* **24**, 1171 (2004)
3. **(a)** Li C P, Wang J F, Su W B, Chen H C, Wang W X, Zang G Z, Xu L, *Ceramics International* **28,** 521 (2002) **(b)** Li C, Wang J, Su W, Chen H, Wang W, *J. Mater. Sci. Tech.* **18**, 283 (2002)
4. Wu J M and Lai C H, *J. Am. Ceram. Soc.* **74**, 3112 (1991)
5. **(a)** Yang S L and Wu J M, *J. Am. Ceram. Soc.***78**, 2203 (1995) **(b)** Wang W Y, Zhang D F, Xu T, Li X F, Zhou T, Chen X L, *Journal of Alloys and Compounds* **335**, 210 (2002) **(c)** Li J, Luo S, Yao W, Zhang Z, *Mater. Lett.* **57**, 3748 (2003)
6. **(a)** Yang S L and Wu J M, *J. Am. Ceram. Soc.* **76**, 145 (1993) **(b)** Santhosh P N, Kharat D K, Date S K, *Mater. Lett.* **28**, 37 (1996)
7. Bueno P R, Pianaro S R, Pereira E C, Bulhoes L O S, Longo E and Varela J A, *J. Appl. Phys.* **84**, 3710 (1998)
8. Cheng J J, Wu J M, *Jpn. J. Appl. Phys.* **35**, 4704 (1996)
9. Yang S L and Wu J M, *J. Mater. Sci. Lett.* **14**, 748 (1995)
10. Nobrega M C S and Mannheimer W A, *J. Amer. Ceram. Soc.* **79**, 1504 (1996)

List of publications

1. Chemical co-precipitation of mixed (Pb + Ti) oxalates precursor for the synthesis of $PbTiO_3$ powder
   S. R. Dhage, Y. B. Khollam, H. S. Potdar, S. B. Deshpande, B. D. Sarwade, and S. K. Date, *Mater. Lett.* 56 (4) 564 (2002)

2. Microwave-hydrothermal preparation of submicron sized spherical magnetite (Fe_3O_4) powders.
   Y.B. Khollam, **S.R. Dhage**, H.S. Potdar, S.B. Deshpande, P.P. Bakare, S.D. Kulkarni, and S.K. Date, *Mater. Lett.* 56 (4) 571 (2002)

3. Effect of variation of molar ratio (i.e. pH) on the crystallization of iron oxide phases in microwave hydrothermal (MH) synthesis.
   S. R. Dhage, Y. B. Khollam H. S. Potdar, S. B. Deshpande, P. P. Bakare, S. R. Sainkar, and S. K. Date, *Mater. Lett.* 57 (2) 457 (2002)

4. Influence of lanthanum on the nonlinear I-V characteristics of SnO_2: Co, Nb
   Sanjay R. Dhage, V. Ravi and S. K. Date, *Mater. Lett.* 57 (3) 727 (2002)

5. Preparation of microwave dielectric $Sn_{0.2}$ $Zr_{0.8}$ TiO_4
   Sanjay R. Dhage, V. Ravi and S.K. Date, *Bull. Mater. Sci.* 26 (2) 215 (2003)

6. Co-precipitation technique for the preparation of nanocrystalline ferroelectric $SrBi_2Ta_2O_9$
   S. R. Dhage, Y. B. Khollam, S. B. Deshpande and V. Ravi, *Mater. Res. Bull.* 38 (11-12) 1601 (2003)

7. Synthesis of ultra fine TiO_2 by citrate gel method
   S. R. Dhage, Renu Pasricha and V. Ravi, *Mater. Res. Bull.* 38 (11-12) 1623 (2003)

8. Influence of various donors on nonlinear I-V characteristics of tin dioxide ceramics
   S. R. Dhage and V. Ravi, *Appl. Phys. Lett.* 83 (22) 4539 (2003)

9. Varistors Based on SnO_2
   Sanjay R. Dhage, Violet Samuel and V. Ravi, *J. Electroceram.* 11 (1-2) 81 (2003)

10. Nonlinear I-V characteristics study of doped SnO_2

S. R. Dhage and V. Ravi and S.K. Date, *Bull. Mater. Sci.* 27 (1) 43 (2004)

11. Nonlinear I-V characteristics of doped SnO_2
S. R. Dhage V.D. Choube and V. Ravi, *Mater. Sci. Eng. B* 110 (2) 168 (2004)

12. Synthesis of $Ce_{0.75}Zr_{0.25}$ by citrate gel method
S.R. Dhage, S.P. Gaikwad, P. Muthukumar and V. Ravi, *Mater. Lett.* 58 (21) 2704 (2004)

13. Synthesis of mesoporous rutile TiO_2
Violet Samuel, P. Muthukumar S.P. Gaikwad, **S.R. Dhage**, and V. Ravi *Mater. Lett.* 58 (20) 2514 (2004)

14. Synthesis of nanocrystalline TiO_2 at 100°C
Sanjay R. Dhage, Vandana D. Choube, Violet Samuel and V. Ravi, *Mater. Lett.* 58 (17-18) 2310 (2004)

15. Synthesis of nanocrystalline SnO_2 powder at 100°C
S.R. Dhage, S.P. Gaikwad, Violet Samuel and V. Ravi *Bull. Mater. Sci.* 27, 221 (2004)

16. Synthesis of bismuth titanate by citrate method
S.R. Dhage, Y.B. Khollam, S.B. Dhespande, H.S. Potdar and V. Ravi, *Mater. Res. Bull.* 39 (13) 1993 (2004)

17. Synthesis of TiO_2 by tartarate gel method
S.R. Dhage, S.P.Gaikwad and V.Ravi, *Bull. Mater. Sci.* 27 (6) 487 (2004)

18. Synthesis of $Ce_{0.75}Zr_{0.25}O_2$ at 100 °C
S.R. Dhage, S.P. Gaikwad, P. Muthukumar and V. Ravi, *Ceramic International*, 31 (1) 211 (2005)

19. Synthesis of bismuth titanate by the urea method
M. Anilkumar, **S.R. Dhage** and V. Ravi, *Mater. Lett.* 59 (4) 514 (2005)

20. Synthesis of fine particles of ZnO at 100 °C
S.R. Dhage, Renu Pasricha and V. Ravi, *Mater. Lett.* 59 (7) 779 (2005)

21. Synthesis of $Sr_{0.5}Ba_{0.5}Nb_2O_6$ by urea method
S.R. Dhage, Renu Pasricha and V. Ravi, *Mater. Lett.* 59 (8-9) 1053 (2005)

22. Coprecipitation method for the preparation of nanocrystalline ferroelectric $SrBi_2Nb_2O_9$
S.P.Gaikwad, **S.R. Dhage**, H.S.Potdar,V.Samuel and V. Ravi, *J. Electroceram.* 14, 83 (2005)

23. Coprecipitation technique for the preparation of ferroelectric $CaBi_4Ti_4O_{15}$
S.P.Gaikwad, **S.R. Dhage** and V. Ravi, *J. Mater. Sci. Mater. Electronics* 16**,** 229 (2005)

24. Synthesis of $BaNb_2O_6$ by the urea method
S.R. Dhage, R. Pasricha and V. Ravi, *Mater. Lett.* 59, 1053 (2005)

25. Synthesis of nanocrystalline Bismuth Oxide at 100°C
M.M. Patil, V.V. Deshpande, **S.R. Dhage** and V.Ravi, *Mater. Lett.* 59, 2523 (2005)

26. Studies on SnO_2-ZrO_2 Solid Solution
S. R. Dhage, Violet Samuel, Renu Pasricha and V. Ravi, *Ceramic International,* (In Press)

27. Varistor property of $SnO_2.CoO.Ta_2O_5$ ceramic modified by barium
S.R. Dhage and V. Ravi, *J. Euro. Ceram. Soc.* (Communicated)

28. Role of Y_2O_3, La_2O_3 and CeO_2 on SnO_2:CoO:Ta_2O_5 varistor system
S. R. Dhage and V. Ravi, *J. Appl. Phys.* (Communicated)

Conferences and workshop

1. National Seminar on Electro and Magneto Ceramics Devices and Systems (NSEMCDS-2002) at Akluj, India (November 2002)

2. International seminar on Recent Advances in Inorganic Materials (RAIM-2002) at IIT Bombay, Mumbai, India (December 2002)

3. National seminar on Engineering Trends in Materials for Electrical Electronic and Magnetic Application (MEEMA-2003) at Pune, India. (November 2003)

4. National workshop on advanced Methods for Materials Characterization (NWMC) at Bhabha Atomic Research Center (BARC) Mumbai-400094, India (November 2004)

5. DAE Solid State Physics Symposium (DAE-SSPS-2004) at Guru Nanak Dev University, Amritsar- 143005, India (December 2004)

6. Symposium on Materials for Automotive Industries, Materials research Society of India (MRSI) at National Chemical Laboratory Pune-411008, India (February 2005)